

AD-A273 844



11

The Pennsylvania State University
APPLIED RESEARCH LABORATORY
P.O. Box 30
State College, PA 16804

3
**THE HIGH REYNOLDS NUMBER FLOW
THROUGH AN AXIAL-FLOW PUMP**

**S DTIC
ELECTE
DEC 17 1993
A**

by

W. C. Zierke
W. A. Straka
P. D. Taylor

Technical Report No. TR 93-12
November 1993

*Original contains color
plates: All DTIC reproductions will be in black and white*

Supported by:
Advanced Research Projects Agency

L.R. Hettche, Director
Applied Research Laboratory

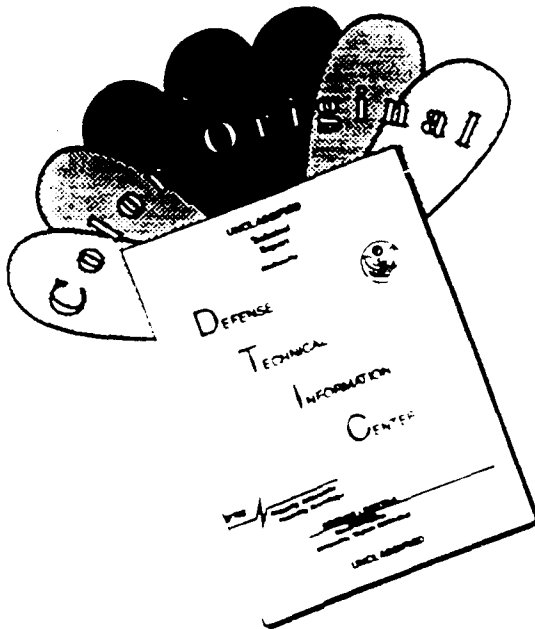
Approved for public release; distribution unlimited

93-30554



93 12 16 034

DISCLAIMER NOTICE



THIS DOCUMENT IS BEST
QUALITY AVAILABLE. THE COPY
FURNISHED TO DTIC CONTAINED
A SIGNIFICANT NUMBER OF
COLOR PAGES WHICH DO NOT
REPRODUCE LEGIBLY ON BLACK
AND WHITE MICROFICHE.

REPORT DOCUMENTATION PAGE

Form Approved
OMB No. 0704-0188

Public reporting burden for this collection of information is estimated to average 1 hour per response, including the time for reviewing instructions, searching existing data sources, gathering and maintaining the data needed, and completing and reviewing the collection of information. Send comments regarding this burden estimate or any other aspect of this collection of information, including suggestions for reducing the burden, to Washington Headquarters Services, Directorate for Information Operations and Reports, 1215 Jefferson Davis Highway, Suite 1204, Arlington, VA 22202-4302, and to the Office of Management and Budget, Paperwork Reduction Project (0704-0188), Washington, DC 20503.

1. AGENCY USE ONLY (Leave blank)			2. REPORT DATE November 1993		3. REPORT TYPE AND DATES COVERED	
4. TITLE AND SUBTITLE The High Reynolds Number Flow Through an Axial-Flow Pump			5. FUNDING NUMBERS N00039-92-C-0100			
6. AUTHOR(S) W. C. Zierke, W. A. Straka, P. D. Taylor						
7. PERFORMING ORGANIZATION NAME(S) AND ADDRESS(ES) Applied Research Laboratory P. O. Box 30 State College, PA 16804			8. PERFORMING ORGANIZATION REPORT NUMBER TR#-12			
9. SPONSORING/MONITORING AGENCY NAME(S) AND ADDRESS(ES) Advanced Research Projects Agency 3701 N. Fairfax Dr. Arlington, Va 22203-1717			10. SPONSORING/MONITORING AGENCY REPORT NUMBER			
11. SUPPLEMENTARY NOTES						
12a. DISTRIBUTION/AVAILABILITY STATEMENT Unlimited			12b. DISTRIBUTION CODE			
13. ABSTRACT (Maximum 200 words) <p>The high Reynolds number pump (HIREP) facility at ARL Penn State has been used to perform a low-speed, large-scale experiment of the incompressible flow of water through a two-blade-row turbomachine. HIREP can involve blade chord Reynolds numbers as high as 6,000,000 and can accommodate a variety of instrumentation in both a stationary and a rotating frame of reference. The objectives of this experiment were to provide a database for comparison with three-dimensional, viscous (turbulent) flow computations, to evaluate the engineering models, and to improve our physical understanding of many of the phenomena involved in this complex flow field.</p> <p>The experimental results include a large quantity of data acquired throughout HIREP. A five-hole probe survey of the inlet flow 37.0% chord upstream of the 1st guide vane (IGV) leading edge is sufficient to give information for the inflow boundary conditions, while some static-pressure information is available to help establish an outflow boundary condition.</p>						
14. SUBJECT TERMS High Reynolds Number Flow, axial-flow, pump, turbomachine, viscous flow					15. NUMBER OF PAGES 242	
					16. PRICE CODE	
17. SECURITY CLASSIFICATION OF REPORT UNCLASSIFIED		18. SECURITY CLASSIFICATION OF THIS PAGE UNCLASSIFIED		19. SECURITY CLASSIFICATION OF ABSTRACT UNCLASSIFIED		20. LIMITATION OF ABSTRACT UNLIMITED

Cont.

Static-pressure distributions are available on the blade surfaces, while surface flow visualization patterns of skin-friction lines are available on blade surfaces and on the endwalls in the vicinity of the blade passages. Five-hole probe measurements exist on an axial plane 49.7% chord downstream of the IGV trailing edge, including information on secondary flows and IGV wakes. This survey includes a Fourier analysis to obtain the spatial harmonic content of the flow. A two-component laser Doppler velocimeter (LDV) velocity survey exists 88.5% chord downstream of the IGV trailing edge, while LDV surveys at 76.2% span include information on the decay of the potential effects upstream of the rotor blades and the wakes downstream of the rotor blades. Additional LDV surveys exist at three measurement planes downstream of the rotor blades, including information on the tip leakage vortices and the rotor blade wakes. These measurement planes are located at 4.8%, 21.4%, and 32.2% chord downstream of the tip of the rotor blade trailing edge. Slow- and fast-response total pressure measurements also exist at this furthest downstream plane. Finally, measurements show the tip leakage vortex trajectory, the rotor blade shaft thrust and torque, and the cavitation performance. In conclusion, the HIREP results have provided experimental detail of many important flow features, been compared with several engineering models, and, finally, should prove to be a worthwhile and challenging test case when used during the validation of numerical computational computer codes.

Abstract

The high Reynolds number pump (HIREP) facility at ARL Penn State has been used to perform a low-speed, large-scale experiment of the incompressible flow of water through a two-blade-row turbomachine. HIREP can involve blade chord Reynolds numbers as high as 6,000,000 and can accommodate a variety of instrumentation in both a stationary and a rotating frame of reference. The objectives of this experiment were to provide a database for comparison with three-dimensional, viscous (turbulent) flow computations, to evaluate engineering models, and to improve our physical understanding of many of the phenomena involved in this complex flow field.

The experimental results include a large quantity of data acquired throughout HIREP. A five-hole probe survey of the inlet flow 37.0% chord upstream of the inlet guide vane (IGV) leading edge is sufficient to give information for the inflow boundary conditions, while some static-pressure information is available to help establish an outflow boundary condition. Static-pressure distributions are available on the blade surfaces, while surface flow visualization patterns of skin-friction lines are available on blade surfaces and on the endwalls in the vicinity of the blade passages. Five-hole probe measurements exist on an axial plane 49.7% chord downstream of the IGV trailing edge, including information on secondary flows and IGV wakes. This survey includes a Fourier analysis to obtain the spatial harmonic content of the flow. A two-component laser Doppler velocimeter (LDV) velocity survey exists 88.5% chord downstream of the IGV trailing edge, while LDV surveys at 76.2% span include information on the decay of the potential effects upstream of the rotor blades and the wakes downstream of the rotor blades. Additional LDV surveys exist at three measurement planes downstream of the rotor blades, including information on the tip leakage vortices and the rotor blade wakes. These measurement planes are located at 4.8%, 21.4%, and 32.2% chord downstream of the tip of the rotor blade trailing edge. Slow- and fast-response total-pressure measurements also exist at this furthest downstream plane. Finally, measurements show the tip leakage vortex trajectory, the rotor blade shaft thrust and torque, and the cavitation performance. In conclusion, the HIREP results have provided experimental detail of many important flow features, been compared with several engineering models, and, finally, should prove to be a worthwhile and challenging test case when used during the validation of numerical computational computer codes.

Accession For	
NTIS	CRA&I
DTIC	TAB
Unpublished	
Justification	
By	
Distribution /	
Availability Codes	
Dist	Avail at J or Special
A-1	

Acknowledgements

We would like to extend our appreciation to the Advanced Research Projects Agency (ARPA) and Mr. Gary W. Jones for supporting this research under the Submarine Technology Program. As the head of the Applied Science Division at the Applied Research Laboratory (ARL) when this program began, Dr. Robert E. Henderson was instrumental in initiating this experiment. Also, as heads of the Fluid Dynamics and Hydroacoustics Departments, respectively, Dr. Michael L. Billet and Dr. Donald E. Thompson gave valuable support and suggestions throughout the program. A special thanks goes to Dr. John J. Adamczyk at the NASA Lewis Research Center for his many helpful suggestions.

Many engineers at ARL Penn State were essential to the completion of this research program. Mr. Carl G. Schott designed the new inlet guide vanes and rotor blades and acted as the project engineer for the first installation of the experiment. Carl continued to give valuable recommendations as we later compared experimental results with his design calculations. Mr. Fred E. Smith worked with the Armstrong Mold Corporation and the Femco Machine Company, as well as our own machine shop, to keep the blade fabrication on schedule. Fred also acted as the test engineer for the first experimental installation. Dr. Howard L. Petrie contributed his expertise to the laser Doppler velocimetry measurements and the laser light sheet visualization. Mr. Michael L. Jonson gave input to areas of the program of interest to the Hydroacoustics Department. Finally, Mr. David R. Stinebring, Mr. Kevin J. Farrell, and Dr. Steven Deutsch were very helpful in many fluid mechanics related issues. Several other engineers and technicians also had key roles in the completion of this research program.

Table of Contents

	<u>Page</u>
List of Tables	vi
List of Figures	vii
Nomenclature	xvi
Introduction	1
Garfield Thomas Water Tunnel	2
High Reynolds Number Pump Facility	3
Experimental Technique	6
Rotor Shaft Torque and Thrust Measurements	6
Blade Static-Pressure Measurements	7
Surface Flow Visualization	9
Cavitation Visualization	11
Laser Light Sheet Visualization	11
Slow-Response Pressure Probes	12
Fast-Response Pressure Probe	15
Laser Doppler Velocimeter	16
Experimental Results and Discussion	20
Inlet Conditions	20
IGV Static-Pressure Distribution	22
IGV Surface Flow Visualization	23
IGV Exit Flow	28
Harmonic Content of the IGV Exit Flow	35
Unsteadiness of the IGV Exit Flow	40
Blade Lean	44
Rotor Blade Static-Pressure Distribution	46
Rotor Shaft Thrust and Torque	47
Rotor Blade Surface Flow Visualization	48
Rotor Blade Exit Flow	52
Harmonic Content of the Rotor Blade Exit Flow	57
Unsteadiness of the Rotor Blade Exit Flow	60
Visualization of the Rotor Tip Leakage Vortex	62
Vortex Models	66
Details of the Rotor Tip Leakage Vortex	68
Cavitation Performance	74

Table of Contents (Cont.)

	<u>Page</u>
Summary and Conclusions	78
Bibliography	81
Appendix A: Five-Hole Probe Uncertainty Analysis	89
Appendix B: Pressure Probe Frequency Response	97
Appendix C: LDV Surveys, Bin Size, and Uncertainty	99

List of Tables

<u>Table</u>		<u>Page</u>
1	Errors in Thrust Measurements	7
2	Radial Locations of Individual Probes of the Five-Hole Probe Rake	14
3	Parameters of the Inlet Boundary Layer on the Tunnel Liner	21
4	Characteristics of the Endwall Boundary Layers between Blade Rows	35
5	Spatial Harmonics in the IGV Exit Flow that Satisfy Accuracy Requirements	38
6	Maximum Nondeterministic or Turbulence Unsteadiness within IGV Wakes	41
7	Characteristics of the Casing Endwall Boundary Layers Downstream of the Rotor Blades	54
8	Spatial Harmonics in the Rotor Blade Exit Flow that Satisfy Accuracy Requirements	59
9	Measured and Corrected Parameters for the Rotor Tip Leakage Vortices	72
10	Data from Five-Hole Probe Calibration Plots	92
11	Uncertainty in Five-Hole Probe Measurements to 95% Confidence	95
12	LDV Surveys Corresponding to Locations Shown in Figure 12	100
13	Precision Errors in Mean Velocity LDV Measurements	103

List of Figures

<u>Figure</u>		<u>Page</u>
1	Garfield Thomas Water Tunnel	104
2	High Reynolds Number Pump Facility	105
3	Computer-Generated Graphical Image of the New HIREP Blades (a) Downstream and Inboard Views (b) Isometric View with Coordinate System	106 107
4	IGV Static-Pressure Tap Locations	108
5	Rotor Blade Static-Pressure Tap Locations	109
6	Monitor Velocity Validation	110
7	Pressure Probe Measurement Locations	111
8	Sample Probe within the Five-Hole Probe Rake	112
9	Schematic of Fast-Response Total-Pressure Probe	113
10	Sensitivity Calibration Curve for the Fast-Response Total-Pressure Probe	114
11	Estimated Amplitude Frequency Response of the Fast-Response Total-Pressure Probe	115
12	LDV Measurement Locations	116
13	Unsteady Velocity Signal	117
14	Inlet Pressure Coefficients from the Five-Hole Probe Radial Survey (37.0% Chord Upstream of the IGV Leading Edge)	118
15	Inlet Velocities from the Five-Hole Probe Radial Survey (37.0% Chord Upstream of the IGV Leading Edge)	119
16	Inlet Boundary Layer on the Tunnel Liner Measured with a Five-Hole Probe	120
17	IGV Static-Pressure Distribution	121
18	IGV Static-Pressure Contours	122

List of Figures (Cont.)

<u>Figure</u>		<u>Page</u>
19	Schematic of Surface Flow Visualization on the IGV Hub Surface	123
20	Evolution of Horseshoe and Passage Vortices (Sieverding and Van den Bosche [1983])	124
21	Schematic of Surface Flow Visualization on the IGV Suction Surface	125
22	Photograph of the Surface Flow Visualization Showing the IGV Suction Surface Corner Separation	126
23	Schematic of Surface Flow Visualization on the IGV Casing Surface	127
24	Schematic of Surface Flow Visualization on the IGV Pressure Surface	128
25	Photograph of the Surface Flow Visualization Showing the IGV Pressure Surface	129
26	Schematic of IGV Secondary Flow: Passage Vortices and Trailing Vortex Sheets	130
27	Schematic of IGV Secondary Flow: Interpretation of Surface Flow Visualization	131
28	Circumferential Variation of Velocity Components 49.7% Chord Axially Downstream of the IGV Trailing Edge: Five-Hole Probe Measurements and Lifting Surface Calculations; (a) 4.8% Span (b) 9.5% Span (c) 19.0% Span (d) 38.1% Span (e) 52.4% Span (f) 61.9% Span (g) 71.4% Span (h) 76.2% Span (i) 81.0% Span (j) 85.7% Span (k) 90.5% Span (l) 95.2% Span	132 133 134 135 136 137 138 139 140 141 142 143

List of Figures (Cont.)

<u>Figure</u>	<u>Page</u>
29 Passage-Averaged IGV Wakes Measured 49.7% Chord Axially Downstream of the IGV Trailing Edge with Five-Hole Probes:	
(a) 4.8%, 9.5%, 19.0%, and 52.4% Span	144
(b) 61.9%, 71.4%, 76.2%, and 81.0% Span	145
30 Secondary Velocity Vectors 49.7% Chord Axially Downstream of the IGV Trailing Edge:	
(a) Lifting Surface Theory Calculations	146
(b) Five-Hole Probe Rake Surveys	147
(c) Five-Hole Probe Radial Surveys	148
31 Total-Pressure Coefficient Contours Measured 49.7% Chord Axially Downstream of the IGV Trailing Edge with Five-Hole Probes	149
32 Circumferentially-Averaged Velocities Measured 49.7% Chord Axially Downstream of the IGV Trailing Edge with Five-Hole Probes	150
33 Circumferentially-Averaged Pressure Coefficients Measured 49.7% Chord Axially Downstream of the IGV Trailing Edge with Five-Hole Probes	151
34 Circumferentially-Averaged Velocities Measured 88.5% Chord Axially Downstream of the IGV Trailing Edge with LDV	152
35 Skewed Boundary Layer Measured Above the Rotating Hub 88.5% Chord Axially Downstream of the IGV Trailing Edge with LDV	153
36 Comparison of Fourier Analysis Using a Full Circumferential Survey and Using a Combination of Individual Passages: Fourier Coefficients of Axial Velocity at 61.9% Span and 49.7% Chord Axially Downstream of the IGV Trailing Edge	154
37 Fourier Coefficients of Velocity Components 49.7% Chord Axially Downstream of the IGV Trailing Edge:	
(a) 4.8% Span	155
(b) 52.4% Span	156
(c) 81.0% Span	157

List of Figures (Cont.)

<u>Figure</u>	<u>Page</u>
38 Spanwise Variation of Fourier Coefficients (Magnitude and Phase) 49.7% Chord Axially Downstream of the IGV Trailing Edge for the Harmonics of Order 13, 26, 39, 52, and 69: (a) Axial Velocity (b) Radial Velocity (c) Tangential Velocity	158 159 160
39 Overall Unsteady Velocity Correlations Measured 88.5% Chord Axially Downstream of the IGV Trailing Edge with LDV	161
40 Nondeterministic Unsteady Velocity Correlations Measured 88.5% Chord Axially Downstream of the IGV Trailing Edge with LDV	162
41 Deterministic Unsteady Velocity Correlations Measured 88.5% Chord Axially Downstream of the IGV Trailing Edge	163
42 Unsteady Potential Flow Effect at 76.2% Span: (a) 28.0% Chord Axially Upstream of the Rotor Blade Leading Edge (b) 18.7% Chord Axially Upstream of the Rotor Blade Leading Edge (c) 9.4% Chord Axially Upstream of the Rotor Blade Leading Edge (d) 4.7% Chord Axially Upstream of the Rotor Blade Leading Edge (e) 2.3% Chord Axially Upstream of the Rotor Blade Leading Edge (f) 0.9% Chord Axially Upstream of the Rotor Blade Leading Edge (g) At the Rotor Blade Leading Edge	164 165 166 167 168 169 170
43 Decay of Deterministic Unsteady Velocity Correlations at 76.2% Chord	171
44 Rotor Blade Static-Pressure Distribution	172
45 Rotor Blade Static-Pressure Contours	173
46 Variation of Rotor Shaft Thrust and Torque with Volumetric Flow Coefficient	174
47 Variation of Rotor Shaft Thrust and Torque with Flow Coefficient	175
48 Schematic of Surface Flow Visualization on the Rotor Blade Hub Surface	176
49 Schematic of Surface Flow Visualization on the Rotor Blade Suction Surface	177

List of Figures (Cont.)

<u>Figure</u>	<u>Page</u>
50 Photograph of the Surface Flow Visualization Showing the Rotor Blade Suction Surface Corner Separation	178
51 Schematic of Surface Flow Visualization on the Rotor Blade Pressure Surface	179
52 Schematic of Surface Flow Visualization on the Rotor Blade Tip Section	180
53 Schematic of Rotor Blade Secondary Flow: Passage Vortices and Trailing Vortex Sheets	181
54 Schematic of Rotor Blade Secondary Flow: Interpretation of Surface Flow Visualization	182
55 Photograph of a Cavitating Rotor Tip Leakage Vortex and a Cavitating Trailing Edge Separation Vortex Near a Rotor Blade Tip Section (Farrell [1989])	183
56 Axial Velocity Contours of LDV Measurements: (a) 4.8% Chord Axially Downstream of the Rotor Tip Trailing Edge (b) 21.4% Chord Axially Downstream of the Rotor Tip Trailing Edge (c) 32.2% Chord Axially Downstream of the Rotor Tip Trailing Edge	184 185 186
57 Tangential Velocity Contours of LDV Measurements: (a) 4.8% Chord Axially Downstream of the Rotor Tip Trailing Edge (b) 21.4% Chord Axially Downstream of the Rotor Tip Trailing Edge (c) 32.2% Chord Axially Downstream of the Rotor Tip Trailing Edge	187 188 189
58 Passage-Averaged Rotor Blade Wakes From LDV Measurements at 76.2% Span: (a) 2.5%, 4.8%, 7.2%, and 11.8% Chord Axially Downstream of the Rotor Blade trailing Edge (b) 16.5%, 21.1%, and 24.6% Chord Axially Downstream of the Rotor Blade Trailing Edge	190 191
59 Circumferential Variation of the Axial Velocity Measured 32.2% Chord Axially Downstream of the Rotor Tip Trailing Edge with LDV	192
60 Circumferential Variation of the Tangential Velocity Measured 32.2% Chord Axially Downstream of the Rotor Tip Trailing Edge with LDV	193

List of Figures (Cont.)

<u>Figure</u>	<u>Page</u>
61 Circumferential Variation of the Axial Nondeterministic Unsteady Velocity Correlation Measured 32.2% Chord Axially Downstream of the Rotor Tip Trailing Edge with LDV	194
62 Circumferential Variation of the Tangential Nondeterministic Unsteady Velocity Correlation Measured 32.2% Chord Axially Downstream of the Rotor Tip Trailing Edge with LDV	195
63 Circumferentially-Averaged Velocities Measured with LDV: (a) 4.8% Chord Axially Downstream of the Rotor Tip Trailing Edge	196
(b) 21.4% Chord Axially Downstream of the Rotor Tip Trailing Edge	197
(c) 32.2% Chord Axially Downstream of the Rotor Tip Trailing Edge	198
64 Spanwise Variation of Total-Pressure Coefficients 32.2% Chord Axially Downstream of the Rotor Tip Trailing Edge (at Two IGV Index Locations)	199
65 Estimated Spanwise Variation of Total- and Static-Pressure Coefficients 32.2% Chord Axially Downstream of the Rotor Tip Trailing Edge (without the Presence of an IGV Wake)	200
66 Contours of the Total-Pressure Variation Coefficient Measured with the Fast-Response, Total-Pressure Probe 32.2% Chord Axially Downstream of the Rotor Tip Trailing Edge	201
67 Contours of the Total-Pressure Coefficient Measured with the Fast-Response, Total-Pressure Probe 32.2% Chord Axially Downstream of the Rotor Tip Trailing Edge	202
68 Secondary Velocity Vectors Calculated 32.2% Chord Axially Downstream of the Rotor Tip Trailing Edge with Lifting Surface Theory	203
69 Fourier Coefficients of Velocity Components 32.2% Chord Axially Downstream of the Rotor Tip Trailing Edge: (a) 9.5% Span	204
(b) 57.1% Span	205
(c) 94.3% Span	206

List of Figures (Cont.)

<u>Figure</u>		<u>Page</u>
70	Spanwise Variation of Fourier Coefficients (Magnitude and Phase) 32.2% Chord Axially Downstream of the Rotor Tip Trailing Edge for the Harmonics of Order 7, 14, 21, 28, and 35: (a) Axial Velocity (b) Tangential Velocity	207 208
71	Power Spectra of the Total-Pressure Measurements 32.2% Chord Axially Downstream of the Rotor Tip Trailing Edge: (a) 9.5% Span (b) 57.1% Span (c) 94.3% Span	209 210 211
72	Overall Unsteady Velocity Correlations Measured with LDV: (a) 21.4% Chord Axially Downstream of the Rotor Tip Trailing Edge (b) 32.2% Chord Axially Downstream of the Rotor Tip Trailing Edge	212 213
73	Nondeterministic Unsteady Velocity Correlations Measured with LDV: (a) 21.4% Chord Axially Downstream of the Rotor Tip Trailing Edge (b) 32.2% Chord Axially Downstream of the Rotor Tip Trailing Edge	214 215
74	Nondeterministic Axial Velocity Correlation Contours of LDV Measurements: (a) 4.8% Chord Axially Downstream of the Rotor Tip Trailing Edge (b) 21.4% Chord Axially Downstream of the Rotor Tip Trailing Edge (c) 32.2% Chord Axially Downstream of the Rotor Tip Trailing Edge	216 217 218
75	Nondeterministic Tangential Velocity Correlation Contours of LDV Measurements: (a) 4.8% Chord Axially Downstream of the Rotor Tip Trailing Edge (b) 21.4% Chord Axially Downstream of the Rotor Tip Trailing Edge (c) 32.2% Chord Axially Downstream of the Rotor Tip Trailing Edge	219 220 221
76	Deterministic Unsteady Velocity Correlations Measured with LDV: (a) 21.4% Chord Axially Downstream of the Rotor Tip Trailing Edge (b) 32.2% Chord Axially Downstream of the Rotor Tip Trailing Edge	222 223

List of Figures (Cont.)

<u>Figure</u>	<u>Page</u>
77 Deterministic Unsteady Velocity Correlations Downstream of a Rotor (Dring, Joslyn, and Hardin [1980]):	
(a) $\phi = 0.77$ and 10% Chord Axially Downstream of the Rotor Blade Trailing Edge	224
(b) $\phi = 0.59$ and 10% Chord Axially Downstream of the Rotor Blade Trailing Edge	225
(c) $\phi = 0.59$ and 50% Chord Axially Downstream of the Rotor Blade Trailing Edge	226
78 Photograph of a Cavitating Rotor Tip Leakage Vortex Emanating from Near the Leading Edge	227
79 Photograph of a Cavitating Rotor Tip Leakage Vortex Near the Trailing Edge	228
80 Schematic of the Relative Skin-Friction Lines Across the Rotor Blade Tip Section and the Position of the Rotor Tip Leakage Vortex in the Blade-to-Blade Plane, as Determined from Cavitation, from LDV Data, and from the Similarity Model of Chen, Greitzer, Tan, and Marble [1991]	229
81 Spanwise Position of the Core of the Rotor Tip Leakage Vortex	230
82 Photograph of a Cavitating Rotor Tip Leakage Vortex with Vortex Kinking	231
83 Photograph of a Cavitating Rotor Tip Leakage Vortex with a Streamwise Gap of Noncavitating Flow	232
84 Vortex Tangential Velocity Distributions for the Rotor Tip Leakage Vortices Measured 4.8%, 21.4%, and 32.2% Chord Axially Downstream of the Rotor Tip Trailing Edge	233
85 Vortex Axial Velocity Distributions for the Rotor Tip Leakage Vortices Measured 4.8%, 21.4%, and 32.2% Chord Axially Downstream of the Rotor Tip Trailing Edge	234
86 Nondimensional Tangential Velocity Distributions for the Rotor Tip Leakage Vortices—Measurements and Ideal Formulations	235
87 Nondimensional Axial Velocity Distributions for the Rotor Tip Leakage Vortices—Measurements and Ideal Formulations	236

List of Figures (Cont.)

<u>Figure</u>	<u>Page</u>
88 Spanwise Distribution of Circulation on the Inlet Guide Vanes and Rotor Blades	237
89 Cavitation Inception at Volumetric Flow Coefficients of 1.36 and 1.22	238
90 Photographs of a Rotor Blade with Vortex Cavitation ($\sigma=0.99$) and a Rotor Blade with Vortex and Gap Cavitation ($\sigma=1.55$)	239
91 Calculations of Cavitation Inception Using the Model of Farrell [1992]	240
92 Schematic and Photograph of Cavitation on the Rotor Blade Suction Surface	241
93 LDV Bin Size Dependence for a Rotor Blade Wake (Tangential Velocity at 76.2% Span and 2.5% Chord Axially Downstream of the Rotor Tip Trailing Edge)	242

Nomenclature

a_n	Fourier coefficients of the cosine terms
A	annular area through HIREP (7.22 ft^2); amplitude of oscillation; cross-sectional area of a cone (Appendix B)
b_n	Fourier coefficients of the sine terms
B	bias error (Appendix C)
c	blade chord; speed of sound (Appendix B)
C_L	design lift coefficient
C_{L_0}	tip lift coefficient at the zero clearance condition
C_m	mass flow rate coefficient = $\frac{\dot{m}}{\rho A V_{ref}}$
C_p	static-pressure coefficient = $\frac{p - p_{ref}}{\frac{1}{2} \rho V_{ref}^2}$
C_{p_T}	total-pressure coefficient = $\frac{p_T - p_{ref}}{\frac{1}{2} \rho V_{ref}^2}$
$C_{\Delta p_T}$	total-pressure variation coefficient = $\frac{\Delta p_T}{\frac{1}{2} \rho V_{ref}^2}$
$C_{p_{static}}$	static-pressure coefficient for five-hole probe calibration (Appendix A)
$C_{p_{total}}$	total-pressure coefficient for five-hole probe calibration (Appendix A)
C_{pitch}	five-hole probe pitch coefficient (Appendix A)

C_Q	torque coefficient = $\frac{M_Q}{\frac{1}{2} \rho V_{ref}^2 A r_{tip}}$
C_T	thrust coefficient = $\frac{F_T}{\frac{1}{2} \rho V_{ref}^2 A}$
C_{yaw}	five-hole probe yaw coefficient (Appendix A)
D	diffusion factor
D_{tip}	rotor blade diameter
\hat{e}_r	unit vector in radial direction
$\hat{e}_{x_{tube}}$	unit vector along the length of a pressure tube
f	frequency (Appendix B)
F	blade force
F_T	rotor shaft thrust
h	rotor tip clearance
H	shape factor $\frac{\delta^*}{\theta}$
HIREP	high Reynolds number pump
i	imaginary unit number = $\sqrt{-1}$ (Appendix B)
IGV	inlet guide vane
J	advance ratio = $\frac{V_{ref}}{nD_{tip}}$; number of experimental variables (Appendix A)

k	velocity potential amplitude variation factor = n/r ; air content correction factor; wave number (Appendix B)
k_s	empirical constant describing the secondary circulation
K_p	pressure coefficient = $\frac{p - p_{ref}}{\frac{1}{2} \rho U_{tip}^2}$
K_Q	torque coefficient $\frac{M_Q}{\rho n^2 D_{tip}^5}$
K_T	thrust coefficient $\frac{F_T}{\rho n^2 D_{tip}^4}$
LDV	laser Doppler velocimeter
m	data sample index within a given discrete storage window or bin
\dot{m}	mass flow rate
M	number of data samples within a given discrete storage window or bin
M_Q	rotor shaft torque
n	rotor shaft speed in revolutions per second; data sample index; harmonic order; normal coordinate
n_w	index of discrete storage windows or bins
N	number of data samples
N_B	number of blades
N_w	number of discrete storage windows or bins

p	static pressure
\hat{p}	acoustic pressure (Appendix B)
p_T	total or stagnation pressure
p_v	vapor pressure (0.5968 psia for water at 85°F)
P,PS	pressure surface
Q	volume flow rate
r	radius (relative to tunnel axis); radius (relative to vortex axis); experimental result (Appendix A)
r_c	vortex core radius
$r_{c_{\infty}}$	vortex core radius which would form for an infinite clearance
R_c	radius of curvature of the meridional projection of the streamlines
s	blade spacing
S,SS	suction surface
S	precision error (Appendix C)
$S^{\bar{v}}$	precision error in the mean velocity (Appendix C)
S^t	precision error in the turbulence intensity (Appendix C)
SNR	signal-to-noise ratio
STANS	parabolic boundary layer code of Crawford and Kays [1976]
t	time
T	period; transfer matrix with elements T_{11} , T_{12} , T_{21} , and T_{22} (Appendix B)

U_e	boundary layer edge velocity
U_{tip}	rotor blade tip speed
U_{X_i}	uncertainty in the measured value X_i to 95% confidence (Appendix A)
\hat{v}	acoustic mass velocity (Appendix B)
\mathbf{V}	velocity (relative to vortex coordinate system)
V	voltage;
	velocity (relative to tunnel coordinate system)
u	local streamwise velocity
V_n	velocity for the n^{th} harmonic
V_p	population mean velocity (Appendix C)
V_{ref}	inlet reference axial velocity
w	local crossflow velocity
W	relative velocity
x_c	distance along the blade chord
x_{tube}	distance along the length of a pressure tube
X_i	experimental variables from $i = 1 \rightarrow J$ (Appendix A)
y	coordinate normal to surface
Y	immersion from casing endwall (Figures 7 and 12)
y_c	distance normal to the camber line
z	axial coordinate
α	vortex radial influx parameter;
	pitch flow angle relative to five-hole probe tip (Appendix A)

β	yaw flow angle relative to five-hole probe tip (Appendix A)
γ	stagger angle
Γ	circulation
$\Gamma_{\text{--}}$	total vortex circulation
δ	boundary layer thickness (where $\kappa = 0.99 U_e$)
δ^*	displacement thickness
$(\Delta K_p)_{\text{mean}}$	difference in K_p across the blade at some mean radius (a radius outside the endwall region)
Δp_T	total-pressure variations from the mean
$\Delta\theta$	change in the θ location of the wake between the trailing edge and the measurement plane
ζ	turbulence intensity (Appendix C)
θ	tangential coordinate; momentum thickness
θ_p	tangential coordinate over a specified period
κ	vortex strength; blade metal angle
λ	ratio of the tip clearance to the maximum thickness of the rotor blade tip section
ν	kinematic viscosity ($0.000008755 \frac{\text{ft}^2}{\text{sec}}$ for water at 85°F)
ρ	fluid density ($1.932 \frac{\text{slugs}}{\text{ft}^3}$ for water at 85°F)

σ blade solidity = c/s ;

$$\text{cavitation number} = \frac{p_{ref} - p_v}{\frac{1}{2} \rho U_{tip}^2}$$

$$\phi \quad \text{flow coefficient} = \frac{V_{ref}}{U_{tip}}$$

angle between the meridional and axial directions

ϕ_n phase angle of the n_{th} harmonic

$$\phi_{vol} \quad \text{volumetric flow coefficient} = \frac{Q}{nD_{tip}^3} \approx \frac{AV_{ref}}{nD_{tip}^3}$$

$\tilde{\Phi}_n$ velocity potential

Φ_0 velocity potential amplitude

ω angular velocity of the vortex core

Ω angular velocity of the rotor

Subscripts

<i>avg</i>	average-passage value
<i>corr</i>	correction for the effects of blade rotation
<i>m</i>	data sample index within a given discrete storage window or bin; meridional direction
<i>max</i>	maximum value
<i>meas</i>	measured value
<i>min</i>	minimum value
<i>n</i>	data sample index; crossflow direction; normal direction
<i>noise</i>	background noise level
<i>r</i>	radial direction
<i>ref</i>	reference measurement
<i>s</i>	streamwise direction
<i>t</i>	rotor blade tip (in figures)
<i>sn</i>	cross-correlation of streamwise and crossflow directions
<i>tap</i>	value at rotor blade pressure tap
<i>tip</i>	rotor blade tip
<i>trans</i>	value at rotor blade pressure transducer
<i>z</i>	axial direction
θ	tangential direction

1	blade row inlet; conical pipe inlet (Appendix B)
1,2,3,4,5	five-hole probe hole numbers (Appendix A)
2	blade row exit; conical pipe exit (Appendix B)
∞	outside of endwall boundary layer

Superscripts

-	ensemble average;
	average value or magnitude (Appendix A)
=	time average;
	circumferential average
\sim	periodic or deterministic quantity;
	circumferential-varying quantity
/	random or nondeterministic quantity

Note

On the figures that plot the overall, deterministic, or nondeterministic unsteady velocity correlations, the figures use the nomenclature $(V_i \ V_j)$ instead of $\overline{(\tilde{V}_i + V'_i)(\tilde{V}_j + V'_j)}$, $\overline{\tilde{V}_i \tilde{V}_j}$, or $\overline{V'_i V'_j}$, respectively.

Introduction

Low-speed, large-scale experiments within multiple-blade-row machines have become increasingly important in the field of turbomachinery over the last several years. There are several reasons for this trend. The first is the increasing use of numerical prediction methods in the design and analysis of multiple-blade-row machines. In order to extend the range of confidence that we have in these numerical codes, we must perform some means of validation by comparing the numerical results with data from well-controlled experiments. A second reason for this experimental trend lies in the fact that despite the great advances in numerical prediction codes, many critical calculations required by the designer cannot yet be performed by solving the governing equations from first principles. Engineering models are still required and these models are still empirical in nature and require experimental data for closure. A final reason for the growing number of multiple-blade-row turbomachinery experiments lies in our lack of physical understanding of many of the phenomena involved in this complex flow field. Many of these phenomena are specific to multiple-blade-row turbomachines and have not been addressed with enough detail.

None of the growing number of low-speed, large-scale, multiple-blade-row experiments has dealt with the incompressible flow of water at large blade-chord Reynolds numbers. In order to extend the range of our numerical prediction codes, flow models, and physical understanding to this incompressible flow problem, we need to perform new experiments. ARL Penn State has a high Reynolds number pump (HIREP) facility that can achieve blade chord Reynolds numbers as high as 6,000,000 and can accommodate a variety of instrumentation in both a stationary and a rotating frame of reference. Farrell [1989] used HIREP to investigate the effect of rotor blade tip clearance on the tip leakage vortex and subsequent vortex cavitation. In this successful cavitation experiment, Farrell [1989] did not acquire the flow field data necessary for either comparing with numerical predictions or describing other important flow regimes. Using new blade designs within HIREP, we have performed an experiment using several types of experimental techniques. The experiment was performed during two different installations of HIREP into the Garfield Thomas Water Tunnel. The first installation focussed primarily on establishing the overall performance of the new blade designs, with the test time extending for three weeks. The initial flow measurements in this first installation were greatly expanded during the second installation, with the test time also expanded to nearly six weeks.

This report describes the facility, including information about the new blade designs, and the experimental technique. Then, the report describes the flow physics, using the experimental data and data analysis. Throughout this discussion, the calculations obtained during the design phase of the program are compared with the data in order to evaluate our design codes. Other pertinent flow models are also compared with the data. The complete description of the experimental results should provide an excellent test case for comparison with numerical computations.

Garfield Thomas Water Tunnel

This experiment was performed in the Garfield Thomas Water Tunnel at ARL Penn State. As seen in Figure 1, this tunnel has a 4-foot diameter, 14-foot long test section which supports water velocities up to 60 ft/sec. Lauchle, Billet, and Deutsch [1989] give a description of the tunnel, as well as some of the basic experimental procedures. These procedures involve accurate control of both the velocity and the pressure within the test section. Velocity control is achieved by varying the drive impeller rotational speed and the pitch of the impeller blades. This impeller is driven by a 2000-hp variable-speed (0-180 rpm) induction motor, while the blade pitch can be varied over 28 degrees by means of a hydraulic servomechanism which operates remotely from the tunnel operating console.

For many years, ARL Penn State has used the Garfield Thomas Water Tunnel for cavitation studies. Cavitation is the gas-liquid region created by a localized pressure reduction produced by dynamic action of the fluid in either the interior or at the boundaries of a liquid. Therefore, control of the static pressure within the test section becomes imperative. Pressure control is achieved by varying the air pressure on top of a large pressure-regulating tank connected to the bottom leg of the tunnel. This tank includes a redwood float that prevents air from coming in contact with a large surface area of water; a necessary feature when one is concerned with gas content effects. Since the gas content does affect cavitation nuclei and subsequent cavitation growth, cavitation experiments employ a water-conditioning, or bypass, system to filter, de-gas, and, if required, change the temperature of the water. Again, Lauchle, Billet, and Deutsch [1989] give the details of these auxiliary systems. Static pressures in the test section can range from 3 to 60 psia. Operation of the bypass system can lower the gas content from 15 ppm by molecular weight down to 2-3 ppm in approximately three hours.

One important flow feature in understanding and perhaps computing the results from this and similar experiments is the level of freestream turbulence. Tunnel turbulence is controlled using a honeycomb placed within the plenum, 9.25 feet upstream of the nine-to-one contraction nozzle. Using a conical hot-film probe mounted on a strut, Robbins [1978] measured the axial component of the freestream turbulence intensity level to be $0.107\% \pm 0.006\%$ with 95% confidence. This value was based on velocities varying from 20 ft/sec to 60 ft/sec measured in the test section that included only the probe and support strut. With the pitch angle of the impeller blades set at 22.5 degrees, Robbins [1978] measured a longitudinal integral length scale of 0.547 ± 0.057 inches with 95% confidence--over the same velocity range. Also, his spectral analysis indicated a normal turbulence spectrum with no indications of large spikes or other abnormalities.

High Reynolds Number Pump Facility

Figure 2 shows a schematic of the high Reynolds number pump facility. HIREP consists of a 42-inch diameter pump stage driven by a 48-inch diameter downstream turbine. The hub has a constant diameter of 21 inches (giving an annular area through the pump of $A = 7.22 \text{ ft}^2$). As shown in Figure 2, the two units rotate together on a common shaft in the 48-inch diameter test section of the Garfield Thomas Water Tunnel—such that the main drive impeller of the tunnel overcomes the energy losses within HIREP. The pump includes a row of inlet guide vanes, a row of rotating blades, and three downstream support struts. The turbine includes a row of variable pitch control vanes, a row of rotating blades, and a downstream cruciform support strut. Farrell, McBride, and Billet [1987] give a more detailed explanation of the HIREP facility.

Farrell, McBride, and Billet [1987] designed the original HIREP blades to investigate the tip leakage vortices that develop in the clearance between the pump rotor blades and the tunnel liner. Subsequent testing showed that these rotor blades experienced a large region of flow separation near the blade roots. In order to provide an experimental flow field in which one might expect better comparisons with numerical computations, Schott [1993] redesigned both the inlet guide vanes and the rotor blades to avoid this massive separation on the rotor blades. In other respects—such as cavitation performance, head rise, flow coefficient, blade numbers, and basic blade shapes—the design is intended to represent typical axial-flow pumps. Figure 3 shows a computer-generated graphical image of these new blades (including the HIREP coordinate system). The rotor blades are designed with significant blade circumferential lean or skew (skewed in the opposite direction of blade rotation), which introduces three-dimensional complexity to the rotor flow field. The streamline curvature method of McBride [1982] was the primary design tool used to calculate the axisymmetric flow field. McBride [1982] includes a total-pressure loss model—although the code does not model the spanwise mixing of these losses through either convection or diffusion. Two methods were used for blade section design and these methods gave very similar blade shapes. One method was the mean streamline method of McBride [1976], while the other method was a modified version of the three-dimensional lifting surface theory of Greeley and Kerwin [1982]. Schott [1993] calculated blade stresses using beam theory during the preliminary design and finite-element analysis during the final design.

In order to reduce the rotor blade separation, Schott [1993] changed the spanwise distribution in flow turning of both the inlet guide vanes and the rotor blades from the original HIREP design. Since flow separation and the resulting losses depend on the amount the flow is diffused through the blade passage, Lieblein, Schwenk, and Broderick [1953] developed a diffusion factor to help provide a limit for diffusion. Serovy [1978] presented a version of the diffusion factor that allows for a change in radius on a streamsurface through a blade passage,

$$D = 1 - \frac{\overline{W_2}}{\overline{W_1}} \pm \frac{r_1 \overline{V_{\theta_1}} - r_2 \overline{V_{\theta_2}}}{(r_1 + r_2) \sigma \overline{W_1}} ; \quad + = \text{stators} \quad - = \text{rotors}$$

At each spanwise location, D depends on the solidity, $\sigma = c/s$, and the upstream and downstream values of the radius, relative velocity, and absolute circumferential velocity on a blade-to-blade streamsurface. Designers normally place a limit between 0.5 and 0.6 on D when designing a blade row (depending upon the span location). This limit is based on a large number of two-dimensional

cascade performance tests. Values of D greater than this limit result in large increases in total-pressure loss because the larger amount of diffusion causes the blade boundary layers to separate. The new, moderately-loaded rotor blade designs resulted in values of D that increased monotonically from 0.12 at the tip to 0.28 at the root. These values indicate that the new design has no risk of separation from the standpoint of flow diffusion. Values of D have little meaning for inlet guide vanes, since the flow accelerates through this type of blade row. The new rotor blades remove the swirl at the tip, but the designed residual swirl increases linearly towards the hub--leaving the possibility for a future design of downstream stationary blades and a rotor/stator interaction experiment.

The new blades designed by Schott [1993] are similar--but more lightly loaded--than the previous HIREP blades discussed by Farrell, McBride, and Billet [1987]. The 13 inlet guide vanes have a chord length of 6.90 inches and a solidity ranging from 1.36 at the hub to 0.68 at the tip. The 7 rotor blades have a chord length of 11.22 inches and a solidity of 1.19 at the hub and a chord length of 10.49 inches and a solidity of 0.56 at the tip. The trailing edge geometry is essentially an asymmetric chisel, with the bevel of the chisel lying on the suction side of the blade and the point of the chisel being somewhat rounded off.

In order for the rotating blades to avoid rubbing the casing endwall, a clearance exists between the rotor tip and the casing. The nominal design value of the clearance was 0.130 inches, which gives a ratio of the tip clearance to the maximum thickness of the blade tip section (λ) of 0.124 and a ratio of the tip clearance to the blade chord of the tip section of 0.0124. During the HIREP installation, we measured the tip clearance statically with a feeler gauge for different blades in both the chordwise and circumferential directions. These static measurements gave an actual clearance of 0.121 ± 0.005 inches with 95% confidence ($\lambda = 0.115 \pm 0.005$). Using the original blades within HIREP, Farrell [1989] implemented a dynamic gap measuring system to show that the low angular speed of the rotor (or changing tunnel conditions) did not change the rotor tip clearance from its static value.

At the design point, the rotor blades rotated clockwise (looking upstream) at 260 rpm which yields a rotor blade tip speed of $U_{tip} = 47.6$ ft/sec (using the nominal tip radius of 1.75 ft). From similarity considerations, one can derive a volumetric flow coefficient,

$$\phi_{vol} = \frac{Q}{nD_{tip}^3} \approx \frac{AV_{ref}}{nD_{tip}^3},$$

where Q is the volume flow rate, n is the rotor shaft speed in revolutions per second, D_{tip} is the rotor blade diameter, and V_{ref} is an inlet reference axial velocity of this nearly uniform inlet flow. V_{ref} was measured as 35 ft/sec, as will be shown later. By adjusting the variable control vanes upstream of the turbine rotor blades, as well as the tunnel impeller, we established the experimental value of ϕ_{vol} to the design value of 1.36. For the same value of V_{ref} , we also set ϕ_{vol} to the off-design values of 1.22 and 1.50, using 290 rpm and 236 rpm, respectively. While this definition is

quite common for work with propellers, work with axial-flow pumps would generally use a flow coefficient of

$$\Phi = \frac{V_{ref}}{U_{tip}}.$$

This definition yields a design value of 0.74 and off-design values of 0.66 and 0.81, as used in the experiment. Finally, propeller designers also define an advance ratio,

$$J = \frac{V_{ref}}{nD_{tip}},$$

which Schott [1993] established as 2.31 for the design point and as 2.07 and 2.54 for the two off-design points used during the experiment.

Both the inlet guide vanes and the rotor blades were made from aluminum castings. These types of castings normally have an rms roughness height that varies from 125 to 250 microns, but were hand finished here to reduce the rms roughness height to 60-80 microns. Blades that required drilling for instrumentation were overcast and then finished using numerically-controlled machining. All of the rotor blade tips were hand finished to ensure a precise value of the tip clearance. The pressure side corner of the rotor tip section was rounded to give a radius of curvature of approximately 25% of the local blade thickness. Gearhart [1966] found that this rounded corner prevented local separation of the flow through the tip clearance and, thus, improved the gap cavitation performance. The suction side corner was rounded slightly to prevent the sharp corner from breaking. Finally, the rotor blade roots and both the tips and roots of the inlet guide vanes were hand finished to include fillets.

In order to insure that the manufactured blade shapes matched the design blade shapes, we inspected the inlet guide vanes using the intelligent robotic inspection system (IRIS) at ARL Penn State as described by Swanson and Holter [1991]. Using a three-axis gantry style robot, this fully-automated, three-dimensional inspection system can manipulate a low-power laser beam for precise determination of dimensional accuracy (within ± 0.0005 inches). With all 13 inlet guide vanes inserted into the hub, IRIS found that the error in stagger angle never exceeded 0.20 degrees, where the normal tolerance is 0.25 degrees. At several different radii, all of the manufactured blade shapes matched well with the design blade shapes—with a maximum offset of less than 0.05 inches in the circumferential direction. Both the instrumented blades and the noninstrumented blades showed good comparisons.

Schott [1993] also designed a ring mechanism that would allow us to index the inlet guide vanes circumferentially. This mechanism permits measurements to be made in the vicinity of the rotor blades for different positions of the inlet guide vanes and, thus, permits a better mapping of the flow field. The ring mechanism allows the inlet guide vanes to be circumferentially indexed in 2 degree increments over 2.5 blade spacings. On a much smaller scale, Schmidt and Okiishi [1977] and Wagner, Okiishi, and Holbrook [1979] used a similar mechanism for acquiring hot-wire data in a multistage, axial-flow fan, while Zierke and Okiishi [1982] made use of this mechanism in acquiring fast-response total-pressure data in the same fan.

Experimental Technique

The large-scale HIREP facility can accommodate a variety of instrumentation in both a stationary and a rotating frame of reference. A high-capacity, low-noise slip ring accommodates many measurements in the rotating frame. An incremental, optical shaft encoder provides rotor angular position and speed. The water temperature was measured in the plenum with a resistance temperature device that measures the change in resistance across a platinum wire and relates this change in resistance to the temperature.

Rotor Shaft Torque and Thrust Measurements

Torque measurements are important for determining the mechanical power required to operate the pump at various flow conditions. For rotor shaft torque measurements, we mounted two 700-ohm strain gauges to each arm of a four-active-arm Wheatstone bridge on the inside of the rotor shaft and this gauge measured the shear strains in the shaft wall. In order to calibrate the gauges, we used two hydraulic cylinders and applied loads through two-foot arms on either side of the shaft, applying the loads in opposite directions. The applied loads were measured using factory-calibrated commercial load cells traceable to the National Institute of Standards and Technology (NIST) with a stated accuracy of 0.15%, including hysteresis and nonlinearity. Even though the arrangement of the gauges minimizes the sensitivity to adverse loads and bending moments, we calibrated with a bending moment applied in conjunction with the applied torque in four orientations in order to determine the crosstalk of the bending moments on the torque calibration. The largest error resulting from the bending moment was 0.21% of the torque calibration coefficient (in ft-lbs/volt). A post-test calibration of these torque gauges showed a 0.38% difference from the pre-test torque calibration coefficient.

For the rotor shaft thrust measurements, we bonded two 240-ohm strain gauges to each arm of a four-active-arm Wheatstone bridge to the rotating hub flange. To calibrate these gauges, we applied axial loads using a hydraulic cylinder and measured these loads using the same 0.15% accurate load cells used in the torque calibration. Once again, we performed thrust calibrations with a bending moment applied in conjunction with the applied thrust, using 16 orientations. Time-varying crosstalk errors from the bending moment ranged from -10% to +12% of the mean thrust calibration coefficient (in lbs/volt), in a nearly four-cycle sinusoidal pattern during one shaft revolution. A measurement of the time-average thrust must average out these time-varying errors.

While the torque measurements provided very accurate data, problems in the thrust measurement technique provided less accurate results. An integrating voltmeter measured the time-average thrust using an integration time of only 0.167 seconds. As a result of this short integration time with respect to the rotating velocity of the shaft, we could not include a full shaft revolution of the thrust gauges in the integration of the time-mean data. Considering the nearly sinusoidal pattern of the errors between the measured thrust and the time-mean thrust, the short integration time caused problems. We estimated the errors by numerically integrating the 16-point calibration data about the mean using Simpson's rule over an aperture angle of rotation, calculated from the test rpm. The aperture angle was applied to all possible positions allowing an estimation of the maximum error. Table 1 shows these errors.

Table 1. Errors in Thrust Measurements

shaft rpm	maximum negative error	mean error	maximum positive error
290	-1.77 %	-0.40%	+0.33%
260	-1.64 %	-0.40%	+0.37%
100	-2.15 %	-0.16%	+1.88%

Another problem affected the rotor shaft thrust measurement. The measuring strain gauges were submitted to a rotor hub pressure different than either the tunnel pressure or atmospheric pressure. A correction factor was required to offset any false readings:

$$\frac{\Delta V}{\Delta p} = 0.0003802 \frac{\text{volts}}{\text{psia}} .$$

Blade Static-Pressure Measurements

In order to measure the time-average static-pressure distributions, we machined pressure taps into inlet guide vanes and rotor blades. One inlet guide vane included a total of 40 pressure taps on its suction surface, while the pressure surface across the blade passage on the adjacent vane also included 40 pressure taps. As shown in Figure 4, each of the blade surfaces included pressure taps with a pattern of 5 spanwise rows corresponding to nominal locations of 10%, 30%, 50%, 70%, and 90% span. The taps were slightly offset from these nominal spanwise locations, as illustrated in Figure 4, to protect the blades from being locally overstressed in a single plane. The staggered taps also helped prevent any possible contamination of the pressure measurements from one tap due to local flow disturbances from the upstream tap. Each of the 5 rows included 8 chordwise pressure taps corresponding to the percent chord locations listed in Figure 4. The pressure taps were connected to tubing, which exited both of the inlet guide vanes through the outer liner and wall of the tunnel to a bank of 40 pressure transducers. Due to the limit of 40 transducers, we completed the pressure measurements for each of the vane surfaces in separate runs with the same flow conditions.

In a similar fashion, a rotor blade passage also included 40 pressure taps per surface at these same nominal values of percent span. Figure 5 illustrates these static-pressure tap locations on the rotor blade surfaces, as projected onto a radial/axial plane. These highly-leaned rotor blades have a leading edge curvature that results in the pressure tap locations on the suction surface in Figure 5 appearing much closer to the leading edge than they actually are. Again, each of the 5 rows included 8 chordwise pressure taps corresponding to the percent chord locations listed in Figure 5. We did not feel that it was necessary to stagger the pressure taps on the rotor blades because of the large blade size and large amount of lean. Tubes connecting the pressure taps exited the rotor blades and connected to a bank of 40 pressure transducers located near the centerline in the rotor hub--again requiring separate runs to complete the pressure measurements for each of the blade surfaces. The

output signal cables from the transducers were placed along the shaft and exited through the high-capacity, low-noise slip ring.

The instrumentation setup for the rotor blades was difficult to implement; the pressure transducers—as well as the tubing connecting the transducers to the pressure taps—were located in a rotating frame of reference. Considering a differential element of tubing between a blade surface pressure tap and a pressure transducer in the hub, one can treat the problem as a one-dimensional momentum balance where the pressure forces are balanced by the component of centrifugal force along the length of the tube:

$$\frac{1}{\rho} \frac{dp}{dx_{tube}} = r \Omega^2 (\hat{e}_r \cdot \hat{e}_{x_{tube}}) = r \Omega^2 \frac{dr}{dx_{tube}} .$$

Integration of this equation yields

$$\Delta p_{corr} = p_{tap} - p_{trans} = \frac{1}{2} \rho \Omega^2 (r_{tap}^2 - r_{trans}^2) ,$$

which we used to correct the measured blade static pressures for the effect of rotation. Note that the equation is independent of the length of the tube and of the path taken by the tube. Since the magnitude of this pressure drop could be appreciable, especially for the outermost pressure taps, we needed to maintain the static pressure in the water tunnel as high as 25 psi above the pressure within the hub to insure that the pressure transducers would see a pressure within their measurement range during the test. Not only was a correction factor required to account for this pressure difference, but the large pressure placed HIREP in a situation where possible damage could occur because of leakage in the waterproof seals. This large pressure difference also resulted in a false measurement of rotor shaft thrust due to the increased loading on the strain gauges in the hub.

All of the time-average pressure measurements utilized pressure transducers in which the sensor was a solid-state piezoresistive silicon element onto which a Wheatstone bridge has been diffused. For the inlet guide vanes, these gage pressure transducers are referenced to atmospheric pressure, while for the rotor blades, the pressure transducers are referenced to the internal pressure within the rotor hub. Prior to the experiment, we calibrated the measured strain in terms of pressure. Also, all of the transducers were bled and zeroed prior to data acquisition.

Blade surface pressure measurements were completed at throughflow velocities of 25, 30, and 35 ft/sec, while establishing values of 1.22, 1.36, and 1.50 for ϕ_{vol} at each velocity. Problems with pressure taps or pressure transducers gave erroneous measurements at 30% span and 31.1% chord of the IGV suction surface and at 50% span and 43.7% chord on the rotor blade pressure surface. As explained in Appendix A, the overall uncertainty in measuring the blade static pressures ranged from 0.06 psi over regions of minimal streamwise pressure gradients to 0.13 psi over regions of large streamwise pressure gradients, as might be found at 90% span on the rotor blade suction surface.

Surface Flow Visualization

For visualization of the flow field in the vicinity of solid surfaces, we used an oil-paint method to visualize the flow pattern very close to the blade and endwall surfaces. If one covers either entire surfaces or spots on surfaces with a thin coat of oil-paint, the shear stress within the flow will carry the oil-paint with it and, in time, will establish a persistent pattern. In a similar oil-streak flow visualization technique, Squire [1962] showed that the direction of the resulting streaks passing through a point on a surface is very close to the direction of the skin-friction line passing through the same point. Tobak and Peake [1979,1982] also concluded that surface flow visualization patterns should be interpreted as being representative of skin-friction lines. Skin-friction lines are very similar to limiting streamlines, which result in the limit as the height between external streamlines and the surface approaches zero. As long as these limiting streamlines remain parallel to the surface, they remain indistinguishable from skin-friction lines. However, in the vicinity of lines of separation, limiting streamlines can rise rapidly and leave the surface. Since lines of separation are themselves skin-friction lines, surface flow visualization patterns may not give an indication of limiting streamlines near regions of separation.

In some regions of separation, the streamwise pressure gradient strongly affects the oil-paint flow by decelerating the flow, thickening the oil-paint film, and causing the oil-paint to accumulate. Tobak and Peake [1979,1982] call this a local separation line--of which a two-dimensional separation line is a good example. If local reattachment occurs, the oil-paint accumulation will stop as the shear stress increases. One must take care when interpreting an oil-paint accumulation region as laminar separation and turbulent reattachment, since the oil-paint pattern might be indicating a region of natural transition instead. The wall shear stress at the beginning of transition can be quite small and cause the oil-paint film to thicken. Through the transition region, the wall shear stress increases to the point where the turbulent shear stress removes the oil-paint film much quicker. Therefore, the oil-paint accumulation can indicate natural transition--although a stronger dependency on oil-paint thickness and run time, combined with the fact that the wall shear stress always remains finite, make transition (especially the end of transition) more difficult to resolve than separation using the oil-paint method.

In order to apply this type of surface flow visualization technique to rotating blades, one must be assured that the centrifugal force does not affect the oil-paint in a different manner than it affects the actual fluid. Arakawa and Tagori [1980] investigated this concern with some fundamental experiments using a rotating disk and a more practical experiment using an axial-flow pump. Using water as the working fluid, they performed surface flow visualization with oil films of different specific gravities and compared the results with three-dimensional boundary layer calculations. As might be expected, the reduction of the specific gravity of the oil film towards that of water gave measured skin-friction lines closer to the calculated skin-friction lines. The reduction in rotor speed, Ω , and the increase in Reynolds number, $r^2\Omega/v$, also gave better comparisons. For our HIREP experiment, we combined gear oil with paint, which itself is a combination of linseed oil and pigment. Both the gear oil and linseed oil have a specific gravity near 0.94 (compared to 1.0 for water). The addition of pigment will add color and should increase both the specific gravity and kinematic viscosity. The increased specific gravity should give a specific gravity of the oil-paint close to that of water, making the added effect of centrifugal force almost negligible. Therefore, this type of surface flow visualization becomes applicable to blades rotating through water--and not applicable for blades rotating through air. The very high kinematic viscosity of the oil-paint increases the time

to establish a persistent pattern, but allows photographs to be taken later without the effect of gravity damaging the pattern.

Interpretation of surface flow visualization patterns can be quite subjective, with a strong dependence on the quality of the patterns. Also, surface flow visualization methods have essentially zero time response and give no information on the flow unsteadiness. However, Tobak and Peake [1979,1982] and Délery [1992] have shown that the application of topological rules to these patterns creates a rational way of understanding time-average, two- and three-dimensional, viscous flows. Their views are based on the work of Lighthill [1963] and Legendre [1977] that view surface flow visualization patterns as skin-friction lines rather than limiting streamlines. Skin-friction lines (and the associated orthogonal surface vortex lines) behave as continuous vector fields which are characterized by critical or singular points—points where the shear stress is zero.

Only two types of singular points exist: nodal points and saddle points. A nodal point is common to an infinite number of skin friction lines which either leave the node—as in a nodal point of separation—or enter a node—as in a nodal point of attachment. If the node has no common tangent line and the skin friction lines either leave or enter the node in a spiral motion, the node is called a spiral node or focus. Skin friction lines originate typically at nodal points of attachment and can disappear into nodal points of separation. Since skin friction lines springing from adjacent nodal points of attachment will tend to run into each other, there must exist between them a saddle point, emanating from which a single skin friction line will act as a barrier between the skin friction lines from the adjacent nodal points and prevent crossing. Only two skin-friction lines—or critical lines (separators)—pass through a saddle point. If the adjacent skin friction lines tend to converge asymptotically onto one of these critical lines, we refer to it as a line of separation (a line near which adjacent limiting streamlines will tend to leave the surface). In regions of larger adverse pressure gradients, the adjacent skin friction lines will converge faster and the adjacent limiting streamlines will "take off" more rapidly. Skin friction lines diverge asymptotically from the other critical line which is called a line of attachment and this pattern will be accentuated in regions of larger favorable pressure gradients. The resulting patterns can provide a three-dimensional skeleton structure of the viscous flow. On an isolated three-dimensional surface, Lighthill [1963] determined that the number of nodal points must exceed the number of saddle points by two. Actually, Perry and Fairlie [1974] and Hunt, Abell, Peterka, and Woo [1978] showed that singular points also exist within the external flow field and additional topological rules apply when considering these external singular points in addition to the surface singular points. Some internal flows also have different topological rules.

Surface flow visualization tests were run at all three flow coefficients after initial tests indicated the optimum oil-paint mixture and thickness, as well as the tunnel run time. After each test, we removed the tunnel hatch, took photographs from many different angles, and physically measured the distances from significant oil-paint regions (such as singular points) to known geometric references. Oil-paint photographs were taken of the suction and pressure surfaces of both inlet guide vanes and rotor blades, of the hub surfaces of both the inlet guide vanes and rotor blades, of the inside surface of the IGV indexing ring (which fits flush with the outer tunnel liner), and of the tip section of the rotor blades.

Cavitation Visualization

The variable pressure system within the Garfield Thomas Water Tunnel provides a means for viewing cavitation. At a desired velocity and flow coefficient, we could lower the tunnel pressure until cavitation occurred on all of the rotor blades where the local static pressures were reduced below the vapor pressure. Then, the tunnel pressure was systematically increased until the cavitation was no longer present and this value of pressure was recorded. Aside from giving information about the cavitation performance of the pump, this technique provides valuable flow visualization results. Since the core of the rotor tip leakage vortex has a relatively low static pressure, cavitation visualization (near inception) allows one to visualize the location and extent of this important feature of the flow field.

Photographs and videos of this cavitation visualization were acquired using stroboscopic lighting triggered by the home pulse of the optical shaft encoder. An adjustable delay between the home pulse and the strobe trigger allows one to vary the angular position of the illuminated region. However, with the low rotational speeds used in this experiment, the video camera cannot integrate the pictures into one continuous image. Therefore, we employed a low-rpm video viewing system developed by Farrell [1989] which captures a stroboscopically illuminated image and maintains a display of this image on a video monitor until the next image has been digitized and placed in memory.

Before performing any cavitation visualization tests, we measured the total gas content within the water with a Van Slyke manometer apparatus, commonly used as a blood gas analyzer. Expressed in moles of air per million moles of water (ppm), the gas content was reduced to 4.9 ppm when evaluating cavitation performance. Some later cavitation photographs were taken with a gas content ranging from 7.4 to 11.7 ppm.

Laser Light Sheet Visualization

In order to visualize the rotor tip leakage vortex in a plane normal to the axial-flow direction, we employed a laser light sheet technique downstream of the rotor blades. Using an argon-ion laser as the light source, we created a light sheet by directing the laser beam through a cylindrical lens. The light sheet entered the test section of the tunnel with a thickness of approximately 3 mm. With the laser and associated optics mounted on a three-axis traversing table, we could position the location of the light sheet at any desired flow field location, normal to the axis of the tunnel. In order to view a section of the laser light sheet, we designed a special periscope and installed it downstream of the rotor blades through the tunnel endwall liner. Specifically, the periscope allowed us to view the light sheet near the casing, in the vicinity of the rotor tip clearance region. We seeded the flow field with 10 micron microballoons (with a specific gravity of 1.1) to provide particles for illumination during flow visualization. During portions of the flow visualization tests, we lowered the tunnel pressure and allowed the tip leakage vortex to cavitate, creating illuminated bubbles for improving both visualization and camera focusing.

One option for visualizing the particles was to pulse the laser light sheet with a beam chopper in order to create a multiple exposed picture for still-frame photography of the light sheet. However, with a mean flow of approximately 35 ft/sec and a 3-mm thick light sheet, we were unable to chop

the beam fast enough to have the same particles in consecutive light pulses. Thus, the resulting still photographs provided no quantitative data. Videos of the laser light sheet were also acquired through the downstream periscope. The video camera itself provided the framing for recording the flow visualization. With the seven rotor blades rotating at 260 rpm, a rotor blade passes through a point in space 30.33 times per second. The framing occurs because this blade rate nearly equals the frame rate of the camera (30 Hz) and is nearly half of the field rate (60 Hz). The drawback of this method is that consecutive video frames are of vortices from consecutive blades rather than a single vortex from the same blade. However, when one considers only the location of the vortices relative to the casing endwall, this method provides adequate results, providing the blade-to-blade variations are small (as they seemed to be). We completed laser light sheet flow visualization tests at the rotor blade midchord, the rotor blade trailing edge, and at distances of 0.5 and 2.0 inches axially downstream of the rotor blade trailing edge.

Slow-Response Pressure Probes

For many of the measurements of the flow field itself, we employed several types of pressure probes within HIREP. At a location 58.6% chord upstream of the IGV leading edge, we placed a pressure tap in the outer liner to measure a reference static pressure, p_{ref} . This pressure tap is located axially in the region where both the hub and the outer liner are cylindrical. Far upstream, near the upper side of the plenum, we measured a reference total pressure, $p_{T_{ref}}$, with a Kiel probe. Assuming no total-pressure losses as the flow accelerated from the plenum to the reference plane, we computed a reference velocity,

$$V_{ref} = \sqrt{\frac{2}{\rho}(p_{T_{ref}} - p_{ref})},$$

which we used for a monitor velocity during the entire experiment.

To validate this method of measuring V_{ref} , we immersed a Pitot-static probe 2.0 inches into the flow from the outer liner--estimated to be well outside of the boundary layer--44.2% chord upstream of the IGV leading edge. Comparisons of the Pitot-static probe measurements and the values of V_{ref} determined from p_{ref} and $p_{T_{ref}}$ were made for various flow conditions to determine if any correction factor needed to be applied to correct V_{ref} . As shown in Figure 6 for values of V_{ref} ranging from 15 ft/sec to 35 ft/sec, the comparisons were excellent and no correction was required.

A five-hole pressure probe was used to measure values of static and stagnation pressure upstream of the inlet guide vanes. Five-hole probes are capable of resolving the three components of velocity as well as the relative yaw and pitch angles of the flow. Treaster and Yocum [1979] give a complete description of the type of five-hole probes employed in this experiment. The probes were calibrated at a speed of 35 ft/sec in a 6-inch diameter water tunnel over the range of pitch and yaw angles of +30 degrees to -30 degrees. Treaster and Yocum [1979] showed that Reynolds number effects on the probes are small.

For radial surveys with this five-hole probe, Figure 7 shows that the axial location of the reference plane is 37.0% chord upstream of the IGV leading edge. At a single circumferential location, this radial survey included measurements at 50 different radii. Figure 7 also shows a measurement location 49.7% chord downstream of the IGV trailing edge which was used for radial surveys with another five-hole probe. In order for the pressure probes to withstand the large hydrodynamic loads during radial surveys, we first inserted a strongback through the tunnel wall and attached it to the stationary hub. The strongback included a radial slot for traversing the probe head and a trailing fin to reduce vortex shedding and subsequent probe vibration. Motion of the probe head within the radial slot increased the uncertainty of the probe measurements. In order to reduce this uncertainty, we kept the probe head in contact with one edge of the slot, approximately 3.5 degrees from the center of the slot. Later, during data reduction, we took this 3.5 degree offset into account when determining velocities and flow angles. The five-hole probe radial surveys downstream of the inlet guide vanes were performed at several different circumferential increments of the inlet guide vanes, in order to capture an IGV wake at several different radii.

While the radial surveys gave excellent resolution in the radial direction, the radial surveys taken at different positions of the IGV ring mechanism gave poor resolution in the circumferential direction. In order to improve this circumferential resolution, we designed and installed a rake of five-hole probes into the hub. The rake consisted of a 21-inch diameter hub that carried six five-hole probes; each probe attached to a half-inch diameter shaft which fit into a slot in the rake hub. Figure 8 shows how a sample rake probe is positioned within the tunnel, including the splitter vanes that reduce vortex shedding and probe vibration. One could adjust the radial and yaw positions of the probe heads by moving the support shaft and locking it in place with a set screw. The probes were spaced evenly around the hub at 60 degree intervals and the entire assembly was rotated 360 degrees, with the rotation controlled by a stepper motor/encoder assembly located in the stationary hub on the upstream side of the inlet guide vanes. Axially, the five-hole probe rake measurements were acquired at the same location as the five-hole probe radial surveys, as shown in Figure 7.

Because of the limited amount of time allotted for the five-hole probe rake measurements, we needed to determine the minimum acceptable number of radial and circumferential measurement locations needed to resolve the character of the nonuniform velocity field. After some initial computations of the flow field using a viscous form of the code of Adamczyk, Mulac, and Celestina [1986] at a low Mach number, we found 12 radial locations that would define the general radial distribution of the flow field. These 12 radii correspond to the experimental measurement locations—divided into two surveys of the five-hole probe rake—as listed in Table 2. The numerical computations also allowed us to determine the acceptable circumferential resolution. We determined that a spacing of less than 0.5 degrees was required to yield an accuracy within 1% for the first 3 harmonics of the spatial harmonic content of the nonuniform velocity field. In order to meet this accuracy requirement, as well as to satisfy constraints resulting from the encoder resolution and gear ratio, we divided the 360 degree survey into 966 increments of 0.373 degrees. With a probe face size of 0.066 inches (across three holes), the spatial resolution of the probe measurement varies from 0.344 degrees at 4.8% span to 0.185 degrees at 95.2% span.

Table 2. Radial Locations of Individual Probes of the Five-Hole Probe Rake

Probe Number	Probe Location in Percent Span	Comments*
1	95.2	contamination from liner vortices; some wall effects
1	90.5	contamination from liner vortices; some wall effects
2	85.7	minor contamination from liner vortices
2	81.0	
3	76.2	
3	71.4	
4	61.9	
4	52.4	
5	38.1	no data (transducer problems)
5	19.0	partial survey (transducer problems)
6	9.5	some calibration problems
6	4.8	some calibration problems

* see section in Experimental Results and Discussion on IGV Exit Flow

Data from each of the two surveys with the five-hole probe rake were acquired with both the current computerized acquisition system (DADR) and a new system (VXI). This repetition served a dual purpose of verifying the new system and providing a check on the repeatability of the measurements from test to test. Not only did the data taken using VXI agree well with the data taken with DADR, the shorter time required for a VXI survey resulted in fewer transducer/probe failures during the course of a survey. For this reason, we selected the VXI surveys as the primary database for the results. In addition to discussing the repeatability of five-hole probe measurements, Appendix A includes a complete uncertainty analysis for both the five-hole probe rake surveys and the five-hole probe radial surveys. In summary, the five-hole probe rake surveys can measure the total velocity magnitude to within 2.6% with 95% confidence, while the five-hole probe radial surveys can measure to within 7.7%. The primary reason for this difference is the uncertainty in the yaw angle of the five-hole probe head within the strongback slot used during the radial surveys. These values of total uncertainty include both precision and bias errors.

As shown in Figure 7, the measurement location 3.38 inches downstream of the trailing edge of the rotor blade tip was used for radial surveys using a Kiel probe to measure the time-average total pressure. As with the radial surveys using the five-hole probes, the Kiel probe moved within a

strongback with a trailing edge fin. A Kiel probe was chosen downstream of the rotor blades since the motion of the rotor blade wakes and vortices relative to the probe changes the local flow angle. The total pressure port of the Kiel probe lies within a sharp-edged venturi-type tube with a 0.125-inch diameter, giving an insensitivity to yaw and pitch flow angles of approximately ± 45 degrees without the strongback. This downstream measurement location also includes a pressure tap on the outer liner.

All of the slow-response pressure probe measurements utilized pressure transducers in which the sensor was a Wheatstone bridge diffused onto a solid-state piezoresistive silicon element. These gage pressure transducers are referenced to atmospheric pressure. However, the measurement of p_{ref} uses a Bourdon tube pressure transducer and is referenced to a vacuum. Again, prior to the experiment, we calibrated the measured strain in terms of pressure. Also, all of the transducers were bled and zeroed prior to data acquisition.

Fast-Response Pressure Probe

In order for a stationary probe to measure the wakes and vortices associated with the rotor blades, the probe must respond fast enough to the time-varying flow field. For this purpose, we designed a fast-response total-pressure probe for a radial survey at the same axial plane as the slow-response Kiel probe--3.38 inches downstream of the trailing edge of the rotor blade tip. Similar to the Kiel probe, the fast-response pressure probe in Figure 9 includes a 20 degree chamfer with a sharp leading edge. Gracey, Latko, and Russell [1951] showed that this design of a total-pressure probe had a ± 25.5 degree range of insensitivity to the local flow angle (within 1% of impact pressure). Figure 9 shows that the 0.375-inch diameter probe was equipped with a subminiature piezoelectric pressure transducer, located close to the probe tip in order to increase the frequency response of the probe. To withstand the large hydrodynamic pressures within HIREP, the transducer consisted of a stainless steel diaphragm with a 0.1-inch diameter that included a two-disk quartz element operating in a thickness-compression mode. In the piezoelectric effect, the quartz crystal elements produce an electric output only when they experience a change in load and, therefore, piezoelectric transducers cannot perform true static measurements. To enhance the signal resolution, the transducer includes an internal microelectronic amplifier. Finally, we sealed the probe to prevent water damage.

Using a calibration device, we performed an impulse calibration to determine the relationship between the probe output voltage and the probe input total pressure. The calibration device employed a fast-acting valve to quickly expose the probe to a precisely known static air pressure. We repeated the impulse calibration at several reservoir pressures in order to verify that the probe sensitivity was linear. A sample impulse calibration in Figure 10 shows a probe sensitivity of 41.6 mv/psi, which compares well with the sensitivity of 43.7 mv/psi provided by the manufacturer for the transducer alone.

The measurement of time-varying total pressures requires knowledge of the frequency response characteristics of the probe. Although the subminiature pressure transducer used here has a natural frequency of 250,000 Hz, the conical shroud upstream of the transducer face (seen in Figure 9) introduces the possibility of a cavity resonance at a much lower frequency. Unfortunately, the calibration device used for the static calibration included a 5 msec rise time and, thus, we could not

use this device to perform a high-frequency dynamic calibration. Instead, we obtained the frequency response analytically. In Appendix B, we have used a transfer matrix derived by Eversman [1976] to calculate the frequency response shown in Figure 11. Using a typically small damping ratio for these types of transducers (approximately 0.02), this frequency response curve shows that the first cavity resonance occurs at 60,000 Hz and that the error is less than 5% for frequencies up to 10,000 Hz. This result confirms that the frequency response of the probe should not affect the measurement in the frequency range of interest, where the rotor blade passing frequency is only 30.33 Hz.

During data acquisition, the transducer output signal was connected via a powering unit to a dynamic signal analyzer. The rotor shaft encoder was also connected to the signal analyzer to act as a trigger and make it possible to synchronize the measurements of the unsteady pressures with the position of the rotor blades. Using a resolution bandwidth of 2.5 Hz, the analyzer used a fast Fourier transform to generate the power spectral density function or autospectral density function. Plotting this function versus frequency yields the power spectrum or autospectrum. For these measurements, we averaged over a sampling time of 64 rotor rotations. In addition to obtaining an autospectrum that included both random and periodic signals, we also employed synchronous-averaging to significantly reduce any random data--data that does not correspond to the rotor blade passing frequency and its multiples. As with the slow-response Kiel probe, the fast-response total-pressure probe moved within a strongback with a trailing fin during the radial surveys.

Laser Doppler Velocimeter

A laser Doppler velocimeter (LDV) was used to acquire nonintrusive measurements of the flow field upstream of the rotor blade row, downstream of the rotor blade row, and in the rotor tip clearance region. A two-component LDV system was employed in a dual backscatter mode, with the 488.0 nm wavelength blue beams used for measuring the axial velocities and the 514.5 nm wavelength green beams used for measuring the tangential velocities. To eliminate directional ambiguity, we used Bragg cells with each component and selected the resulting frequency shifts from the electronic downmixers to optimize data rates for the various measurement locations. In the dual backscatter mode, the light scatter from seed particles passing through the measurement volume was collected through the transmitting lens and focused on an aperture in front of a photodetector. Two counter processors--along with a master interface--filtered and digitized the information from the photodetectors for processing and storage on a personal computer.

The argon-ion laser and associated optics were mounted on a three-axis traversing table. The table was used to position the location of the beam cross-over spot (or measurement volume) at the desired flow field location. Most measurements were made on the test section centerline through a specially designed window. The window had an inner contour radius of 21 inches and an outer radius of 63.54 inches. The two radii of curvature were required to produce a near-zero net magnification cylindrical lens for the laser optical system. In other words, the window allowed both beams for each component of velocity to cross at the same location. In actuality, measurements of the component cross-over locations showed that the tangential component measurement volume tended to be slightly

closer to the outer window by the amount

$$\Delta r = r_\theta - r_z = -0.0171 r_z + 0.2111 ,$$

where r_θ and r_z are the measurement volume radial locations of the tangential and axial components in inches from the hub.

Data were collected using a field point measurement method. In this procedure, the measurement volume remains stationary, and each LDV measurement sample is tagged with the angular position of the rotor—via the optical shaft encoder and a rotating machinery resolver. The water tunnel¹ was seeded with 1.5 μm silicon carbide particles to increase the data collection rates. Even so, the data rates were, at times, disappointingly low. Therefore, a non-coincidence or random acquisition method was used to significantly increase the data rate. (In other words, the axial and tangential velocity components were not taken simultaneously.) In order to decrease biasing due to large differences in data rate in both channels, we reduced the gain on the channel with the highest data rate so that the data rates were approximately the same. Typically, for every position of the LDV measurement volume, a total of 100,000 samples were obtained, of which approximately 50% were axial velocity measurements and the other 50% tangential.

Figure 12 shows the locations at which we acquired LDV data. The radial survey furthest downstream of the rotor blades corresponds to the radial surveys taken downstream of the rotor blades with both the slow-response and fast-response total-pressure probes, as shown in Figure 7. Table 12 in Appendix C provides further information about the symbols shown in Figure 12 that describe details of the LDV data acquisition. Appendix C also gives some information on the uncertainty of the LDV measurements. The precision errors in the mean velocity measurements range from 0.1% to 2.4%, with the larger errors corresponding to regions with high turbulence levels. The precision errors in the turbulence intensities range from 6.0% to 8.5%. The total uncertainty in these measurements also depend on bias errors, which are briefly discussed in Appendix C.

The LDV does not measure the instantaneous velocity $V(t)$ continuously in the manner that a fast-response measuring device such as a hot-wire probe would. Instead, the LDV measures discrete samples of $V(t)$. At each radial location, the LDV measures N particle samples, with each sample n given a value of θ depending on the encoder-measured circumferential location of the rotating shaft. In the stationary frame of reference, the values of θ corresponding to rotor rotation can represent values of time. Therefore, the instantaneous velocity $V(t)$ is represented by the discretized velocity V_n . This unsteady velocity can be decomposed into a time-average velocity, $\bar{\bar{V}}$, a periodic or deterministic unsteady velocity, \bar{V} , and a random or nondeterministic unsteady velocity, V' :

$$V(t) = V_n = \bar{\bar{V}} + \bar{V} + V' .$$

Figure 13 shows this velocity decomposition. The entire rotor rotation through 2π can be divided into N_w discrete storage windows or bins, as shown for one period, T , in Figure 13. Any storage window contains M particle samples with each sample m having a value of θ within the bounds of that particular window. Statistically, the velocity samples within each storage window yield an

ensemble-averaged velocity,

$$\bar{V} = \frac{1}{M} \sum_{m=1}^M V_m ,$$

a random or nondeterministic unsteady velocity,

$$V' = V_m - \bar{V} ,$$

and an ensemble-averaged variance,

$$\overline{V'^2} = \frac{1}{M-1} \sum_{m=1}^M (V_m - \bar{V})^2 .$$

This variance shows the level of nondeterministic unsteadiness at an average value of θ within a particular discrete storage window—a level of unsteadiness which is either partially or entirely due to the turbulence.

The time-average of the entire unsteady velocity signal,

$$\overline{\overline{V(t)}} = \frac{1}{T} \int_0^T V(t) dt ,$$

could be found by averaging over all N samples in the entire discretized velocity signal. However, the particles are more likely to be measured in the freestream regions of the flow field and less likely to be measured in regions involving boundary layers, wakes, or vortices—because of problems in entraining particles into these regions. Therefore, averaging over all N samples could yield a velocity bias in calculating the time-average velocity. In order to alleviate this bias problem, one can obtain the time-average velocity by averaging all of the ensemble-averaged velocities in each storage window,

$$\overline{\overline{V}} = \frac{1}{N_w} \sum_{n_w=1}^{N_w} \bar{V}$$

where N_w represents the total number of windows. This type of averaging is essentially an area averaging technique that gives the circumferential average value of the time-average velocity. Also, the level of nondeterministic unsteadiness of the entire velocity signal can be found by averaging the

variances in each storage window,

$$\overline{\overline{V'^2}} = \frac{1}{N_w} \sum_{n_w=1}^{N_w} \overline{V'^2} .$$

This total variance gives the circumferential-average level of nondeterministic unsteadiness.

At this point, one can determine the periodic or deterministic unsteady velocity,

$$\tilde{V} = \bar{V} - \overline{\bar{V}} .$$

This deterministic unsteady velocity is a function of the average θ or t corresponding to a particular storage window. To show the level of deterministic unsteadiness (a type of unsteadiness that correlates with rotor shaft speed), one can compute the variance

$$\overline{\overline{\tilde{V}^2}} = \frac{1}{N_w} \sum_{n_w=1}^{N_w} (\bar{V} - \overline{\bar{V}})^2$$

for each component. Also, one can compute the correlation

$$\overline{\overline{\tilde{V}_z \tilde{V}_\theta}} = \frac{1}{N_w} \sum_{n_w=1}^{N_w} (\bar{V}_z - \overline{\bar{V}}_z)(\bar{V}_\theta - \overline{\bar{V}}_\theta)$$

to see how well the axial and tangential components of the deterministic unsteady velocity correlate with one another. Finally, if one computes the variance of all N samples in the entire velocity signal,

$$\overline{\overline{(\tilde{V} + V')^2}} = \frac{1}{N} \sum_{n=1}^N (V_n - \overline{\bar{V}})^2 ,$$

one obtains information on the level of overall unsteadiness. The entire velocity signal varies because of both the deterministic and nondeterministic unsteadiness. This overall unsteadiness level can also be computed from the previously defined levels of deterministic and nondeterministic unsteadiness—if one assumes that the deterministic and nondeterministic unsteady velocities do not correlate with one another,

$$\overline{\overline{(\tilde{V} + V')^2}} = \overline{\overline{\tilde{V}^2}} + \overline{\overline{V'^2}} .$$

Experimental Results and Discussion

Using the experimental techniques just described, we measured the flow within HIREP. The temperature of the water within the flow field generally increased during a day of testing, with a maximum increase of about 8°F. For the entire experiment, the temperature ranged from 75°F to 92°F, with an average value of about 85°F. This average temperature yields average properties of density, kinematic viscosity, and vapor pressure of

$$\rho = 1.932 \frac{\text{slugs}}{\text{ft}^3},$$

$$v = 0.000008755 \frac{\text{ft}^2}{\text{sec}},$$

and

$$p_v = 0.5968 \text{ psia}.$$

All of the experimental measurements were acquired at specific values of ϕ_{vol} and V_{ref} . Once the desired velocity was reached for a given test, we adjusted the variable pitch control vanes of the turbine in order to provide the desired flow coefficient and rotor rotational speed. In this manner, flow measurements could be taken over a range of ϕ_{vol} and V_{ref} . Any losses in transporting the fluid around the closed-loop tunnel were overcome by the main drive impeller of the tunnel. Also, the tunnel was pressurized during all tests to eliminate cavitation, when desired. All of the results in this report are at the design values of 1.36 for ϕ_{vol} and 35 ft/sec for V_{ref} , unless otherwise noted.

Inlet Conditions

Using a calibrated five-hole pressure probe, we measured the static and stagnation pressures at one circumferential position at the reference plane 37.0% chord axially upstream of the inlet guide vanes, as shown in Figure 7. Figure 14 shows these results compared with the design values computed using the streamline curvature method. Both the static and total pressures are shown in coefficient form,

$$C_p = \frac{P - P_{ref}}{\frac{1}{2} \rho V_{ref}^2}.$$

Three repeat measurements were acquired at each radial position. The total-pressure survey shows a uniform flow with a boundary layer on the tunnel liner. Meanwhile, the static-pressure survey shows a curved profile which matches fairly well with the streamline curvature calculations. Despite the fact that this reference plane is located where the hub and outer liner are cylindrical, a more detailed look at the streamline curvature results shows that the streamlines at this axial location still exhibit some curvature which results in a mild radial pressure gradient. The static-pressure profile also behaves

rather strangely in the region of the casing boundary layer, although this behavior may result from a small amount of radial or swirling flow in the vicinity of the probe immersion slot or some other local flow disturbance, such as a liner vortex (see the later section on the IGV exit flow).

Figure 15 shows the inlet velocity profiles as measured with the five-hole probe. The radial and tangential velocities are quite small, as expected, and the measured magnitudes are smaller than the uncertainty of the measurements themselves (see Appendix A)—except possibly in the vicinity of the probe immersion slot. In the past, LDV measurements have shown that the residual swirl in the bare tunnel is negligible. Slight increases in both the radial and tangential velocities appear in the region of the casing boundary layer and, hence, the probe immersion slot or some other local flow disturbance may be affecting the data acquired in this region. The axial velocities are nearly uniform—with a slight curvature due to the radial pressure gradient that is visible from the streamline curvature calculations. A monitor velocity measurement was acquired with each five-hole probe measurement and Figure 15 shows these measurements on the tunnel liner which contained the reference static-pressure tap. Using an average static-pressure measurement from this tap of $p_{ref} = 43.2$ psia, the monitor velocity gives a nominal reference velocity of $V_{ref} = 35$ ft/sec. The measured axial velocity profile results in a mass flow rate coefficient of,

$$C_m = \frac{\dot{m}}{\rho A V_{ref}} = \frac{2\pi}{AV_{ref}} \int V_z r dr = 0.939 .$$

The axial velocity and total-pressure measurements show that a significant boundary layer exists on the tunnel liner, while the boundary layer on the hub must have a boundary layer thickness less than 0.3 inches. In an expanded scale, Figure 16 shows the liner boundary layer in more detail. From this plot, the liner boundary layer appears laminar. Integrating the measurement points, we can obtain some parameters to characterize the boundary layer, as seen in Table 3. The resulting shape factor of 2.56 also indicates that this boundary layer is laminar. However, we can use these parameters to compute a momentum thickness Reynolds number of 29,400 and it would be difficult to imagine a boundary layer other than a fully turbulent boundary layer existing at this Reynolds number. Perhaps wall effects or the probe immersion slot has influenced the measurements near the tunnel liner—causing the boundary layer to appear laminar and casting doubts on the two data points closest to the liner and on the calculated integral parameters.

Table 3. Parameters of the Inlet Boundary Layer on the Tunnel Liner

Edge Velocity	U_e	34.7 ft/sec
Boundary Layer Thickness	δ	0.71 inches
Displacement Thickness	δ^*	0.228 inches
Momentum Thickness	θ	0.089 inches
Shape Factor	H	2.56

As a further analysis of the inlet boundary layers, we performed some simple numerical computations. Using some in-house codes, we first generated a computational grid and then computed the potential flow for the flow field from the tunnel plenum to the reference measurement plane. Next, using the boundary layer code STANS developed by Crawford and Kays [1976], we computed both the hub and casing boundary layers. Because of the low turbulence intensity and the strongly accelerating flow field, the value of the momentum thickness Reynolds number for which transition begins should be rather large. Under similar conditions, Abu-Ghannam and Shaw [1980] report values as large as 1300. Using this value, STANS predicts a fully-turbulent hub boundary layer with a value of δ that is slightly less than 0.3 inches. The relatively large boundary layer on the tunnel liner results from the leading edge of the liner being very blunt. The blunt leading edge creates an adverse streamwise pressure gradient just upstream of the leading edge and this, in turn, causes the boundary layer leaving the tunnel nozzle to separate and reattach on the liner further downstream. This separation bubble causes the boundary layer at the reference plane to be much thicker on the liner than on the hub. STANS does predict this separation, causing this parabolic boundary layer code to diverge. After we estimated the size of the separation bubble, STANS predicted the boundary layers up to the reference plane by marching over the estimated separation bubble. The predicted liner boundary layer was much thicker than the predicted hub boundary layer, and this predicted liner boundary layer was both fully turbulent and quite close in thickness to the measured liner boundary layer.

IGV Static-Pressure Distribution

The measured inlet flow establishes a flow through the inlet guide vanes with a chord Reynolds number of 2,300,000. Static-pressure taps, with locations shown in Figure 4, allowed us to measure the IGV static-pressure distribution. To be consistent with the analysis further downstream where U_{tip} is the most reliable velocity measurement, we present these data using an alternative definition of the pressure coefficient,

$$K_p = \frac{P - P_{ref}}{\frac{1}{2} \rho U_{tip}^2}.$$

Figure 17 shows the measured IGV static-pressure distributions at five spanwise locations. Also, Figure 17 shows the design calculations that Schott [1993] computed using lifting surface theory.

All five spanwise static-pressure distributions in Figure 17 show very similar shapes, indicating that the IGV flow field is nearly two-dimensional. Except at 10% span, these pressure distributions exhibit a streamwise pressure gradient on the suction surface that is favorable over the first 20% chord, vanishes, and then becomes strongly adverse over the last 20% chord. On the pressure surface, the streamwise pressure gradient is mildly favorable through 70% chord and then becomes mildly adverse. At 10% span, the hub endwall seems to have slightly altered the incidence angle, eliminating the favorable pressure gradient on the suction surface and creating an adverse pressure gradient over the first 20% chord of the pressure surface. The distributions calculated from lifting surface theory show excellent agreement with the measurements, although the hub endwall effect on incidence is not calculated. Both the measurements and calculations show that the blade section lift, obtained from integrating each static-pressure distribution, appears larger near midspan and decreases

toward the endwalls. Actually, the design parameters of Schott [1993] show that the maximum lift should occur at 42% span.

Additional static-pressure measurements were acquired for all three flow coefficients after setting V_{ref} equal to 15 and 35 ft/sec and for the design flow coefficient with values of V_{ref} equal to 15, 20, 25, 30, and 35 ft/sec. The pressure distributions for all of these conditions remained essentially the same since the chord Reynolds numbers remained quite large and the flow coefficients were never too far off design.

Using the measured static pressures to obtain an outer boundary condition for velocity, we again used the boundary layer code STAN5 developed by Crawford and Kays [1976] to compute the boundary layer characteristics on both IGV surfaces. We also used the model developed by Abu-Ghannam and Shaw [1980] that shows transition should begin for a momentum thickness Reynolds number of about 400 for our flow conditions. For the typical case at 50% span, the boundary layer calculations show that natural transition should begin near 15% chord and end near 30% chord for both the suction and pressure surfaces. Since no adverse pressure gradient exists in this region, transition simply results from the large Reynolds number. Also, even though the calculations show no separation through the 94.1% chord location on the suction surface, calculations in this adverse pressure gradient show signs that separation will occur between 94.1% chord and the trailing edge. The chisel trailing edge should in fact force separation.

Figure 18 shows contour plots of the static-pressure coefficients on both the suction and pressure surfaces. Again, the suction surface appears two dimensional with a strong adverse streamwise pressure gradient near the trailing edge that should lead to separation. The pressure surface shows the hub endwall effect on incidence angle. Also, the pressure surface shows a radial pressure gradient towards the trailing edge, a gradient that will later be shown to be significant.

IGV Surface Flow Visualization

Before attempting to interpret the IGV surface flow visualization patterns, we first analyzed hundreds of photographs together with physical length measurements taken immediately after each test. We ran surface flow visualization tests for the design flow coefficient ($\phi_{vol} = 1.36$) and two off-design flow coefficients ($\phi_{vol} = 1.22, 1.50$)—using the reference velocity, V_{ref} , of 35 ft/sec. No noticeable difference was found when observing the patterns at the two off-design flow coefficients. The resulting patterns have been drawn on various projected surfaces. Figure 19 shows the reconstruction of the oil-paint pattern (shown in blue) on the hub surface of the inlet guide vanes for the design flow coefficient. The dark gray surface with the bold black border represents a footprint of the designed blade section at the hub, while the light gray region surrounding this blade section represents the extension of the fillet onto the hub surface. The inlet and exit flow vectors in Figure 19 are the design flow vectors at the hub as determined from the streamline curvature solution.

The first region of interest in Figure 19 is the region on the hub surface near the blade leading edge. Just upstream of the point where the leading edge fillet merges into the hub surface, one can identify a saddle point. Between the saddle point and the blade leading edge, the skin friction lines move upstream and, despite the fact that the oil-paint photographs were not as distinct in this region, one must surmise that a nodal point of attachment exists somewhere on the blade leading edge. The

critical skin friction line that passes through the saddle point and forms a C-pattern around the blade is a line of separation. In general, as the fluid approaches the blade, the flow will slow down and stagnate somewhere near the blade leading edge—creating an adverse pressure gradient. Within the endwall boundary layer on the hub, this adverse pressure gradient causes the boundary layer to separate, with the point of zero shear stress occurring at the saddle point. As the two legs of the separation line bend around the blade, the vorticity in the separated boundary layer rolls up to form what is commonly called a "horseshoe vortex" or "necklace vortex." Alternatively, one could represent the hub boundary layer as a vortex line in the circumferential direction. This vortex line convects downstream around the blade leading edge, resulting in segments of this vortex line on each side of the blade with vorticity in the streamwise direction, or a horseshoe vortex.

Past investigations have shown that the formation of vortices other than the primary horseshoe vortex can occur in the leading edge region. However, we could not identify the additional singular points required for the formation of these other vortices. Also, other investigators have identified another C-shaped skin friction line between the leading edge and the separation line passing through the saddle point. This additional skin friction line is usually easier to identify than the separation line because of an accumulation of the substance used in the surface flow visualization test. For flow around a circular cylinder, Baker [1980] and Eckerle and Langston [1987] claim that this line is a secondary line of separation (or a local separation line) associated with the roll up of the horseshoe vortex. For flow in a wing-body junction, Devenport and Simpson [1989] claim that this line is a line of low streamwise shear (not a line of separation or reattachment) and that this line merges into the separation line somewhere downstream. In our case, we could not identify this second skin-friction line from an accumulation of oil-paint. Again, remember that the oil-paint photographs were not as distinct in this region. Perhaps this line coincides very closely with the separation line passing through the saddle point. Another point of interest is the effect of the fillet on the formation of the horseshoe vortex. Devenport, Agarwal, Dewitz, Simpson, and Poddar [1990] performed a study of this effect in the flow past a wing-body junction. Essentially, the fillet simply increased the radius of the leading edge and displaced the horseshoe vortex a little further from the wing. They also measured a small increase in the size and strength of the horseshoe vortex when a fillet was present.

Most previous investigations of horseshoe vortices through surface flow visualization and other experimental techniques have focussed either on nonlifting bodies—such as cylinders or struts—or on turbine blades with a large amount of flow turning. However, a few investigators have shown surface flow visualization patterns of the horseshoe vortex around compressor blades, lifting bodies with only a small amount of flow turning. Dong, Gallimore, and Hodson [1987] showed a pattern on a rotor hub surface, while Schulz and Gallus [1988] showed a pattern on a stator hub surface. Both of these patterns were very similar to our surface flow visualization pattern in Figure 19. In all of these cases, the pressure side leg of the horseshoe vortex separation line moved downstream into the midpassage region. This is different from the case of a large turning turbine blade, where Sieverding [1985] shows that the pressure side leg of the separation line actually interacts with the suction surface of the adjacent blade, creating a corner vortex. Also in agreement with the compressor blade patterns, Figure 19 shows that the suction side leg of the separation line moves up onto the suction surface. This movement is the result of the flow overturning in the hub endwall region.

As fluid passes through any turbomachine blade passage, the turning flow creates a circumferential pressure gradient. Within the endwall boundary layer, the momentum of the flow is reduced and the flow cannot follow the turning flow path as imposed by the blade design. The

circumferential pressure gradient causes the flow to overturn and this, subsequently, causes the suction side leg of the horseshoe vortex separation line to move up onto the suction surface. Figure 19 shows the overturning of the flow exiting the inlet guide vanes by comparing the oil-paint pattern with the design flow angle. This overturning flow also initiates the vortical motion that results in the classical secondary flow called a passage vortex. Again, representing the endwall boundary layer as a vortex line, the turning of the vortex line through the blade passage yields a component of vorticity in the streamwise direction, vorticity that makes up the passage vortex. The vortical motion that initiates the passage vortex rotates the flow in the same sense as the pressure side leg of the horseshoe vortex. In their turbine blade cascade, Sieverding and Van den Bosch [1983] used colored smoke visualization to show that the pressure side leg of the horseshoe vortex simply merges into the passage vortex. The suction side leg of the horseshoe vortex rotates with the opposite sense and wraps around the passage vortex. From their colored smoke visualization, Sieverding and Van den Bosch [1983] presented a schematic of two streamsurfaces convecting through their turbine blade passage. As shown in Figure 20, this schematic shows the interaction of these vortices.

Figure 21 shows the reconstruction of the oil-paint pattern on the suction surface of an inlet guide vane. For the most part, the flow on the suction surface appears to be two dimensional. The vertical dotted lines enclose a region where the oil-paint accumulated, which would indicate either natural transition or transition through a separation bubble. Since the IGV static-pressure distribution of Figure 17 shows no sign of an adverse streamwise pressure gradient in this region, one would expect the oil-paint accumulation to indicate natural transition. The oil-paint pattern indicates that transition should begin near 18% chord, compared to the previously calculated value near 15% chord. The oil-paint accumulation ends near 41% chord, while the calculation showed transition ending near 30% chord. Recall that the oil-paint method should give a better indication for the beginning of transition than for the end of transition. In fact, the downstream end of this oil-paint accumulation did vary with different run times used from test to test.

Proceeding downstream near the hub, one notices flow moving from the hub endwall up onto the suction surface as a result of the flow overturning. A saddle point occurs near 88% chord and 6% span. The separation line passing through this saddle point moves downstream, with one leg moving up the span and the other leg moving back toward the hub. This latter leg of the separation line probably moves back up the suction surface and into the spiral node located near 97% chord and 3% span. Another spiral node, near 95% chord and 8% span, also exists within this three-dimensional corner separation. The flow entering this second spiral node seems to have originated in the pressure surface boundary layer, turned around the trailing edge, and moved upstream on the suction surface. Schulz and Gallus [1988] also found skin friction lines moving around the trailing edge and upstream along the suction surface. However, their corner separation--as well as the ones found by Joslyn and Dring [1985] and Dong, Gallimore, and Hodson [1987]--was much larger with more backflow and more radial outflow. These compressor studies were made with higher-loaded blades that resulted in more overturning of the flow on the hub endwall and, hence, a larger corner separation region. Also, the inlet guide vanes used in this study are an accelerating blade row which would tend to minimize separation.

The separation line passing through the saddle point on the suction surface of Figure 21 forms the three-dimensional corner separation. Figure 22 shows a photograph of this three-dimensional corner separation on one of the inlet guide vanes. Beginning at the saddle point and moving along the legs of the separation line, the limiting streamlines will leave the surface and form a dividing surface of separation. A concentrated vortex filament will extend into the external flow field from each of

the spiral nodes. Then, the dividing surface of separation will roll-up around each of these vortex filaments and convect downstream. Therefore, the vortical cores about which these dividing surfaces coil begin at spiral nodes. In this case, the three-dimensional corner separation also contains a secondary separation. Near this corner on the hub surface, Figure 19 shows the existence of another saddle point just downstream of the trailing edge. One leg of the separation line proceeds downstream and, beginning at the saddle point, the limiting streamlines leave the hub surface along this line to form a dividing surface of secondary separation. Again, the vortical core about which this dividing surface coils begins at the spiral node located in the trailing edge region of Figure 19. Also, note that the skin-friction lines converging asymptotically onto this secondary separation line seem to be emanating from a nearby attachment line.

Further radially outward on the IGV suction surface of Figure 21 at about 19% span, one finds that the trailing edge separation pattern changes. Photographs of this region showed a significant accumulation of oil-paint and, following Tobak and Peake [1979,1982], we refer to this line as a line of local separation—which in this case represents two-dimensional separation. This two-dimensional separation occurs over the last 5% chord—a separation forced by the chisel trailing edge. Boundary layer calculations showed the likelihood of this trailing edge separation. Near the IGV tip, at about 96% span and 97% chord, one finds another spiral node of separation. The separation line entering this spiral node passes through a saddle point near the IGV trailing edge on the casing endwall, as seen in Figure 23. Figure 23 shows that the other leg of the separation line passing through this trailing edge saddle point proceeds downstream and, beginning at the saddle point, the limiting streamlines leave the casing surface along this line to form a dividing surface of separation. The vortical core about which this dividing surface coils begins at the spiral node located in the trailing edge region of Figure 21. As was the case on the hub endwall, the skin-friction lines converging asymptotically onto this separation line on the casing endwall in Figure 23 seem to be emanating from a nearby attachment line.

The reconstruction of the oil-paint pattern on the casing endwall of Figure 23 shows a topology for the formation of the horseshoe vortex that is nearly identical to the topology on the hub endwall. Again, a saddle point exists just upstream of the leading edge and a nodal point of attachment probably exists on the leading edge itself. The pressure side leg of the separation line passing through this saddle point moves downstream into the midpassage region, while the suction side leg moves downstream and then onto the suction surface because of the overturning of the flow in the casing boundary layer. Note the radial downward flow near the tip region of the IGV suction surface in Figure 21. The blade sections at the IGV tip are designed for less fluid turning than the root blade sections. Therefore, the skin-friction lines on the casing endwall show less overturning than the skin-friction lines on the hub endwall and the resulting passage vorticity should not be as large. While the suction side leg of the separation line never migrated beyond the outer edge of the blade fillet on the hub endwall, the suction side leg moved well beyond the fillet on the casing endwall, before moving back onto the suction surface. The larger endwall boundary layer and the smaller amount of overturning within this boundary layer contribute to this difference in topology.

Previously, we showed that the incoming endwall boundary layer on the casing was much larger than the boundary layer on the hub endwall. And yet, the skin-friction lines on both endwalls show that the topology for the formation of the horseshoe vortex is nearly identical. Other investigators have also shown that, qualitatively, the structure of this three-dimensional separation does not change with incoming boundary layer thickness. For both laminar and turbulent boundary layers interacting with a circular cylinder, Baker [1979,1980] showed that the vertical dimensions of

the resulting vortex system did not change with incoming boundary layer thickness, although the separation lines moved slightly closer to the leading edge as the boundary layer became thinner. With or without a fillet, Devenport, Agarwal, Dewitz, Simpson, and Poddar [1990] also found that changes in the incoming boundary layer thickness did not qualitatively alter the structure of the horseshoe vortex--including the surface flow visualization pattern. For flow through a turbine blade cascade, Gregory-Smith, Graves, and Walsh [1988] found no change in the position of the downstream vortex loss core with incoming boundary layer thickness, although changes in thickness did have some effect on the intensity of the vortex loss core. This vortex loss core consists of the pressure side leg of the horseshoe vortex merged into the passage vortex.

To conclude the analysis of the surface flow visualization on the inlet guide vanes, Figure 24 shows a reconstruction of the oil-paint pattern on the pressure surface. As with the compressor blade experiments of Joslyn and Dring [1985], Dong, Gallimore, and Hodson [1987], and Schulz and Gallus [1988], the flow over the pressure surface appears very two dimensional. Similar to the suction surface, the vertical dotted lines on the pressure surface enclose a region where the oil-paint accumulated. With no adverse streamwise pressure gradient shown in Figure 17, this oil-paint accumulation indicates natural transition. This oil-paint accumulation extended from 15% chord to 25% chord, matching fairly well with the calculated transition region ranging from 15% chord to 30% chord. Also shown in Figure 24 are two dotted skin-friction lines that begin just downstream of the leading edge and move downstream in a triangular configuration. We noticed this type of pattern at various times and places on both the pressure and suction surfaces. Within a laminar flow region, Stanbrook [1962] classified these patterns as wedges of turbulent flow from isolated excrescences. In our case, local lumps within the oil-paint or, more likely, surface irregularities probably caused a local separation and immediate transition of the shear layer from laminar to turbulent. Figure 25 shows a photograph of the oil-paint pattern on the pressure surface with at least three well-defined turbulent flow wedges. Notice how these wedges begin in the laminar flow region, upstream of the oil-paint accumulation that indicates natural transition.

On the pressure surface and near the trailing edge, Figures 24 and 25 show some radial movement of the skin-friction lines. The design parameters of Schott [1993] show that the lift coefficient and circulation reach maximum values at 42% span and decrease toward both endwalls--decreasing the area within the blade section pressure distributions. Depending on the blade loading distribution, a decreasing lift corresponds to a decreasing pressure on the pressure surface, an increasing pressure on the suction surface, or both. Therefore, the resulting radial pressure gradient can cause the flow to move radially away from the point of maximum lift on the pressure surface and/or move radially toward the point of maximum lift on the suction surface. From the pressure coefficient contour plots of Figure 18, we notice that the changing circulation results in a radial pressure gradient on the pressure surface, but not on the suction surface. As the boundary layers on the pressure and suction surfaces merge to form a wake, the spanwise vorticity from the pressure surface boundary layers opposes the spanwise vorticity from the suction surface boundary layers, and the resulting spanwise vorticity in the wake will eventually decay from viscous diffusion. The radial motion of the flow on the pressure surface turns a portion of the spanwise vorticity into the streamwise direction and this streamwise vorticity is shed into the wake as trailing vorticity--vorticity that will decay much slower than the spanwise vorticity in the wake. Near the hub, the resulting streamwise vorticity will be directed upstream, while near the casing, the resulting streamwise vorticity will be directed downstream. Close to the endwalls, three-dimensional effects lead to some radial flow on the suction surface that will also create streamwise vorticity.

The development of trailing vorticity from a spanwise change in circulation has been known for a long time, with a basis in three-dimensional wing theory. In turbomachinery blades, however, Smith [1955] concluded that the turning of the circumferential vorticity in the incoming endwall boundary layers can also influence this trailing vortex sheet. Remember that the turning of the vorticity in an endwall boundary layer also creates the passage vortex. The blade wakes will be located between passage vortices from adjacent blade passages and these passage vortices can induce a motion within the wake opposite to the rotation in the passage vortices. Likewise, the vortex sheet created by a spanwise change in blade circulation can induce a motion within the blade passages. Actually, the vortex sheet and the passage vortices simply coexist. One is not actually the cause of the other. For a blade row such as the HIREP inlet guide vanes with a maximum circulation located near midspan, the velocities in the wakes induced by the passage vortices will likely rotate in the same direction as the trailing vortex sheet created by the spanwise gradient in circulation. Figure 26 shows how the passage vortices and trailing vortex sheets might appear downstream of the inlet guide vanes.

The analysis of the surface flow visualization on the inlet guide vanes can be summarized in Figure 27. Note that we have performed the analysis using time-average patterns of flow separation even though most regions of flow separation are unsteady. Figure 27 shows our interpretation of the three-dimensional skeleton structure of the secondary flow through the inlet guide vanes. The flow overturning on both endwalls moves the suction side leg of the horseshoe vortex back towards the suction surface and causes the vortex to lift off the surface. The pressure side leg of the horseshoe vortex moves into the midpassage region and eventually becomes part of the passage vortex illustrated in Figure 26. Figure 27 also shows a fairly complex three-dimensional corner separation in the junction of the suction surface and the hub endwall—including a secondary separation. In the corner of the suction surface and the casing endwall, Figure 27 shows a smaller and less complex three-dimensional separation. Finally, a two-dimensional separation occurs at the trailing edge of the suction surface.

IGV Exit Flow

The surface flow visualization on the inlet guide vanes and endwalls provided us with a means to interpret the three-dimensional skeleton structure of the secondary flow exiting the inlet guide vanes. Next, the five-hole probe measurements 49.7% chord axially downstream of the IGV trailing edge, as shown in Figure 7, will provide the measured structure of this secondary flow. One might anticipate that some of the vortex structures (indicated in Figures 26 and 27) from these lightly-loaded vanes may be too weak to show up in the measurements, especially given the nonuniform structure of the measurement locations. Presentation of the data will include comparisons with expected values, as calculated during the design phase of the study. Therefore, some background information is required before presenting the data.

As mentioned previously, Schott [1993] modified a version of the three-dimensional lifting surface theory of Greeley and Kerwin [1982], which he used as one of his design tools. For flow over a turbomachinery blade at a high Reynolds number, viscous effects cause the generation of circulation around the blade. The magnitude of this circulation is defined by Joukowski's hypothesis as the amount required to move the stagnation point to the sharp trailing edge which, in turn, eliminates boundary layer separation. One can model the blade circulation with a "bound" vortex

using lifting surface theory which represents a blade with a series of spanwise bound vortex lines, as well as singularity lines using sources and sinks to model the blade thickness. At a high Reynolds number with no separation, the blade boundary layers create a thin wake with spanwise vorticity of both signs, with no net effect on the flow field. However, recall that a spanwise change in circulation will create streamwise vorticity within the wake, which is shed downstream as a trailing vortex sheet. This streamwise vorticity will have an effect on the flow field and lifting surface theory must model this vortex sheet with vortex lines. Schott [1993] used lifting surface theory to help design the HIREP blade rows for a specified mass flow rate and blade circulation. Using bound and trailing vortex lines, the blade sources and sinks, and the vortices used to model the endwalls, the lifting surface code iterates to find the strength and position of these singularities required to induce the proper potential flow through the blade rows. In the final solution, the blades, endwalls, and trailing vortex sheets must be streamsurfaces and the imposed Kutta condition allows for a smooth, unseparated flow past the trailing edge.

Referring back to Table 2, we attempted to measure the flow field at 12 radial positions using a five-hole probe rake. Figure 28 shows a series of plots where the axial, radial, and tangential velocity components are plotted around the entire circumference for all 12 radial positions. A few items must be addressed before examining these data in more detail. All 6 probes within the five-hole probe rake were inserted into a half-inch diameter shaft, which can affect the measurements of the local pitch flow angle and radial velocity. However, we accounted for the effect of the shaft on the probe measurements by calibrating the probes with an identical half-inch diameter shaft. Unfortunately, the shaft of Probe 6 was recessed below the hub surface, decreasing the effect of the shaft on the measurements. Even though we calibrated Probe 6 with a smaller shaft than the other probes, the probe calibration still took this shaft effect into account, and the probe measured too much downward radial velocity at the 4.8% span location and (to a lesser degree) at the 9.5% span location. In addition, pressure transducer problems continually plagued Probe 5 during the experiment--leaving the measurements at 19.0% span with only a partial survey and the measurements at 38.1% span with no data at all.

Two more problems occurred in the five-hole probe measurements near the casing. Within HIREP, sections of a tunnel liner are attached to the tunnel wall to create the casing endwall. After the experiment, we identified axially-running seams between these liner sections, as well as seams associated with the liner section attached to the tunnel hatch. At these same circumferential locations, the data at 95.2%, at 90.5%, and, to some extent, at 85.7% span showed significant flow structures that we could not explain from the flow through the inlet guide vanes. Evidently, vortex structures lifted off the casing endwall from these seams and contaminated the data. Also, the presence of the casing endwall itself seemed to affect the local pitch flow angle and radial velocity measured by Probe 1 at both 95.2% and 90.5% span--an effect not accounted for by the probe calibration. As a result, Probe 1 measured too much upward radial velocity at these spanwise locations.

With these measurement problems in mind, we refer back to the series of data plots in Figure 28. First, examine the circumferential variation in radial velocity. The five-hole probe data compares very well with the lifting surface calculations. The measurements have some offset from the calculations in the vicinity of the two endwalls where we know the five-hole probes have problems measuring the radial velocity. However, the shapes of the measured distributions remain very similar to the calculated distributions in the absence of contamination from the liner vortices. From the hub outward to the 38.1% span location, the radial velocity changes abruptly across the vortex sheet from positive on the suction side to negative on the pressure side. Then, from 52.4% span outward to the

casing, the radial velocity changes abruptly from negative to positive, moving in the same direction. Recall that the location of maximum lift on the inlet guide vanes occurred at 42% span and that the streamwise trailing vorticity above and below this location would be of different signs. This is consistent with these radial velocity distributions. Therefore, the excellent comparison with the lifting surface calculations confirms that the measured distribution is an indication of the trailing vortex sheet. Jessup, Schott, Jeffers, and Kobayashi [1985] compared lifting surface calculations with LDV measurements acquired downstream of a propeller and they also found an excellent agreement between calculations and measurements in the vicinity of the trailing vortex sheet.

If the trailing vortex sheet was purely radial, only the radial velocities would change across the sheet. However, if the trailing vortex sheet was radially skewed, the tangential velocity (and to a very small degree, the axial velocity) would also change across the sheet. Since the inlet guide vanes in HIREP turn the flow more near the hub than near the casing, the trailing vortex sheet will become radially skewed as it convects downstream and this skewed sheet leads to the circumferential variation in the tangential velocities of Figure 28. These variations differ considerably from what one might expect if one considered this flow field to be composed of a spanwise stacking of two-dimensional streamsurfaces. If this were the case, the flow on the suction side of the wake would experience undeturning because of the separated suction surface boundary layer, while the flow on the pressure side of the wake might experience a slight overturning of the flow. These predominately viscous effects would change in the vicinity of the endwall boundary layers which cause significantly more undeturning of the flow. Even though the inlet guide vanes would appear to create a rather two-dimensional flow field, the variations in the tangential velocities of Figure 28 indicate a strong three-dimensional behavior because of the effect of the radially-skewed trailing vortex sheet.

Figure 28 shows the variation in the experimentally measured tangential velocities compared with the lifting surface calculations. Near the hub endwall and to a lesser extent near the casing endwall, the data show more undeturning of the wake flow than the calculations show. As discussed with the surface flow visualization patterns, the endwall boundary layers lead to an undeturning of the flow, an effect not captured with the lifting surface theory. Away from the endwalls, the comparisons of measurements and calculations are fair, with the data indicating some blade-to-blade differences. For the locations where the data show more overturning than the calculations do, the blade-to-blade differences are probably related to the trailing vortex sheets. In this case, local instabilities of the vortex sheets to small disturbances could deform the local shape of the sheets and give rise to variations in tangential velocity across the sheets. Also, recall that the passage vortex created by the inlet guide vanes turning the vorticity in the endwall boundary layers can also affect the trailing vortex sheet, and small blade-to-blade variations in this phenomenon may arise. For the locations where the data show slightly more undeturning than the calculations, the blade-to-blade differences may be related to the separation of the IGV suction surface boundary layers. Local surface irregularities that led to the turbulent wedges in the surface flow visualization patterns might have been one reason why the local separation characteristics varied and led to some isolated undeturning of the flow.

Figure 28 also shows the circumferential variation in axial velocity at the various spanwise locations. Obviously, the inviscid lifting surface calculations show only the slight variations associated with the radially-skewed trailing vortex sheet. The data show the viscous wakes, with the streamwise direction being much closer to the axial direction than the circumferential direction. The viscous wakes are much deeper near the hub endwall as a result of the small three-dimensional corner separation shown in Figures 21 and 27. Any blade-to-blade differences in the wakes at the various

spanwise locations are probably related to local variations in the separation characteristics on the IGV suction surface.

In order to provide wake data for comparisons with numerical predictions, one needs to examine average-passage wakes. First, the streamwise velocity is defined as the vectorial sum of the circumferential-mean velocities in the axial and tangential directions. These local circumferential means involve area averages,

$$\bar{V} = \frac{\int_0^{\theta} V d\theta}{\int_0^{\theta} d\theta},$$

at each spanwise location over all the IGV passages for the five-hole probe rake surveys, except at 19.0% span where only a partial survey was acquired. While the circumferential location of the wake centerline was always within $\pm 1\%$, we still matched the minimum velocity points for each wake before the area averaging in order to eliminate uncertainties on the position of the wake in determining the uncertainties on the shape of the wake. Avoiding the three spanwise locations contaminated by liner vortices, Figure 29 shows the average-passage IGV wakes in the streamwise direction. Again, the viscous wakes are much deeper and asymmetric near the hub endwall as a result of the small three-dimensional corner separation. Away from the hub, the wakes are much shallower and more symmetric (with only about eight data points defining these wakes). The 95% confidence bands represent the repeatability of the wakes from blade to blade. The larger 95% confidence bands at 19.0% span result from fewer IGV wakes being used to form the average-passage wake.

In order to better view the structure of the secondary flow, Figure 30 shows secondary velocity vectors from lifting surface theory, the five-hole probe rake surveys, and the five-hole probe radial surveys (with all three plots using the same vector length scale). Secondary flow is defined as the flow perpendicular to the primary flow, although some slight differences arise in how to define the primary flow. Smith [1955] defined the primary flow as the flow computed on the axisymmetric and blade-to-blade streamsurfaces, while Hawthorne [1955, 1957] defined the primary flow as the computed inviscid flow. Figure 30 shows secondary velocity vectors defined similar to those of Smith [1955], with the local circumferential-mean velocity subtracted from the measured and calculated velocities. The area averaging for the five-hole probe radial surveys and the lifting surface calculations are taken over a single IGV passage. Also, even though the primary flow direction has been turned, these radial and tangential velocity vectors lie within a plane normal to the axial direction.

Figure 30 shows an excellent comparison between the lifting surface calculations and the five-hole probe rake survey. Near the casing, we improved this comparison by showing consecutive passages with only a small amount of contamination from the liner vortices. As anticipated, several of the secondary vortex structures in Figure 27 do not appear in the vector plots of Figure 30, since they are either too weak or are filtered out by the nonuniform grid of measurement locations. Since the lifting surface calculations used a uniform inlet flow, only the spanwise change in blade circulation produces the trailing vortex sheet and the passage vortex structures. The strength and positions of these structures generally compare well with the five-hole probe rake measurements. Possible explanations for the observed differences are the turning of the inlet vorticity and the

pressure side legs of the horseshoe vortices. The five-hole probe radial surveys also compare well with the position of the trailing vortex sheet, but the coarse circumferential spacing of the measurements and the greater uncertainty of the measurements (see Appendix A) leads to poorer overall comparisons.

As noted before, comparing the secondary velocity vector plots in Figure 30 clearly shows the location of the wake and trailing vortex sheet--with the sheet beginning to appear as two separate vortex structures rather than a thin sheet of many small vortices. As the trailing vortex sheet convects downstream, the sheet tends to deform, until the sheet eventually rolls-up into two concentrated vortex structures rotating in opposite directions. As a matter of fact, lifting surface theory represents this phenomenon by modelling the trailing vortex sheet with a radial distribution of vortex lines through some prescribed transition length. Downstream of this transition length, the theory simply models the two concentrated vortex structures with two vortex lines, a rolled-up hub vortical core and a rolled-up tip vortical core. Finally, the viscous effects on these vortex structures are idealized by assigning a finite core radius to the two modelling vortex lines.

For the same two passages used for the secondary velocity vectors, Figure 31 shows contours of the total-pressure coefficients measured with the five-hole probe rake. Recall from the inlet conditions that Figure 14 showed a very uniform distribution of total pressure, except within the boundary layer on the casing endwall. Therefore, the low total pressures within the contours of Figure 31 represent high total-pressure losses. As expected for these lightly-loaded inlet guide vanes, most of these losses are concentrated in the viscous wakes. These wake losses increase near the hub endwall because of the effect of the three-dimensional corner separation. Joslyn and Dring [1985], Dong, Gallimore, and Hodson [1987], and Schulz and Gallus [1988] also found that their three-dimensional corner separations led to higher losses. Within the casing endwall boundary layer, the total-pressure coefficients are even smaller, but they were also small upstream of the inlet guide vanes.

Figure 32 shows the circumferentially-averaged velocities from the five-hole probe measurements compared with the design calculations from the streamline curvature method. Remember that the liner vortices affected the circumferential averages near the casing endwall. The measurements show larger axial velocities away from the endwalls since this core flow has been accelerated by the presence of the endwall boundary layers, an effect not included in the streamline curvature method (as realized by designers). The measured tangential velocities compare well with the streamline curvature calculations, with the measurements showing a small amount of undeturning near the endwalls. The measured radial velocities are all near the expected value of zero, with the previously mentioned measurement problems occurring near the endwalls. Note that the circumferentially-averaged values using the five-hole probe rake surveys and the five-hole probe radial surveys show excellent agreement. Figure 33 shows the corresponding circumferentially-averaged values of the static- and total-pressure coefficients. Again, the values using the five-hole probe rake surveys and the five-hole probe radial surveys show good agreement for the static-pressure coefficients. The measured static-pressure gradient appears to be less than the calculated gradient. The greater measurement uncertainty in the radial surveys (see Appendix A) seems to yield total-pressure coefficients that are higher than either the rake measurements or the streamline curvature calculations. In fact, away from the endwalls, the measured total-pressure coefficients are larger than unity, which should not be the case.

Moving axially from 49.7% to 88.5% chord downstream of the IGV trailing edge, we measured the axial and tangential velocities using an LDV (as seen in Figure 12). Here, circumferential means involve averaging the LDV data at a single circumferential location for a complete revolution of the rotating blades. At this circumferential location, no IGV wakes or liner vortices were present. Figure 34 shows these circumferentially-averaged velocities compared with the design calculations from the streamline curvature method. As with the five-hole probe measurements, the LDV measurements show the acceleration of the core flow due to the blockage from the endwall boundary layers. Also, the LDV data do not include averaging over the low axial velocity regions in the IGV wakes. The measured tangential velocities compare very well with the design calculations except near the endwalls, where both the measured axial and tangential velocities show a growth in the endwall boundary layers. Near the casing endwall, the LDV measurements differed from the five-hole probe measurements; the LDV measurements showed an overturning of the flow, while the five-hole probe measurements showed a small undeturning of the flow. Perhaps the presence of the liner vortices in the data used to obtain circumferential averages have affected the five-hole probe results near the casing endwall. Once again, note that the overturning showed by the LDV data do not include the effects of IGV wakes.

In regions away from the inlet guide vane wakes, we can extract information about the endwall boundary layers from both the five-hole probe radial surveys and the LDV surveys. Before examining these boundary layers, one should take note of an interesting characteristic of endwall boundary layers. As discussed by Taylor [1959], when the flow along a stationary hub encounters a rotating hub, a boundary layer will result in which the velocity varies in direction, as well as in magnitude, with distance from the hub: a skewed boundary layer. Figure 35 shows the skewed boundary layer on the rotating hub within HIREP, as measured with the LDV. Taylor [1959] also pointed out that skewed endwall boundary layers can result from secondary flows. For instance, the endwall boundary layer passing through the inlet guide vanes will turn more near the wall than in the outer part of the boundary layer—resulting in a skewed boundary layer. Near the origin of a horseshoe vortex, where an endwall flow approaches a surface—such as a blade—and creates a three-dimensional separation, Johnston [1960a, 1960b] showed that skewed boundary layers will form away from the stagnation streamlines. From their experiment, Moore and Richardson [1957] felt that the crossflow within these three-dimensional boundary layers actually energized the boundary layers. Energizing the endwall boundary layers may help prevent separation, although one must consider separation of these boundary layers to be a three-dimensional phenomenon, following the topology described by Tobak and Peake [1979, 1982] and Délery [1992]. Finally, Hunter and Cumpsty [1982] showed that skewed boundary layers on the casing endwall entering a rotor produced much more streamwise vorticity than that produced by the flow turning. Considering the complexity of the flow, Taylor [1960] felt that skewed boundary layers would be the rule rather than the exception within a turbomachine.

In order to characterize the skewed endwall boundary layers, we followed the procedure used by Moore and Richardson [1957] and Johnston [1960a, 1960b] by defining the displacement and momentum thicknesses relative to the streamwise and normal directions established at the edge of the

boundary layer:

$$\delta_s^* = \int_0^\delta \left(1 - \frac{u}{U_e} \right) dy ,$$

$$\theta_s = \int_0^\delta \frac{u}{U_e} \left(1 - \frac{u}{U_e} \right) dy ,$$

$$\delta_n^* = \int_0^\delta \frac{w}{U_e} dy ,$$

$$\theta_n = \int_0^\delta \left(\frac{w}{U_e} \right)^2 dy ,$$

and

$$\theta_m = \int_0^\delta \frac{w}{U_e} \left(1 - \frac{u}{U_e} \right) dy .$$

Within the definitions of these integral parameters, U_e is the boundary layer edge velocity in the streamwise direction, defined as the vector sum of the axial and tangential velocities at a distance δ from the endwall. The direction of U_e establishes the direction of the streamwise velocities, u , and the crossflow velocities, w , throughout the boundary layer. An additional integral parameter, θ_m , is defined that represents a cross-correlation momentum thickness. All of these integral parameters are found in the momentum integral equations for a turbulent boundary layer with crossflow, as first developed by Mager [1951]. Typically, the shape factor is defined for the streamwise velocity profile,

$$H = \frac{\delta_s^*}{\theta_s} .$$

Table 4 summarizes the integral parameters of both the casing and hub endwall boundary layers measured at 49.7% and 88.5% chord axially downstream of the IGV trailing edge. The boundary layer on the casing seems to have decreased through the inlet guide vanes (an accelerating flow) and then increased downstream toward the rotor blades. In the absolute coordinate system, these boundary layers show a slight skewness, which may be caused by secondary flow. The hub boundary layer has increased through the inlet guide vanes and also developed a slight skewness due to secondary flow. Then, as the hub boundary layer continued to grow, it reached the rotating portion

of the hub and developed a significant skewness in the opposite direction. As with the casing boundary layer measured upstream of the inlet guide vanes, the endwall boundary layers measured downstream of the inlet guide vanes have larger values of the shape factor than expected. Schlichting [1979] gives traditional values of the shape factor between 1.3 and 2.2 for turbulent boundary layers and between 2.3 and 3.5 for laminar boundary layers. Momentum thickness Reynolds numbers for all of these endwall boundary layers would indicate that they are all clearly turbulent and, yet, only the LDV measured casing boundary layer has a shape factor within the turbulent regime. Since calculations of the integral parameters depend strongly on the data measured very close to the wall, these large shape factors cast doubt on the first few points measured near the endwalls.

Table 4. Characteristics of the Endwall Boundary Layers Between Blade Rows

Parameter	Five-Hole Probe Measurements 49.7% Chord Axially Downstream of the IGV Trailing Edge		LDV Measurements 88.5% Chord Axially Downstream of the IGV Trailing Edge	
	Casing Endwall Boundary Layer	Hub Endwall Boundary Layer	Casing Endwall Boundary Layer	Hub Endwall Boundary Layer
U_e	36.6 ft/sec	36.4 ft/sec	35.8 ft/sec	36.8 ft/sec
δ	0.58 inches	0.39 inches	0.80 inches	0.77 inches
δ_s^*	0.155 inches	0.137 inches	0.156 inches	0.261 inches
θ_s	0.067 inches	0.050 inches	0.075 inches	0.084 inches
H	2.31	2.74	2.08	3.11
δ_n^*	0.018 inches	0.007 inches	0.017 inches	-0.128 inches
θ_n	0.0008 inches	0.0001 inches	0.0007 inches	0.0534 inches
θ_{sn}	0.005 inches	0.002 inches	0.005 inches	-0.096 inches

Harmonic Content of the IGV Exit Flow

The downstream rotor blades will interact with the nonuniform flow created by the inlet guide vanes and respond to generate forced vibration and noise. Most unsteady response codes assume that all time unsteadiness is purely harmonic and treat distortions in the nonuniform inflow as gusts. Therefore, these response calculations are performed on a harmonic by harmonic basis, with a different gust used for each calculation. In order to simulate the nonuniform inflow as a convected gust, one needs to consider the nonuniform inflow as a harmonic function in space. After decomposing the nonuniform inflow into a circumferential-average and a circumferential-varying

velocity, one can describe the velocity by a Fourier series

$$V(z,r,\theta) = \bar{V}(z,r) + \tilde{V}(z,r,\theta) = \frac{a_0}{2} + \sum_{n=1}^{\infty} \tilde{V}_n(z,r,\theta) ,$$

where the velocity for the n^{th} harmonic is

$$\tilde{V}_n = a_n \cos(n\theta) + b_n \sin(n\theta) = |\tilde{V}_n| \cos(n\theta - \phi_n) .$$

We can define the amplitude and phase of the circumferentially-varying velocity as

$$|\tilde{V}_n|(z,r) = \sqrt{a_n^2 + b_n^2}$$

and

$$\phi_n(z,r) = \tan^{-1}(b_n/a_n) ,$$

where

$$a_n(z,r) = \frac{1}{\pi} \int_{-\pi}^{\pi} V \cos(n\theta) d\theta$$

and

$$b_n(z,r) = \frac{1}{\pi} \int_{-\pi}^{\pi} V \sin(n\theta) d\theta .$$

Here, we consider the harmonic content of the entire circumference of the nonuniform inflow and not just the harmonic content over one IGV spacing. This allows for the general case of a circumferentially nonuniform flow upstream of the inlet guide vanes or any circumferential variation in the inlet guide vanes themselves.

A Fourier analysis was completed for all three velocity components at the 11 radial positions in which data existed from the five-hole probe rake surveys (see Table 2). The Fourier analysis of most of the data was straightforward. However, data at 85.7%, 90.5%, and 95.2% span included contamination from liner vortices at some circumferential locations, while the data at 19.0% span had no data at some circumferential locations. For these spanwise locations, we could not perform a Fourier analysis around the entire circumference. In order to circumvent this problem, we first curve fit a 1,950-point spline to each data set of velocity versus angular location (except at 19.0% span)—although one must remember that this spline is created from 966 actual data points. Then, we divided each spline into 13 individual wake files of 150 points each. The good wake files were then selected and Fourier analyzed over a single vane passage period of 27.7 degrees. The values of $|\tilde{V}_n|$ and ϕ_n , determined from the Fourier analysis represent the average values of the individual wakes analyzed at a given radius. Computed confidence bands represent the precision index of the mean at a 95%

confidence level. In order to verify that the values of $|\bar{V}_n|$ and ϕ_n obtained by averaging the Fourier analyzed individual wake files yields the same values as applying the analysis to the entire circumference, we compared the two approaches at 61.9% span, a radial location where no problems occurred while acquiring data around the circumference. The comparison of the values of $|\bar{V}_n|$, shown in Figure 36, indicates that the two approaches are equivalent in terms of resolving the harmonic content associated with the inlet guide vane number and its multiples.

For three sample spanwise locations, Figure 37 shows the magnitude of the circumferentially-varying velocity downstream of the inlet guide vanes as a spatial harmonic function of the harmonic order, n . As expected, large velocity magnitudes (normalized by U_{np}) occur for those harmonics associated with the number of inlet guide vanes and its multiples. For a circumferentially-uniform inflow and for an identical flow from vane passage to vane passage, all of the remaining harmonics would be zero. However, Figure 37 shows that the harmonics not associated with $n=13$ or multiples are nonzero and these harmonics establish the background noise floor.

Background noise consists of two parts: a nondeterministic or random component associated with fluctuations in the test conditions or instrumentation and a deterministic component associated with actual circumferential variations in the flow. Previous studies in the Garfield Thomas Water Tunnel have shown that for similar five-hole probe rake measurements, the random background noise floor varies inversely with the square root of the number of circumferential data points. Using the results of these previous studies, we estimate that our random background noise floor for $|\bar{V}_n|$ should occur at 0.047% of U_{np} . The plots of Figure 37 show that the background noise floor is always larger than this estimated random component. The elevated deterministic component occurs because the flow is not identical within each vane passage, as shown in Figure 28.

Establishment of a background noise floor allows us to consider how many harmonics are significant by evaluating the signal-to-noise ratio (*SNR*). In terms of decibels, one can define the signal-to-noise ratio as

$$SNR = 20 \log(|\bar{V}_n|_{meas}) - 20 \log(|\bar{V}_n|_{noise}) .$$

In order to determine the minimum acceptable *SNR*, one assumes that the measured velocity includes the average-passage value plus a contribution from the noise, nondeterministic and deterministic. Assuming that the noise is not spatially correlated with the average-passage velocity, a Fourier analysis yields

$$|\bar{V}_n|_{meas}^2 = |\bar{V}_n|_{avg}^2 + |\bar{V}_n|_{noise}^2$$

or, in terms of decibels,

$$20 \log(|\bar{V}_n|_{avg}) = 10 \log(|\bar{V}_n|_{meas}^2 - |\bar{V}_n|_{noise}^2) .$$

Eliminating the noise term, one obtains

$$20 \log(|\bar{V}_n|_{avg}) = 20 \log(|\bar{V}_n|_{meas}) + 10 \log(1 - 10^{-SNR/10}).$$

Therefore, an accuracy within 1 dB for the measured value of $|\bar{V}_n|$ requires a $SNR \geq 7 \text{ dB}$. For the 11 spanwise positions of five-hole probe rake data, Table 5 shows how many harmonics lie above the background noise floor and how many satisfy the signal-to-noise requirement. Note that the contamination from liner vortices has eliminated many of the significant axial harmonics. However, the alternative method of computing the harmonics from selected vane passages does allow us to compute these harmonics with some confidence. Actually, for a SNR greater than 3 dB, one can correct the harmonic coefficients by subtracting the background noise floor from the measurements.

Table 5. Spatial Harmonics in the IGV Exit Flow that Satisfy Accuracy Requirements.

% Span	Harmonics above the Background Noise Floor			Harmonics with $SNR \geq 7 \text{ dB}$		
	Axial	Radial	Tangential	Axial	Radial	Tangential
4.8	1 → 11	1 → 11	1 → 11	1 → 9	1 → 9	1 → 8
9.5	1 → 10	1 → 9	1 → 8	1 → 8	1 → 7	1 → 6
19.1	—	—	—	—	—	—
52.4	1 → 12	1 → 5	1 → 12	1 → 7	1 → 2	1
61.9	1 → 12	1 → 11	1 → 11	1 → 10	1 → 6	1 → 3
71.4	1 → 10	1 → 6	1 → 3	1 → 8	1 → 6	1 → 2
76.2	1 → 13	1 → 14	1 → 11	1 → 11	1 → 8	1 → 3
81.0	1 → 15	1 → 15	1 → 15	1 → 4	1 → 12	1 → 6
85.7	1 → 13	1 → 15	1 → 15	4 → 9	1 → 8	1 → 9
90.5	6 → 13	1 → 15	1 → 15	6 → 13	1 → 14	1 → 14
95.2	1 → 3	1 → 13	1 → 10	1 → 3	1 → 10	1 → 7

Even the harmonics that are considered to be significantly above the background noise floor have magnitudes ranging from 4.0% of U_{tip} down to values below 0.1% of U_{tip} . Although these values might seem too low to create any meaningful unsteady response by downstream blade rows, many investigators have proved otherwise. Jessup, Boswell, and Nelka [1977] have measured similarly small harmonics within the nonuniform flow entering a surface ship propeller and, indeed, they measured significant unsteady forces and moments on the propeller rotating shaft. Within a multistage compressor, Manwaring and Fleeter [1990] measured unsteady pressures on blades that

responded to harmonic levels of the same order of magnitude as those measured in HIREP. Manwaring and Wisler [1992] report similar findings in both axial-flow compressors and turbines. All of these findings show that unsteady blade response requires a harmonic content of a nonuniform inflow that includes many harmonic orders—even harmonic orders with magnitudes as small as 0.1% of U_{tip} . Therefore, for the purposes of this unsteady response, either an experimental or computational determination of the nonuniform inflow must resolve the flow detail required to obtain the necessary harmonic content. Ideally, all of the harmonics above the random background noise floor should be considered.

The flow characteristics of Figure 28 affect the harmonic content shown in Figure 37. First, observe the plots in Figure 37 corresponding to Fourier coefficients of axial velocity. Recall from Figure 28 that the small three-dimensional corner separation led to deeper and wider wakes at 4.8% span, relative to the wakes at 52.4% and 81.0% span. These deeper and wider wakes increased the magnitude of the lower-order harmonics and decreased the magnitude of the higher-order harmonics. At 52.4% and 81.0% span, the smaller wakes are much sharper, increasing the importance of the higher harmonics. These results correspond to an analysis performed by Gallus, Lambertz, and Wallman [1980]. They performed a parametric analysis using the empirical wake equations of Silverstein, Katzoff, and Bullivant [1939] for a single airfoil without camber. Again, this parametric analysis showed that the magnitude of the lower-order harmonics increased and the magnitude of the higher-order harmonics decreased with increases in wake width. For the Fourier coefficients of radial velocity, several harmonics at 4.8% and 81.0% span are significant, but only a few harmonics are significant at 52.4% span. The circumferential distribution of radial velocity in Figure 28 shows only a small variation at 52.4% span since this location corresponds closely to where the vorticity in the trailing vortex sheet changes signs and the radial velocities in the passage vortices change direction. One final observation can be drawn from all the velocity components in Figure 28, especially from the Fourier coefficients of tangential velocity: The background noise floor is smallest at 4.8% span, larger at 81.0% span, and the largest at 52.4% span. The level of the background noise floor is directly related to the amount of blade-to-blade variation of the velocity distributions shown in Figure 28. Near midspan, an increase in blade-to-blade variation also reduces the number of tangential harmonics that are significantly above the background noise floor, as seen in Table 5.

Since only the harmonics associated with the number of inlet guide vanes and its multiples are significant, Figure 38 shows how $|\tilde{V}_n|/U_{tip}$ and ϕ_n vary as a function of percent span for the first five of these significant harmonics. The 95% confidence bands represent the repeatability of the amplitudes and phases from blade to blade. These confidence bands for the first harmonic ($n = 3$) are typical of those confidence bands for the other harmonics. Over most of the span, the harmonics of $|\tilde{V}_n|/U_{tip}$ do not change with radius for the axial and radial components. The enlarged wakes near the hub increase $|\tilde{V}_n|/U_{tip}$ for all five harmonics, while the liner vortices near the casing also increase $|\tilde{V}_n|/U_{tip}$ for all five harmonics. The harmonic values of $|\tilde{V}_n|/U_{tip}$ for the tangential component show a deficit near midspan, where the largest blade-to-blade variations occur. Figure 38 also shows that the phase angle of the first harmonic of axial velocity does not change with radius. With the inlet guide vanes imparting swirl into the flow, the wakes will move a distance $\Delta\theta$ between the IGV trailing edge and the measurement plane. With the phase angle defined relative to a radial

line, the phase angle for higher-order harmonics should experience greater variations according to

$$\Delta\phi_n = n \Delta\theta .$$

Therefore, the higher-order axial velocity harmonics in Figure 38 show an increase in phase angle with decreasing radius because of the larger amount of swirl near the hub. This type of information can help one design a downstream rotor blade row to minimize unsteady interactions with the IGV wakes. The phase angle for the radial velocity harmonics follows a similar trend as the axial component, while the tangential component shows a more haphazard trend because of blade-to-blade variations.

Unsteadiness of the IGV Exit Flow

The next set of figures shows the level of unsteady flow, as computed from the LDV data downstream of the inlet guide vanes and upstream of the rotor blades. With no IGV wakes present in the measurement volume, Figure 39 shows that the level of overall unsteadiness remains both small and constant over most of the span. Very near the endwalls, however, the level of overall unsteadiness increases rapidly. We can gain further insight into this flow unsteadiness by decomposing the overall unsteadiness into a nondeterministic unsteadiness and a deterministic unsteadiness. As shown in Figure 40, the circumferentially-averaged levels of nondeterministic unsteadiness are very close to zero over most of the span and then increase rapidly near the endwalls. In this case, the nondeterministic unsteadiness consists primarily of turbulence, with possibly some influence from an unsteady motion of upstream separation regions and vortices. Comparing Figures 39 and 40 shows that the overall unsteadiness in the endwall regions is predominately turbulent or nondeterministic. Away from the endwalls, we also attempted to measure the turbulence levels within an IGV wake. Establishing the position of the IGV wakes from the five-hole probe rake measurements allowed us to move the LDV measurement volume circumferentially to align with the position of a wake. Table 6 presents the results for the maximum values of nondeterministic unsteadiness or turbulence intensity. In terms of the nondeterministic unsteady flow correlations, the unsteadiness within an individual IGV wake appears to be significant, but an average about the circumference of the machine would yield values much less than the levels of nondeterministic unsteadiness within the endwalls in Figure 40. In terms of the more familiar turbulence intensities, the values ranged from 5.5% to 8.7% and tracked closely with the percentage of velocity deficit—a common approximation for planar wakes.

Figure 41 shows the level of deterministic unsteadiness upstream of the rotor blades. For the most part, the deterministic unsteadiness has a small, but constant, value over the whole span and this unsteadiness can be attributed to periodic motion of the circumferentially nonuniform pressure field from the downstream rotor blades. Away from the endwalls, this potential flow effect accounts for all of the overall unsteadiness shown in Figure 39. A slight increase in the potential flow unsteadiness does occur very close to the hub since this measurement is acquired closer to the upstream rotor blades where the potential field is stronger (see Figure 12).

The influence of turbulent velocity correlations on the mean flow field depends upon their gradient, as seen in the Reynolds-averaged Navier-Stokes equations, and these circumferentially-averaged measurements show that this influence is confined to the endwall regions. At specific

circumferential locations, these gradients appear in blade boundary layers and wakes as well. Similarly, the influence of the deterministic unsteady velocity correlations also depends upon their gradient, as seen in the average-passage equations derived by Adamczyk [1985]. Our circumferentially-averaged measurements show that when the deterministic unsteadiness consists of only potential flow effects, radial gradients do not exist and the unsteady potential flow should not affect the mean flow.

Table 6. Maximum Nondeterministic Unsteadiness or Turbulence within IGV Wakes

Unsteady Flow Parameter	52.4 % Span		81.0 % Span		95.2 % Span	
	Wake	Freestream	Wake	Freestream	Wake	Freestream
$100 \times \frac{\overline{V_z'^2}}{U_{tip}^2}$	0.2378	0.0045	0.1694	0.0047	0.3897	0.0086
$100 \times \frac{\overline{V_\theta'^2}}{U_{tip}^2}$	0.2525	0.0027	0.2262	0.0009	0.2171	0.0046
$\sqrt{\frac{\overline{V_z'^2}}{\overline{V_s^2}}}$	0.0640	0.0088	0.0547	0.0091	0.0867	0.0129
$\sqrt{\frac{\overline{V_\theta'^2}}{\overline{V_s^2}}}$	0.0659	0.0068	0.0632	0.0040	0.0647	0.0094

Figure 41 also shows another interesting feature: The cross-correlation between the measured axial and tangential components of the deterministic unsteady velocity is zero. Since the unsteady disturbance is potential, one can express this disturbance with a velocity potential,

$$\tilde{\Phi}_n(z, \theta) = \Phi_0 e^{-kz} \cos(n\theta - \phi_n),$$

that varies sinusoidally in the circumferential direction and decays exponentially in the axial direction. The velocity potential is assumed to be independent of r and to contain several harmonics in the circumferential direction, similar to the nonuniform flow created by the IGV wakes. The velocity

potential must satisfy Laplace's equation,

$$\frac{\partial^2 \tilde{\Phi}_n}{\partial z^2} + \frac{1}{r^2} \frac{\partial^2 \tilde{\Phi}_n}{\partial \theta^2} = 0 ,$$

which it does if $k = n/r$. From the definition of the velocity potential, one can obtain the distortion velocities in the axial and circumferential directions,

$$\tilde{V}_z = -\frac{\partial \tilde{\Phi}_n}{\partial z} = \frac{n \Phi_0}{r} e^{-nz/r} \cos(n\theta - \phi_n)$$

and

$$\tilde{V}_\theta = -\frac{1}{r} \frac{\partial \tilde{\Phi}_n}{\partial \theta} = \frac{n \Phi_0}{r} e^{-nz/r} \sin(n\theta - \phi_n)$$

Note that the two components are 90 degrees out of phase with one another. We can integrate to find the cross-correlation,

$$\begin{aligned} \overline{\tilde{V}_z \tilde{V}_\theta} &= \frac{n}{2\pi} \int_0^{2\pi/n} \frac{n^2 \Phi_0^2}{r^2} e^{-2nz/r} \cos(n\theta - \phi_n) \sin(n\theta - \phi_n) d\theta \\ &= \frac{n^2 \Phi_0^2}{2\pi r^2} e^{-2nz/r} \left[\frac{1}{2} \sin^2(n\theta - \phi_n) \right]_0^{2\pi/n} \\ &= 0 . \end{aligned}$$

Hence, the measurements agree with the analytical solution that the cross-correlation should be zero.

Just as the downstream rotor blades will interact with the nonuniform flow created by the inlet guide vanes, the inlet guide vanes can interact with the periodic motion of the nonuniform potential flow around the downstream rotor blades. With both of these types of unsteady interactions in mind, Kemp and Sears [1953] first used unsteady thin airfoil theory to compute the unsteady lift on blades under the influence of unsteady interactions. As might be expected, they found that the unsteady response of upstream stator blades to the relative motion of downstream rotor blades depended strongly on the axial spacing between the blade rows and the amount of steady loading on the rotor blades. They predicted that the unsteady lift on these stator blades could be as high as 18% of the steady lift.

To view this nonuniform potential flow in more detail, Figure 12 shows the locations of seven LDV surveys at 76.2% span starting at the rotor leading edge and moving axially upstream. Again, with no IGV wakes present, Figure 42 shows the circumferential variation of the measured velocity components compared to values calculated from lifting surface theory. At 28.0% chord axially upstream of the rotor blades, Figure 42 shows that the circumferential variation over one rotor blade

spacing is small and that, indeed, the axial and tangential components of velocity are out of phase with one another. As expected for this potential flow effect, the measurements compare very well with lifting surface theory, with the calculations showing almost no circumferential variation in radial velocity. Jessup, Schott, Jeffers, and Kobayashi [1985] also found excellent comparisons between lifting surface calculations and LDV measurements acquired upstream of a propeller. As one moves closer to the rotor blades, the potential flow variation increased substantially, with the measured and calculated values continuing to give excellent agreement. However, the flow shows a few noteworthy characteristics. First, the circumferential variations become much less sinusoidal and more harmonics are required to represent these variations. Next, although the circumferentially-averaged value of radial velocity remains close to zero, lifting surface theory shows that a significant circumferential variation of the radial velocities does exist. The swept leading edge, the blade lean, and the spanwise variation in blade loading all contribute to the three-dimensional nature of the potential flow effects upstream of the rotor blades.

For the seven LDV surveys shown in Figure 42, we can again compute the levels of deterministic unsteadiness. Figure 43 shows how this potential unsteadiness decays as one moves upstream from the rotor blade leading edge. Away from the rotor blade leading edge, the cross-correlation between the measured axial and tangential components of the deterministic unsteady velocity is zero, matching our previous two-dimensional analysis. Within 10% chord of the leading edge, however, the increased three-dimensional nature of the potential flow produces nonzero cross-correlations. The lifting surface theory calculations show the same trend as the LDV measurements.

We can extend our two-dimensional analysis to the auto-correlations. First, for the correlation involving the axial component of the deterministic unsteady velocity, we can integrate to find

$$\begin{aligned}\overline{\tilde{V}_z \tilde{V}_z} &= \frac{n}{2\pi} \int_0^{2\pi/n} \frac{n^2 \tilde{\Phi}_0^2}{r^2} e^{-2nz/r} \cos^2(n\theta - \phi_n) d\theta \\ &= \frac{n^2 \tilde{\Phi}_0^2}{2\pi r^2} e^{-2nz/r} \left[\frac{n\theta - \phi_n}{2} + \frac{1}{4} \sin(2n\theta - 2\phi_n) \right]_0^{2\pi/n} \\ &= \frac{n^2 \tilde{\Phi}_0^2}{2r^2} e^{-2nz/r}.\end{aligned}$$

Similarly, integration to find the correlation involving the tangential component yields

$$\overline{\tilde{V}_\theta \tilde{V}_\theta} = \frac{n^2 \tilde{\Phi}_0^2}{2r^2} e^{-2nz/r}.$$

This two-dimensional analysis shows that these correlations are identical, as do the measurements in Figure 43 at locations at least 9.3% chord axially upstream of the rotor blade leading edge. Also, as shown in Figure 42, these locations show a nearly sinusoidal variation and the harmonic corresponding to the number of rotor blades (7) should represent these variations well. Thus, we can compute the analytical decay rate and use a least-squares fit of this exponential decay to the

correlation data at least 9.3% chord axially upstream of the rotor blade leading edge. Figure 43 shows this exponential decay. As was the case with the cross-correlations becoming nonzero, both the measurements and the lifting surface theory calculations of Figure 43 show that the two auto-correlations differ from one another, within 10% chord of the leading edge. For these locations, more harmonics are required to represent the circumferential variations in the axial and tangential velocities and each harmonic has a different decay rate. Also, the three-dimensional effects become much more pronounced near the leading edge.

One final point needs to be addressed concerning the upstream influence of the rotor blades. Hobson and Shreeve [1991] acquired LDV data upstream of their cascade of compressor blades and also measured significant variations in the axial and tangential velocities due to potential effects from the downstream blades. Also, they emphasized that their measurements showed significant increases in the local turbulence intensities and Reynolds stresses in the region of the stagnation streamline. Our measurements also showed significant increases in the local turbulence intensities in the vicinity of the stagnation streamline. For our data, however, the turbulent fluctuations did not change. Since local turbulence intensity is normalized by the local mean velocity, the small velocities in the vicinity of the stagnation streamline simply elevated the freestream turbulence levels through a scaling effect.

Blade Lean

As mentioned previously, the rotor blades have a significant blade circumferential lean or skew (see Figure 3). If one describes a three-dimensional blade as the stacking of two-dimensional blade sections, blade lean occurs when the blade sections are stacked in a non-radial manner; the stacking axis leans in the circumferential direction. In fact, one should consider blade lean as a facet of a three-dimensional blade rather than the stacking of two-dimensional blade sections. Indeed, away from the stacking axis, even a radial blade can have lean or skew. The HIREP rotor blades have negative lean, since the suction surface points toward the hub surface. In terms of skew, the rotor blades have backward skew, since the blade is skewed away from the direction of rotation. The reason Schott [1993] designed a leaned rotor blade was to minimize the interaction of the rotor blades with the fairly radial wakes convecting from the upstream inlet guide vanes. Therefore, the interaction of these IGV wakes with the leaned rotor blade sections at different radii would be out of phase with one another. This out-of-phase interaction helps reduce the adverse effects of forced vibration and noise. Schott [1993] used backward skewed blades, as opposed to forward skewed blades, in order to reduce rotor blade stress.

The effect of blade lean on the flow field can be seen from the governing equations for incompressible flow. Making the assumption of axisymmetric flow ($\partial/\partial\theta = 0$) and using a set of orthogonal, curvilinear coordinates in the circumferential, meridional, and normal directions ($V_n = 0$), one can use the momentum equation in the n -direction to derive

$$\frac{1}{\rho} \frac{\partial p}{\partial n} = \frac{V_\theta^2}{r} \cos(\phi) + \frac{V_m^2}{R_c} + \frac{1}{\rho} F_n .$$

This is called the radial equilibrium equation and is used in the streamline curvature method for turbomachinery design. Within this equation, V_m is the meridional velocity (defined as the vectorial

sum of the axial and radial velocities), R_c is the radius of curvature of the meridional projection of the streamlines, ϕ is the angle between the meridional and axial directions, and F is the blade force. For HIREP, the meridional and axial directions are nearly the same and this yields:

$$\frac{1}{\rho} \frac{\partial p}{\partial r} = \frac{V_\theta^2}{r} + \frac{V_\phi^2}{R_c} + \frac{1}{\rho} F_r.$$

For a radial blade ($F_r = 0$), the centripetal acceleration and the streamline curvature establish a radial pressure gradient. The centripetal acceleration term is always positive and will tend to establish a radial pressure gradient with higher pressures occurring toward the blade tip. Near the endwalls, the curvature of the streamlines must be small, but away from the endwalls—especially for high aspect ratio blades—the streamline curvature term can become significant. The introduction of blade lean will not affect the change in tangential momentum, so the tangential velocities and centripetal acceleration remain the same. However, blade lean will create a blade force that can affect the radial pressure gradient. For positive lean, the pressure surface points toward the hub surface and the blade force acts radially inward. Near the endwalls, this inward radial blade force increases the pressure near the hub and reduces the pressure near the casing. Walker [1987] reviewed several investigations that showed both experimentally and numerically that this pressure change will occur. A velocity decrease will accompany the pressure rise near the hub and the streamlines will move outward, creating additional streamline curvature. For low aspect ratio blades, Walker [1987] found that blade lean affected the radial pressure gradient through the entire blade passage. This effect decays very rapidly away from the blade because streamline curvature cannot maintain this new radial pressure gradient. For high aspect ratio blades, he found that the effect of blade lean on the radial pressure gradient was counteracted by streamline curvature away from the endwalls—streamline curvature partly induced by the blade lean. Negatively leaned blades—such as the HIREP rotor blades—will have the opposite effect on the radial pressure gradient.

Walker [1987] and others have investigated how blade lean affects the flow field and, thus, the blade performance. Although much of this work has dealt with turbine stator blades, it might shed some light on the behavior of leaned or skewed pump rotor blades. Blades with compound lean seem to perform best. These blades have positive lean near the hub and negative lean near the casing. Although a consensus has not been reached on the exact mechanism, blades with positive lean result in decreased losses at the hub and increased losses at the tip. Blades with compound lean result in decreased overall losses, with decreased losses occurring near both endwalls and some increased losses occurring near midspan. Compound blade lean helps to increase the pressure near the endwalls, especially near the trailing edge. As a result, flow diffusion is reduced and boundary layer transition and separation can be delayed.

Using this axisymmetric flow model as an explanation, the negative lean or backward skew in the HIREP rotor blades will globally raise the pressure near the tip and reduce the pressure near the hub. This axisymmetric model does not indicate local effects on either the pressure or suction surfaces. Nevertheless, using the explanation of Walker [1987], flow diffusion will decrease near the tip and increase near the hub. This change in flow diffusion should decrease the risk for separation near the tip and increase the risk of separation near the hub.

Rotor Blade Static-Pressure Distribution

The acceleration of the flow through the inlet guide vanes and the larger chord lengths of the rotor blades produce larger chord Reynolds numbers for the rotor blades than for the inlet guide vanes. Using the circumferentially-averaged streamwise (absolute) velocities measured upstream of the rotor blades, we can compute chord Reynolds numbers for the rotor blades ranging from 3,600,000 at 90% span up to 3,900,000 at 10% span. More appropriately, using relative velocities, the chord Reynolds numbers range from 5,500,000 at 90% span down to 4,100,000 at 10% span. These chord Reynolds numbers combine with the blade section designs to establish the rotor blade static-pressure distributions shown in Figure 44 for the five spanwise locations of static-pressure taps in Figure 5. Figure 44 shows both the measured values of K_p and the design calculations that Schott [1993] computed using lifting surface theory.

Figure 44 shows that the spanwise static-pressure distributions vary more for the rotor blades than for the inlet guide vanes—especially on the pressure surface. The suction surface shows a favorable streamwise static-pressure gradient over the first 20% chord that vanishes and becomes adverse over the last 40% chord—a similar trend shown by the lifting surface calculations. The static-pressure distributions exhibit more spanwise variation on the pressure surface, but the pressure gradients, whether favorable or adverse, are much milder than on the suction surface for most of the blade. At 90% span, however, the streamwise pressure gradients on the pressure surface become more substantial than they are at smaller spanwise locations. On the pressure surface, the lifting surface calculations show much less spanwise variation than the measurements, with the calculations underpredicting the pressures near the trailing edge—especially at 90% span. While the measurements showed a slightly adverse pressure gradient near the leading edge at 10% span changing to a favorable pressure gradient at 90% span, the calculations always showed a very mild favorable pressure gradient. Also, note that integrating the pressure distributions gives values of lift that are about twice as large for the rotor blades than for the inlet guide vanes—with the maximum lift occurring at 22% span for the rotor blades, according to the design parameters of Schott [1993].

In order to establish a small test matrix, we acquired additional rotor blade static-pressure distributions for values of V_{ref} equal to 15, 20, 25, 30, and 35 ft/sec, at all three flow coefficients. Similar to the changing conditions on the inlet guide vanes, these changing conditions had little effect on the character of the rotor blade pressure distribution. Again, the chord Reynolds numbers remained quite large and the flow coefficients were never too far off design, so one would not expect significant changes in the pressure distributions.

Similar to the analysis on the inlet guide vanes, we used the boundary layer code STAN5 of Crawford and Kays [1976] to compute the boundary layer characteristics on both rotor blade surfaces. Again using a value of 400 for the momentum thickness Reynolds number at the beginning of transition, STAN5 showed that natural transition should take place from 10% chord to 20% chord on both surfaces. For the large chord Reynolds number on these rotor blades, this result appeared independent of either spanwise location or the different streamwise static-pressure gradients. In fact, the only reason for the transition region moving slightly upstream on the rotor blades relative to the inlet guide vanes was the increase in chord Reynolds number. However, one must note that the calculated position and length of the transition region is highly dependent on the selection of the value of the momentum thickness Reynolds number for which transition will begin. The favorable streamwise gradient over the first 20% chord of the suction surface will increase this momentum

thickness Reynolds number and cause a slight shift of the transition region towards the trailing edge. Also, an increase in freestream turbulence will decrease this momentum thickness Reynolds number and cause a shift of the transition region towards the leading edge. We chose a freestream turbulence intensity of 1.5% compared with the bare tunnel value of 0.107%—a choice consistent with the cascade measurements of Zierke and Deutsch [1989]. In addition, the interaction of the rotor blade boundary layers with the periodic passing of the IGV wakes leads to wake-induced transition. Mayle [1991] and others have shown that wake-induced transition can cause the laminar and transitional boundary layers on the rotor blade to become intermittently turbulent due to the passing of the highly-turbulent IGV wakes.

Figure 45 shows contour plots of the static-pressure coefficients on both the suction and pressure surfaces. The suction surface appears very two dimensional with a strong adverse streamwise pressure gradient that should lead to trailing edge separation. Even though the STANS calculations show no separation through the 94.8% chord location on the suction surface, the calculations in this adverse pressure gradient show signs that separation will occur between 94.8% chord and the trailing edge. Although the pressure surface appears more three dimensional in Figure 45, the strong radial pressure gradient that appeared near the trailing edge of the inlet guide vanes does not appear on the rotor blades.

Rotor Shaft Thrust and Torque

Any change of the axial momentum of the fluid passing through the rotor blades produces an axial force and the reaction to this fluid force gives rise to the rotor shaft thrust, F_T . Similarly, any change in angular momentum produces a reaction moment or torque, M_Q , about the rotor shaft. The rate of energy transferred from the rotating blades to the fluid is the product of this torque and the angular velocity of the rotor, Ω . From similarity considerations, one can derive the thrust and torque coefficients,

$$K_T = \frac{F_T}{\rho n^2 D_{tip}^4}$$

and

$$K_Q = \frac{M_Q}{\rho n^2 D_{tip}^5} .$$

As with the definitions of ϕ_{vol} and J , these coefficients are not truly nondimensional since n includes rotor shaft revolutions (and not radians). However, from past experience with propellers, these definitions have represented the most suitable definitions for the application of propeller characteristics to aerodynamic or hydrodynamic calculations.

Figure 46 shows K_T and K_Q plotted versus ϕ_{vol} , while Figure 47 shows K_T and K_Q plotted versus ϕ . All the data show the expected decrease of thrust and torque with increasing flow

coefficient, with only small variations in torque. We measured only a small variation in flow coefficient and, thus, a small portion of the performance curves—primarily because of limitations set by the performance of the downstream turbine. The most revealing element of Figures 46 and 47 is the comparison of the experimental thrust and torque with the design values at the design flow coefficient. While the torque measurements matched very well (about 2% low), the thrust measurements were about 16% high. From the experimental technique section on rotor shaft torque and thrust measurements, recall that problems hampered our ability to measure thrust.

Unlike the experimental measurements, future numerical solutions of the HIREP flow field cannot directly resolve forces and moments on the rotor shaft. However, comparisons of thrust and torque can still be made. Since the thrust results from the integrated pressure distribution (and slightly from the integrated surface shear stress distribution) on the blade yielding a net axial force, one can think of a thrust coefficient as a pressure coefficient where the integrated pressure distribution gives F_T/A :

$$C_T = \frac{F_T}{\frac{1}{2} \rho V_{ref}^2 A} .$$

Comparably, the integrated pressure distribution can yield a net torque and one could define a torque coefficient as

$$C_Q = \frac{M_Q}{\frac{1}{2} \rho V_{ref}^2 A r_{tip}} .$$

These coefficients can easily be converted into the previously defined K_T and K_Q . Unfortunately, our measured rotor blade static-pressure distributions lacked the necessary detail to give accurate integrated values of thrust and torque.

Rotor Blade Surface Flow Visualization

As with the inlet guide vanes, photographs and physical length measurements allowed us to reconstruct surface flow visualization patterns of the rotor blades on various projected surfaces. Again, we ran surface flow visualization tests for the design flow coefficient ($\phi_{vol} = 1.36$) and two off-design flow coefficients ($\phi_{vol} = 1.22, 1.50$)—using the reference velocity, V_{ref} , of 35 ft/sec. Relative to patterns observed at the design flow coefficient, only slight differences were found when observing the patterns at the two off-design flow coefficients—primarily in the location of critical points and critical lines. Figure 48 shows the reconstruction of the oil-paint pattern (shown in blue) on the hub surface of the rotor blades for the design flow coefficient. Again, the dark gray surface with the bold black border represents a footprint of the designed blade section at the hub, while the light gray region surrounding this blade section represents the extension of the fillet onto the hub surface. Note that the blade lean changes how the fillet blends onto the hub surface on the pressure and suction sides of the blade. The relative flow vectors in Figure 48 are the design flow vectors at the hub as determined from the streamline curvature solution.

The skin-friction lines of Figure 48 show the same topology for the formation of the horseshoe vortex as shown on both HIREP IGV endwalls, the rotor hub surface of Dong, Gallimore, and Hodson [1987], and the stator hub surface of Schulz and Gallus [1988]. The saddle point was located on the outer edge of the leading edge fillet and a line of separation passed through this saddle point, forming a C-pattern. Again, we were unable to find any other critical points, critical lines, or lines of oil-paint accumulation; however, a nodal point of attachment must exist somewhere on the leading edge. The boundary layer separates along the separation line and rolls-up to form the horseshoe vortex. The pressure side leg of the horseshoe vortex convects into the midpassage region and eventually merges with the passage vortex, while the suction side leg moves up along the suction surface and eventually wraps around the passage vortex. Even for these lightly-loaded blades, a circumferential pressure gradient exists and causes the suction side leg of the separation line to move up onto the suction surface. However, comparing the exiting skin-friction lines with the design flow vector in Figure 48 indicates that this circumferential pressure gradient produces very little overturning of the flow very close to the hub endwall. One reason for this small amount of overturning could be the blockage from what appears to be a substantial corner separation where the suction surface trailing edge meets the hub, as shown in the reconstruction of the oil-paint pattern on the suction surface in Figure 49. Schulz and Gallus [1988] found that very large corner separation regions will create a blockage that will even cause the pressure side separation line of the horseshoe vortex to be swept back towards the pressure surface.

Recall that Schott [1993] redesigned the rotor blades to reduce the corner separation. Although the comparison of our results in Figure 49 with those of Farrell [1989] shows some success in reducing this corner separation, the region of flow separation is still significant. This result might appear even more surprising if one remembers that the diffusion factor at the root blade section was 0.28--well below the limiting value between 0.5 and 0.6 that indicates the risk of separation. However, recall that, according to Walker [1987], negative blade lean can increase the diffusion near the hub. For their compressor stator blades, Schulz and Gallus [1988] also calculated diffusion factors--which increased with increasing angle of attack--and they showed that for small angles of attack, the corner separation region formed with a value of D at the hub of less than 0.4. The empirically-based diffusion factor comes from two-dimensional cascade data and does not seem to correlate with three-dimensional separation. The two-dimensional boundary layer calculation using STAN5 also failed to indicate any separation other than very close to the trailing edge.

Figure 50 shows a photograph of the oil-paint pattern in the vicinity of the three-dimensional corner separation. The topology of this separation region includes a saddle point on the hub surface of Figure 48, just downstream of the suction side of the trailing edge. One leg of the separation line passing through this saddle point enters a spiral node of separation near 91% chord and 6% span on the suction surface, as seen in Figure 49. Figure 48 shows that the other leg of the separation line proceeds downstream and, beginning at the saddle point, the limiting streamlines leave the hub surface along this line to form a dividing surface of separation. The vortical core about which this dividing surface coils begins at the spiral node. Similar separation lines proceeded downstream of the trailing edge on both IGV endwall surfaces and the corresponding spiral nodes of separation seem to indicate that the dividing surfaces of separation would coil towards the suction surface (the same sense as the suction side legs of the horseshoe vortices). For the case on the rotor hub surface, the spiral node indicates that the dividing surface of separation would coil towards the pressure surface. This difference is caused by the hub rotating under this separation surface.

Figure 49 shows that a line of local separation exists on the suction surface, moving from 70% chord near the hub to 96% chord near the tip. The downstream zone of separation varies from the three-dimensional corner separation near the hub—including the spiral node of separation—to a more two-dimensional type of separation over most of the span. Just upstream of this local separation line, the skin-friction lines begin to migrate radially outward. Also, skin-friction lines emanating from the pressure surface have moved around the trailing edge within the separation zone—similar to the skin-friction lines on the stator blades of Schulz and Gallus [1988]—and also migrate radially outward. The reason for this radial motion in an otherwise two-dimensional flow can be seen from an evaluation of the radial equilibrium equation,

$$\frac{1}{\rho} \frac{\partial p}{\partial r} = \frac{V_\theta^2}{r} + \frac{V_m^2}{R_c} + \frac{1}{\rho} F_r .$$

Within the blade passage, the positive centripetal acceleration term establishes a radial pressure gradient, with the largest pressures occurring near the tip. Previously, we showed that the negative lean of these rotor blades will increase this radial pressure gradient, especially near the endwalls. Closer to the suction surface (within the boundary layers), the tangential velocities become larger and, at the blade surface, they take on the value of the blade rotational speed. This increase in V_θ creates an imbalance in the radial equilibrium equation, and the larger centripetal acceleration causes fluid to move radially outward. The radial pressure gradient within the blade passage does not show up on the surface pressures of Figure 45 since the separation changes the character of the pressure distribution near the trailing edge.

Because of the radially outward flow near the trailing edge, the surface of separation that lifts off the blade at the local separation line rolls-up into a spanwise vortex. Near the casing, this vortex moves into the circumferential direction, away from the suction surface as the blade rotates in the other direction. Farrell [1989] also used oil-paint surface flow visualization and found similar patterns on the suction surface of his rotor blades. In addition, he was able to visualize this vortex as it moved away from the suction surface in the circumferential direction by lowering the tunnel pressure until the vortex began to cavitate. As we will show later, we were unable to obtain a low enough tunnel pressure for our vortex to cavitate. Evidently, the higher-loaded rotor blades used by Farrell [1989] created a stronger vortex from the trailing-edge separation and the lower pressure within this vortex core led to cavitation at a higher tunnel pressure.

Figure 51 shows the reconstruction of the oil-paint pattern on the pressure surface of a rotor blade. The flow over the pressure surface appears very two dimensional. Neither the pressure nor suction surfaces on the rotor blade showed any signs of oil-paint accumulation that would indicate the presence of transition—even though boundary layer calculations indicated a transition region exists between 10% and 20% chord. One possible explanation for the failure of the oil-paint to accumulate might be the presence of wake-induced transition from the periodic passing of IGV wakes. Thus, the time-average wall shear stress becomes larger near the region where natural transition would normally occur—preventing an accumulation of the oil-paint. Also, remember that oil-paint patterns indicating natural transition depend more on oil-paint thickness and run time than do patterns indicating separation.

Near the trailing edge of the pressure surface, Figure 51 indicates that the rotor blades exhibit more two-dimensionality than the skin-friction lines for the inlet guide vanes shown in Figure 24. Even though the design parameters of Schott [1993] show that the lift coefficient and circulation reach maximum values at 22% span and decrease toward both endwalls, we could not clearly detect the existence of any radial motion of the skin-friction lines near the trailing edge. This does not mean that the changing spanwise circulation does not lead to a trailing vortex sheet, it simply means that we could not detect any radial motion from the photographs we had of this significantly leaned rotor blade.

One very significant pattern does show up on the pressure surface oil-paint pattern of Figure 51: A radial outward flow exists over the top 8% of the span. In order for the rotating blade to avoid rubbing the casing endwall, a clearance exists between the rotor tip and the casing. Because of this clearance, the high pressure fluid in the pressure surface boundary layer moves through the clearance towards the low pressure region near the suction surface. Figure 52 shows the skin-friction lines associated with the relative leakage flow across the rotor blade tip section. Notice how these skin-friction lines on the rotor blade tip section are not parallel. Near the leading edge, the skin-friction line was tilted 1 degree from the circumferential direction, while near the trailing edge, the skin-friction line was tilted 16 degrees from the circumferential direction. Also, recall that the pressure side corner of the rotor blade tip section was rounded to prevent local separation of the leakage flow; therefore, the oil-paint pattern shows no sign of separation. As the leakage flow moves through the clearance, it interacts with the throughflow across the suction surface. The interaction of these two flows causes the sheet of vorticity passing through the clearance from the pressure surface boundary layer to roll-up into a tip leakage vortex.

Within the HIREP flow field, the tip leakage vortex proves to be the most dominant flow structure. In addition to accumulating vorticity from the pressure surface boundary layer, the rotation of the blades can allow vorticity from the casing endwall boundary layer to merge into the tip leakage vortex. Also, the fluid in the leakage flow does not receive the momentum increase that the fluid in the rotor passage receives. This lack of momentum transfer, coupled with the irrecoverable streamwise vorticity, leads to large total-pressure losses. Streamwise vorticity also takes a long time to decay and these rotating tip leakage vortices can then interact with any downstream blades or struts. Finally, the low pressure associated with the vortex core can lead to cavitation.

The secondary flow downstream of the rotor blades can be summarized in Figures 53 and 54. Figure 53 illustrates the existence of passage vortices and trailing vortex sheets, while Figure 54 summarizes the analysis of the surface flow visualization on the rotor blades. Again, note that we have performed the analysis using time-average patterns of flow separation even though most regions of flow separation are unsteady. Also, note that the secondary flows—including the skewed endwall boundary layers—developed upstream of the rotor blades can affect the incidence angle and the subsequent development of the secondary flows downstream of the rotor blades. Horlock [1963] found that the effect of the secondary flow downstream of one blade row on flow turning can be the opposite of the expected effect because of the secondary flow upstream of the blade row. Within any multiple-blade-row turbomachine, one must account for the effects of secondary flow on all downstream blades.

Figure 54 shows our interpretation of the three-dimensional skeleton structure of the secondary flow through the rotor blades. The flow overturning on the hub endwall moves the suction side leg of the horseshoe vortex back towards the suction surface and causes the vortex to lift off the surface.

The pressure side leg of the horseshoe vortex moves into the midpassage region and eventually becomes part of the passage vortex. The presence of the rotor tip clearance should alleviate the adverse pressure gradient that separates the casing endwall boundary layer and forms a horseshoe vortex. For a very small tip clearance, however, Inoue and Kuroumaru [1989] claimed that they found some evidence of the existence of a horseshoe vortex. Figure 54 also shows a three-dimensional corner separation in the junction where the suction surface meets the hub endwall--with a vortex filament leaving the blade surface. This three-dimensional corner separation region might be even larger if not for the presence of the periodic passing of turbulent IGV wakes over the rotor blade surfaces. Schulz, Gallus, and Lakshminarayana [1990] found this to be true for their stator blade corner separation, with and without an upstream rotor blade row. Radial outward flow from centrifugal effects cause the otherwise two-dimensional separation to roll-up into a vortex, migrate up the trailing edge, and finally move circumferentially away from the suction surface as the blade rotates. Figure 55 shows a cavitation photograph taken by Farrell [1989] of both this vortex and the tip leakage vortex. This photograph shows that the trailing-edge separation vortex lies closer to the casing than the tip leakage vortex. Further cavitation visualization performed by Farrell [1989] showed that these two vortices--rotating with the same sense--will eventually roll-up into a single vortex as they propagate downstream. The tip leakage vortex is also shown schematically in Figure 54 and this dominant flow structure will appear later in many measurements downstream of the rotor blades.

Rotor Blade Exit Flow

Downstream of the rotor blades, we measured the axial and tangential velocities with the LDV in three axial planes as shown in Figure 12. The first plane was 4.8% chord axially downstream of the tip of the rotor blade trailing edge. Because of the swept trailing edge of the rotor blades, Figure 12 shows that this first plane included measurement locations down to only 81.0% span and this location occurred 0.7% chord axially upstream of the rotor blade trailing edge (using the local chord). Shadows from the passing of the leaned rotor blades significantly reduced the data acquisition rate at smaller spanwise locations. The second LDV measurement plane was 21.4% chord axially downstream of the tip of the rotor blade trailing edge and went as low as 2.0% span. While this 2.0% span location occurred 3.8% chord axially downstream of the rotor blade trailing edge, it actually occurred only 0.8% chord axially downstream if one takes the fillet into account (again using the local chord). Finally, the third LDV measurement plane was 32.2% chord axially downstream of the tip of the rotor blade trailing edge and also went as low as 2.0% span. This 2.0% span location occurred 13.8% chord axially downstream of the rotor blade trailing edge, or 10.2% chord axially downstream if one takes the fillet into account.

Before analyzing the LDV data downstream of the rotor blades, we found the circumferential locations of the IGV wakes upstream of the rotor blades using the five-hole probe data. Then, using the flow velocities and angles from the streamline curvature solution, we tracked the IGV wakes as they convected through the rotor blades in an approximate manner. For the circumferential index position of the inlet guide vanes used for the LDV measurements, this analysis showed that no IGV wake was present in the vicinity of the LDV measurement volume at any of the three axial measurement planes.

With all of the LDV data resolved into one degree storage windows, Figure 56 shows contour plots of the axial velocity at the three axial planes downstream of the rotor blades, while Figure 57 shows contour plots of the tangential velocity. All six contour plots clearly show the existence of the skewed rotor blade wakes, with the nonuniform nature of these wakes arising from computing contours using data from coarsely-spaced, discrete measurement locations. In other words, the spanwise varying contours within the rotor blade wakes do not indicate any physical phenomenon. The wakes at the second measurement plane are skewed about 33 degrees, while the wakes at the third measurement plane are skewed about 35 degrees. The rotor blades themselves have 30 degrees of skew and some residual swirl remains in the flow, especially near the hub. Therefore, the amount of skew in the rotor blade wakes seems very reasonable.

Figure 12 also shows the locations of LDV surveys at 76.2% span, starting near the rotor blade trailing edge and moving downstream. These surveys allowed us to measure the decay of the rotor blade wakes as seen in Figure 58. For seven chordwise locations axially downstream of the rotor blade trailing edge, Figure 58 shows average-passage wake profiles of the streamwise velocity. The 95% confidence bands in Figure 58 illustrate the repeatability in measuring the seven different rotor blade wakes. While the width and the depth of the wake change with downstream distance, the rotor blade wakes do not experience the exponential decay of the rotor blade potential disturbance measured at the same spanwise location, but upstream of the rotor blades. In fact, outside of the wakes themselves, Figure 58 shows that the variation in freestream velocity is affected by the downstream potential flow from periodic motion of the circumferentially nonuniform pressure field from the upstream rotor blades, and this potential disturbance does decay faster than the wakes.

At the furthest downstream measurement plane, the LDV data provide information on the relative importance between the wakes and the tip leakage vortices in the casing endwall region. Near this endwall, Figure 59 presents variations in the axial velocities around the circumference of the machine. At 88.1% span, Figure 59 shows axial velocity deficits associated with the rotor blade wakes. Also at 88.1% span, the regions of increased axial velocity between the wakes result from the three-dimensional influence of the tip leakage vortices. Just closer to the endwall, at 90.5% span, the wakes have a similar deficit, but the tip leakage vortices also have a similar axial velocity deficit--with a broader profile. For the axial velocity distributions at radial locations even closer to the endwall, notice how the flow structures associated with the tip leakage vortices dominate the structures associated with the wakes, having much deeper and broader profiles. With these strong deficits in axial velocity, the tip leakage vortices would have a strong impact on any downstream blades or struts. While many investigators have examined the detrimental effects of blades interacting with wakes created by upstream blades with relative motion, Binder [1985] and Binder, Forster, Mach, and Rogge [1987] have shown that secondary vortices downstream of a row of turbine stator blades will have strong unsteady interaction effects with downstream rotor blades. Not only will the velocity deficits associated with secondary vortices create unsteady interaction effects in the same manner as wakes, Binder [1985] and Binder, Forster, Mach, and Rogge [1987] find that the interaction of blades with vortices can lead to vortex breakdown, which gives rise to a large increase in turbulent fluctuations.

Figure 60 shows the circumferential variation in tangential velocity at the same locations as the axial velocity variations in Figure 59. Again, the tangential velocity variations show the dominance of the tip leakage vortices within the casing endwall regions. Figures 61 and 62 show the corresponding distributions of the axial and tangential nondeterministic unsteady flow correlations, which also show the dominance of the tip leakage vortices. As we will show later, the

nondeterministic unsteadiness associated with tip leakage vortices involves turbulence, as well as a random motion of the vortex structures themselves. In terms of turbulence intensity, the wakes within the casing endwall region reach maximum values of 14.9% for axial turbulence intensity and 12.1% for tangential turbulence intensity. Using the same freestream velocity for normalization, the tip leakage vortices reach values of 21.2% for axial turbulence intensity and 22.6% for tangential turbulence intensity. All of the variations in velocities and unsteadiness have been examined at the two upstream measurement planes. Although similar in shape, these distributions show larger velocity deficits and increased unsteadiness levels—a trend consistent with viscous decay. Also, variations associated with potential flow effects are more evident at the upstream planes.

So far, the LDV data has shown the existence of rotor blade wakes and strong tip leakage vortices. Within the circumferential region between the tip leakage vortex from one blade and the wake from the next blade, the LDV data shows that casing endwall boundary layers do exist at all three measurement planes. Some of the fluid from the casing boundary layer convects through the rotor tip clearance and into the tip leakage vortex, while some of the fluid is entrained directly into the vortex. Despite this loss of boundary layer fluid, much of the boundary layer remains intact and is simply altered in direction by the motion of the rotor blades. The rotating blades do not remove the casing boundary layer—as calculations show that either viscous or turbulent diffusion could not reestablish the boundary layer before the passing of the next rotor blade. Table 7 gives the boundary layer characteristics for all three of these boundary layers, where the edge velocities are essentially in the axial direction.

Table 7. Characteristics of the Casing Endwall Boundary Layers Downstream of the Rotor Blades

Parameter	First Axial LDV Measurement Plane	Second Axial LDV Measurement Plane	Third Axial LDV Measurement Plane
U_e	33.0 ft/sec	33.7 ft/sec	33.4 ft/sec
δ	1.24 inches	1.19 inches	1.15 inches
δ^*	0.208 inches	0.252 inches	0.199 inches
θ	0.134 inches	0.152 inches	0.125 inches
H	1.55	1.66	1.59

Figures 56 and 57 also show data obtained near the hub for the second and third LDV measurement planes. Before proceeding, however, one should take note that data was difficult to obtain in this region because of the problems in focussing the laser beams that far from the tunnel window. For the second plane, this data acquisition problem coupled with the close proximity to the separation off the trailing edge fillet led to poorly defined velocity contours. Despite this problem, Figures 56 and 57 clearly show that some type of flow structure exists near the hub—possibly from the horseshoe vortices. First, note that the corner separation has led to much larger wakes in the hub endwall region. This corner separation, as depicted in Figure 54, along with the significantly skewed

boundary layers along the hub endwall give rise to the pattern in the axial velocity contours and the circumferential gradients in the tangential velocity contours.

Next, we can find local circumferential means of the LDV data at each spanwise location, again using area averages.

$$\bar{V} = \frac{\int_0^{\theta} V d\theta}{\int_0^{\theta} d\theta} .$$

One must remember that these circumferential means involve averaging the data at a single circumferential location for a complete revolution of the rotating blades and does not involve averaging around the circumference of the machine. Therefore, the averaging contains no IGV wakes. For all three LDV measurement planes, Figure 63 shows the circumferential means of the axial and tangential velocities compared with the streamline curvature design calculations. The axial velocity deficit and the undeturning of the flow near the casing endwall results from a circumferential average of the endwall boundary layer, the rotor blade wakes, and, especially, the tip leakage vortices. The rotor blade wakes, the corner separation, and the highly-skewed endwall boundary layer produce the axial velocity deficit near the hub endwall. Since the streamline curvature method only takes these endwall effects into account with a modest total-pressure loss model, the calculated axial velocities in the core flow are underpredicted in order to conserve mass flow. Note that curvature in the streamlines produces spanwise gradients in static pressure and, therefore, in axial velocity—a result shown by both the calculations and the measurements.

At the same axial position as the third LDV measurement plane, we also performed radial surveys with a slow-response Kiel probe, in order to measure the time-average total pressures. Two repeat surveys were completed at two different circumferential index positions of the inlet guide vanes. While the laser beams for the LDV measurements entered from the side of the tunnel, the Kiel probe was inserted from the top of the tunnel. Thus, the LDV and Kiel probe measurements were acquired at different circumferential positions and, therefore, at different positions relative to the IGV wakes. Figure 64 shows the results of these total-pressure measurements. Again, using upstream measurements and streamline curvature calculations, we approximated how the IGV wakes would convect through the rotor blades and into the measurement plane. For the two circumferential index positions of the inlet guide vanes, the total-pressure deficits shown in Figure 64 at 11.2% and 83.3% span match closely with our analysis of the locations of the IGV wakes. Otherwise, the total-pressure profiles appear very similar to the axial velocity profile in Figure 63.

Comparing the total-pressure profile downstream of the inlet guide vanes in Figure 33 with the profile downstream of the rotor blades in Figure 64 shows the expected overall increase in total pressure imparted by the rotor blades. However, the total-pressure deficits in the endwall regions are greater downstream of the rotor blades, indicating that the corner separation and tip clearance vortices are important mechanisms for generating total-pressure losses. As mentioned previously, Joslyn and Dring [1985], Dong, Gallimore, and Hodson [1987], and Schulz and Gallus [1988] also found that their three-dimensional corner separations led to higher losses. In other experimental investigations, Inoue, Kuroumaru, and Fukuhara [1986], Yaras and Sjolander [1990], and Storer and Cumpsty [1991] have shown that tip clearance flows also lead to high losses. The total-pressure loss

model within the streamline curvature method failed to adequately model these high losses near the endwalls. Finally, Figure 64 shows the existence of total-pressure losses within the IGV wakes.

Again referring to Figure 64, note that we measured the static pressure on the casing at this axial location. These static-pressure measurements might prove useful in establishing a downstream boundary condition for future numerical computations. The static-pressure coefficient did vary slightly with the circumferential position of the inlet guide vanes. The two measured values of $C_p = 0.432$ and $C_p = 0.482$ give an indication of the static-pressure rise through HIREP. Figure 65 shows our estimate of how the static-pressure coefficient varies spanwise at this furthest downstream axial plane. Using the total-pressure measurements of Figure 64, without including the IGV wakes, along with the axial and tangential velocities of Figure 63, we computed static-pressure coefficients--assuming that the circumferential-mean values of radial velocity were zero. These estimated static-pressure coefficients differ somewhat from the streamline curvature calculations, calculations which correspond with radial equilibrium. One explanation for this difference is that the negative blade lean will increase the pressure near the tip and decrease the pressure near the root--an effect not included in the streamline curvature solution. Remember that these estimates represent circumferential averages: The local static pressures will vary considerably in the casing endwall region, with low static pressures expected in the cores of the tip leakage vortices.

At the same axial measurement plane used to acquire data with the slow-response Kiel probe, we also performed a radial survey with a fast-response total-pressure probe. This probe continuously measured data with a response time fast enough to resolve the total pressures for instantaneous angular positions of the rotor--positions measured via the optical encoder. Even though piezoelectric transducers cannot measure the mean value of total pressure, they do provide excellent measurements of the total-pressure variation about the mean, Δp_T . For different circumferential positions of the rotor, Figure 66 shows how the total pressure varies from the mean in terms of a pressure coefficient,

$$C_{\Delta p_T} = \frac{\Delta p_T}{\frac{1}{2} \rho V_{ref}^2} .$$

As with the LDV measurements of axial and tangential velocity, the total pressure variations of Figure 66 clearly show the structure of the rotor tip clearance vortices and the skewed rotor blade wakes. The low total pressures in these regions--especially in the tip clearance vortices--indicate that these are regions of large total-pressure losses.

Since the slow-response Kiel probe measures time-average total pressures, we added these time-average values to the total-pressure variations measured with the fast-response probe to obtain the actual values of total pressure downstream of the rotor blades. This addition was performed for two radial surveys taken at the same circumferential index position of the inlet guide vanes. Figure 67 shows how these actual total pressures vary circumferentially. Since the variations in total pressure were small relative to the time-average values, Figure 67 does not show the vortex and wake structures as clearly as Figure 66. Also, note that the slight deficit in total pressure at 83.3% span--along the entire circumference--signifies the presence of an IGV wake (see Figure 64).

Since our LDV measurements did not include radial velocity data, we cannot present measurements of the secondary velocity vectors corresponding to the total-pressure measurements in

Figures 66 and 67. The surface flow visualization combined with known secondary flow characteristics to lead to the secondary flow schematics in Figures 53 and 54. Some of these secondary flow characteristics can be examined further by observing the lifting surface theory calculations obtained by Schott [1993] while designing the rotor blades. Figure 68 presents these calculations. The magnitude of the secondary velocity vectors downstream of the rotor blades is much greater than downstream of the more lightly-loaded inlet guide vanes (as seen in Figure 30). With no incoming boundary layers used in this type of calculation, lifting surface theory predicts secondary flow based only on the spanwise variation in circulation and the corresponding shed vortex sheet. One difference occurs in computing the flow through the inlet guide vanes and the rotor blades. For the inlet guide vanes, the vortex line that models the bound vorticity at the vane tip aligns with the vortex line that models the casing endwall--diminishing the strength of the resulting vortex line. For the rotor blades, the tip clearance separates these two vortex lines and a jet of fluid is induced between them, with the fluid moving through the clearance from the pressure surface to the suction surface. Also, the circulation of the blade tip vortex line does not cancel with the circulation of the vortex line on the casing endwall--thus increasing the shed vorticity at the blade tip. The calculations contain no specific model of the tip leakage vortex itself. Similar to Figure 30 downstream of the inlet guide vanes, Figure 68 shows that the trailing vortex sheet has deformed and rolled-up into two concentrated vortex structures rotating in opposite directions. The structure closest to the casing is much stronger, since the spanwise variation in circulation is greater near the blade tip. Also, this stronger vortex structure near the casing has induced a larger and stronger passage vortex than the one induced near the hub.

Harmonic Content of the Rotor Blade Exit Flow

The nonuniform flow created by the rotor blades can interact with any downstream blades or struts, which, in turn, can respond to generate forced vibration and noise. As we did with the five-hole probe rake data downstream of the inlet guide vanes, we can perform a Fourier analysis of the LDV data downstream of the rotor blades. For three sample spanwise locations, Figure 69 shows the magnitude of the circumferentially-varying velocity downstream of the rotor blades as a spatial harmonic function of the harmonic order, n . Once again, this harmonic content involves data at a single circumferential location for a complete revolution of the rotating blades. No IGV wakes are present. The largest velocity magnitudes (normalized by U_{tip}) in Figure 69 occur for those harmonics associated with the number of rotor blades and its multiples. The other harmonics establish the background noise floor. Using one degree storage windows, the LDV measurements contain 360 data points from which we can estimate that the random background noise floor should occur at 0.077% of U_{tip} . As with the harmonic content of the IGV exit flow (Figure 37), the elevated deterministic component of the background noise floor for the rotor blade exit flow (Figure 69) occurs because the flow is not identical within each blade passage. Using the same signal-to-noise ratio analysis as in the IGV exit flow, Table 8 shows how many harmonics in the rotor blade exit flow (for sample spanwise locations) lie above the background noise floor and how many satisfy the signal-to-noise requirement.

Figure 69 shows the harmonic content for both the axial and tangential velocity measurements at three spanwise locations. Comparing the harmonics for the axial velocity at 9.5% and 57.1% span, one notices that the lower-order harmonics are larger and that the higher-order harmonics are smaller near the hub. The presence of the rotor blade corner separation enlarges the wakes near the hub, relative to the wakes near midspan. As also shown by Gallus, Lambertz, and Wallman [1980]

and by our IGV exit flow, these wider wakes increase the lower-order harmonics and decrease the higher-order harmonics. Near the casing, Figures 59 and 60 showed how the tip leakage vortices dominate the rotor blade wakes for the axial and tangential velocity distributions, respectively. These much broader velocity profiles have a significant effect on the harmonic content at 94.3% span, relative to midspan. The lower-order harmonics increase near the casing, while the higher-order harmonics fall-off rapidly into the background noise floor. Notice that both the axial and tangential velocity components show that the sixth harmonic ($n = 42$) then increases, followed by a second fall-off. The relative distributions of large- and small-scale velocity nonuniformities in Figures 59 and 60 account for this trend. The lower-order harmonics depend on the large-scale tip leakage vortices, while the higher-order harmonics depend on the small-scale wakes. At 98.1% and 99.1% span, the fourth harmonic falls into the background noise and the fifth harmonic increases to a level above the noise, as indicated in Table 8. Also, the background noise floor is higher near the casing, indicating that more blade-to-blade variations occur in the flow near the casing where both tip leakage vortices and wakes are present.

Figure 70 shows how $|\tilde{V}_n|/U_{tip}$ and ϕ_n vary as a function of percent span for the first five significant harmonics. The values of $|\tilde{V}_n|/U_{tip}$ decrease with increasing radius, corresponding to decreasing wake widths. This trend continues towards the casing, except for the first two harmonics, which show rapid increases near the casing because of the presence of the tip leakage vortices. The phase angles in Figure 70 increase with increasing radius with each higher harmonic showing a greater increase. One can explain this trend by first observing the rotor blade lean at the trailing edge where the wakes originate. Since the phase angle is defined relative to a radial line, the wake at the measurement plane is offset an amount $\Delta\theta$ relative to this radial line because of the circumferential blade lean at the trailing edge. Also, the small amount of residual swirl in the flow can cause a further offset between the trailing edge and measurement plane. The spanwise variation in phase angle is directly related to the blade lean and residual swirl by

$$\Delta\phi_n = n \Delta\theta .$$

Near the casing, however, the tip leakage vortices seem to alter this ideal relationship. The spanwise variation in phase angle due to the blade lean can lead to an out-of-phase interaction between the rotor blade wakes and any downstream radial blades or struts.

The harmonic content of the total-pressure field should correspond to the harmonic content of the velocity field, as shown in Figure 69. At the same spanwise locations as these Fourier analyses of the LDV data, Figure 71 shows power spectra as obtained by the signal analyzer from the fast-response total-pressure probe. In this figure, the 2.5 Hz bandwidth has been corrected to 1 Hz. The first harmonic ($n = 7$) in Figure 69 corresponds to the rotor blade-passing frequency of 30.33 Hz in Figure 71. All of the data points of the synchronous-averaged power spectrum in Figure 71 correspond to this blade-passing frequency and its multiples, since the random data has been significantly reduced by synchronous averaging. These data follow the same trend as the LDV harmonic data in Figure 69. Relative to the flow near midspan, the higher-frequency data falls-off more rapidly near the hub because of the enlarged total-pressure loss region associated with the corner separation. The tip leakage vortices near the casing create an even larger total-pressure loss region and this enlarged total-pressure deficit, in turn, causes the higher-frequency data to fall-off even more rapidly.

Table 8. Spatial Harmonics in the Rotor Blade Exit Flow
that Satisfy Accuracy Requirements

% Span*	Harmonics above the Background Noise Floor		Harmonics with $SNR \geq 7 \text{ dB}$	
	Axial	Tangential	Axial	Tangential
1.9	1 → 14	1 → 14	1 → 14	1 → 14
7.6	1 → 14	1 → 14	1 → 14	1 → 14
9.5	1 → 14	1 → 14	1 → 14	1 → 14
19.1	1 → 14	1 → 14	1 → 14	1 → 14
28.6	1 → 14	1 → 14	1 → 14	1 → 14
38.1	1 → 14	1 → 14	1 → 14	1 → 14
47.6	1 → 14	1 → 14	1 → 14	1 → 14
57.1	1 → 14	1 → 14	1 → 14	1 → 14
66.7	1 → 14	1 → 14	1 → 14	1 → 14
81.0	1 → 14	1 → 14	1 → 14	1 → 14
85.7	1 → 14	1 → 14	1 → 14	1 → 14
90.5	1 → 13	1 → 12	1 → 12	1 → 11
94.3	1 → 4 1 → 7	1 → 6 8	1 → 3 6 → 7	1 → 4 6 & 8
98.1	1 → 5	1 → 7	1 → 3 5	1 → 7
99.1	1 → 5	1 → 7	1 → 4 5	1 → 6

*as computed for the axial velocities

Figure 71 also shows the autospectrum which includes both random or nondeterministic unsteady total pressures and periodic or deterministic unsteady total pressures. When the data points from the synchronous-averaged power spectrum correspond exactly to the peaks in the autospectrum, nondeterministic unsteadiness does not exist at those frequencies. At higher-frequency peaks in the autospectrum, the peaks do not align with the data points from the synchronous-averaged power spectrum--showing an increased importance of nondeterministic unsteadiness. This increased amount of nondeterministic unsteadiness is particularly noticeable in the autospectrum peaks near the casing. Later, we will discuss an unsteady wandering effect of the tip leakage vortices, an unsteadiness that

does not correlate with shaft speed and is, therefore, nondeterministic. An increased turbulence level can also be associated with the tip leakage vortices. At midspan and near the hub, the data points from the synchronous-averaged power spectrum align well with the peaks in the autospectrum for the first five harmonics. Then, at higher frequencies, the nondeterministic unsteadiness becomes increasingly more important. Note that at very high frequencies, some broad peaks occur in the autospectrum near both the hub and the casing, but not near midspan. These broad peaks may correspond to unsteadiness of vortices and separation regions, although one would expect these types of unsteadiness to occur at low frequencies—not high frequencies.

Unsteadiness of the Rotor Blade Exit Flow

As inherent with all turbomachines, the flow downstream of the HIREP rotor blades exhibits a significant amount of unsteadiness. The periodic motion of rotor blade wakes and secondary vortices, such as the tip leakage vortices, will create an unsteady interaction with any downstream blades or struts--resulting in forced vibration and noise. As with any complex, high Reynolds number flow, the existence of turbulence has a strong influence on the time-mean flow and one must account for this turbulence when performing computations. Adamczyk [1992] examined how deterministic unsteadiness can also affect the time-mean flow and, thus, the performance of the blade rows. He concludes that one must also account for the effects of deterministic unsteadiness when performing computations for a multiple-blade-row turbomachine. Relative to the rotating blades, the deterministic unsteadiness primarily involves the interaction of the rotor blades with the IGV wakes. Also, the interaction of these IGV wakes with the rotor blade wakes can prove to be important. However, for the LDV data downstream of the HIREP rotor blades, the IGV wakes were not present and we cannot make any conclusions concerning their effects.

Figure 72 shows the level of overall unsteadiness for the two furthest downstream LDV measurement planes of Figure 12. While most of the unsteadiness seems to be concentrated near the endwalls for the plane 32.2% chord axially downstream of the rotor blade tip, the plane 21.4% chord downstream shows elevated levels of unsteadiness throughout. As we did with the IGV exit flow, we can gain further insight into this flow unsteadiness by decomposing the overall unsteadiness into a nondeterministic unsteadiness and a deterministic unsteadiness. Figure 73 shows the circumferentially-averaged levels of nondeterministic unsteadiness for the same two planes. First, let us concentrate on the region near the hub. Remember that the closest measurement location to the hub is located at 2% span and only 0.8% of the local chord downstream of the trailing edge fillet—a flow region periodically imbedded within the corner separation illustrated in Figure 54 and presented in the velocity contours of Figures 56 and 57. The presence of this corner separation and the rotor blade wakes have elevated the nondeterministic unsteadiness through increased levels of turbulence and unsteady vortex shedding. This elevated unsteadiness particularly affects the variance involving axial velocity fluctuations, with a maximum intensity occurring at 6% span and some increased intensities up to 60% span. Further downstream, the next plane shows that the nondeterministic unsteadiness has decayed significantly in the hub region, with only a minimal effect beyond 6% span.

Near the casing, Figure 73 also shows elevated levels of the circumferentially-averaged nondeterministic unsteadiness. Further observation shows, that unlike the unsteadiness near the hub, the nondeterministic unsteadiness near the casing does not decay very rapidly. The reason for this slower decay rate can be found in the contour plots of axial nondeterministic unsteadiness in

Figure 74 and of tangential nondeterministic unsteadiness in Figure 75. Figures 74 and 75 show that the tip leakage vortices dominate the nondeterministic unsteadiness near the casing and these vortices consist of streamwise vorticity that decays quite slowly. While turbulence no doubt plays an important role in the level of nondeterministic unsteadiness associated with the tip leakage vortices, we shall show later that these vortices wander in an unsteady manner and this unsteadiness also influences the level of nondeterministic unsteadiness. Also, note how the contour plot of Figure 74 reveals the elevated levels of axial nondeterministic unsteadiness just downstream of the rotor blade trailing edge near the hub.

The levels of nondeterministic unsteadiness in Figure 73 fail to fully explain the levels of overall unsteadiness in Figure 72. In order to complete the explanation, we need to examine the levels of deterministic unsteadiness shown in Figure 76. At the furthest downstream plane, Figure 76 shows that the periodic passing of the tip leakage vortices and, to a lesser extent, the rotor blade wakes creates elevated levels of deterministic unsteadiness near the casing. Elevated levels also appear near the hub, where the larger wakes and streamwise vortices created by the corner separation rotate in a periodic fashion. The smaller levels of deterministic unsteadiness throughout the midspan region are created by the passing rotor blade wakes, with some influence from potential flow effects. Recall that the circumferentially nonuniform pressure field from the upstream rotor blades creates this potential flow effect and that this effect decays exponentially. Therefore, the furthest upstream plane in Figure 76 shows an increased potential flow effect, especially near the hub where the measurements have a closer proximity to the rotor blade trailing edge. Although the deeper rotor blade wakes and stronger secondary vortices in the upstream plane will increase the levels of deterministic unsteadiness, the rapid increase in unsteadiness as one proceeds from 75% span to the hub indicates that potential flow effects play the most important role in the higher levels of deterministic unsteadiness relative to the downstream plane.

Much of the interest in providing measurements and analysis of both the nondeterministic and deterministic unsteadiness has been inspired by the derivation of the average-passage equations by Adamczyk [1985]. Just as gradients in the turbulent correlations create stress-like terms that must be modelled, Adamczyk [1985] shows that gradients in the deterministic unsteady flow correlations also create stress-like terms that must be modelled, if one wants to compute the average-passage flow field associated with a blade row within a multiple-blade-row turbomachine. The HIREP measurements show that the vast majority of the gradients in the unsteady velocity correlations exist in the endwall regions. Very near the blade, however, three-dimensional potential flow effects create radial gradients in the deterministic unsteady flow correlations.

Only a few researchers have previously presented measurements of deterministic unsteady flow correlations. Dring, Joslyn, and Hardin [1980] presented these correlations as a result of their five-hole probe measurements downstream of a compressor rotor. With these measurements preceding the derivation of the average-passage equations for three-dimensional flow, the inspiration for presenting these correlations resulted from the simultaneous work of Sehra and Kerrebrock [1981], who noted how these correlations affect the computation of the circumferential-average flow through a turbomachine. Stressing the fact that this circumferential-average flow is not an axisymmetric flow, Sehra and Kerrebrock [1981] introduced these deterministic unsteady flow correlations into a streamline curvature code. With this code in mind, Dring, Joslyn, and Hardin [1980] presented the deterministic unsteady flow correlations presented in Figure 77 using the same form as the HIREP correlations.

The first plot of Figure 77 shows the deterministic unsteadiness measured by Dring, Joslyn, and Hardin [1980] for a flow coefficient of $\phi = 0.77$ and a position nominally 10% chord downstream of the rotor blade trailing edge. Actually, the data near the hub was closer to the trailing edge than the data near the casing, since their rotor blades included a swept trailing edge--although not as severe as the HIREP rotor blades. Dring, Joslyn, and Hardin [1980] could not obtain five-hole probe data near the hub, since a very large corner separation--or corner stall--existed for this flow coefficient. Otherwise, the deterministic unsteadiness behaved very similar to that of our HIREP flow, with the corner separation elevating the unsteadiness near the hub and the tip leakage vortices elevating the unsteadiness near the casing. The levels of elevated deterministic unsteadiness, however, are larger for these highly-loaded rotor blades relative to the moderately-loaded HIREP rotor blades. Also, note that Dring, Joslyn, and Hardin [1980] obtained the correlations involving the radial deterministic unsteady velocity. These radial flow correlations are smaller than the other correlations, although a large gradient in the radial flow correlation appears very close to the casing.

The second plot of Figure 77 shows the deterministic unsteadiness at a flow coefficient of $\phi = 0.59$. For this case, the region of corner separation decreases and only the variance involving the axial velocity fluctuations appears significant in the hub endwall region. Overall, however, the levels of deterministic unsteadiness have increased for this flow coefficient. The explanation for these increased levels appears to be that this flow coefficient leads to increased loading and, therefore, to a stronger potential flow effect. The strength of this potential flow effect at each spanwise location depends on the blade spanwise loading distribution. Further downstream, at a position nominally 50% chord downstream of the rotor blade trailing edge, Figure 77 shows that this potential flow effect decays and the deterministic unsteadiness appears similar to our HIREP flow--with a significant contribution by the tip leakage vortices near the casing and a smaller contribution by the corner separation near the hub. For this flow coefficient, the radial flow correlations appear insignificant.

From the similarities shown by our data and the data of Dring, Joslyn, and Hardin [1980], one might suspect that the deterministic unsteadiness in most turbomachines behaves in a similar fashion, with the flow in the endwall regions dominating the unsteadiness. However, Adamczyk [1992] derived the deterministic unsteady velocity correlations from the data of Dring, Blair, Joslyn, Power, and Verdon [1988], acquired from a low-speed, axial-flow turbine. The larger flow turning within the turbine blades produced much larger passage vortices than in either our HIREP flow or the compressor flow measured by Dring, Joslyn, and Hardin [1980]. These strong secondary vortices generated large levels of deterministic unsteadiness in the midspan region, along with smaller--but still significant--levels near the casing, as a result of the tip leakage vortices. In conclusion, one requires knowledge of the wakes and, especially, the secondary vortices before determining the location and levels of flow unsteadiness in a turbomachine.

Visualization of the Rotor Tip Leakage Vortex

As mentioned previously, the tip leakage vortex is the dominant flow structure within HIREP. Therefore, the next several sections of this report will focus on this important phenomenon. In this section, we shall examine the position of the tip leakage vortex through two types of flow visualization: cavitation visualization and laser light sheet visualization.

The relatively low static pressure within the core of the tip leakage vortex allowed us to visualize cavitation within the core at low tunnel pressures. Photographs—and videos—such as the one presented in Figure 78, show the existence of some cavitating bubbles originating in the clearance near the rotor blade leading edge. Most of the cavitation, however, appears to begin near the suction surface at 15% chord—a position very close to the measured minimum pressure point on the suction surface at 90% span (see Figure 44). Inoue and Kurokumaru [1989] and Storer and Cumpsty [1991] contend that the onset of the vortex sheet rolling-up into the tip leakage vortex occurs near the point of minimum pressure on the suction surface. At this location, the pressure difference across the clearance reaches a maximum, creating a larger leakage jet. Therefore, this origin of the vortex marks the position where the core pressure becomes low enough to establish a cavitating flow.

The cavitation photographs of Figures 78 and 79 show the circumferential position of the tip leakage vortex within the rotor blade passage. The vortex remains quite close to the suction surface until near 80% chord, where it begins to migrate away from the blade. After analyzing many such photographs and two video tapes, we sketched the envelope that enclosed the cavitating vortices from all seven blades at different times. Figure 80 includes this sketch, along with the relative skin-friction lines across the rotor blade tip section as determined from the surface flow visualization. Downstream of the cavitating part of the tip leakage vortex, Figure 80 shows the circumferential position of the vortex center as determined from the LDV data at the three axial measurement planes. Also, recall from Figure 12 that we attempted to measure the flow within the clearance region at five chordwise and three radial locations. Within the clearance regions themselves, reflections off the blade tips gave erroneous data. Farrell [1989] also had this problem for small clearances. However, while the LDV measurement volume was located outside of the clearance regions and within the blade passages, we could measure data. Figure 80 shows our estimates of the circumferential position of the vortex from these LDV measurements. Remember that these estimates are based on data at only three closely spaced radial measurement locations. The uncertainty in the position of the vortex increases near the blade leading edge where the vortex has yet to roll-up and near the trailing edge where the vortex center has moved to a radial position inboard of the LDV measurements.

Before discussing further details of the position of the tip leakage vortex, let us discuss another piece of information included in Figure 80—the position of the vortex core as computed from the model of Chen, Greitzer, Tan, and Marble [1991]. Similar to the case of a slender body in an external flow, they modelled the three-dimensional, steady flow in the tip clearance region as a two-dimensional, unsteady flow. If they assumed that deviations in the streamwise velocity are much smaller than the average streamwise velocity, the equations describing the flow in the streamwise direction decoupled from the equations describing the flow in the transverse or crossflow plane. This decoupling is similar to the model of Rains [1954], who considered the leakage flow normal to the camber line as a potential jet through a sharp-edged orifice with a discharge coefficient. The decoupling allowed Chen, Greitzer, Tan, and Marble [1991] to consider translation along the streamwise direction as analogous to moving in time, and they computed the tip clearance flow and the roll-up of the vortex as an unsteady process in successive crossflow planes. They assumed an inviscid flow through a blade represented by the camber line only, a camber line with a radius of curvature much larger than the chord. The pressure difference driving the flow through the clearance was well represented by the average loading at the mean radius (or some blade section outside the endwall region). Finally, they used a vortex method as the computational procedure, allowing them to compute the velocities only on the vortex sheets at each time step.

After comparing their model with experimental data covering a large range of clearances, loading, and flow coefficients, Chen, Greitzer, Tan, and Marble [1991] found that the vortex trajectories within the blade passage were well described by a single similarity solution curve and equation,

$$\frac{y_c}{x_c} = \frac{0.46 \cos(\gamma)}{\phi} \sqrt{\frac{1}{2} (\Delta K_p)_{\text{mean}}} ,$$

where y_c is the distance normal to the camber line, x_c is the distance along the blade chord, γ is the stagger angle (58.1 degrees for the HIREP rotor blade tip section), and $(\Delta K_p)_{\text{mean}}$ is the difference in K_p across the blade at some mean radius (a radius outside the endwall region). Figure 80 shows the trajectory of the tip leakage flow within HIREP using this similarity solution ($y_c = 0.14 x_c$). Over the first half of the blade, this zero blade thickness model computes a trajectory that remains within the clearance established by the actual blade thickness. Further downstream, however, the computed trajectory matches very well with the vortex cavitation. Besides the zero blade thickness approximation, another problem may arise when comparing the calculations with measurements near the leading edge. As seen from the pressure distribution at 90% span in Figure 44, the streamwise pressure gradients near the leading edge are larger than near midchord. Therefore, in the vicinity of the leading edge, the flow acceleration in the streamwise direction may be comparable with the acceleration across the tip clearance and the equations describing these two flow directions should be coupled here--violating the approximations used in the model. Also, recall that the onset of the vortex sheet rolling-up into the tip leakage vortex occurred closer to 15% chord than to the leading edge.

The similarity solution of Chen, Greitzer, Tan, and Marble [1991] holds within the blade passage to a point normal to the camber line at the blade trailing edge. Beyond this point, the trajectory of the tip leakage vortex must be computed using their complete model. The presence and proximity of the casing endwall requires their vortex method of computation to include an image vortex system. Within the blade passage, this image vortex system differs from the one used downstream of the blade passage, and this different image vortex system changes the induced velocities in the tip leakage vortex--giving a slope discontinuity in the vortex core trajectory. They report that even though the actual influence of the blade should drop off in a finite distance, their calculations with this slope discontinuity matched experimental results well. Figure 80 shows that our cavitation visualization also showed a change in slope of the vortex core trajectory at a location normal to the camber line at the blade trailing edge--exactly as the complete model would predict. Further downstream, Figure 80 shows that the trajectory of the vortex core as determined from the LDV measurements has changed slope once again. Here, the vortex core follows the relative flow direction, as determined from the streamline curvature solution, with a 5 degree deviation. Relative to a line tangent to the camber line at the trailing edge, the deviation angle of the vortex core trajectory is 24 degrees. As the vortex loses strength and convects downstream of the rotor blades, one would certainly expect that it would convect with the mean flow.

Another phenomenon occurs in the trailing edge region that may affect the vortex core trajectory and vortex kinking. As shown schematically in Figure 54 and in the cavitation photograph of Farrell [1989] in Figure 55, the trailing-edge separation vortex moves into the circumferential

direction, away from the suction surface as the blade rotates in the other direction. Figures 54 and 55 also show that this second vortex lies closer to the casing than the tip leakage vortex. These two vortices pass one another, at different radii, near the trailing-edge plane and the interaction of these two vortices may affect the vortex core trajectory. This interaction should occur for any rotor blades where the centrifugal effects create a radial flow on the suction surface with some trailing-edge separation. In their tip leakage vortex experiment, Inoue and Kuroumaru [1989] also measured a strong radial velocity moving up the suction surface trailing edge into the endwall region. While the trailing-edge separation vortex is smaller in strength than the tip leakage vortex, it can induce an additional downstream velocity component onto the tip leakage vortex which may help the trajectory move back into the relative flow direction.

As the tip leakage vortex convects downstream, the position of the vortex core moves radially. Looking through a periscope from a position downstream of the rotor blades, we observed the tip leakage vortex from a video camera during the laser light sheet visualization. The position of each frame in the video corresponded to an individual rotor blade. Visualizing the oncoming vortices at three axial positions of the laser light sheet and analyzing the LDV measurements at three different axial positions allowed us to track the radial position of the tip leakage vortices. Figure 81 presents the radial position of the tip leakage vortex within HIREP. The error bars on the position determined from the laser light sheet visualization represent 95% confidence bands, while the error bars on the positions determined from the LDV data represent the uncertainty that the vortex core may actually lie on an adjacent radial measurement location. Figure 81 shows that most of the radial migration of the vortex core takes place within the blade passage, with only a slight radial migration taking place downstream of the blade trailing edge. The model of Chen, Greitzer, Tan, and Marble [1991] indicates that the vortex core remains at nearly a constant radial location downstream of the trailing edge. Similar to our data, Inoue, Kuroumaru, and Fukuahara [1986] report a small decrease in the radial position of the center of the vortex with streamwise direction.

Aside from giving the location of the tip leakage vortex, both types of flow visualization also showed the unsteadiness of the tip leakage vortex. Other investigators have also observed this spatial vortex wandering. For a tip vortex trailing behind a wing or hydrofoil, Reed [1973] and Baker, Barker, Bohaf, and Saffman [1974] observed oscillations and random wandering of the vortex as it convected downstream and they attributed this unsteadiness to freestream turbulence. Using double-pulsed holography, Green [1988] performed another study of the tip vortex trailing behind a hydrofoil. He found that the primary source of core unsteadiness is associated with global core flow structure instabilities. Reconstruction of holograms allowed him to observe both vortex kinking and a second and rather chaotic unsteadiness that he labelled mini-vortex breakdown. Most of his unsteadiness was located where the initially large axial velocity excess within the vortex core would rapidly decelerate. For flows with a rotor tip clearance, Straka and Farrell [1992] extended the analysis of the tip leakage vortex data acquired in HIREP by Farrell [1989] and found the existence of vortex wandering and kinking. Besides the effects of freestream turbulence and vortex core instabilities, they noted that the unsteady interaction of the rotor blades with the wakes from the inlet guide vanes can contribute to the unsteadiness of the tip leakage vortex. Finally, within an axial-flow turbine, Yamamoto and his colleagues [1993] acquired hot-wire measurements of the tip leakage vortex emanating from the clearance region between stator blades and the endwall located downstream of a row of rotor blades. They found that both the strength and size of the tip leakage vortex changed with time.

Similar to the observations made by Straka and Farrell [1992], we observed unsteady wandering and kinking of our tip leakage vortices using videos and photographs taken during our cavitation visualization tests. The photograph in Figure 82 shows an example of vortex kinking. In some instances, we also observed gaps where the tip leakage vortex did not cavitate, as seen in Figure 83. While the vortex wandering and kinking appeared at all locations where the vortex core cavitated, this unsteadiness was most evident near the trailing edge where the vortex core trajectory changed slopes. Some interaction with the trailing-edge separation vortex may increase the unsteadiness of the tip leakage vortex. Further downstream, the laser light sheet visualization showed that the tip leakage vortex experienced an unsteady wandering in the circumferential and radial directions.

One detrimental effect of vortex wandering involves time-average flow measurements. Velocity measurements through the vortex core must be fast enough to avoid averaging errors induced by the unsteady motion of the core. For time-average measurements, such as our LDV measurements, the effect of vortex wandering is to broaden the measured velocity profiles and reduce the magnitude of the maximum vortex tangential velocity. Straka and Farrell [1992] developed an oscillating vortex model that approximates how vortex wandering affects time-average velocity profiles. Using this model and their data, they applied least-squared cubic curve fits to find empirical relationships between the apparent and instantaneous values of core size and relative maximum tangential velocity. We also used cavitation visualization to obtain an amplitude of oscillation in the circumferential direction normalized by an estimate of the vortex core radius, $A/r_c = 2.1$. For a broadened velocity profile measured with an LDV, this parameter gives an apparent core radius that is 2.04 times larger than the actual vortex core radius, while the measured maximum relative tangential velocity will be 0.64 times the actual value. In addition, our laser light sheet visualization allowed us to observe the oscillation in the radial direction. While observations allowed us to estimate an amplitude of oscillation in the radial direction of 0.2 inches, we could not estimate the instantaneous core size. Therefore, we could not apply the model of Straka and Farrell [1992] in the radial direction.

Vortex Models

Visualization of the rotor tip leakage vortex provided very important information on the position of the vortex, as well as information on the vortex unsteadiness. However, for a complete analysis, one must also examine details about the velocity profiles and strength of the vortex. In order to examine these details associated with any vortex in a measured velocity field, one can compare the measurements with ideal formulations of a vortex velocity distribution. First, one must transform the data from a cylindrical coordinate system associated with the turbomachine to a cylindrical coordinate system aligned with the axis of the vortex. In the case where no measurements exist of V , in the turbomachine coordinate system, one can attempt to find an angle between the axial direction of the turbomachine and the axial direction of the vortex and, then, transform the velocity components using this angle. Either before or after transforming the velocity components, one should also make sure that the axial and tangential velocities are velocity perturbations caused by the presence of the vortex. One can simulate these velocity perturbations by subtracting the circumferential-average velocities from the locally measured velocities. Finally, one must take the effect of vortex wandering into account.

The simplest example of an ideal vortex formulation is the circular vortex called "Rankine's combined vortex" or simply a "Rankine vortex." This vortex is a combination of solid-body rotation within the vortex core--where the angular velocity, ω , and vorticity are constant--and a potential vortex outside the vortex core--where the flow contains no vorticity. The two combined vortices meet at the vortex core radius, r_c , where the maximum tangential or azimuthal velocity occurs:

$$V_\theta = \omega r$$

for $r \leq r_c$, and

$$V_\theta = \frac{\omega r_c^2}{r}$$

for $r \geq r_c$. The total strength of the Rankine vortex is ωr_c^2 and the total circulation is $\Gamma_\infty = 2\pi r_c (V_\theta)_{max}$. In nondimensional terms, we obtain

$$\frac{V_\theta}{(V_\theta)_{max}} = \frac{r}{r_c}$$

for $r \leq r_c$, and

$$\frac{V_\theta}{(V_\theta)_{max}} = \frac{r_c}{r}$$

for $r \geq r_c$.

The core of a Rankine vortex contains no shear forces. However, shear forces do exist in the outer potential vortex and the outer flow must extract kinetic energy from the vortex core in order to make this shearing of fluid particles possible--energy that eventually dissipates into heat. Therefore, the friction of the fluid particles at the interface of the two combined vortices eventually slows the rotation of the vortex core and the Rankine vortex decays. In order for a vortex to continuously receive kinetic energy and not decay, there must be a radial velocity component that carries the energy from outside the vortex into the core. Burgers [1948] found an analytical solution of the Navier-Stokes equations for laminar flow in which the inward radial convection of angular momentum in a vortex just balances the outward radial diffusion. The velocity components of this "Burgers vortex" are

$$V_r = -\alpha r,$$

$$V_\theta = \frac{\kappa}{r} (1 - e^{-\alpha r^2/2\kappa}),$$

and

$$V_z = 2\alpha z ,$$

where α is a measure of the radial influx ($\alpha > 0$), κ is the vortex strength, and ν is the kinematic viscosity. Maxworthy, Hopfinger, and Redekopp [1985] used a least-squares fit of the Burgers vortex to experimental data and obtained

$$\frac{V_\theta}{(V_\theta)_{max}} = \frac{1.39r_c}{r} \left[1 - e^{-1.28(r/r_c)^2} \right]$$

and a total circulation adjusted to the experimental data of $\Gamma_* = 1.39[2\pi r_c (V_\theta)_{max}]$.

The axial velocity for the Burgers vortex is uniform at any axial station—a condition contrary to experimental observation. Measured vortices show that the axial velocity varies with r and that the vorticity lines bend into spirals. Near the origin of a vortex sheet rolling-up into a vortex and in regions where the vortex core contracts, the axial velocity near the axis is larger than that at the outer edge of the vortex. Maxworthy, Hopfinger, and Redekopp [1985] measured a concentrated vortex with this axial velocity excess or jet and their least-squares fit yielded

$$\frac{V_z}{(V_z)_{max}} = e^{-0.54(r/r_c)^2} .$$

When the vortex core expands in the presence of an adverse pressure gradient or simply from viscous decay, the axial velocity will decrease near the axis more than at the outer edge of the vortex—eventually leading to a wake-like velocity profile. Garg and Leibovich [1979] used a similar axial velocity profile to the one used by Maxworthy, Hopfinger, and Redekopp [1985] in order to fit both jet-like and wake-like velocity profiles from data of a vortex confined within a tube. The same expression provided acceptable fits to both types of profiles, with a negative sign used for the wake-like profile (and $(V_z)_{min}$ replacing $(V_z)_{max}$).

The equations for the Rankine vortex and the Burgers vortex can now be used with the LDV data in the analysis of the rotor tip leakage vortex measured in HIREP. For simplicity, the equation for axial velocity presented by Maxworthy, Hopfinger, and Redekopp [1985] will be included as part of the Burgers vortex.

Details of the Rotor Tip Leakage Vortex

Beginning in the pressure surface boundary layer near the rotor blade tip, a vortex sheet passes through the clearance. Under the influence of the induced velocity field of the vortex sheet, the free edge of the vortex sheet curls over and takes the form of a spiral with a continually increasing number of turns: the roll-up of the tip leakage vortex. As opposed to a wing or a rotor blade tip without an endwall, the higher blade loading produces a larger pressure difference between the pressure and suction sides of the blade, and this pressure difference produces a jet of fluid that carries the vortex sheet through the clearance. Storer and Cumpsty [1991] show that this distinct jet of low-loss fluid occurs downstream of the minimum pressure location on the suction surface. Beside the

curling of the free edge of the vortex sheet, the formation of the tip leakage vortex also includes the strong interaction between the leakage jet and the throughflow--further complicating the roll-up of the vortex. Storer and Cumpsty [1991] feel that the interaction of the leakage jet and the throughflow produces an intense shearing that is the principal mechanism of the high loss associated with tip leakage vortices.

The roll-up of the tip leakage vortex produces a swirling flow about the centerline of the vortex. Using the procedure outlined in the previous section, we determined the tangential or azimuthal velocity about the vortex axis at the three downstream LDV measurement planes. First, we subtracted the circumferential-average values (using area averaging) from the measured axial and tangential velocities. Then, using Figure 80, we found that the angle between the axis of the vortex and the axis of HIREP was 63 degrees--an angle that allowed us to transform the data to a cylindrical coordinate system aligned with the axis of the vortex. For each of the seven tip leakage vortices (from each rotor blade), we found the point of minimum axial velocity--in order to give us the circumferential location of the centers of the seven vortices. At each of these circumferential locations, we plotted the tangential velocity distribution along a radial line. This tangential distribution could only be plotted along a radial line since the original LDV measurements contained no radial velocity data.

At all three axial planes, Figure 84 shows the tangential velocity distribution within the seven different tip leakage vortices and within an average tip leakage vortex. At 4.8% chord downstream of the tip of the rotor blade trailing edge, Figure 84 shows that the minimum and maximum values of tangential velocity differ--giving an asymmetric vortex. The presence of the casing endwall seems to interfere with the rolling-up of the tip leakage vortex. Also, recall that we acquired data in this plane down to only 81.0% span because of the swept trailing edge. Further downstream to positions 21.4% and 32.2% chord axially downstream of the tip of the blade trailing edge, the vortex appears to dissipate, with decreases in the magnitude of both the minimum and maximum values of tangential velocity. The laser light sheet visualization also showed signs of a more dissipated vortex structure in going from 4.8% chord to 19.1% chord downstream.

A strong coupling exists between the tangential and axial velocities of a vortex. The instabilities in the initial roll-up of a vortex can lead to either an excess or deficit of the axial velocity in the vortex core, relative to the freestream. As the vortex begins to convect downstream within the blade passage, the circulation (and maximum tangential velocity) about the core increases as more vorticity is continuously wound into the core region. From the conservation of momentum across the vortex,

$$\frac{\partial p}{\partial r} = \rho \frac{V_\theta^2}{r},$$

this increase in vorticity and tangential velocity causes a drop in the centerline pressure which, in turn, increases the axial velocity. Batchelor [1964] discusses the theory of axial velocities in tip vortices in more detail.

For tip vortices without the presence of an endwall, several investigators have found this jet-like behavior in axial velocity. For instance, Singh and Uberoi [1976] used a hot-wire probe to measure the tip vortices from a wing at an angle of attack. The tip vortex, which originated near the

leading edge, contained an axial jet in the vortex core near the trailing edge. This jet decayed to zero in about 2.4 chord lengths and then further decayed into a wake-like structure, with an expansion in the core size. Two chord lengths downstream of the trailing edge, Orloff [1974] acquired LDV data through the tip vortex at three angles of attack. While he measured axial velocity defects at the two lowest angles of attack, he measured an axial velocity excess at the highest angle of attack. Measurements showed that the higher loading at the increased angle of attack gave a tip vortex with larger tangential velocities. Again, the larger tangential velocities reduce the pressure at the centerline of the vortex, which increases the axial velocity. Finally, in a similar wing experiment, Lee and Schetz [1985] used a five-hole probe to measure the tip vortex six chord lengths downstream of the trailing edge at chord Reynolds numbers ranging from 210,000 to 1,500,000. While changes with downstream distance due to viscous diffusion are slow, they found large changes in the vortex structure with Reynolds number. The tangential velocity--and, thus, the axial velocity--increased with Reynolds number until the largest chord Reynolds number yielded an axial jet, even at a distance six chord lengths downstream of the trailing edge.

For tip leakage vortices, the vortex structure changes because of the presence and proximity to the endwall. At a position 34.0% chord axially downstream of the tip of the rotor blade trailing edge, Straka and Farrell [1992] analyzed LDV data in a similar manner as the analysis reported here. Note that these measured vortex characteristics result from an experiment with a blade chord Reynolds number of 3,900,000. For large tip clearances ($\lambda = 0.547$ and $\lambda = 0.540$), they report large tangential velocities and jet-like profiles of axial velocity. As the clearance decreases ($\lambda = 0.329$), the tangential velocity decreases and the axial velocity vanishes. Finally, for small clearances ($\lambda = 0.279$ and $\lambda = 0.099$), the tangential velocity reduces further, giving wake-like profiles of axial velocity. Also, the lack of axisymmetry in the vortices for smaller clearances results from the close proximity of the endwall. In order to help explain the differences in vortex structure with changing clearance, Straka and Farrell [1992] found that for smaller clearances, the vortices originate closer to the leading edge and that these vortices experience more vortex kinking and oscillation.

As a possible explanation for the change in vortex structure with changing clearance, consider the pressure field in the flow external to the vortex. Within the blade passage--especially near the suction surface, closer to the vortex--the vortex convects through a region with an adverse pressure gradient. The static pressure within the core of the vortex increases as the vortex convects through this external adverse pressure gradient and reduces the axial velocity. Also, as Erickson [1981] points out, the pressure increase within the core will be larger than that of the external flow. This result occurs because the external adverse pressure gradient also reduces the tangential velocity of the vortex which, in turn, increases the static pressure in the core and reduces the axial velocity. Downstream of the blade passage, the external pressure gradient diminishes and the vortex changes form only in response to viscous effects, requiring hundreds of vortex core diameters for significant structural changes. As the clearance increases, the loading of the tip section decreases and less of the circulation is retained at the blade tip. Instead, more circulation is shed into the vortex. This reduction in blade loading also decreases the streamwise adverse pressure gradient--resulting in larger axial velocities in the tip leakage vortices corresponding to larger clearances.

In a different, but related explanation, consider the leakage flow as the clearance increases and more circulation is shed into the tip leakage vortex. From oil-paint patterns, Farrell [1989] found that the angle between the relative skin-friction lines and the chord line decreased with increasing

clearance. Erickson [1981] considered the familiar spiral sheet model of the vortex (shown schematically in Figure 54), where the inclination of the spiralling vortex lines to the vortex axis is such as to make them all induce a downstream component of velocity along the axis. If the streamlines move in a circular motion along the vortex sheet and the orthogonal vortex lines move parallel to the vortex axis, one has a circular vortex with no axial velocity. Relative to the axis, larger inclinations of the vortex lines induce larger velocities along the axis. This result corresponds to a decreasing angle between the streamlines and the vortex axis. Therefore, from the relative skin-friction lines observed by Farrell [1989], increases in clearance should give a larger component of velocity along the vortex axis.

Our nondimensional clearance ($\lambda = 0.124$) fell between the two smallest clearances of Farrell [1989] and Straka and Farrell [1992]. Therefore, as expected, our measurements showed a wake-like profile in axial velocity for all three axial measurement planes. Figure 85 shows these axial velocity distributions for the seven different tip leakage vortices and for an average tip leakage vortex. At 4.8% chord downstream of the tip of the rotor blade trailing edge, Figure 85 shows this wake-like structure with an excess in axial velocity very close to the casing endwall. Moving further axially to 21.4% chord downstream of the tip of the trailing edge, the vortex becomes larger, but with a larger defect in axial velocity. One can explain this by noting that the reduced tangential velocity at this plane (see Figure 84) will cause the centerline pressure to increase and the axial velocity to decrease.

At 32.2% chord downstream of the tip of the rotor blade trailing edge, viscous dissipation appears to reduce the defect in axial velocity. From Figure 84, note that the tangential velocities also decrease; the usual coupling between that tangential and axial velocities does not hold. Also, from both the tangential and axial velocity profiles, note that the structure of the asymmetric vortex appears to be changing faster than one might expect from viscous dissipation alone. Again, the presence and proximity of the casing endwall seems to be having a strong influence on the tip leakage vortex. Phillips and Head [1980] suggest that large-scale motions within the turbulent endwall boundary layer will obscure and absorb the tip leakage vortex. Barker and Crow [1977] studied the interaction of a vortex pair with a wall. In the vicinity of the wall, the vortex showed a strong eccentricity, with the normally circular vortex core becoming elliptical. The deformed vortex core then became unsteady. Further complications occur in the formation of the tip leakage vortices within HIREP; namely, the casing endwall affected the vortices before they were fully rolled-up. If one measured these vortices even farther downstream, they might exhibit the "rebounding" or "bouncing" effect that airplane wing tip vortices experience when interacting with the ground.

The tip leakage vortices can now be presented in a dimensionless form and compared with ideal velocity distributions. First, the distance between the minimum and maximum tangential velocities defines the diameter of the vortex core, with the center of the core located half way in between these two core edges. Since the casing endwall has such a strong effect, we take $(V_\theta)_{\max}$ at the edge of the core furthest from the endwall. With these values, Figure 86 presents the nondimensional tangential velocity profiles for the tip leakage vortices at all three axial measurement planes, compared to the Rankine and Burgers vortices. The measured vortices at all three axial positions are similar, with the strong asymmetry giving a larger peak in tangential velocity at the edge of the core nearest to the endwall. The vortex furthest upstream compares better with the Burgers vortex than the downstream vortices. Next, using the minimum axial velocity with the Maxworthy, Hopfinger, and Redekopp [1985] empirical fit for the Burgers vortex, Figure 87 presents the nondimensional axial velocity profiles for all three tip leakage vortices. These asymmetric vortices all

have minimum values of axial velocity that vary slightly from the vortex centers as found from the tangential velocity profiles. Also, the measured axial velocity gradients appear larger than those indicated by the Burgers vortex.

The measured values of r_c and $(V_\theta)_{max}$ allow us to compute the total circulation of the tip leakage vortex, $\Gamma_u = 2\pi r_c (V_\theta)_{max}$. Using the oscillating vortex model of Straka and Farrell [1992] and the amplitude of oscillation determined from the cavitation visualization, $A/r_c = 2.1$, we corrected the vortex parameters for the averaging effect of vortex wandering. Table 9 presents all of these vortex parameters at all three measurement planes. As also seen in Figure 86, Table 9 shows that the size of the vortex initially grows and then remains constant, while the values of $(V_\theta)_{max}$ decrease as the vortex convects downstream. Also, Table 9 shows a decrease in Γ_u with increasing axial distance. Actually, one might expect the vortex circulation to increase as it leaves the blade passage since streamwise vortices within the trailing vortex sheet should be wound into the tip leakage vortex. However, viscous dissipation can reduce $(V_\theta)_{max}$ and, thus, reduce the circulation—with the casing endwall seemingly increasing this dissipation. Two other points must be considered. First, a further examination of Figure 86 will show that the density of LDV data near the edge of the vortex core farthest from the casing endwall may not be sufficient—increasing the uncertainty of the vortex core parameters. Second, the values of $(V_\theta)_{max}$ taken at this edge of the vortex core may not be representative of the actual values of $(V_\theta)_{max}$ within this asymmetric, elliptical vortex core—resulting in smaller estimates of the circulation.

Table 9. Measured and Corrected Parameters for the Rotor Tip Leakage Vortices

z/c_{tip}	0.048	0.214	0.322
Measured Values			
r_c (inches)	0.54	0.66	0.66
$(V_\theta)_{max}$ (ft/sec)	6.02	4.25	2.70
Γ_u (ft ² /sec)	1.70	1.48	0.94
Values Corrected for Circumferential Wandering			
r_c (inches)	0.26	0.32	0.32
$(V_\theta)_{max}$ (ft/sec)	9.41	6.64	4.22
Γ_u (ft ² /sec)	1.28	1.11	0.71

As mentioned previously, not all of the bound circulation in the blade is shed downstream into the rotor tip leakage vortex--unlike the case of a tip vortex without the presence of an endwall.

Lakshminarayana and Horlock [1962] first suggested changing their lifting line model to account for the circulation retained at the blade tip, and this modification formed the basis for the improved model of Lakshminarayana [1970]. Later, using the leakage jet model of Rains [1954], Lewis and Yeung [1977] developed another model for the retained lift. These models imply that the fluid between the tip and the endwall will effectively experience a lift force that is related to the circulation shed into the tip leakage vortex.

For our blades, we can determine the circulation at all spanwise locations by computing

$$\Gamma = \frac{2\pi}{N_B} (r_2 \bar{\bar{V}}_{\theta_2} - r_1 \bar{\bar{V}}_{\theta_1})$$

along a streamsurface around the entire circumference of the machine, where N_B is the number of blades. Assuming cylindrical streamsurfaces, we used measured values of tangential velocity to compute the spanwise variation of circulation on both the inlet guide vanes and the rotor blades. Figure 88 shows these experimental values compared with the design values of circulation used in the lifting surface theory. The experimental and design values of circulation compare well for the inlet guide vanes, while some discrepancies occur for the more highly-loaded rotor blades. One discrepancy occurs near the hub, where the three-dimensional corner separation has obviously affected the blade circulation. However, a more noticeable discrepancy occurs near the casing. The effect of the liner vortices on the rotor blade incidence offers one possible explanation for the experimental circulation being larger than the design circulation near the casing. Also, some of the local peaks in the experimental values of circulation occur from integrating the data through the tip leakage vortex, which has a small component of vorticity in the spanwise direction.

Figure 88 shows that the value of circulation at the rotor blade tip is roughly $3.5 \text{ ft}^2/\text{sec}$, and that the circulation decreases across the clearance, where the circulation should vanish at the casing. Referring back to Table 9, we can estimate the shed circulation as $\Gamma_s = 1.28 \text{ ft}^2/\text{sec}$ in the tip leakage vortex near the trailing edge--after correcting for the effects of wandering. Thus, 73.2% of the total circulation is retained at the blade tip. For the rotor clearance within HIREP, the model of Lakshminarayana [1970] predicts that 71.9% of the circulation will be retained at the blade tip, while the model of Lewis and Yeung [1977] predicts 84.1%. Both of these models resulted from experimental data, and these data--along with the data of Inoue, Kuroamaru, and Fukuhara [1986], Farrell [1989], and Yaras and Sjolander [1990]--show a large scatter in retained circulation. One problem occurs in the various methods of estimating the retained lift from different types of data. And even though a broadly applicable model does not exist, these correlations to allow a designer to perform trade-off studies at normal operating clearances ($\lambda = 0.1$ to 0.3).

Cavitation Performance

Dynamic reduction of local pressure within the flow field at essentially constant temperature can result in the visible growth of vapor-filled cavities or bubbles. This condition is called cavitation. Since static pressure controls cavitation, the local pressure coefficient,

$$C_p = \frac{P - P_{ref}}{\frac{1}{2} \rho V_{ref}^2},$$

becomes an important parameter. In the absence of bubble dynamic effects, one can assume that cavitation inception occurs when the minimum value of static pressure equals the liquid vapor pressure. This leads to the definition of an important parameter for categorizing cavitating flows called the cavitation number,

$$\sigma = -C_{p_{min}} = \frac{P_{ref} - P_v}{\frac{1}{2} \rho V_{ref}^2}.$$

In a turbomachine, one can better quantify cavitation performance using a more accurately defined dynamic pressure,

$$\sigma = \frac{P_{ref} - P_v}{\frac{1}{2} \rho U_{tip}^2},$$

which takes into account the rotation of the blades. Lower values of cavitation number indicate better cavitation performance.

Limited cavitation occurs at an intermediate value of σ where there is a small amount of cavitation in the flow and is determined experimentally by two methods. Using the first method, known as incipient cavitation, one holds the velocity constant—eliminating all cavitation—and then decreases the pressure until cavitation appears at the inception pressure. Using the second method, known as desinent cavitation as first defined by Holl [1960], one holds the velocity constant—establishing a cavitating flow—and then increases the pressure until cavitation disappears at the desinence pressure. Hysteresis occurs in the cavitation cycle and Holl and Treaster [1966] showed that the desinent value of σ is typically larger than the incipient value of σ ; and therefore, by the definition of σ , the desinence pressure is typically larger than the inception pressure. Thus, desinent cavitation is a more conservative value in determining cavitation performance. Also, because of the hysteresis in the cavitation cycle, desinent cavitation proves to be a more repeatable method than incipient cavitation.

With a gas content of 4.9 ppm, desinent cavitation tests were conducted on all seven HIREP rotor blades at $V_{ref} = 35$ ft/sec and at values of ϕ_{vol} of 1.22 and 1.36. Tip leakage vortex cavitation was found to be the limiting form of cavitation in HIREP. As a simple example, one can model the tip leakage vortex as a Rankine vortex, as shown previously. Due to the swirling motion of the vortex,

conservation of momentum shows that a pressure gradient exists across the vortex,

$$\frac{\partial p}{\partial r} = \rho \frac{V_\theta^2}{r}.$$

The minimum pressure occurs where this gradient vanishes and, using the tangential velocity equations for a Rankine vortex, the minimum pressure must occur at the center of the vortex core. Integrating from the vortex center outward, one can obtain the minimum pressure coefficient,

$$C_{p_{min}} = \frac{p_{min} - p_\infty}{\frac{1}{2} \rho U_{tip}^2} = -2 \left(\frac{V_{\theta_{max}}}{U_{tip}} \right)^2 = -2 \left(\frac{\Gamma_\infty}{2\pi r_c U_{tip}} \right)^2.$$

With the minimum pressure occurring at the center of the vortex core, the pressure in the core of the tip leakage vortex will decrease to the vapor pressure far before the pressure in the surrounding fluid. Farrell [1989] used this Rankine vortex for his model of tip leakage vortex cavitation. Similar to our results, Farrell [1989] found that tip leakage vortex cavitation was the limiting form of cavitation for his HIREP rotor blades, at all of the tested tip clearances. Farrell [1989] used rotor blades where the ratio of the tip clearance to the maximum thickness of the tip section (λ) varied from 0.099 to 0.540, while our new rotor blade design had a value of 0.124.

Mitchell [1958] and Shuba [1984] both claimed that for small tip clearances, gap cavitation could be the limiting form of cavitation. Similar to our rotor blades, the blade tips used by Mitchell [1958] were rounded on the pressure surface with a radius approximately equal to the tip clearance. Mitchell [1958] felt that large incidence angles caused by the tip section being imbedded within the endwall boundary layer changed the tip pressure distribution and created gap cavitation for small values of λ . Also, for his smaller-scale experiment, he felt that the clearance flow for $\lambda < 0.12$ was either laminar or transitional-flow more likely to separate and cause gap cavitation. Observation of his inception cavitation photographs for small values of λ show that it is difficult to distinguish between gap cavitation and vortex cavitation. Following the recommendations made by Gearhart [1966], Shuba [1984] also found that rounding the pressure side of the blade tips minimized gap cavitation. Shuba [1984] also felt that stronger viscous stresses occur in clearances where $\lambda < 0.1$ which can lead to separation and gap cavitation—especially for high values of rpm. However, he never found gap cavitation for $\lambda > 0.15$ and when vortex cavitation occurred over the whole range of clearances (for specific endwall boundary layers and blade rpm), $\lambda = 0.15$ was an optimum clearance for cavitation performance.

Figure 89 shows the cavitation inception results for each of the 7 rotor blades as a function of the two tested volumetric flow coefficients. At each ϕ_{vol} , one blade (and to a lesser extent, one other blade) showed larger values of σ . Cavitation photographs in Figure 90 show one blade that has a small value of σ along with the blade that has a larger value of σ . Both blades show vortex cavitation within the tip leakage vortex. However, the blade with a larger value of σ also shows some gap cavitation. Inspection of the blades established the presence of a few nicks on the pressure side of the tip section which caused the leakage flow to separate, giving a lower minimum pressure.

This local separation resulted in gap cavitation and, thus, a larger cavitation index. Cavitating vortex filaments from these local separations follow the relative skin-friction lines found in the oil-paint patterns of Figure 52 and merge into the tip leakage vortex. The subjective method of calling cavitation can also give rise to variations in σ .

The determination of the cavitation number corresponding to cavitation inception gives an important limiting condition for the pump performance. We have compared our data with two models. Farrell [1989] performed an extensive investigation of rotor tip leakage vortex cavitation using the original blade rows within HIREP. The intent of his investigation was to formulate a correlation of flow and blade geometry parameters to allow one to predict the minimum pressure in the tip leakage vortex during the design exercise. Using a Rankine vortex model, Farrell [1989] set out to develop submodels for the vortex circulation and core radius. As the tip clearance increased, his measurements showed that the circulation shed from the blade tip increased and the circulation retained by the blade tip decreased. His ∇V flow field data showed more circulation in the vortex than what could be attributed to circulation shed from the blade tip alone. Application of the resulting model to the pump data of Rains [1954] and Mitchell [1958] confirmed this observation. Vorticity from the casing endwall boundary layer and from an interaction with the trailing-edge separation vortex emanating from the rotor blade suction surface could help explain the additional circulation.

Farrell and Billet [1993] have amended the original model of Farrell [1989] with a term to account for this additional circulation and a submodel for the vortex core radius,

$$\sigma \approx 0.0977 \frac{C_{L_0}}{k} \left[\frac{W_1 (1 - e^{-14h/c_{tip}}) + 0.18 W_{1,\infty}}{(1 - e^{-6\lambda}) U_{tip}} \right]^2 \left[\frac{W_{1,\infty} c_{tip}}{v} \right]^{0.29},$$

where k is an air content correction factor. The Cavitation Committee at the 19th International Towing Tank Conference [1990] discussed the sensitivity of tip vortex cavitation to dissolved gas content, with nuclei formation due to supersaturation in vortex cores leading to cavitation inception. Using our measurements of the casing endwall boundary layer upstream of the rotor blades, we used this model to compare with our cavitation data, as shown in Figure 91. This model requires an estimate of the tip lift coefficient at the zero clearance condition, C_{L_0} , as well as the inlet relative velocities at the tip, W_1 , and outside of the endwall boundary layer, $W_{1,\infty}$. Figure 91 shows that the model of Billet and Farrell [1993] is conservative and gives estimates of σ that are slightly larger than our data. Smaller tip clearances result in a rapid degradation in cavitation performance, and larger tip clearances (beyond the optimum value of 0.2 for λ) give a small degradation in cavitation performance. Cavitation performance also appears to be worse for the off-design condition where $\Phi_{vol} = 1.22$.

After viewing the vortex cavitation from the tip leakage vortex, we further reduced the tunnel static pressure. At a tunnel pressure of 11.3 psi (and a gas content of 7.4 ppm), two additional types of cavitation were observed on the suction surface of the rotor blades. First, a transient type of cavitation was observed emanating from the minimum pressure location. At this position, the cavities grew rapidly and travelled downstream, appearing as large bubbles. This type of cavitation is called travelling-bubble cavitation and does not appear to be attached to the blade surface. These travelling bubbles will rapidly collapse as they convect into regions of higher pressure. In the corner region

near the rotor blade trailing edge and the hub and in a small region along the span of the trailing edge, the cavitation appeared as a sheet or patch. This observation is an additional sign that boundary layer separation has occurred in these regions. Here, the flow detached from the blade and enclosed the cavities which remain attached to the blade surface in what is commonly called fixed-patch cavitation. The large amount of mixing within the separation region prevents individual cavities from growing very large. Holl and Carroll [1981] showed that fixed-patch cavitation appears as a quasi-steady pocket of cavitation that appears fixed to the surface. This pocket can change in size since the separation region can fluctuate in time. Figure 92 shows vortex, travelling-bubble, and fixed-patch cavitation on the HIREP rotor. The schematic in Figure 92 shows the entire rotor blade, while the photograph in Figure 92 shows only the lower portion of the blade within the tunnel window.

Summary and Conclusions

The high Reynolds number pump (HIREP) facility at ARL Penn State has been used to perform a low-speed, large-scale experiment of the incompressible flow of water through a multiple-blade-row turbomachine. With a nearly uniform inlet condition, the incompressible fluid within HIREP flows through a cylindrical annulus containing only two blade rows—blade rows that are more lightly loaded than what normally occurs in practice. Despite these simplifications, the experimental data acquired within HIREP show that the flow field is still very complicated and will provide a challenging test case for comparison with numerical computations.

At first glance, one might observe that the HIREP blades have produced a rather two-dimensional flow field. However, a further analysis of the data shows that three-dimensional effects are significant. One very prominent example occurs in the corner where the trailing edge of the rotor blade suction surface meets the hub. While the two-dimensional diffusion factor shows that these moderately-loaded rotor blades should not separate, surface flow visualization shows that a very strong corner separation does indeed occur. At low tunnel pressures, this strong corner separation leads to fixed-patch cavitation. Downstream of the rotor blades, the corner separation leads to large blade wakes and large total-pressure losses. Also, a smaller region of three-dimensional separation occurs near this same corner on the inlet guide vanes, with an even smaller separation region occurring near the corner where the IGV suction surface trailing edge meets the casing. These regions of separation, together with the endwall separation upstream of the IGV and rotor blade leading edges, show that three-dimensional effects dominate boundary layer separation within HIREP.

As with boundary layer separation, the actual locations of boundary layer transition may differ from the expected locations. While the endwall boundary layers were all fully turbulent, the surface flow visualization and an analysis using the blade static-pressure measurements both showed that transition began between 15% and 18% chord on both IGV surfaces—even with the inlet guide vanes having a chord Reynolds number of 2,300,000—for which one might expect transition to occur closer to the leading edge. With even larger chord Reynolds numbers, boundary layer transition on both surfaces of the rotor blades began near 10% chord according to an analysis using the blade static-pressure measurements. However, the surface flow visualization showed no signs of transition. While this oil-paint technique has uncertainties in locating transition, the presence of wake-induced transition from the periodic passing of IGV wakes may also affect the location of transition, as well as the oil-paint pattern.

Even with the simple characteristics of HIREP compared to many turbomachines, secondary flows prevail within the flow field. These secondary flows and the relative motion of the stationary and rotating hubs can lead to strongly skewed endwall boundary layers, which produce streamwise vorticity. Surface flow visualization shows the topology for the development of horseshoe vortices and vortices emanating from the three-dimensional separation regions on the blades; however, flow field measurements fail to exhibit these vortices, since they are either too weak or are filtered out by the nonuniform grid of the measurement locations. Nevertheless, the flow field measurements do show the presence of secondary flows. With very small incoming endwall boundary layers and very small blade turning, one might not expect significant passage vortices downstream of the inlet guide vanes that result from the turning of the inlet vorticity. However, five-hole probe measurements show significant secondary flow within the passages. Observations of the surface flow visualization and comparisons of the five-hole probe data with three-dimensional lifting surface theory calculations

show that the main contribution to forming these secondary flows comes from a spanwise variation in circulation along the inlet guide vanes. This variation creates a skewed trailing vortex sheet that convects downstream, induces passage velocities, and deforms to eventually roll-up into two concentrated vortex structures rotating in opposite directions. Also, local instabilities of the vortex sheets to small disturbances—as well as changes in local blade boundary layer separation characteristics from surface irregularities—led to some blade-to-blade variations in the data.

The dominant secondary flow structure within HIREP is the rotor blade tip leakage vortex. The tip leakage vortex results in large total-pressure losses and vortex cavitation, the limiting form of cavitation within HIREP. From the strong coupling that exists between the tangential and axial velocities of a vortex, one would expect the initial formation of an excess or jet of axial velocity in the vortex core, relative to the freestream. However, the adverse pressure gradient in the region of the tip leakage vortex and the angle at which vortex lines are wound into the vortex for this small tip clearance lead to the existence of a deficit in axial velocity in the vortex core at the downstream measurement planes. These velocity deficits are much larger and broader than the velocity deficits associated with the rotor blade wakes, which could lead to a strong periodically unsteady interaction with any downstream blades or struts—increasing the adverse effects of forced vibration and noise. A detailed analysis of the tip leakage vortex also shows a strong asymmetry. For this small clearance, the presence and proximity of the casing endwall affect the roll-up, shape, dissipation, and unsteadiness of the tip leakage vortex.

The combination of the trailing-edge separation on the rotor blade suction surface and the centripetal acceleration that causes an outward radial flow results in the formation of a trailing-edge separation vortex that moves radially up the trailing edge and then turns in the circumferential direction near the casing, moving in the opposite direction of blade rotation. Farrell [1989] showed cavitation photographs of this secondary vortex (see Figure 51). This trailing-edge separation vortex lies closer to the casing endwall than the tip leakage vortex and seems to have an influence on the trajectory of the tip leakage vortex core. This trajectory appears to change near the blade row trailing edge.

The tip leakage vortex also has a strong impact on the flow unsteadiness downstream of the rotor blades. Both the nondeterministic and deterministic unsteadiness increase in the vicinity of the tip leakage vortex. The nondeterministic unsteadiness increases because of increased turbulence levels in the vortex and because of vortex wandering and kinking. Freestream turbulence, vortex structure instabilities, unsteady interaction with IGV wakes, and the influence of the casing endwall all influence vortex wandering and kinking. This type of unsteady motion, along with similar unsteadiness associated with other vortices and separation regions, will certainly add to the difficulties associated with turbulence modelling during numerical computations of a turbomachinery flow field. However, a potentially more important modelling problem will occur when solving the average-passage equations for a multiple-blade-row turbomachine. One must model the effects on the average-passage flow field from the deterministic unsteadiness—any unsteadiness that correlates with shaft speed. Our data shows that the tip leakage vortex is a strong contributor to the level of deterministic unsteadiness.

The periodic motion of the tip leakage vortices and the vortices and enlarged blade wakes created by the rotor blade corner separation have the strongest effects on the level of deterministic unsteadiness. Away from the endwalls, the periodic motion of the blade wakes have a much smaller effect on the unsteadiness level. The circumferentially nonuniform pressure field very close to a

blade row can also affect deterministic unsteadiness; however, the amount of this potential flow variation decays exponentially with distance from the blade row. Nevertheless, very close to the highly-leaned rotor blades, large spanwise gradients in deterministic unsteadiness occur as a result of this potential flow. As with the modelling of turbulent fluctuations, it is the gradient in deterministic unsteady fluctuations that is important for modelling.

The experimental measurements and subsequent data analysis have improved our physical understanding of this complex flow field. During the data analysis, we also evaluated several engineering models, especially the models used during the design of the HIREP blades: the streamline curvature method and lifting surface theory. The streamline curvature method provided good comparisons with the circumferentially-averaged flow field data, although the total-pressure loss models used within the code were not sufficient in the endwall regions. The lifting surface theory gave three-dimensional calculations showing good agreement with the blade static-pressure distributions and the trailing vortex sheets, a major source of secondary flow. However, these calculations cannot resolve boundary layers, separation regions, and wakes--problems that will be worse for higher blade loadings and at off-design conditions. We also used some vortex models during the analysis. A tip leakage vortex trajectory model gave very good results in the downstream portion of the rotor blade passage. Two models of the vortex velocity distribution helped show that the casing endwall caused the actual tip leakage vortex to be quite asymmetric. Finally, a vortex cavitation model showed reasonable agreement with our data.

The HIREP experimental measurements provide an excellent database for comparisons with three-dimensional, viscous (turbulent) flow computations. A five-hole probe survey of the inlet flow 37.0% chord upstream of the IGV leading edge is sufficient to give information for the inflow boundary conditions, while some static-pressure information is available to help establish an outflow boundary condition. Static-pressure distributions are available on the blade surfaces, while surface flow visualization patterns of skin-friction lines are available on blade surfaces and on the endwalls in the vicinity of the blade passages. Five-hole probe measurements exist on an axial plane 49.7% chord downstream of the IGV trailing edge, including information on secondary flows and IGV wakes. This survey includes a Fourier analysis to obtain the spatial harmonic content of the flow. For the purposes of unsteady rotor blade response to a nonuniform inflow, the experimental or computational determination of the flow must resolve the flow detail required to obtain the necessary harmonic content. A two-component LDV velocity survey exists 88.5% chord downstream of the IGV trailing edge, while spanwise surveys at 76.2% span exist of the decay of the potential effects upstream of the rotor blades and the wakes downstream of the rotor blades. Additional LDV surveys exist at three measurement planes downstream of the rotor blades, including information on the tip leakage vortices and the rotor blade wakes. These measurement planes are located at 4.8%, 21.4%, and 32.2% chord downstream of the tip of the rotor blade trailing edge. Slow- and fast-response total-pressure measurements also exist at this furthest downstream plane. Finally, measurements show the tip leakage vortex trajectory, the rotor blade shaft thrust and torque, and the cavitation performance. Taken as a whole, the HIREP experimental database should prove to be a worthwhile and challenging test case when used during the validation of numerical computational computer codes.

Bibliography

Abu-Ghannam, B. J. and Shaw, R., "Natural Transition of Boundary Layers--The Effects of Turbulence, Pressure Gradient and Flow History," *Journal of Mechanical Engineering Science*, Vol. 22, No. 5, pp. 213-228, 1980.

Adamczyk, J. J., "Model Equation for Simulating Flows in Multistage Turbomachinery," ASME Paper 85-GT-220, 1985.

Adamczyk, J. J., Mulac, R. A., and Celestina, M. L., "A Model for Closing the Inviscid Form of the Average-Passage Equation System," *Transactions of the ASME, Journal of Turbomachinery*, Vol. 108, pp 180-186, October 1986.

Adamczyk, J. J., "Unsteady Aerodynamic Interaction Effects on Turbomachinery Blade Life and Performance," AIAA Paper 92-0149, Presented at the 30th Aerospace Science Meeting and Exhibit, Reno, Nevada, January 6-9, 1992.

Arakawa, C. and Tagori, T., "Fundamental Experiments of Oil Films on a Rotating Disk," *Flow Visualization II*, Edited by W. Merzkirch, pp. 127-131, Proceedings of the Second International Symposium on Flow Visualization, Bochum, West Germany, September 9-12, 1980.

Baker, C. J., "The Laminar Horseshoe Vortex," *Journal of Fluid Mechanics*, Vol. 95, Part 2, pp. 347-368, November 1979.

Baker, C. J., "The Turbulent Horseshoe Vortex," *Journal of Wind Engineering and Industrial Aerodynamics*, Vol. 6, pp. 9-23, 1980.

Baker, G. R., Barker, S. J., Bohaf, K. K., and Saffman, P. G., "Laser Anemometer Measurements of Trailing Vortices in Water," *Journal of Fluid Mechanics*, Vol. 65, Part 2, pp. 325-336, 1974.

Barker, S. J. and Crow, S. C., "The Motion of Two-Dimensional Vortex Pairs in a Ground Effect," *Journal of Fluid Mechanics*, Vol. 82, Part 4, pp. 659-672, 1977.

Batchelor, G. K., "Axial Flow in Trailing Line Vortices," *Journal of Fluid Mechanics*, Vol. 20, Part 4, pp. 645-658, 1964.

Binder, A., "Turbulence Production Due to Secondary Vortex Cutting in a Turbine Rotor," *Transactions of the ASME, Journal of Engineering for Gas Turbines and Power*, Vol. 107, pp. 1039-1046, October 1985.

Binder, A., Forster, W., Mach, K., and Rogge, H., "Unsteady Flow Interaction Caused by Stator Secondary Vortices in a Turbine Rotor," *Transactions of the ASME, Journal of Turbomachinery*, Vol. 109, pp. 251-257, April 1987.

Burgers, J. M., "A Mathematical Model Illustrating the Theory of Turbulence," *Advances in Applied Mechanics*, Vol. 1, pp. 171-199, 1948.

Brophy, M. C., Treaster, A. L., Stinebring, D. R., and Welz, J. P., "Optimization of a Five-Hole Probe Wake Measuring Device," ARL Penn State Technical Memorandum TM-87-156, Applied Research Laboratory, The Pennsylvania State University, August 28, 1987.

Cavitation Committee, "Report of the Cavitation Committee," Proceedings of the 19th International Towing Tank Conference, Madrid, Spain, September 16-22, 1990.

Chen, G. T., Greitzer, E. M., Tan, C. S., and Marble, F. E., "Similarity Analysis of Compressor Tip Clearance Flow Structure," *Transactions of the ASME, Journal of Turbomachinery*, Vol. 113, pp. 260-271, April 1991.

Coleman, H. W. and Steele, W. G., *Experimentation and Uncertainty Analysis for Engineers*, John Wiley and Sons, 1989.

Crawford, M. E. and Kays, W. M., "STANS-A Program for Numerical Computation of Two-Dimensional Internal and External Boundary Layer Flows," COSMIC Program No. LEW-13009, NASA CR-2742, 1976.

Délery, J. M., "Physics of Vortical Flows," *Journal of Aircraft*, Vol. 29, No. 5, pp. 856-876, 1992.

Devenport, W. J. and Simpson, R. L., "Time Dependent Structure in Wing-Body Junction Flows," *Turbulent Shear Flows VI*, Springer-Verlag, pp. 232-248, 1989.

Devenport, W. J., Agarwal, N. K., Dewitz, M. B., Simpson, R. L., and Poddar, K., "Effects of a Fillet on the Flow Past a Wing-Body Junction," *AIAA Journal*, Vol. 28, No. 12, pp. 2017-2024, December 1990.

Dong, Y., Gallimore, S. J., and Hodson, H. P., "Three-Dimensional Flows and Loss Reduction in Axial Compressors," *Transactions of the ASME, Journal of Turbomachinery*, Vol. 109, pp. 354-361, July 1987.

Dring, R. P., Joslyn, H. D., and Hardin, L. W., "Experimental Investigation of Compressor Rotor Wakes," United Technologies Research Center, Technical Report AFAPL-TR-79-2107, January 1980.

Dring, R. P., Blair, M. F., Joslyn, H. D., Power, G. D., and Verdon, J. M., "The Effects of Inlet Turbulence and Rotor/Stator Interaction on the Aerodynamics and Heat Transfer of a Large-Scale Rotating Turbine Model," NASA Contractor Report 4079, 1988.

Eckerle, W. A. and Langston, L. S., "Horseshoe Vortex Formation Around a Cylinder," *Transactions of the ASME, Journal of Turbomachinery*, Vol. 109, pp. 278-285, April 1987.

Erickson, G. E., "Vortex Flow Correlation," Air Force Wright Aeronautical Laboratories Technical Report, AFWAL-TR-80-3143, (Northrop Corporation Report NOR-80-152), January 1981.

Eversman, W., "A Reciprocity Relationship for Transmission in Non-Uniform Hard Walled Ducts without Flow," *Journal of Sound and Vibration*, Vol. 47, pp. 515-521, 1976.

Farrell, K. J., McBride, M. W., and Billet, M. L., "High Reynolds Number Pump Facility for Cavitation Research," ASME International Symposium on Cavitation Research Facilities and Techniques--1987, FED-Vol. 57, edited by J. W. Holl and M. L. Billet, pp. 61-68, 1987.

Farrell, K. J., "An Investigation of End-Wall Vortex Cavitation in a High Reynolds Number Axial-Flow Pump," M.S. Thesis, Department of Mechanical Engineering, The Pennsylvania State University, May 1989.

Farrell, K. J. and Billet, M. L., "A Correlation of Leakage Vortex Cavitation in Axial Flow Pumps," submitted to the Transactions of the ASME, *Journal of Fluids Engineering*, 1993.

Gallus, H. E., Lambertz, J., and Wallmann, Th., "Blade-Row Interaction in an Axial-Flow Subsonic Compressor Stage," Transactions of the ASME, *Journal of Engineering for Power*, Vol. 102, No. 1, pp. 169-177, January 1980.

Garg, A. K. and Leibovich, S., "Spectral Characteristics of Vortex Breakdown Flowfields," *Physics of Fluids*, Vol. 22, No. 11, pp. 2053-2064, November 1979.

Gearhart, W. S., "Tip Clearance Cavitation in Shrouded Underwater Propulsors," *AIAA Journal of Aircraft*, Vol. 3, No. 2, March-April 1966.

Gracey, W., Letko, W., and Russell, W. R., "Wind-Tunnel Investigation of a Number of Total-Pressure Tubes at High Angles of Attack, Subsonic Speeds," NACA Technical Note 2331, April 1951.

Greeley, D. S. and Kerwin, J. E., "Numerical Methods for Propeller Design and Analysis in Steady Flow," *SNAME Transactions*, Vol. 90, pp. 415-453, 1982.

Green, S. I., "Trailing Vortex Core Unsteadiness--An Exploratory Study of Reynolds Number Effects," AIAA First National Fluid Dynamics Congress, July 1988.

Gregory-Smith, D. G., Graves, C. P., and Walsh, J. A., "Growth of Secondary Losses and Vorticity in an Axial Turbine Cascade," Transactions of the ASME, *Journal of Turbomachinery*, Vol. 110, pp. 1-8, January 1988.

Hawthorne, W. R., "Rotational Flow Through Cascades; Part I - The Components of Vorticity," *Quarterly Journal of Mechanics and Applied Mathematics*, Vol. 8, No. 3, p. 280, September 1955.

Hawthorne, W. R., "Some Aerodynamic Problems of Aircraft Engines," *Journal of the Aeronautical Sciences*, Vol. 24, No. 10, pp. 713-730, October 1957.

Hobson, G. and Shreeve, R., "Inlet Turbulence Distortion and Viscous Flow Development in a Controlled-Diffusion Compressor Cascade at Very High Incidence," AIAA Paper 91-2004, presented at the 27th Joint Propulsion Conference, Sacramento, CA, June 24-26, 1991.

Holl, J. W., "An Effect of Air Content on the Occurrence of Cavitation," *Transactions of the ASME, Journal of Basic Engineering*, Series D, Vol. 82, pp. 941-946, 1960.

Holl, J. W. and Treaster, A. L., "Cavitation Hysteresis," *Transactions of the ASME, Journal of Basic Engineering*, Series D, pp. 199-212, March 1966.

Holl, J. W. and Carroll, J. A., "Observations of the Various Types of Limited Cavitation on Axisymmetric Bodies," *Transactions of the ASME, Journal of Fluids Engineering*, Vol. 103, pp. 415-420, September 1981.

Horlock, J. H., "Annulus Wall Boundary Layers in Axial Compressor Stages," *Transactions of the ASME, Journal of Basic Engineering*, Vol. 85, No. 1, pp. 55-65, March 1963.

Hunt, J. C. R., Abell, C. J., Peterka, J. A., and Woo, H., "Kinematical Studies of the Flows Around Free or Surface-Mounted Obstacles; Applying Topology to Flow Visualization," *Journal of Fluid Mechanics*, Vol. 86, Part 1, pp. 179-200, 1978.

Hunter, I. H. and Cumpsty, N. A., "Casing Wall Boundary-Layer Development Through an Isolated Compressor Rotor," *Transactions of the ASME, Journal of Engineering for Power*, Vol. 104, pp. 805-818, October 1982.

Inoue, M., Kuroumaru, M., and Fukuwara, M., "Behavior of Tip Leakage Flow Behind an Axial Compressor Rotor," *Transactions of the ASME, Journal of Engineering for Gas Turbines and Power*, Vol. 108, pp. 7-14, January 1986.

Inoue, M. and Kuroumaru, M., "Structure of Tip Clearance Flow in an Isolated Axial Compressor Rotor," *Transactions of the ASME, Journal of Turbomachinery*, Vol. 111, pp. 250-256, July 1989.

Jessup, S. D., Boswell, R. J., and Nelka, J. J., "Experimental Unsteady and Time Average Loads on the Blades of the CP Propeller on a Model of the DD-963 Class Destroyer for Simulated Modes of Operation," David W. Taylor Naval Ship Research and Development Center, DTNSRDC-77/0110, December 1977.

Jessup, S. D., Schott, C. G., Jeffers, M. F., and Kobayashi, S., "Local Propeller Blade Flows in Uniform and Sheared Onset Flows using LDV Techniques," David W. Taylor Naval Ship Research and Development Center, DTNSRDC-85/007, February 1985.

Johnston, J. P., "On the Three-Dimensional Turbulent Boundary Layer Generated by Secondary Flow," *Transactions of the ASME, Journal of Basic Engineering*, Vol. 82, pp. 233-248, March 1960.

Johnston, J. P., "The Turbulent Boundary Layer at a Plane of Symmetry in a Three-Dimensional Flow," *Transactions of the ASME, Journal of Basic Engineering*, Vol. 82, pp. 622-628, September 1960.

Joslyn, H. D. and Dring, R. P., "Axial Compressor Stator Aerodynamics," *Transactions of the ASME, Journal of Engineering for Gas Turbines and Power*, Vol. 107, pp. 485-493, 1983.

Kemp, N. H. and Sears, W. R., "Aerodynamic Interference Between Moving Blade Rows," *Journal of the Aeronautical Sciences*, Vol. 20, No. 9, pp. 585-598, September 1953.

Lakshminarayana, B. and Horlock, J. H., "Tip Clearance Flow and Losses for an Isolated Compressor Blade," British A.R.C. Report and Memorandum 3316, 1962.

Lakshminarayana, B., "Methods of Predicting the Tip Clearance Effects in Axial Flow Turbomachinery," *Transactions of the ASME, Journal of Basic Engineering*, Vol. 92, pp. 467-480, September 1970.

Lauchle, G. C., Billet, M. L., and Deutsch, S., "High-Reynolds Number Liquid Flow Measurements," *Frontiers in Experimental Fluid Mechanics*, pp. 95-157, edited by M. Gad-el-Hak, Springer-Verlag Berlin Heidelberg, 1989.

Lee, H. and Shetz, J. A., "Experimental Results for Reynolds Number Effects on Trailing Vortices," *Journal of Aircraft*, Vol. 22, No. 2, pp. 158-160, February 1985.

Legendre, R., "Lignes de Courant d'un Ecoulement Permanent: Décollement et Séparation," *La Recherche Aérospatiale*, No. 1977-6, pp. 327-335, 1977.

Lewis, R. I. and Yeung, E. H. C., "Vortex Shedding Mechanisms in Relation to Tip Clearance Flows and Losses in Axial Fans," British A.R.C. Report and Memorandum 3829, 1977.

Lieblein, S., Schwenk, F. C., and Broderick, R. L., "Diffusion Factor for Estimating Losses and Limiting Blade Loadings in Axial-Flow-Compressor Blade Elements," NACA RM E53 D01, June 8, 1953.

Lighthill, M. J., "Attachment and Separation in Three-Dimensional Flow," Section II 2-6 of *Laminar Boundary Layers*, Edited by L. Rosenhead, Oxford University Press, pp. 72-82, 1963.

Mager, A., "Generalization of Boundary-Layer Momentum-Integral Equations to Three-Dimensional Flows Including those of Rotating Systems," NACA TN 2310, March 1951.

Manwaring, S. R. and Fleeter, S., "Periodic Rotor-Blade Aerodynamics Including Loading Effects," *Journal of Propulsion*, Vol. 6, No. 5, pp. 590-597, September-October 1990.

Manwaring, S. R. and Wisler, D. S., "Unsteady Aerodynamics and Gust Response in Compressors and Turbines," ASME paper 92-GT-422, presented at the 37th ASME International Gas Turbine and Aeroengine Congress and Exposition, June 1-4, 1992.

Maxworthy, T., Hopfinger, E. J., and Redekopp, L. G., "Wave Motions on Vortex Cores," *Journal of Fluid Mechanics*, Vol. 151, pp. 141-165, 1985.

Mayle, R. E., "The Role of Laminar-Turbulent Transition in Gas Turbine Engines," Transactions of the ASME, *Journal of Turbomachinery*, Vol. 113, pp. 509-537, October 1991.

McBride, M. W., "Refinement of the Mean Streamline Method of Blade Section Design," ASME Paper 76-WA/FE-11, December 1976.

McBride, M. W., "Engineering Design Method for Axial and Mixed Flow Hydraulic Machinery," ASME Small Hydro Power Fluid Machinery, pp. 73-80, 1982.

Mitchell, A. B., "An Experimental Investigation of Cavitation Inception in the Rotor Blade Tip Region of an Axial Flow Pump," Admiralty Research Laboratory, ARL/R1/G/HY/11/2, August 1958.

Moore, R. W., Jr. and Richardson, D. L., "Skewed Boundary-Layer Flow Near the End Walls of a Compressor Cascade," Transactions of the ASME, Vol. 79, pp. 1789-1800, November 1957.

Orloff, K. L., "Trailing Vortex Wind-Tunnel Diagnostics with a Laser Velocimeter," *Journal of Aircraft*, Vol. 11, No. 8, pp. 477-482, August 1974.

Patrick, W. P., "Flowfield Measurements in a Separated and Reattached Flat Plate Turbulent Boundary Layer," NASA Contractor Report 4052, March 1987.

Perry, A. E. and Fairlie, B. D., "Critical Points in Flow Patterns," *Advances in Geophysics*, Vol. 18B, Academic Press, pp. 299-315, 1974.

Phillips, W. R. C. and Head, M. R. "Flow Visualization in the Tip Region of a Rotating Blade Row," *Journal of Mechanical Sciences*, Vol. 22, pp. 495-521, 1980.

Rains, D. A., "Tip Clearance Flows in Axial Flow Compressors and Pumps," Hydromechanics and Mechanical Engineering Laboratories, California Institute of Technology, Report No. 5, 1954.

Reed, R. E., "Properties of the Lateral Random Oscillations of Trailing Vortices Observed in Wind-Tunnel Tests," Neilson Engineering and Research, Inc., NEAR TR 47, January 1973.

Robbins, B. E., "Water Tunnel Turbulence Measurements behind a Honeycomb," *Journal of Hydraulics and Acoustics*, Vol. 12., pp. 122-128, 1978.

Schlichting, H., *Boundary-Layer Theory*, Seventh Edition, McGraw-Hill, Inc., 1979.

Schmidt, D. P. and Okiishi, T. H., "Multistage Axial-Flow Turbomachine Wake Production, Transport, and Interaction," *AIAA Journal*, Vol. 15, No. 8, pp. 1138-1145, August 1977.

Schott, C. G., "Design of an Experimental Pump Stage of the HIREP Facility," ARL Penn State Technical Memorandum No. 91-68, Applied Research Laboratory, The Pennsylvania State University, September 1993.

Schulz, H. D. and Gallus, H. E., "Experimental Investigation of the Three-Dimensional Flow in an Annular Compressor Cascade," *Transactions of the ASME, Journal of Turbomachinery*, Vol. 110, pp. 467-478, October 1988.

Schulz, H. D., Gallus, H. E., and Lakshminarayana, B., "Three-Dimensional Separated Flow Field in the Endwall Region of an Annular Compressor Cascade in the Presence of Rotor-Stator Interaction: Part I--Quasi-Steady Flow Field and Comparison with Steady-State Data," *Transactions of the ASME, Journal of Turbomachinery*, Vol. 112, No. 4, pp. 669-678, October 1990.

Sehra, A. K. and Kerrebrock, J. L., "Blade-to-Blade Flow Effects on Mean Flow in Transonic Compressors," *AIAA Journal*, Vol. 19, No. 4, pp. 476-483, April 1981.

Serovy, G. K., "Axial-Flow Compressor Aerodynamics," Chapter 17 of *The Aerothermodynamics of Aircraft Gas Turbine Engines*, AFAPL-TR-78-52, edited by G. C. Oates, July 1978.

Shuba, B. H., "An Investigation of Tip-Wall Vortex Cavitation in an Axial-Flow Pump," M.S. Thesis, Department of Aerospace Engineering, The Pennsylvania State University, 1984.

Sieverding, C. H. and Van den Bosch, P., "The Use of Colored Smoke to Visualize Secondary Flows in a Turbine-Blade Cascade," *Journal Fluid Mechanics*, Vol. 134, pp. 85-89, September 1983.

Sieverding, C. H., "Recent Progress in the Understanding of Basic Aspects of Secondary Flows in Turbine Blade Passages," *Transactions of the ASME, Journal of Engineering for Gas Turbines and Power*, Vol. 107, pp. 248-257, April 1985.

Silversten, A., Katzoff, S., and Bullivant, W. K., "Downwash and Wake Behind Plain and Flapped Airfoils," NACA Report 651, 1939.

Singh, P. I. and Uberoi, M. S., "Experiments on Vortex Stability," *Physics of Fluids*, Vol. 19, No. 12, pp. 1858-1863, December 1976.

Smith, L. H., Jr., "Secondary Flow in Axial-Flow Turbomachinery," *Transactions of the ASME*, Vol. 77, pp. 1065-1076, October 1955.

Squire, L. C., "The Motion of a Thin Oil Sheet Under the Boundary Layer on a Body," in *Flow Visualization in Wind Tunnels Using Indicators*, AGARDograph 70, Compiled by R. L. Maltby, pp. 7-28, April 1962.

Stanbrook, A., "The Surface Oil Flow Technique for Use in High Speed Wind Tunnels," in *Flow Visualization in Wind Tunnels Using Indicators*, AGARDograph 70, Compiled by R. L. Maltby, pp. 39-49, April 1962.

Storer, J. A. and Cumpsty, N. A., "Tip Leakage Flow in Axial Compressors," *Transactions of the ASME, Journal of Turbomachinery*, Vol. 113, pp. 252-259, April 1991.

Straka, W. A. and Farrell, K. J., "The Effect of Spatial Wandering on Experimental Laser Velocimeter Measurements of the End-Wall Vortices in an Axial-Flow Pump," *Experiments in Fluids*, Vol. 13, pp. 163-170, 1992.

Swanson, P. D. and Holter, N. S., "Turbomachinery Inspection Using the Intelligent Robotic Inspection System," ARL Penn State Technical Memorandum TM-90-295, Applied Research Laboratory, The Pennsylvania State University, August 1, 1991.

Taylor, E. S., "The Skewed Boundary Layer," *Transactions of the ASME, Journal of Basic Engineering*, Vol. 81, pp 297-304, September 1959.

Tobak, M. and Peake, D. J., "Topology of Two-Dimensional and Three-Dimensional Separated Flows," AIAA Paper 79-1480, presented at the AIAA 12th Fluid and Plasma Dynamics Conference, Williamsburg, Virginia, July 23-25, 1979.

Tobak, M. and Peake, D. J., "Topology of Three-Dimensional Separated Flows," *Annual Review of Fluid Mechanics*, Vol. 14, pp. 61-85, 1982.

Treaster, A. L. and Yocom, A. M., "The Calibration and Application of Five-Hole Probes," *Transactions of the Instrument Society of America*, Vol. 18, No. 3, pp. 23-34, 1979.

Wagner, J. H., Okiishi, T. H., and Holbrook, G. J., "Periodically Unsteady Flow in an Imbedded Stage of a Multistage, Axial-Flow Turbomachine," *Transactions of the ASME, Journal of Engineering for Power*, Vol. 101, No. 1, January 1979.

Walker, P. J., "Blade Lean in Axial Turbines: Model Turbine Measurements and Simulation by a Novel Numerical Method," Ph.D. Dissertation, Department of Engineering, University of Cambridge, December 1987.

Yaras, M. and Sjolander, S. A., "Development of the Tip-Leakage Flow Downstream of a Planar Cascade of Turbine Blades: Vorticity Field," *Transactions of the ASME, Journal of Turbomachinery*, Vol. 112, pp. 609-617, October 1990.

Zierke, W. C. and Okiishi, T. H., "Measurement and Analysis of Total-Pressure Unsteadiness Data from an Axial-Flow Compressor Stage," *Transactions of the ASME, Journal of Engineering for Power*, Vol. 104, No. 2, pp. 479-488, April 1982.

Zierke, W. C. and Deutsch, S. "The Measurement of Boundary Layers on a Compressor Blade in Cascade," NASA Contractor Report 185118, July 1989.

Appendix A: Five-Hole Probe Uncertainty Analysis

All experimental results contain a certain degree of uncertainty that one must consider when analyzing these results. Here, we shall consider the uncertainty associated with our five-hole pressure probe measurements--using a standard uncertainty analysis, such as the one outlined by Coleman and Steele [1989]. For a general case of an experimental result, r , as a function of J variables X_i ,

$$r = r(X_1, X_2, \dots, X_J),$$

the uncertainty of the result is given by

$$U_r = \left[\left(\frac{\partial r}{\partial X_1} U_{X_1} \right)^2 + \left(\frac{\partial r}{\partial X_2} U_{X_2} \right)^2 + \dots + \left(\frac{\partial r}{\partial X_J} U_{X_J} \right)^2 \right]^{\frac{1}{2}},$$

where U_{X_i} are the uncertainties in the measured values X_i . The uncertainties correspond to our estimates of the combination of bias and precision error. For most of this uncertainty analysis, we attempted to estimate the uncertainties to 95% confidence.

For the five-hole probe measurements, Treaster and Yocum [1979] gave data reduction equations and calibration plots that yield the proper functional relationships. First, we need to consider the uncertainty associated with measuring pressure values with the pressure transducers. The manufacturers of the pressure transducers used in this experiment state that the uncertainty is 0.05 psi. Repeatability tests performed at ARL Penn State using our transducer calibration procedure show that we can actually do better than this specification when using transducers on a single card, as we do for five-hole probe measurements. This uncertainty for five-hole probe measurements would actually be 0.02 psi, while the uncertainty in the blade static-pressure measurements would be 0.05 psi, since more than one transducer card was employed. Considering the blade static-pressure measurements for a moment, we can consider the bias error for a single transducer to be 0.05 psi and the precision error to be the 95% confidence level of the data scatter during the test. This data scatter gives a precision error ranging from 0.03 psi--in regions with minimal streamwise pressure gradients--to 0.12 psi--in regions of large streamwise pressure gradients, as might be found at 90% span on the rotor blade suction surface. Using the root-sum-square technique, we can combine the bias and precision errors to obtain overall uncertainties ranging from 0.06 psi to 0.13 psi in measuring the blade static pressures.

Most of the uncertainty analysis for our five-hole probe measurements will focus on the bias portion of the uncertainty. Later, we will combine this estimate of the bias error with an estimate of the precision error to determine the total uncertainty. Within the five-hole probe data reduction, Treaster and Yocum [1979] defined an average pressure,

$$\bar{p} = \frac{1}{4}(p_2 + p_3 + p_4 + p_5),$$

using pressures measured from the holes in the yaw plane, p_2 and p_3 , and in the pitch plane, p_4 and p_5 . This equation yields

$$U_{\bar{p}} = \frac{1}{2} U_{p_2}$$

using the general uncertainty equation.

The next step in establishing the uncertainty of the five-hole probe measurements is to establish the uncertainty of the measured yaw and pitch flow angles (angles relative to the probe tip). Treaster and Yocom [1979] defined yaw and pitch coefficients as

$$C_{yaw} = \frac{p_2 - p_3}{p_1 - \bar{p}}$$

and

$$C_{pitch} = \frac{p_4 - p_5}{p_1 - \bar{p}}.$$

Using these functional equations, the general uncertainty equation yields

$$U_{C_{yaw}} = C_{yaw} \left[\left(\frac{U_{p_2}}{p_2 - p_3} \right)^2 + \left(\frac{-U_{p_3}}{p_2 - p_3} \right)^2 + \left(\frac{-U_{p_1}}{p_1 - \bar{p}} \right)^2 + \left(\frac{U_{\bar{p}}}{p_1 - \bar{p}} \right)^2 \right]^{\frac{1}{2}}$$

and

$$U_{C_{pitch}} = C_{pitch} \left[\left(\frac{U_{p_4}}{p_4 - p_5} \right)^2 + \left(\frac{-U_{p_5}}{p_4 - p_5} \right)^2 + \left(\frac{-U_{p_1}}{p_1 - \bar{p}} \right)^2 + \left(\frac{U_{\bar{p}}}{p_1 - \bar{p}} \right)^2 \right]^{\frac{1}{2}}.$$

In order to compute these uncertainties, we need to evaluate the calibration curves for the type of five-hole probe being used and where we expect most of the data to be situated on these curves. The five-hole probes used in the radial surveys and the rake surveys are of a different design. Also, the probes used within the rake were turned in the yaw direction (by 14.7 degrees) to be more aligned with the expected flow direction, while the probes used for the radial surveys were aligned axially. Thus, the two types of probes had different calibration curves and most of the data was situated on different regions of these curves. For the five-hole probe rake surveys, we found typical values for C_{yaw} and C_{pitch} of 0.1 and 0.2, respectively. Also, $(p_1 - \bar{p})$ was typically near 6 psi. These values yield uncertainties for the yaw and pitch coefficients of approximately 0.005. For the radial surveys, we found typical values for C_{yaw} and C_{pitch} of -1.5 and 0.1, respectively, with 4 psi being a typical value of $(p_1 - \bar{p})$. Using absolute values, these values yield an uncertainty for the yaw coefficient of 0.01 and an uncertainty for the pitch coefficient of 0.007.

Values for the pitch flow angle, α , and yaw flow angle, β , come from calibration plots, so we replace the partial derivatives in the general uncertainty equation with finite differences to obtain

$$U_\alpha = \left[\left(\frac{\Delta \alpha}{\Delta C_{yaw}} U_{C_{yaw}} \right)^2 + \left(\frac{\Delta \alpha}{\Delta C_{pitch}} U_{C_{pitch}} \right)^2 \right]^{\frac{1}{2}}$$

and

$$U_\beta = \left[\left(\frac{\Delta \beta}{\Delta C_{yaw}} U_{C_{yaw}} \right)^2 + \left(\frac{\Delta \beta}{\Delta C_{pitch}} U_{C_{pitch}} \right)^2 \right]^{\frac{1}{2}}.$$

Table 10 shows typical maximum values for these finite differences as determined from the five-hole probe calibration plots. Using these values for the rake surveys, we can determine the uncertainty in measuring the pitch and yaw flow angles to be 0.5 degrees. For the radial surveys, we obtain an uncertainty for measuring the pitch flow angle to be 2.0 degrees and an uncertainty for measuring the yaw flow angle to be 1.1 degrees. Additional uncertainties must also be considered for measuring the yaw flow angle. First, the uncertainty in aligning the five-hole probe within the calibration mounting device is 0.1 degrees. Next, for the five-hole probe rake, the uncertainty in aligning each probe within the rake is also 0.1 degrees. However, for the radial surveys, the five-hole probe slides within a strongback and we estimate that the uncertainty caused by the probe yawing within the strongback is 3.5 degrees. This uncertainty also includes aligning the probe with the tunnel axis. In order to prevent this uncertainty from becoming even larger, we kept the probe head in contact with one edge of the strongback slot, approximately 3.5 degrees from the center of the slot. Later, during data reduction, we took this 3.5 degree offset into account when determining velocities and flow angles. Using a root-sum-square of these uncertainties gives a total uncertainty in measuring the yaw flow angle of 0.5 degrees for the rake measurements and 3.7 degrees for the radial surveys.

Within the five-hole probe data reduction, the computation of the flow angles leads to the computation of pressure coefficients. These coefficients are not defined in the same manner as the pressure coefficients used to help define a flow field. They are simply coefficients used to compute flow velocities from five-hole probe calibration plots. The uncertainty in measuring these coefficients can be found from

$$U_{C_{p_{total}}} = \left[\left(\frac{\Delta C_{p_{total}}}{\Delta \alpha} U_\alpha \right)^2 + \left(\frac{\Delta C_{p_{total}}}{\Delta \beta} U_\beta \right)^2 \right]^{\frac{1}{2}}$$

and

$$U_{C_{p_{static}}} = \left[\left(\frac{\Delta C_{p_{static}}}{\Delta \alpha} U_\alpha \right)^2 + \left(\frac{\Delta C_{p_{static}}}{\Delta \beta} U_\beta \right)^2 \right]^{\frac{1}{2}}.$$

Table 10. Data from Five-Hole Probe Calibration Plots

Finite Difference Approximations of Various Slopes	Typical Maximum Values (degrees)		Finite Difference Approximations of Various Slopes	Typical Maximum Values (1/degrees)	
	Rake Surveys	Radial Surveys		Rake Surveys	Radial Surveys
$\frac{\Delta \alpha}{\Delta C_{yaw}}$	100	200	$\frac{\Delta C_{p_{total}}}{\Delta \alpha}$	0.01	0.02
$\frac{\Delta \alpha}{\Delta C_{pitch}}$	10	10	$\frac{\Delta C_{p_{total}}}{\Delta \beta}$	0.01	0.06
$\frac{\Delta \beta}{\Delta C_{yaw}}$	10	10	$\frac{\Delta C_{p_{static}}}{\Delta \alpha}$	0.01	0.01
$\frac{\Delta \beta}{\Delta C_{pitch}}$	100	150	$\frac{\Delta C_{p_{static}}}{\Delta \beta}$	0.01	0.05

Again, Table 10 shows typical maximum values for these finite differences as determined from the five-hole probe calibration plots. Using these values, we can determine the uncertainty in measuring the total-pressure coefficient to be 0.01 for the rake measurements and 0.23 for the radial surveys. Also, the uncertainty for the static-pressure coefficient is 0.01 for the rake measurements and 0.19 for the radial surveys.

Finally, Treaster and Yocum [1979] computed the squared value of the magnitude of the velocity vector from

$$\bar{V}^2 = \frac{2}{\rho} (p_1 - \bar{p})(1 + C_{p_{static}} - C_{p_{total}}).$$

This equation leads to the uncertainty equation,

$$U_{\bar{V}^2} = \bar{V}^2 \left[\left(\frac{U_{p_1}}{p_1 - \bar{p}} \right)^2 + \left(\frac{U_{\bar{p}}}{p_1 - \bar{p}} \right)^2 + \left(\frac{U_{C_{p_{static}}}}{1 + C_{p_{static}} - C_{p_{total}}} \right)^2 + \left(\frac{U_{C_{p_{total}}}}{1 + C_{p_{static}} - C_{p_{total}}} \right)^2 \right]^{\frac{1}{2}}.$$

Finding the magnitude of the velocity vector from the squared value leads to

$$U_{\bar{V}} = \frac{U_{\bar{V}^2}}{2\bar{V}}.$$

Next, we require values of $C_{p_{\text{rake}}}$ and $C_{p_{\text{radial}}}$. The uncertainty in velocity can be quite sensitive to these values. For the rake surveys, we found typical values of 0.1 and 0.5 for $C_{p_{\text{rake}}}$ and $C_{p_{\text{radial}}}$, respectively. Then, using the measured reference velocity of 35 ft/sec as a typical velocity magnitude, we can compute the uncertainty of measuring velocity with a five-hole probe as 0.2 ft/sec for the rake measurements. For the radial surveys, we found typical values of -0.4 and 0.7 for $C_{p_{\text{rake}}}$ and $C_{p_{\text{radial}}}$, respectively. Again using 35 ft/sec, we can compute the uncertainty of measuring velocity with a five-hole probe as 2.5 ft/sec for the radial surveys. Brophy, Treaster, Stinebring, and Welz [1987] performed a series of five-hole probe measurements behind a hydrofoil, both in the freestream and within the hydrofoil wake. They obtained estimates of repeatability and comparisons with LDV measurements. As shown in Appendix C, higher turbulence levels result in higher precision errors for LDV measurements of mean velocity. Higher turbulence levels also lead to higher precision errors in five-hole probe measurements. The largest uncertainty of these hydrofoil measurements occurred in the highly turbulent wakes and was estimated to be 0.9 ft/sec. This precision error can be combined with the previously computed bias error to obtain an overall uncertainty of 0.9 ft/sec for the rake measurements and 2.7 ft/sec for the radial surveys, using the root-sum-square technique.

Knowing the uncertainty for the magnitude of the velocity vector, we can now compute the uncertainty in measuring the axial, radial, and tangential components of the velocity. Treaster and Yocom [1979] computed these components as

$$V_z = \bar{V} \cos\alpha \cos\beta,$$

$$V_r = \bar{V} \sin\alpha,$$

and

$$V_\theta = \bar{V} \cos\alpha \sin\beta.$$

The corresponding uncertainty equations for these components are

$$U_{V_z} = \left[(U_{\bar{V}} \cos\alpha \cos\beta)^2 + (-U_\alpha \bar{V} \sin\alpha \cos\beta)^2 + (-U_\beta \bar{V} \cos\alpha \sin\beta)^2 \right]^{\frac{1}{2}},$$

$$U_{V_r} = \left[(U_{\bar{V}} \sin\alpha)^2 + (U_\alpha \bar{V} \cos\alpha)^2 \right]^{\frac{1}{2}},$$

and

$$U_{V_0} = \left[(U_{\bar{V}} \cos\alpha \sin\beta)^2 + (-U_a \bar{V} \sin\alpha \sin\beta)^2 + (U_b \bar{V} \cos\alpha \cos\beta)^2 \right]^{\frac{1}{2}}.$$

In many typical situations, both the yaw and pitch flow angles are nearly zero relative to the probe head. However, angles of nearly zero may give a false value of uncertainty and, therefore, we chose more extreme values for the flow angles downstream of the inlet guide vanes. For the rake surveys, we obtain 5 degrees for both α and β , while for the radial surveys, we obtain -4 degrees for α and -19 degrees for β . Using these values, we computed the values of the uncertainties, which are summarized in Table 11. Note that the uncertainty values of the yaw and pitch angles must be converted from degrees into radians. The uncertainty in the yaw angle moving within the strongback significantly affects the uncertainty of the measured quantities when using the radial surveys. Also, the rather large uncertainty of 2.0 degrees in measuring the pitch flow angle in the radial surveys strongly affects the uncertainty in the radial velocity measurements. For the IGV exit flow, this uncertainty arises from operating away from the center of the calibration plots because the probe head was not aligned with the expected flow direction. The radial surveys upstream of the inlet guide vanes should have a smaller uncertainty for measuring both the pitch flow angle and the radial velocity.

In addition to computing the uncertainty of measuring the velocity with a five-hole probe, we can now compute the uncertainty of measuring the total and static pressures with a five-hole probe. Treaster and Yocom [1979] found the total pressure from

$$p_T = p_1 - C_{p_{total}} (p_1 - \bar{p})$$

and the static pressure from

$$p = \bar{p} - C_{p_{static}} (p_1 - \bar{p}).$$

The general uncertainty equation then yields

$$U_{p_T} = \left[((1 - C_{p_{total}}) U_{p_1})^2 + (C_{p_{total}} U_{\bar{p}})^2 + (-(p_1 - \bar{p}) U_{C_{p_{total}}})^2 \right]^{\frac{1}{2}}$$

and

$$U_p = \left[(-C_{p_{static}} U_{p_1})^2 + ((1 + C_{p_{static}}) U_{\bar{p}})^2 + (-(p_1 - \bar{p}) U_{C_{p_{static}}})^2 \right]^{\frac{1}{2}}.$$

These equations give the uncertainties shown in Table 11.

Table 11. Uncertainty in Five-Hole Probe Measurements to 95 % Confidence

Measured Quantity	Uncertainty for Rake Surveys	Percent Uncertainty for Rake Surveys	Uncertainty for Radial Surveys	Percent Uncertainty for Radial Surveys
α	0.5 degrees	-	2.0 degrees	-
β	0.5 degrees	-	3.7 degrees	-
\bar{V}	0.9 ft/sec	2.6%	2.7 ft/sec	7.7%
V_z	0.9 ft/sec	2.6%	2.6 ft/sec	7.9%
V_r	0.3 ft/sec	9.8%	1.5 ft/sec	61.4%
V_θ	0.3 ft/sec	9.9%	2.1 ft/sec	18.5%
p_T	0.06 psi	-	0.92 psi	-
p	0.06 psi	-	0.76 psi	-

One item should be mentioned concerning the uncertainty of the five-hole probe measurements, even though it is not included in the formal uncertainty analysis. During the experiment, we observed vibration of the five-hole probes used during the rake surveys. The gearbox backlash resulted in excessive free play of the five-hole probe rake assembly in the circumferential direction, complicating both the acquisition and interpretation of the data. The primary problem resulted from flow induced oscillations of the rake hub, which fed back through the gearbox to the encoder shaft. When the data acquisition program attempted to read the encoder position after a step, continuous motion of the encoder shaft made the reading of a specific position impossible—resulting in a device time-out error and an interruption of the survey.

Although the backlash of the gearbox was measured to be 0.7 degrees prior to the test, we expected that the torque generated by the tangential flow across the probe supports would keep the rake/gearbox assembly locked in the counter-clockwise direction (looking upstream), thus eliminating the effect of the backlash after zeroing the rake position under flow conditions. Unfortunately, the pressure field generated by the downstream rotating blades apparently forced the rake in the same direction as the rotor blade rotation, setting up an oscillation as the probes were forced clockwise by the rotor blade flow potential effect and then counter-clockwise by the flow torque. This circumferential vibration moved the entire five-hole probe rake assembly as a unit at a frequency corresponding to the rotor shaft rate. This frequency was verified by illuminating the five-hole probe rake with a strobe that was synchronized to the rotor rpm. The strobe "froze" the motion of both the rotor blades and the rake probes. The magnitude of this oscillation was measured to be $\pm 1/16$ inch at the tip of Probe 1 (95.2% span), corresponding to a rotational vibration of ± 0.175 degrees.

Aside from the problems this vibration caused with the encoder, there was also some question as to its effect on the accuracy of the velocity measurements. The VXI data acquisition system sampled

the five-hole probe pressures at a rate of 120 samples/second and averaged the samples over a 2 second interval. This averaging process was designed to reduce pressure variations at the wake shedding frequency; however, it should also effectively average the circumferential probe motions to yield a mean value at the center of the probe vibration range. The effect of this spatial averaging is to shift the circumferential measurement location to the center of the vibration range. In addition to the shift in angular location, there will also be a difference in magnitude between the spatially averaged and exact values of the velocity at the shifted measurement location. In order to see if this difference is significant, consider the worst case location, across the center of a wake. For a vibration of ± 0.175 degrees, the spatially averaged value is within 1% of the true value at the wake center.

Appendix B: Pressure Probe Frequency Response

The fast-response total-pressure probe used in this experiment included a subminiature pressure transducer with a natural frequency of 250,000 Hz. However, the conical shroud upstream of the transducer face (seen in Figure 9) introduces the possibility of a cavity resonance at a much lower frequency. In order to analytically compute the frequency response characteristics of the probe with the transducer and cavity, we used a transfer matrix that Eversman [1976] derived for the converging section of a conical pipe (where the subscript 1 represents the probe inlet and the subscript 2 represents the location of the transducer face). In terms of the acoustic four-pole parameters, the acoustic mass velocity, \hat{v} , and the acoustic pressure, \hat{p} , at two locations along a cone are related by this transfer matrix according to

$$\begin{bmatrix} \hat{p}_1 \\ \hat{v}_1 \end{bmatrix} = \begin{bmatrix} T_{11} & T_{12} \\ T_{21} & T_{22} \end{bmatrix} \begin{bmatrix} \hat{p}_2 \\ \hat{v}_2 \end{bmatrix},$$

where, for the case of zero mean flow,

$$\begin{aligned} T_{11} &= \left\{ \frac{z_2}{z_1} \cos[k(z_1 - z_2)] + \frac{1}{kz_1} \sin[k(z_1 - z_2)] \right\} \\ T_{12} &= i \frac{c}{A_2} \left\{ \frac{z_2}{z_1} \sin[k(z_1 - z_2)] \right\} \\ T_{21} &= i \frac{A_2}{c} \left\{ \frac{z_1}{z_2} \sin[k(z_1 - z_2)] - \frac{(z_1 - z_2)}{kz_2^2} \cos[k(z_1 - z_2)] \right\} \\ T_{22} &= \left\{ \frac{z_1}{z_2} \cos[k(z_1 - z_2)] - \frac{1}{kz_2} \sin[k(z_1 - z_2)] \right\}. \end{aligned}$$

Here, c is the speed of sound, $k = 2\pi f/c$ is the wave number, f is the frequency, A_2 is the exit cross-sectional area of the cone, and $i = \sqrt{-1}$ is the imaginary unit number. Since the acoustic mass velocity is close to zero at the solid face of the transducer ($\hat{v}_2 \approx 0$), one can write the acoustic pressure transfer equation as

$$\hat{p}_1 \approx T_{11} \hat{p}_2$$

and this yields the desired transfer function,

$$\frac{\hat{p}_2}{\hat{p}_1} \approx \frac{kz_1}{kz_2 \cos[k(z_1 - z_2)] + \sin[k(z_1 - z_2)]}.$$

This transfer function implies that at low frequencies, where $k(z_2 - z_1) \ll 1$, the relation between acoustic pressures reduces to

$$\frac{\hat{p}_2}{\hat{p}_1} \approx \frac{kz_1}{kz_2 + k(z_1 - z_2)} = 1.$$

At higher frequencies, the first resonance will occur when

$$kz_2 \cos[k(z_1 - z_2)] + \sin[k(z_1 - z_2)] \approx 0$$

or

$$-kz_2 \approx \tan[k(z_1 - z_2)]$$

These frequency limits allow us to plot the frequency response in Figure 11. In creating this frequency response curve, we assumed that the probe would have a very small damping ratio, similar to the damping ratio for these types of transducers (approximately 0.02). This frequency response curve shows that the first cavity resonance occurs at 60,000 Hz and that the error is less than 5% for frequencies up to 10,000 Hz. This result confirms that the frequency response of the probe should not affect the measurement in the frequency range of interest.

Appendix C: LDV Surveys, Bin Size, and Uncertainty

Figure 12 illustrates the locations at which we acquired LDV data, with each survey given a corresponding letter symbol from A to M. Table 12 provides further information about the surveys corresponding to these symbols, including the test name, the number of runs, and the location of the LDV measurements.

As shown in Figure 12 and Table 12, LDV surveys A and B were performed to determine the details of the near and far rotor blade wakes. Each of these measurements were taken over a single rotor blade passage or approximately 51.4 degrees. Surveys C through F were completed to measure the details of the IGV wakes at four spanwise locations. The non-rotating nature of the inlet guide vanes posed a unique problem in taking data that would transverse the IGV wakes. To solve this problem, we acquired data for surveys C through F by moving the LDV measurement volume in the tangential direction—off the tunnel centerline, where the curvature in the tunnel window presented a small problem in finding the exact location of the measurement volume. For all of the other surveys, we kept the LDV measurement volume on the tunnel centerline. As with surveys A and B, surveys C through F were completed over a single rotor blade passage.

At the single spanwise location of 76.2% span, we performed surveys G and J at 13 axial positions for the full 360 degrees of rotor rotation. Survey G measured the level and decay of the potential effects upstream of the rotor blades, while survey J measured the level and decay of the potential effects and wakes downstream of the rotor blades. Within the rotor tip clearance region, we acquired data in survey I at 0%, 12.5%, 25%, 50%, and 100% of the tip chord for three radial locations in the clearance region. These tip clearance measurements, however, proved to be challenging due to the small tip clearance in the present HIREP design. Laser beam reflections off the tunnel window and blade surfaces made much of these data suspect. Nevertheless, since we acquired these data for the full 360 degrees of rotor rotation, data in survey I acquired between rotor blades gave more reasonable results.

Figure 12 and Table 12 show that radial surveys H, K, L, and M provided the primary LDV measurements, again covering the full 360 degrees of rotor rotation. Survey H was completed 3.0 inches upstream of the rotor blade tip leading edge, while surveys K, L, and M were taken at axial locations 3.375, 0.5, and 2.25 inches behind the rotor blade tip trailing edge, respectively. Each of these radial surveys included approximately 29 radial locations from the tunnel endwall liner (or casing) to the hub—with the exception of radial survey L which included 15 radial locations from the endwall to a location where the measurement volume crossed the blade trailing edge.

Using the field point measurement method, we obtained LDV data with a stationary measurement volume and tagged each LDV measurement sample with the angular position of the rotor via an optical shaft encoder and a rotating machinery resolver. In analyzing these data, we divided the entire blade rotation of 360 degrees into discrete angular storage windows or bins. These bins are used to statistically determine circumferential variations due to the blade rate, as well as any blade-to-blade variations. However, a trade-off arises when deciding how small one should make the bin size. On one hand, smaller bin sizes result in finer circumferential resolution and decrease the chance of averaging important circumferential features. On the other hand, smaller bin sizes result in fewer data samples per bin in which to perform a statistical analysis—giving higher standard deviations.

Table 12. LDV Surveys Corresponding to Locations Shown in Figure 12

Survey	Test #	# of Runs	Axial Measurement Locations	Radial Measurement Locations, Y	Tangential Locations	Range of Encoder (°)	# of K Points Per Run
A	0318DH1	6	0.05 ± .05" BRTTE	0.1, 0.2, 0.6, 1.0, 2.5, 4.5"	Tunnel Centerline	22.5°→73.9°	50→100
B	0318DH3	6	3.375" BRTTE	0.1, 0.2, 0.6, 1.0, 2.5, 4.5 "	Tunnel Centerline	22.5°→73.9°	50→100
C	0319DH1	17	3.05" IRTLE	2.0"	-2.0→0.9"	22.5°→73.9°	10→100
D	0319DH1/2	18	3.05" IRTLE	0.5"	-0.5→2.4"	22.5°→73.9°	10→100
E	0319DH3	13	3.05" IRTLE	5.0"	-2.0→0.4	22.5°→73.9°	10→100
F	0319DH4	16	3.05" IRTLE	9.5"	-1.8→0.3	22.5°→73.9°	10→100
G	0319DH5	7	0, 0.1, 0.25, 0.5, 1.0, 2.0, 3.0" IRLE	2.5"	Centerline	Full 360°	100
H	0320DH1 0326DH1	20 29	3.0" IRTLE	0.1 → 9.0" 0.15 → 10.3"	Centerline	Full 360°	50→100
I	0327DH1 0402DH1	15 15	0, 12.5, 25, 50, 100 % Tip Chord	0.075, 0.10, 0.12"	Centerline	Full 360°	50→100
J	0327DH2	7	1.0, 1.25, 1.5, 2.0, 3.0, 3.375" BRTTE	2.5"	Centerline	Full 360°	100
K	0330DH1	29	3.375" BRTTE	0.1 → 10.3"	Centerline	Full 360°	50→100
L	0331DH1	15	0.5" BRTTE	0.1 → 2.0"	Centerline	Full 360°	100
M	0401DH1	30	2.25" BRTTE	0.1 → 10.2"	Centerline	Full 360°	25→100

BRTTE = Behind rotor tip trailing edge
 IRTLE = In front of rotor tip leading edge location

In analyzing the LDV measurements in the HIREP experiment, we completed a trade-off study to determine the best bin sizes in which to reduce the data. As an example, Figure 93 shows a rotor blade wake analyzed as a function of rotor position for various bin sizes—with the ensemble-averaged velocity plotted for each bin. For bin sizes greater than 0.5 degrees, Figure 93 shows that over-averaging smears out the wake deficit. For smaller bin sizes, such as 0.1 and 0.25 degrees, the number of data samples per bin decreases below 35 for a single component of velocity (using the typical 50,000 sample size survey per component). Figure 93 shows that this reduced number of samples in performing the ensemble averaging within each bin leads to a very uneven wake profile when the bin size equaled 0.1 degrees. Even though the profile corresponding to a bin size of 0.25 degrees appeared quite acceptable, some bins contained as few as 8 or 9 samples—giving an unacceptable confidence in the data. Therefore, for LDV surveys requiring a small circumferential resolution—such as the details of wakes and vortices—we chose a bin size of 0.5 degrees. In other surveys, we chose a bin size of 1.0 degree in order to reduce the standard deviations associated with the ensemble averaging within each bin.

After deciding on the size of the storage window or bin, one still needs to consider the uncertainty in determining quantities such as velocity and turbulence intensity from the LDV measurements. Patrick [1987] developed a procedure to quantify this uncertainty. His uncertainty analysis includes considerations for bias (fixed) and precision (random) errors. Uncertainty in LDV measurements include bias errors from laser beam geometry, the counter processors, and the seeding, as well as precision errors from data processing. Data processing errors result from averaging a finite number of measured samples per data point. The laser beam geometric errors include, among others, the positioning uncertainty of the measurement volume, probe volume angular sensitivity, fringe spacing uncertainty, beam orientation bias, and finite probe volume bias. The processor bias results from errors in clock synchronization, quantizing errors, threshold limit errors, pedestal removal filter errors, and electronic induced noise. Finally, the seeding bias includes errors associated with seed injection flow distortion, the arrival rate of seed passing through the probe volume, and particle lag in accelerating flows. Patrick [1987] shows that the total uncertainty in LDV measurements can be determined by combining the precision and bias errors,

$$U_{total} = \pm(B + t_{0.95} S),$$

where B is the total root-sum-square values of the elemental bias errors, $t_{0.95}$ is the value from the Student's t test for a 95% confidence level (which approaches 1.96 for large sample sizes), and S is the precision error of the measurements.

The data processing errors are random errors which result from the averaging of a finite number of data samples to obtain mean velocity and turbulence intensity measurements. In LDV measurements, the measured velocity does not remain constant during the elapsed sampling time—it

fluctuates because of turbulence. As a result, the precision error for any finite number of measurements of a fixed quantity can be calculated by

$$S = \sqrt{\frac{1}{M-1} \sum_{m=1}^M (V_m - \bar{V})^2},$$

where

$$\bar{V} = \frac{1}{M} \sum_{m=1}^M V_m.$$

The precision error calculated by S is an estimate of the rms turbulence level. For an infinite number of samples, M , S becomes the exact measurement of the turbulence. However, for a finite number of samples, both the rms turbulence level, ζ , and the mean sample velocity, \bar{V} , will deviate from the true turbulence and mean velocity of the flow by precision errors S^ζ and $S^{\bar{V}}$, respectively. Patrick [1987] uses a Chi-squared distribution for the mean square turbulence intensity. Therefore, for large sample sizes ($M > 50$) the precision error of the turbulence intensity measurement can be determined by

$$\frac{S^\zeta}{\zeta} = \frac{1}{\sqrt{2M}}.$$

Relative to mean velocity measurements, the sampling distribution of V_m is "normal" about the population mean, V_p , with a standard deviation of V_p / \sqrt{M} . Therefore, Patrick [1987] shows that the precision error in the mean velocity measurement can be estimated by

$$\frac{S^{\bar{V}}}{V_p} = \frac{\zeta}{\sqrt{M}}.$$

For the present investigation, we acquired the LDV measurements with 100,000 samples at each measurement position for the entire rotor rotation. The majority of the results presented in this report were reduced into 1 degree bins—with a few surveys for wake and vortex measurements reduced into 0.5 degree bins. Given these 1.0 and 0.5 degree bin sizes, the average number of samples per measurement location per component are 140 and 70, respectively. From the previous equations, the precision error in the turbulence intensity measurements on average will range from 6.0% to 8.5%, depending on the bin size. The precision errors of the mean velocity, however, depend on the measured turbulence levels. Table 13 presents values of the precision error in mean velocity for various turbulence levels.

Table 13. Precision Errors in Mean Velocity LDV Measurements

Bin Size	Turbulence Level				
	0.01	0.05	0.10	0.15	0.20
0.5 degrees	0.1%	0.6%	1.2%	1.8%	2.4%
1.0 degrees	0.1%	0.4%	0.8%	1.3%	1.7%

In the procedure for quantifying LDV errors, Patrick [1987] discusses a total of 18 different types of bias sources of uncertainty. When evaluating these uncertainties, he assumes that many of these bias errors are negligible—including the pedestal removal filter error, the threshold limit error, the finite probe volume bias, the particle acceleration bias, the negative velocity bias, the frequency broadening bias, and the flow distortion bias. Many of the remaining bias errors, although not negligible, are relatively small compared to the precision errors. For the LDV system used by Patrick [1987], which is similar to the one used in the present investigation, the processor bias errors did not exceed 0.6%. Also, for the mean velocity measurements, the beam geometry bias errors never exceeded 0.8%, with the probe volume location bias giving the largest influence. The combined effect of the seeding bias errors on the mean velocity uncertainty was also shown to be small. For turbulence intensity measurements, many of the bias errors become much more important. For the present investigation, however, we did not explicitly calculate the individual and total bias errors, but these errors should be fairly similar to those calculated by Patrick [1987].

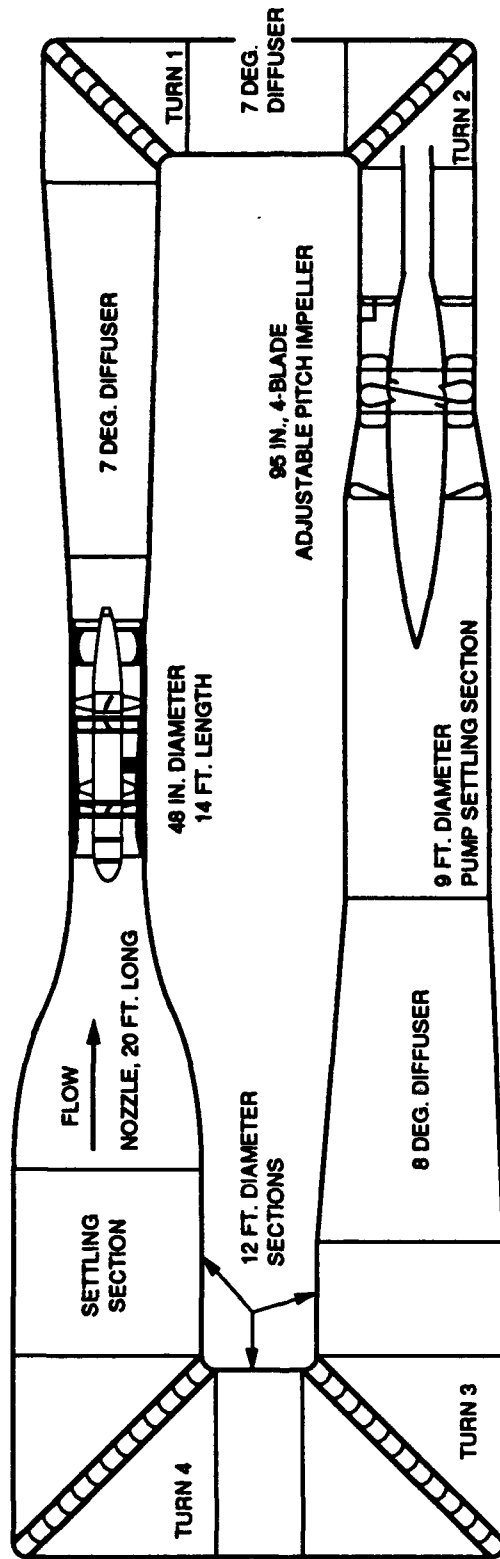


Figure 1. Garfield Thomas Water Tunnel

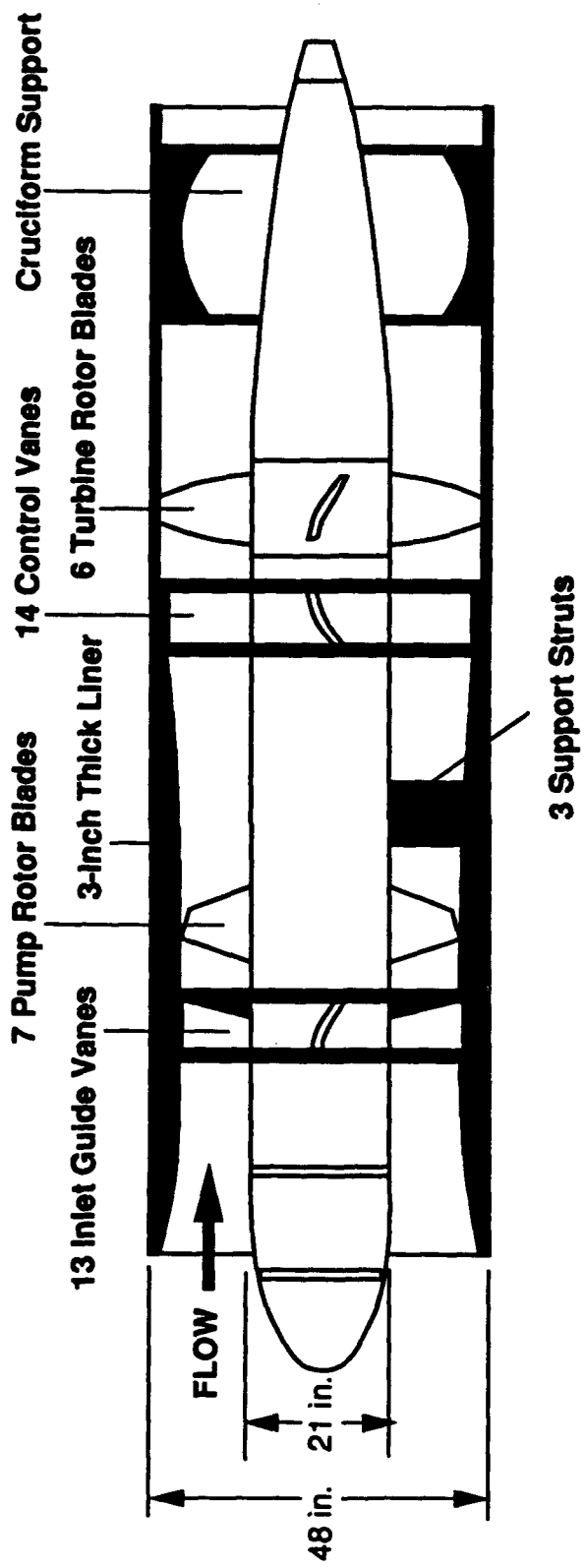


Figure 2. High Reynolds Number Pump Facility

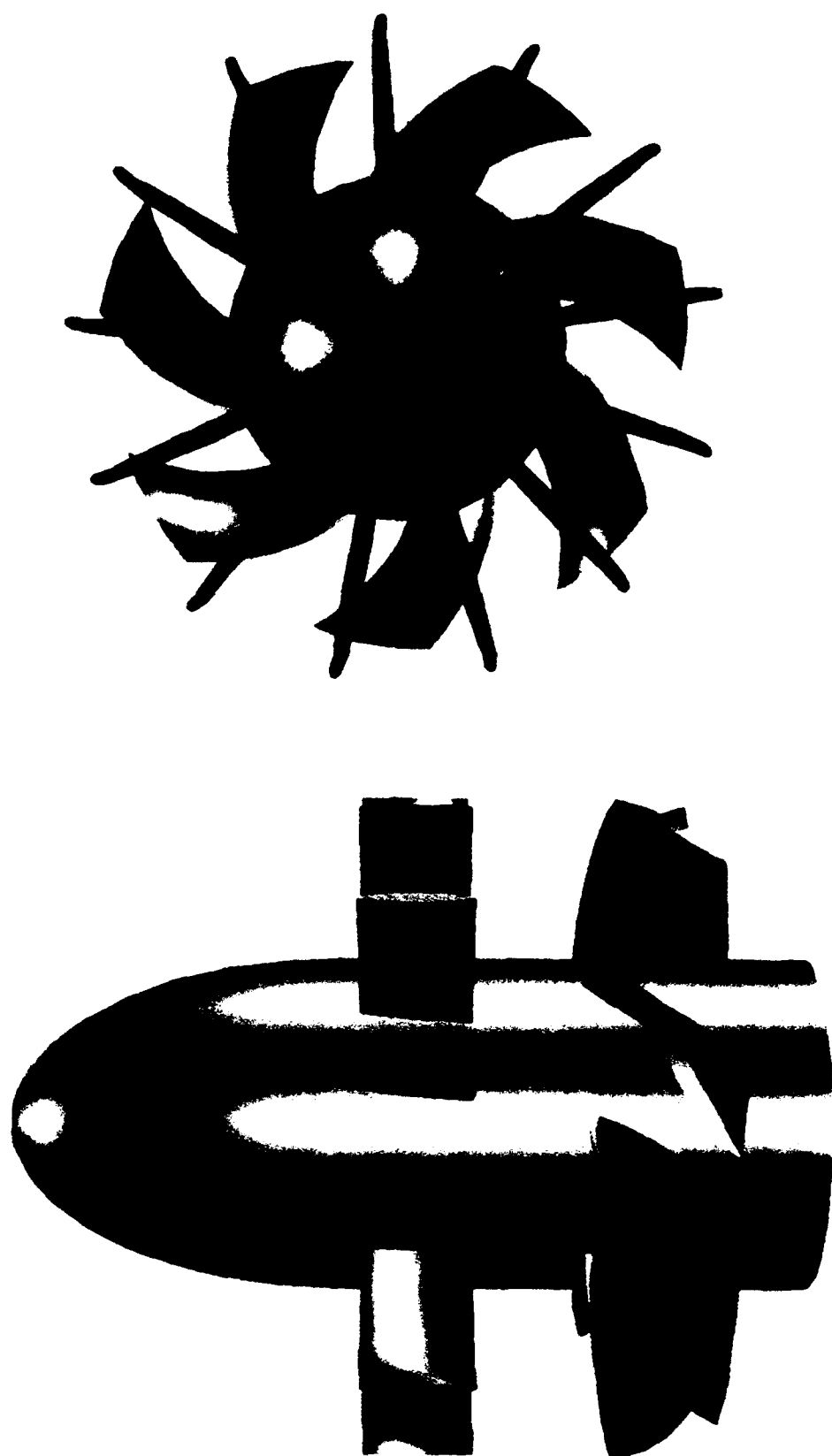


Figure 3. Computer-Generated Graphical image of the New HIREP Blades;
a) Downstream and Inboard Views

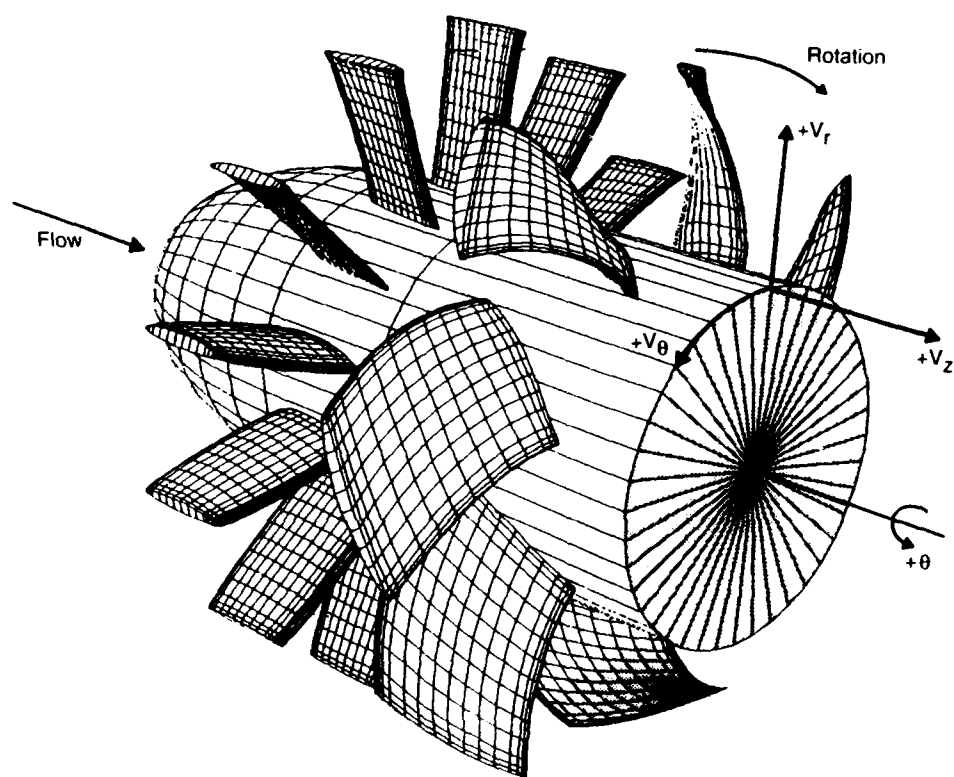


Figure 3. Computer-Generated Graphical Image of the New HIREP Blades;
b) Isometric View with Coordinate System

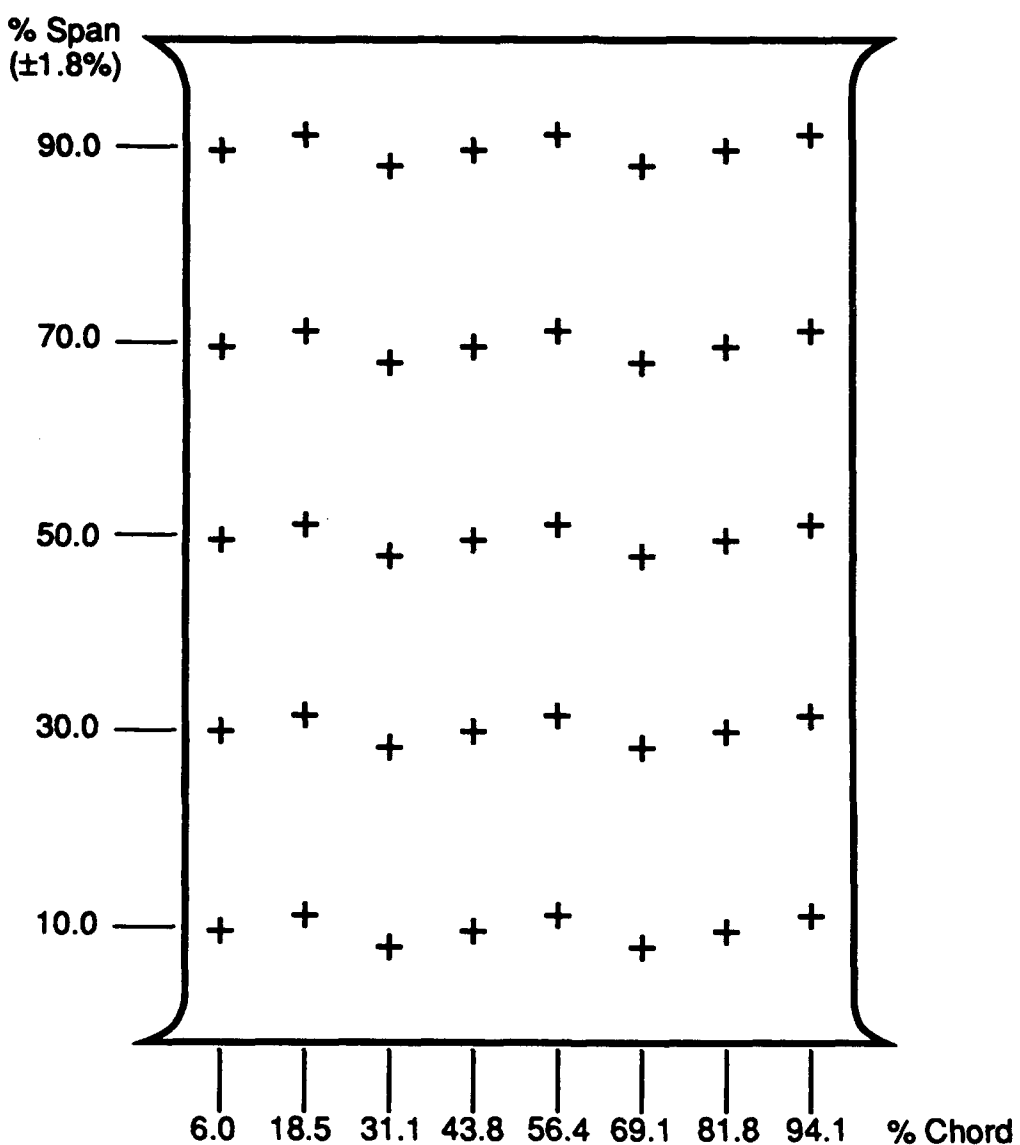


Figure 4. IGV Static-Pressure Tap Locations

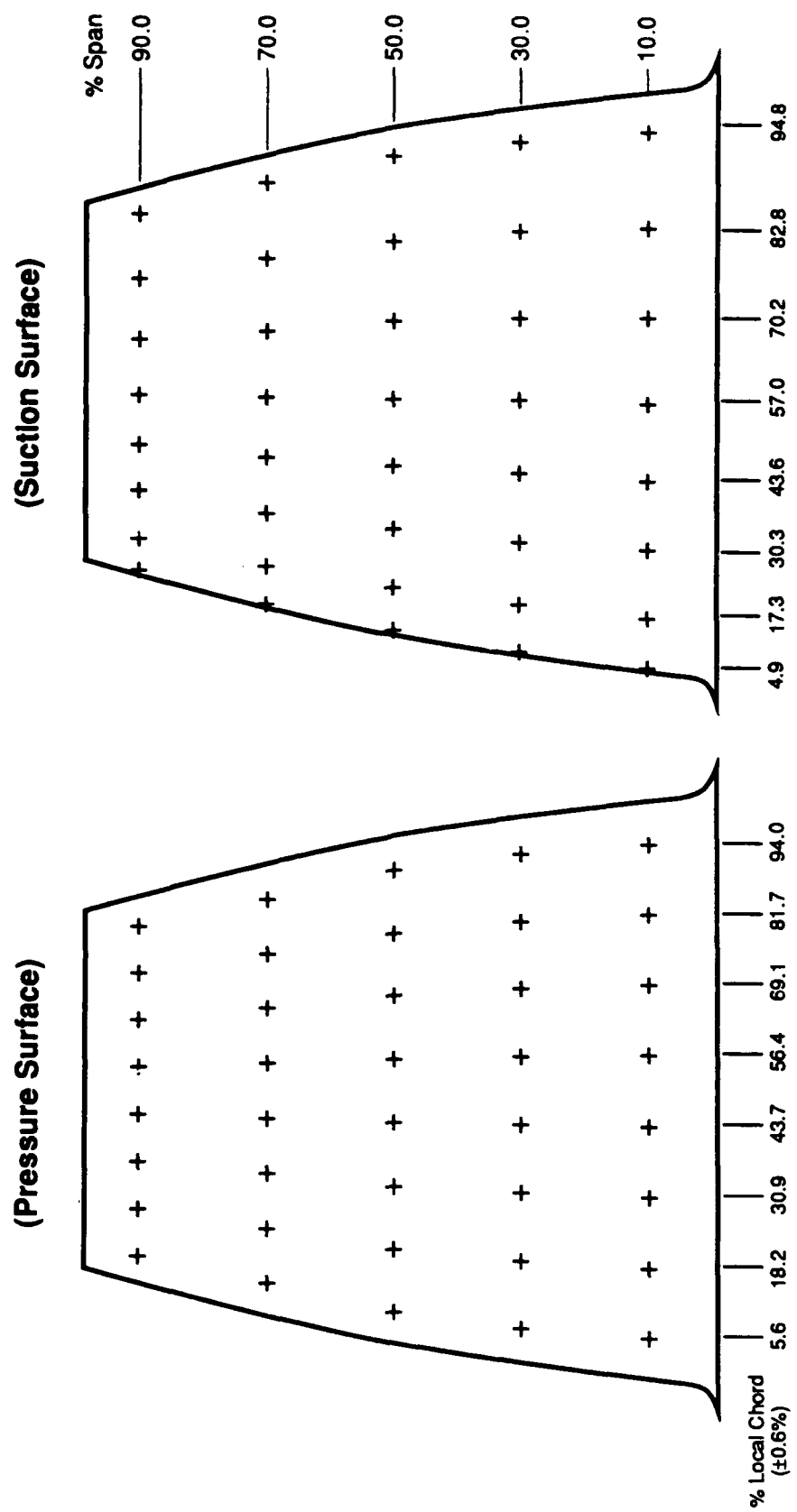


Figure 5. Rotor Blade Static-Pressure Tap Locations

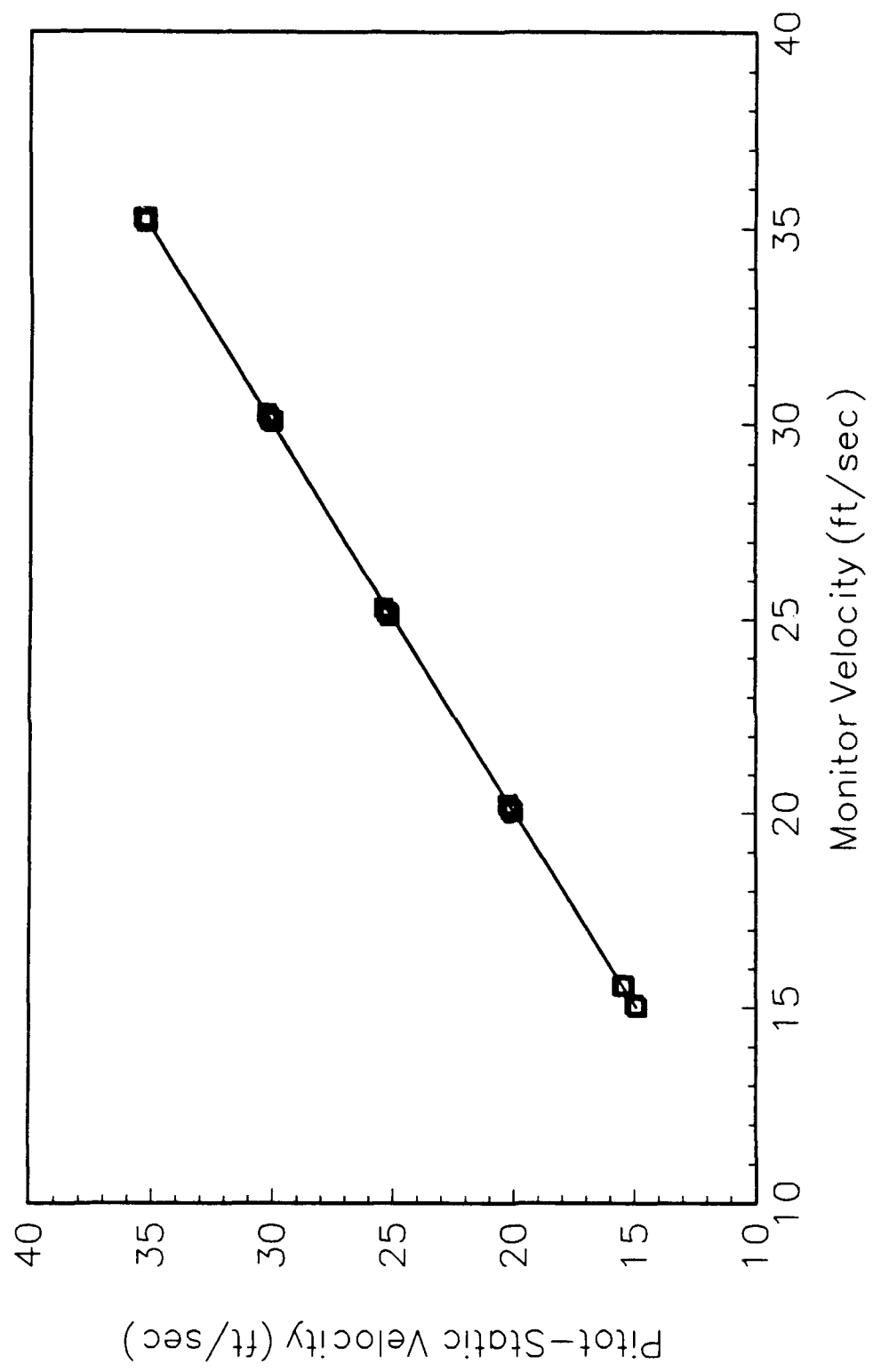


Figure 6.

Monitor Velocity Validation

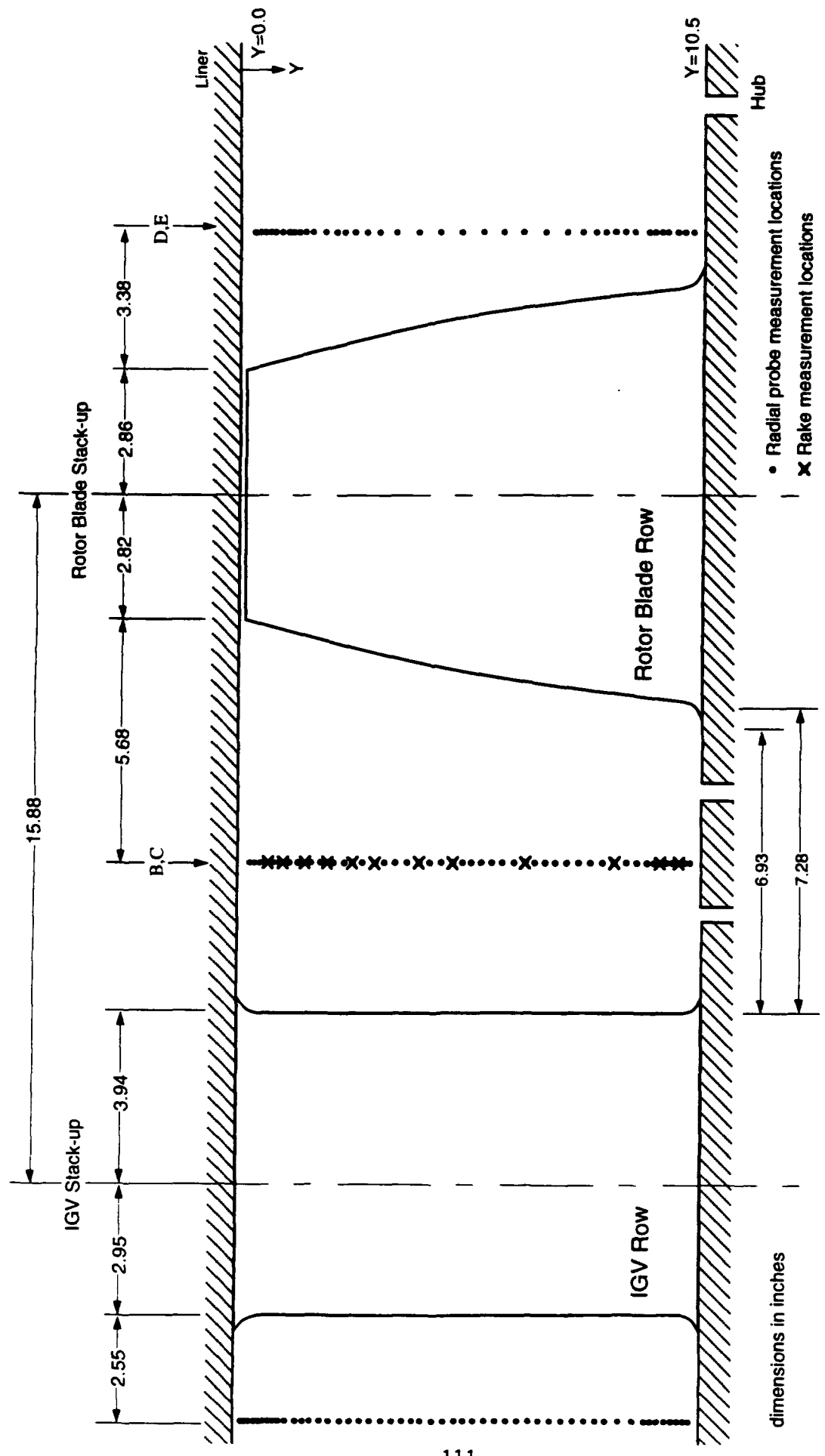


Figure 7. Pressure Probe Measurement Locations

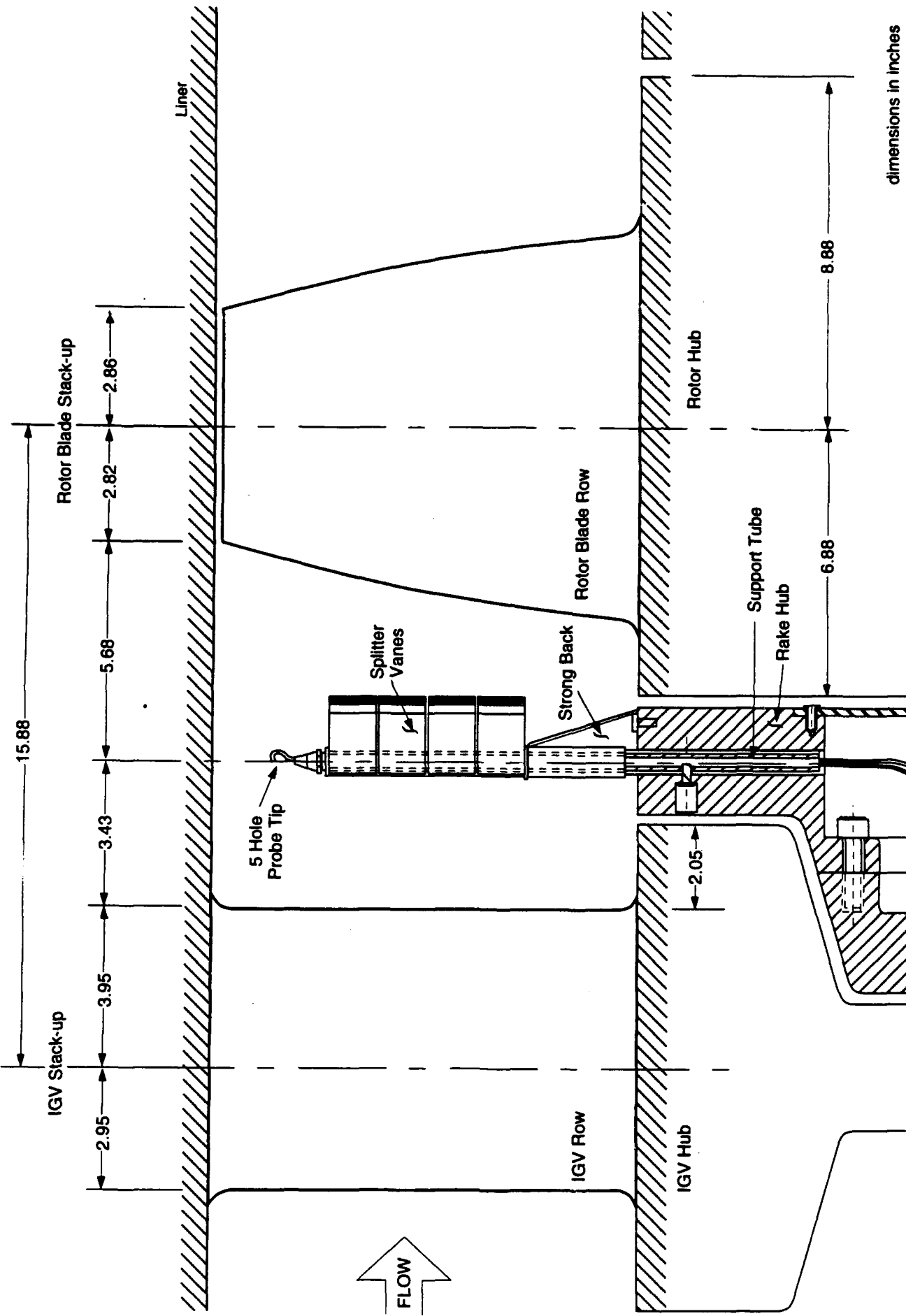


Figure 8. Sample Probe Within the Five-Hole Probe Rake

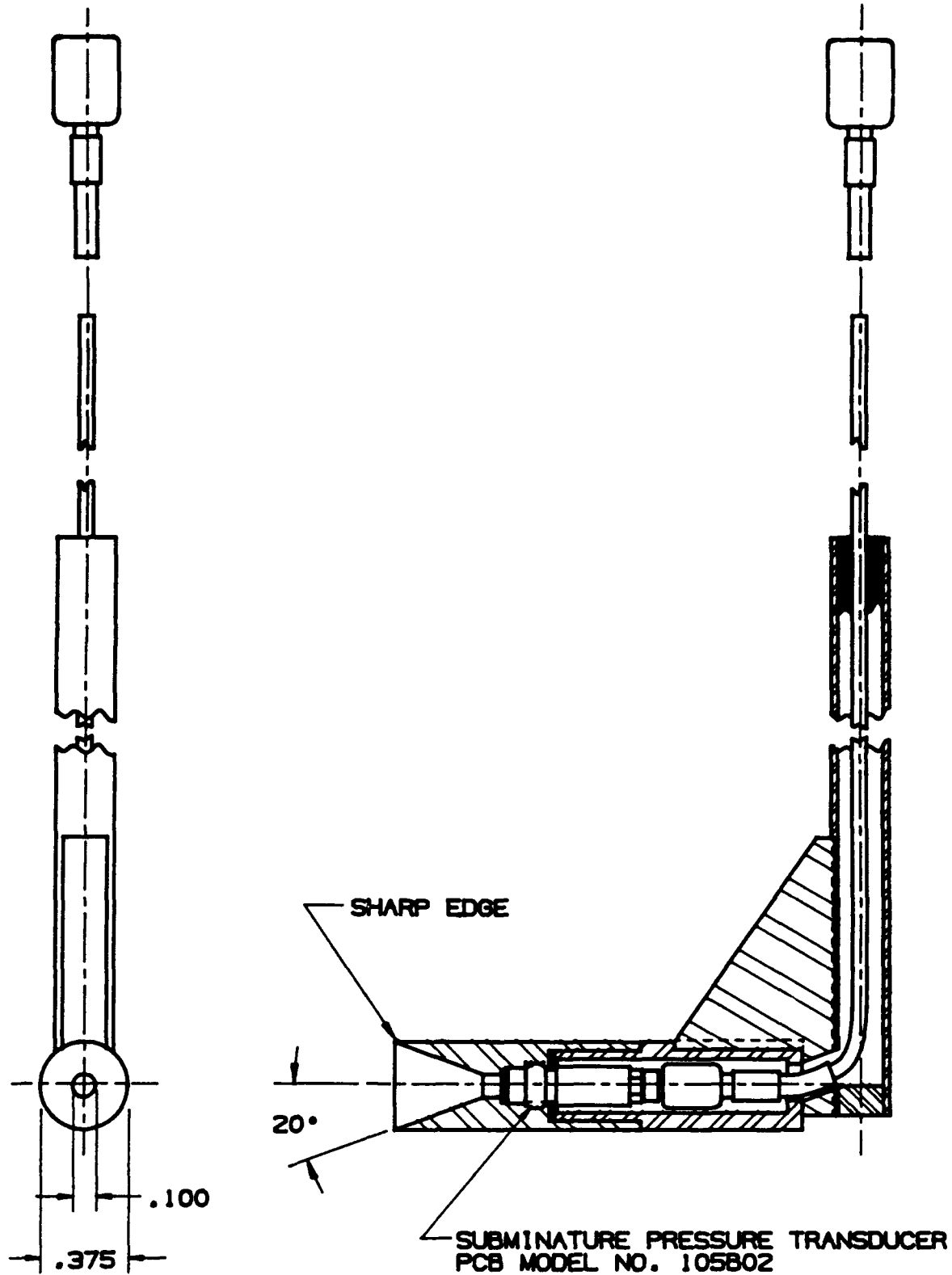


Figure 9. Schematic of Fast-Response Total-Pressure Probe

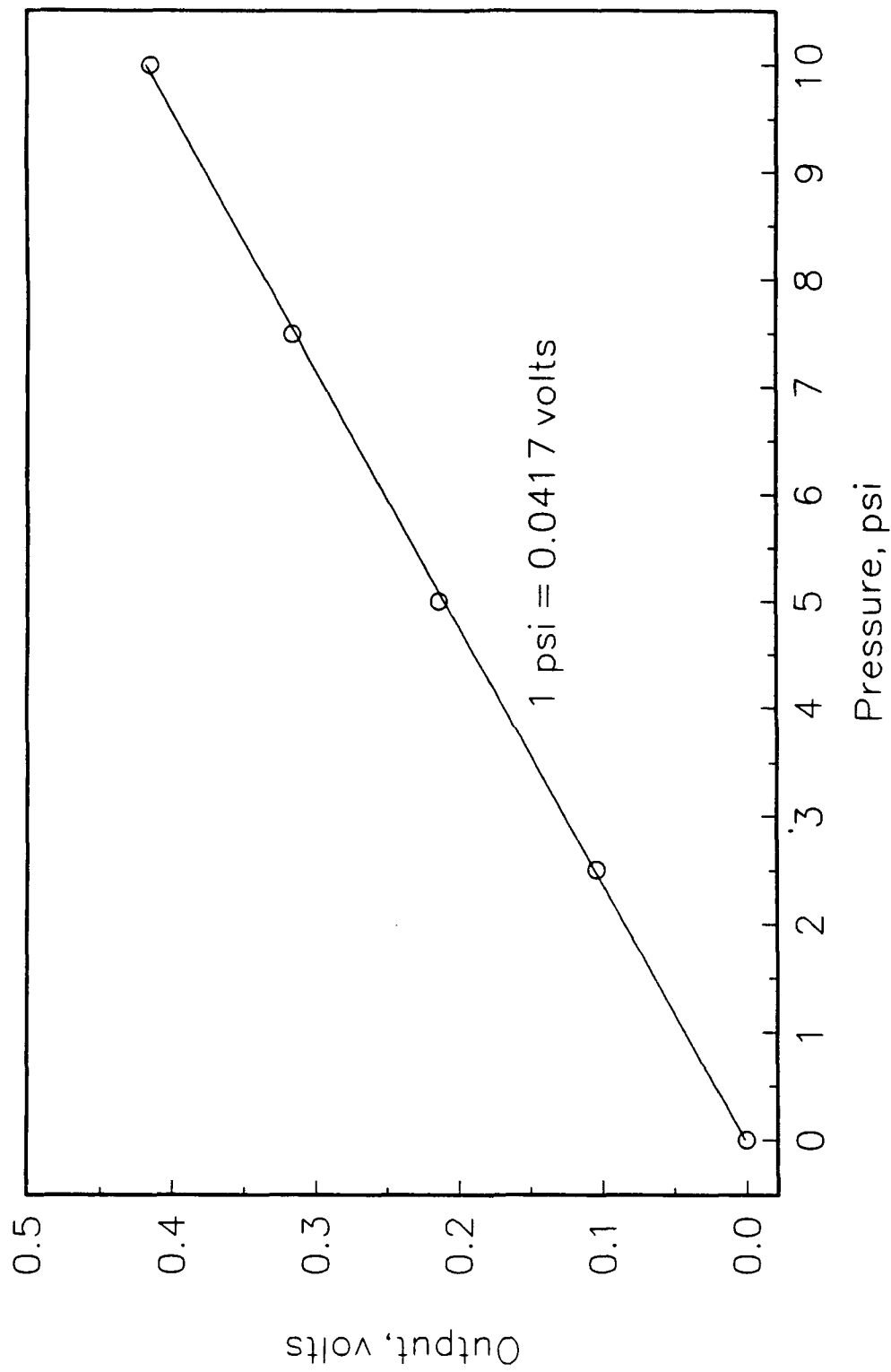


Figure 10. Sensitivity Calibration Curve for the Fast-Response Total-Pressure Probe

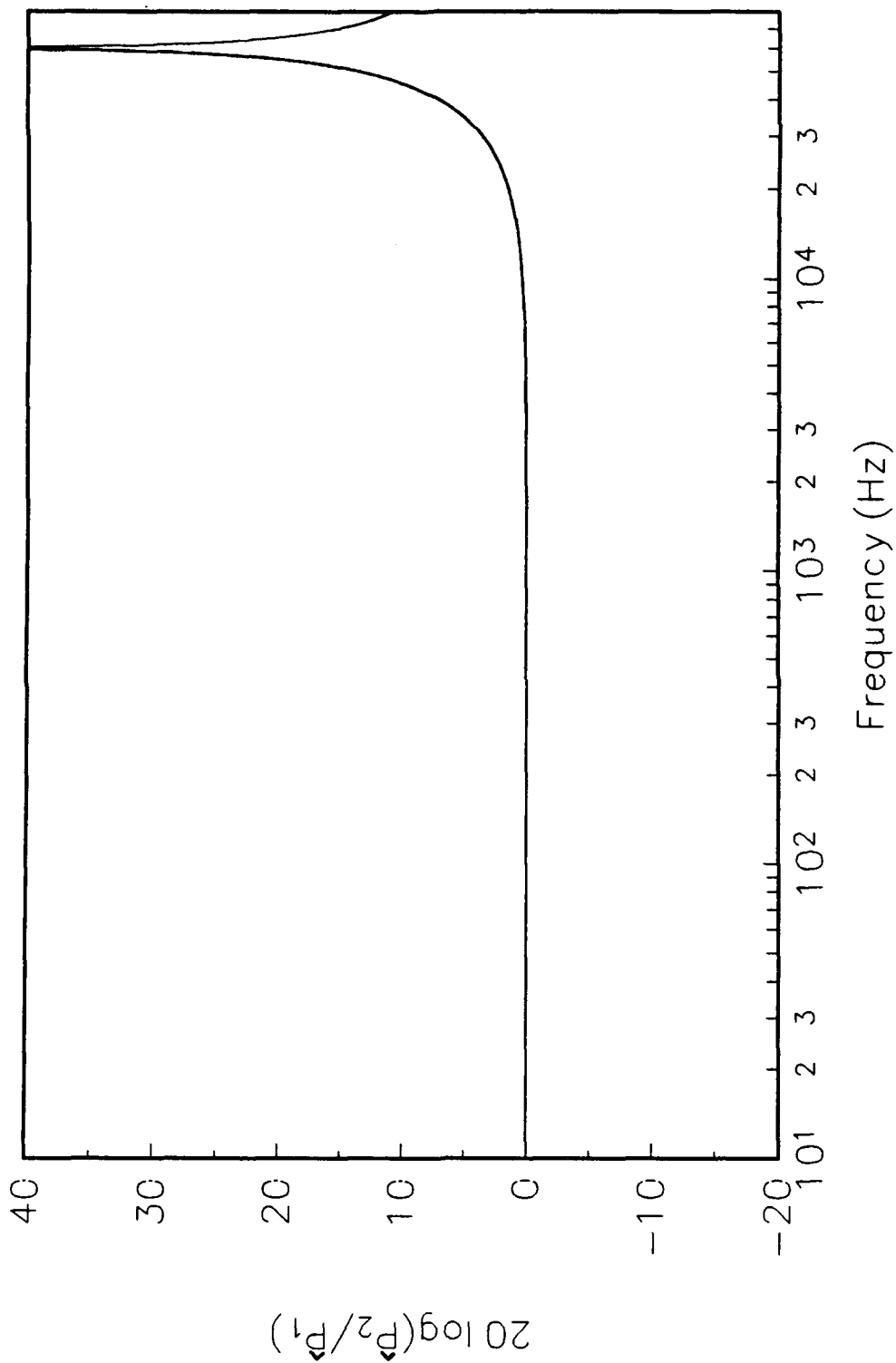


Figure 11. Estimated Amplitude Frequency Response of the Fast-Response Total-Pressure Probe

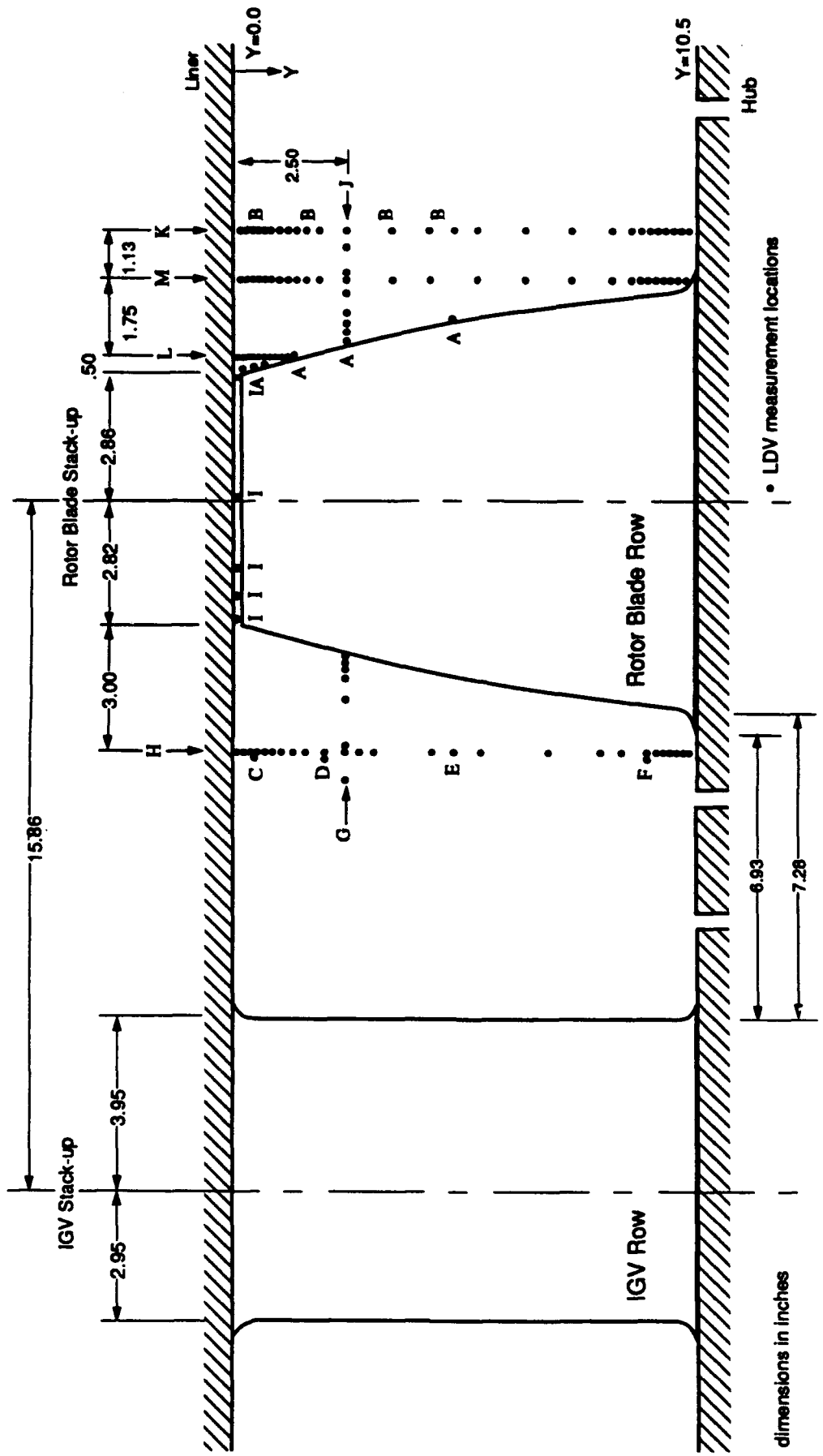


Figure 12. LDV Measurement Locations

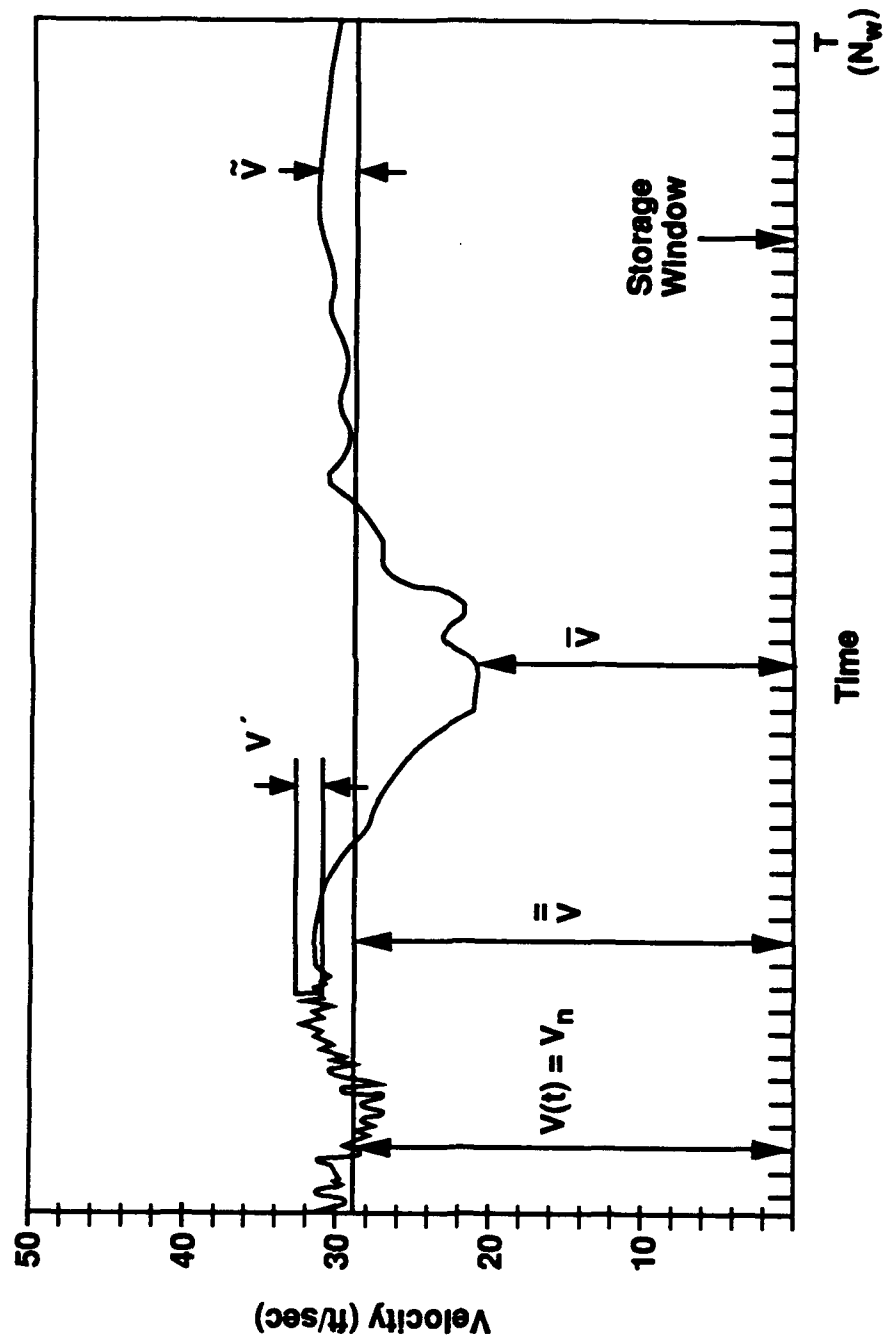


Figure 13. Unsteady Velocity Signal

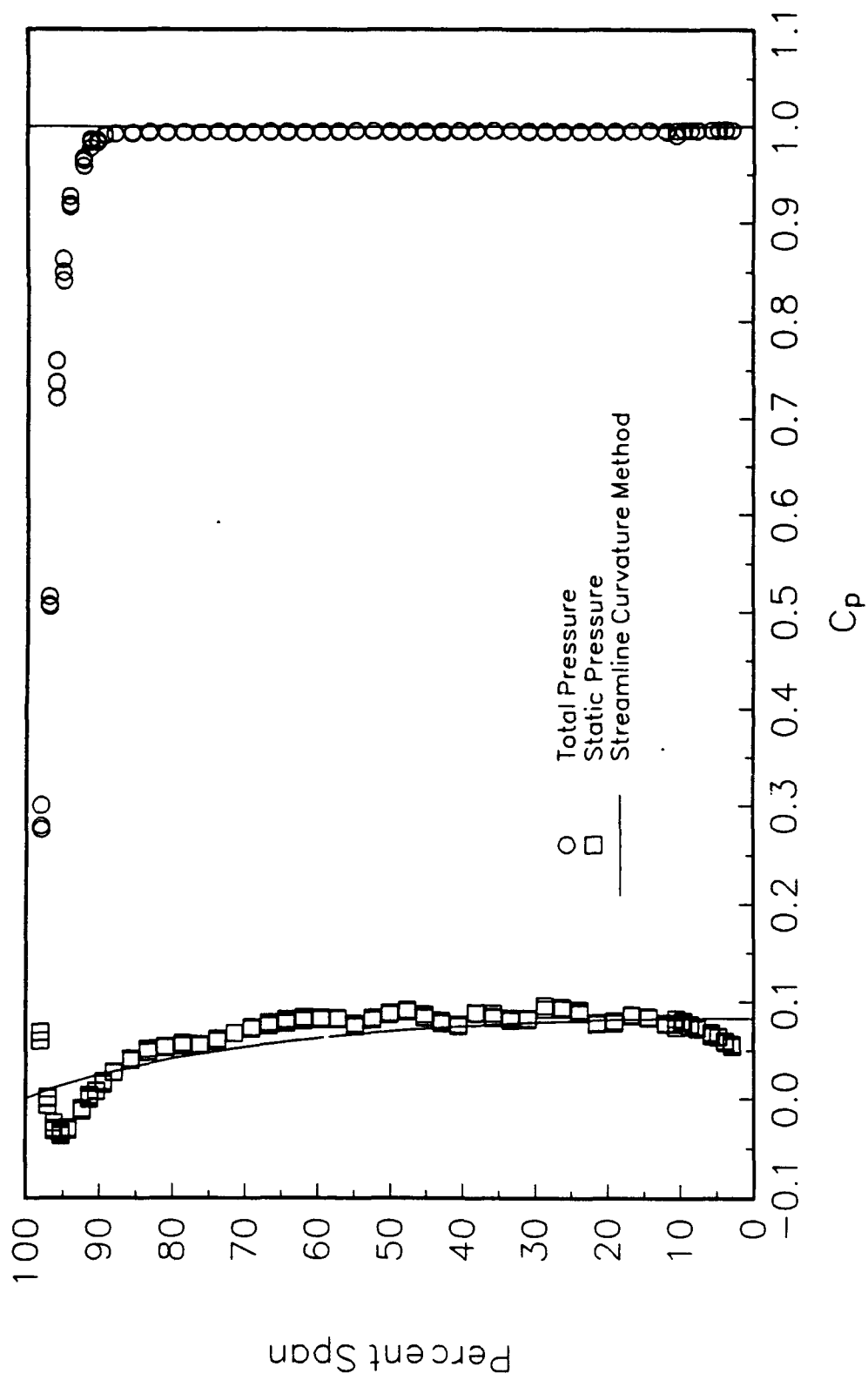


Figure 14. Inlet Pressure Coefficients from the Five-Hole Probe Radial Survey (37.0%) Chord Upstream of the IGV Leading Edge)

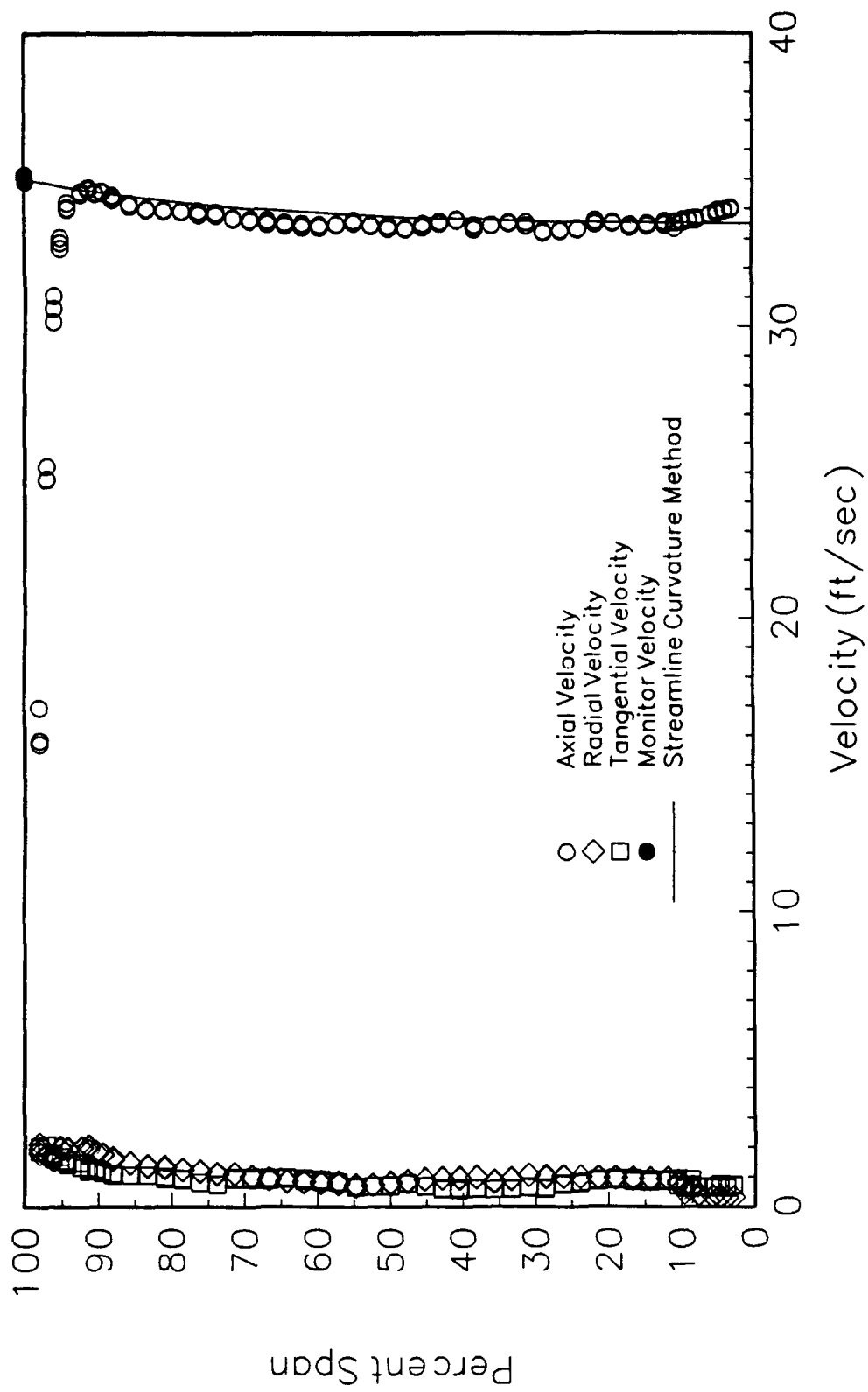


Figure 15. Inlet Velocities from the Five-Hole Probe Radial Survey (37.0% Chord Upstream of the IGV Leading Edge)

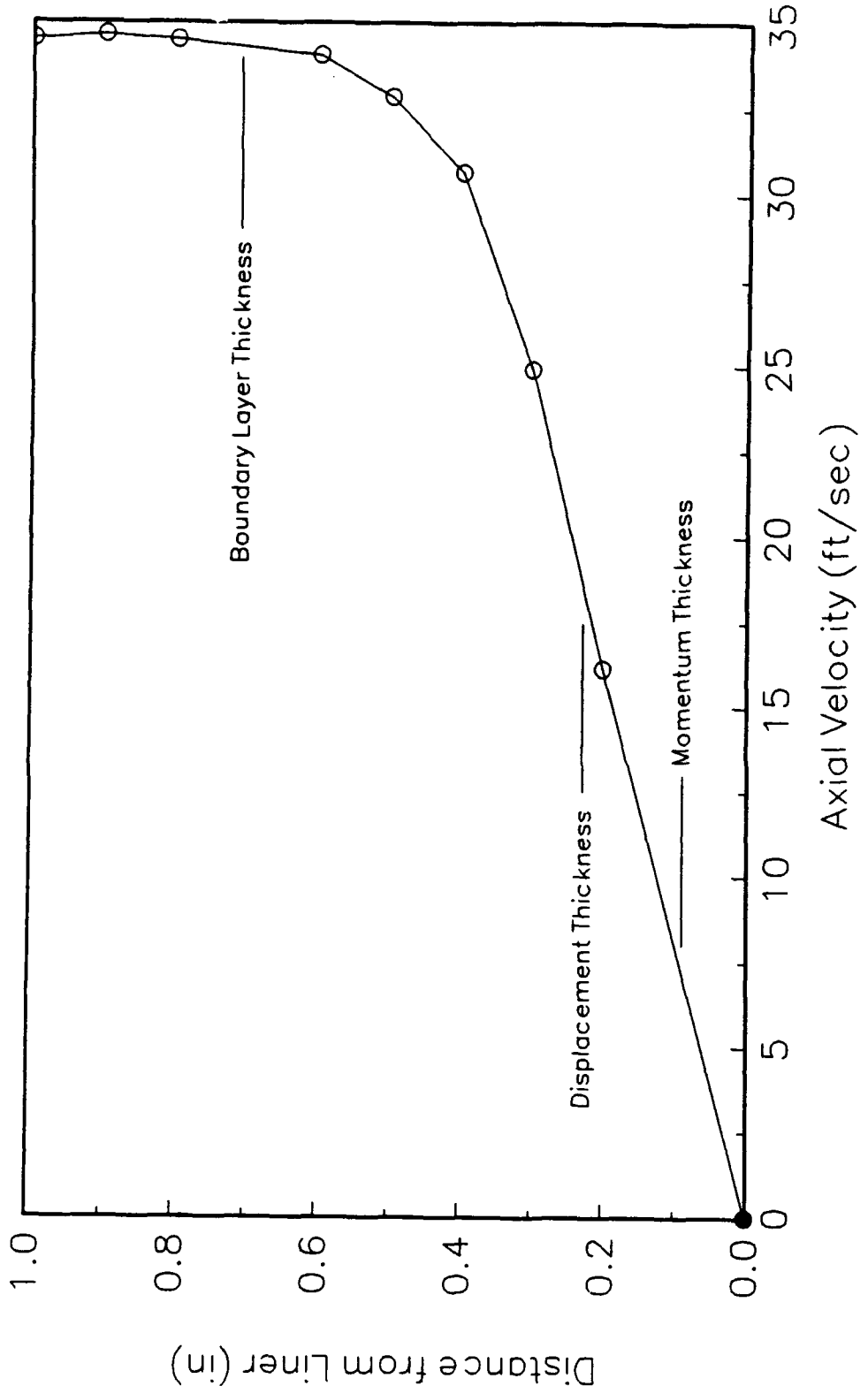


Figure 16. Inlet Boundary Layer on the Tunnel Liner Measured with a Five-Hole Probe

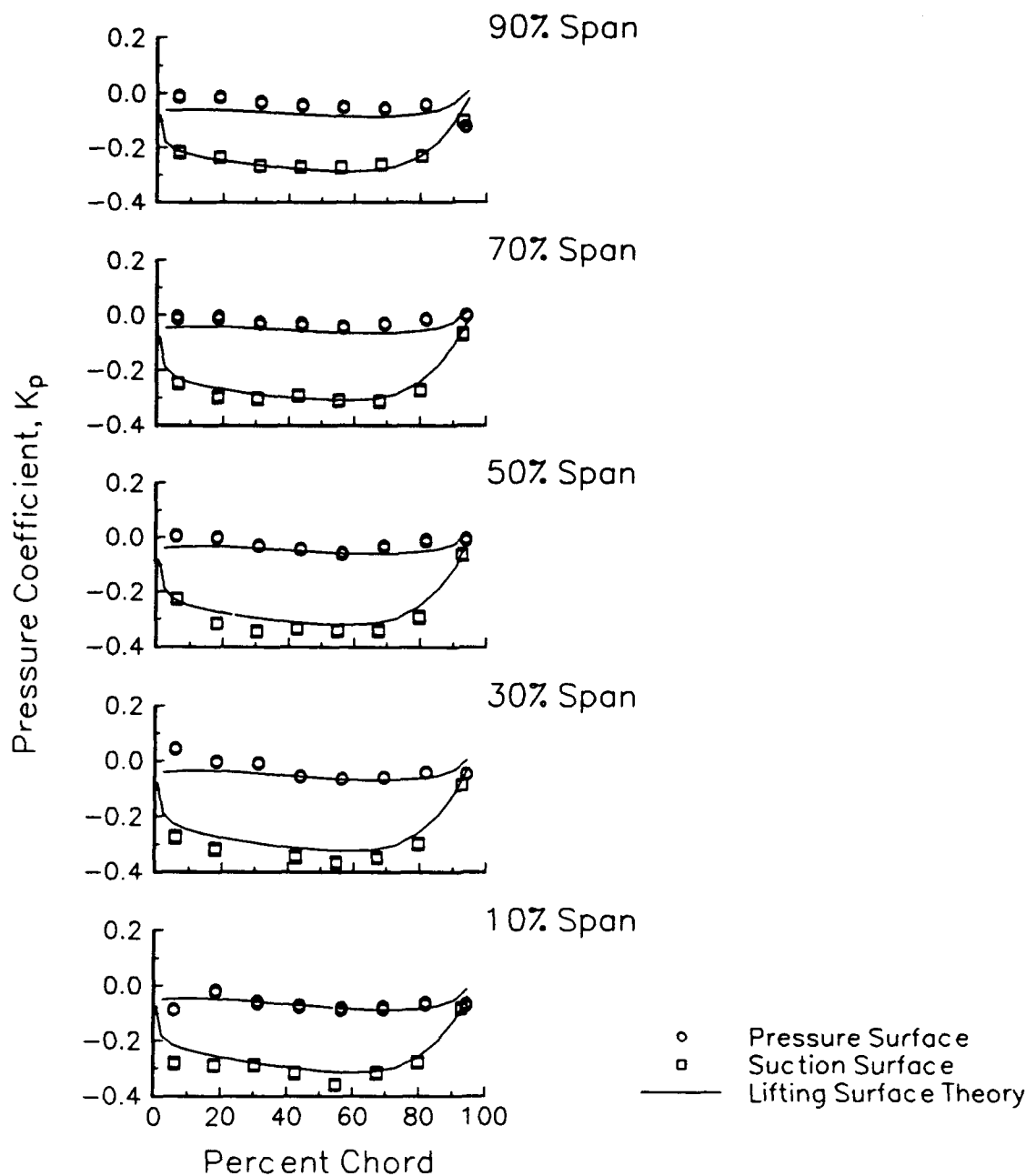


Figure 17. IGV Static-Pressure Distribution

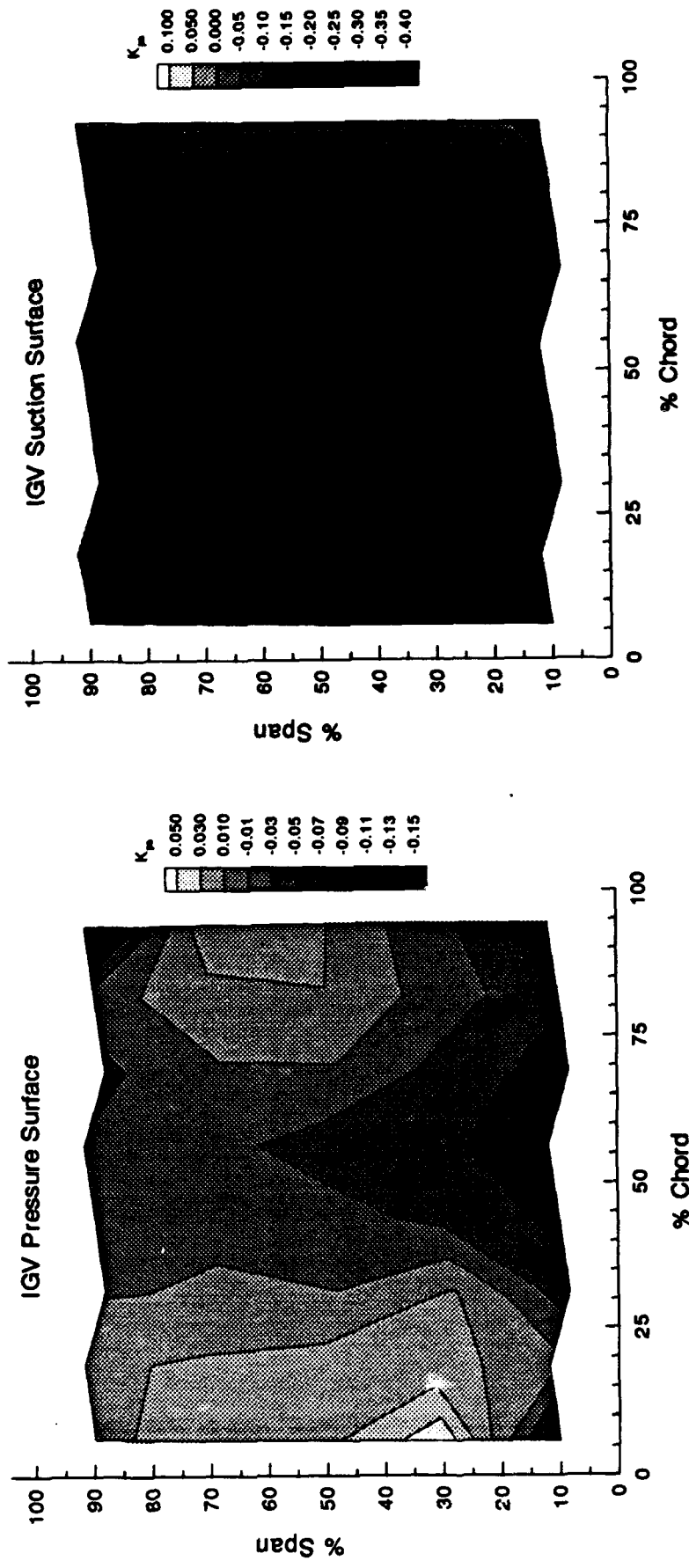


Figure 18. IGV Static-Pressure Contours

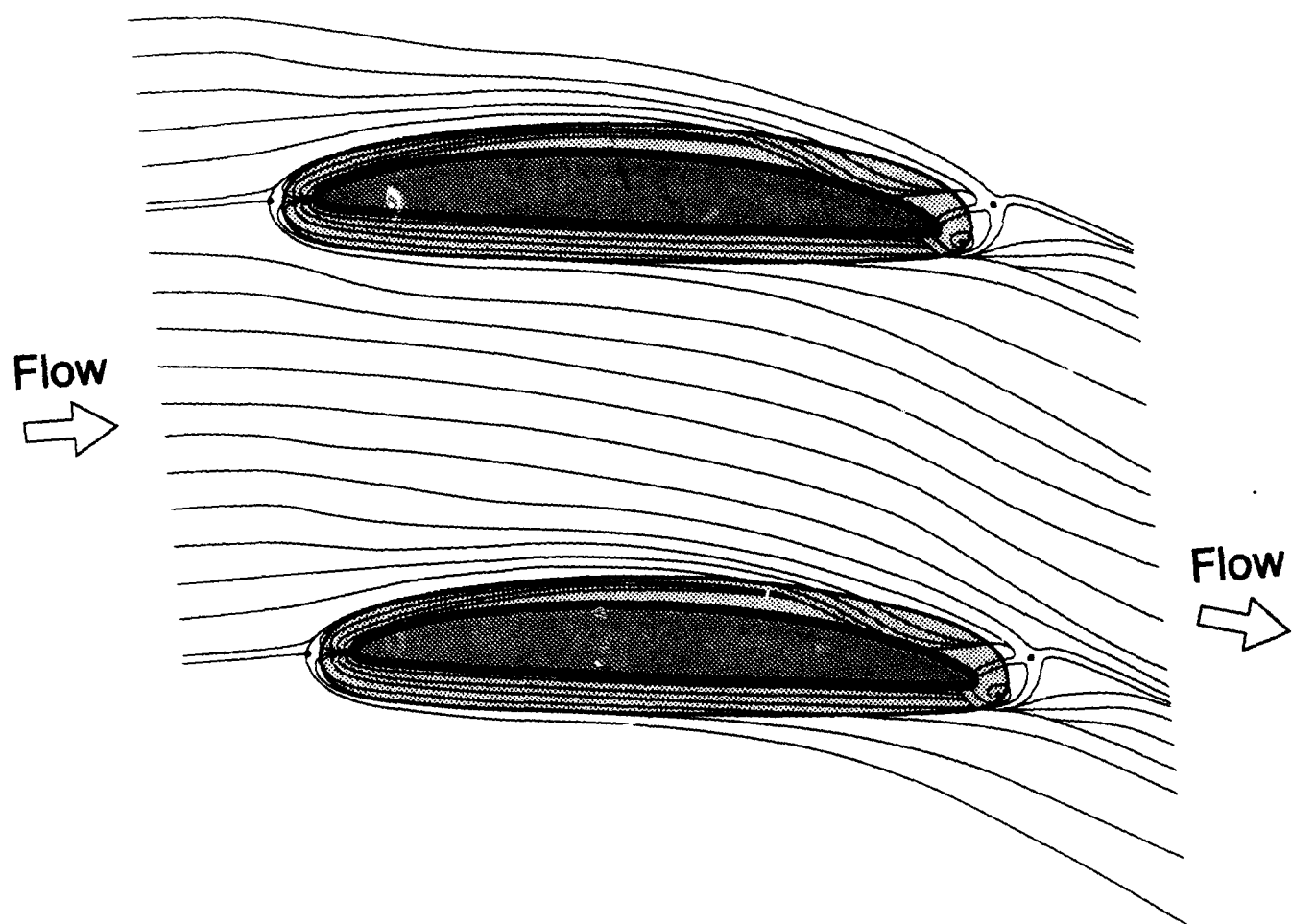
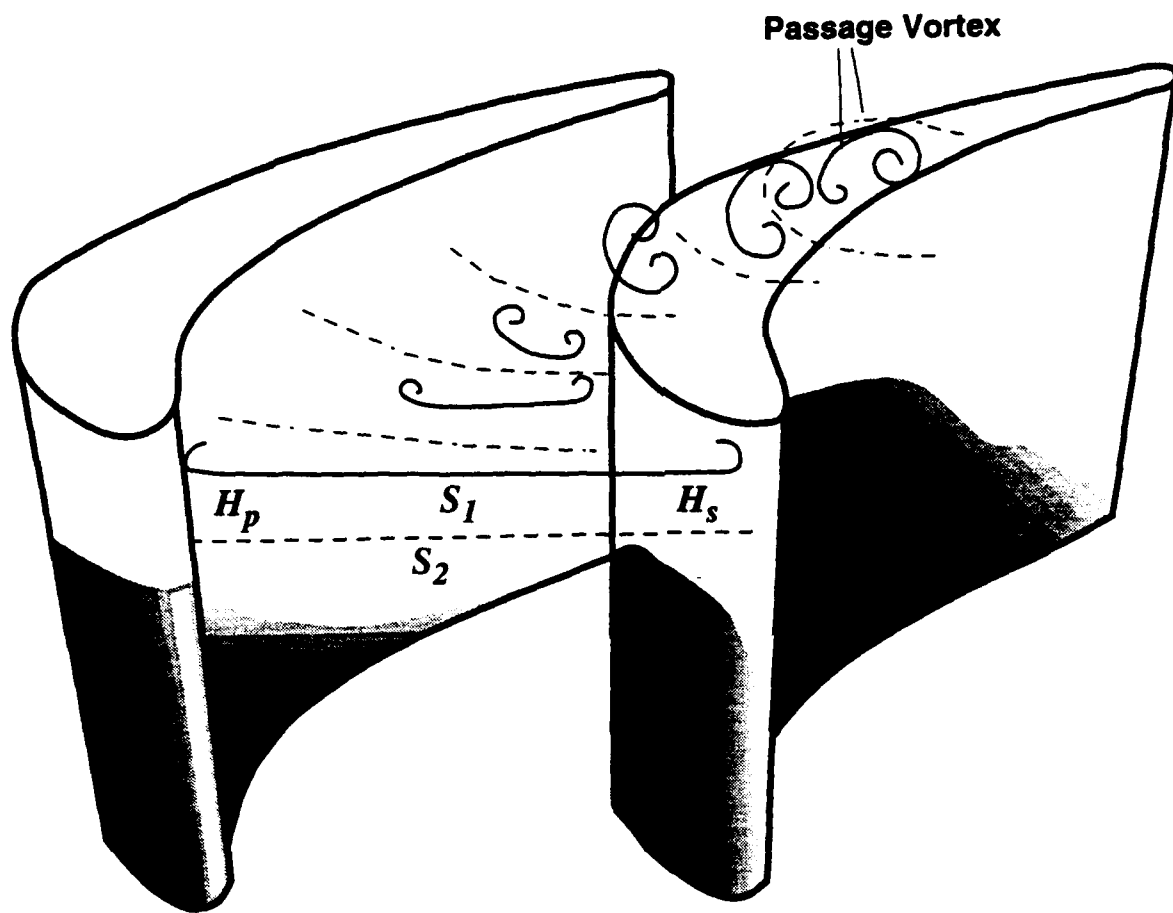


Figure 19. Schematic of Surface Flow Visualization on the IGV Hub Surface



S_1 – Streamsurface 1

S_2 – Streamsurface 2

H_p – Pressure Side Leg of the Horseshoe Vortex

H_s – Suction Side Leg of the Horseshoe Vortex

Figure 20. Evolution of Horseshoe and Passage Vortices
(Sieverding and Van den Bosche [1983])

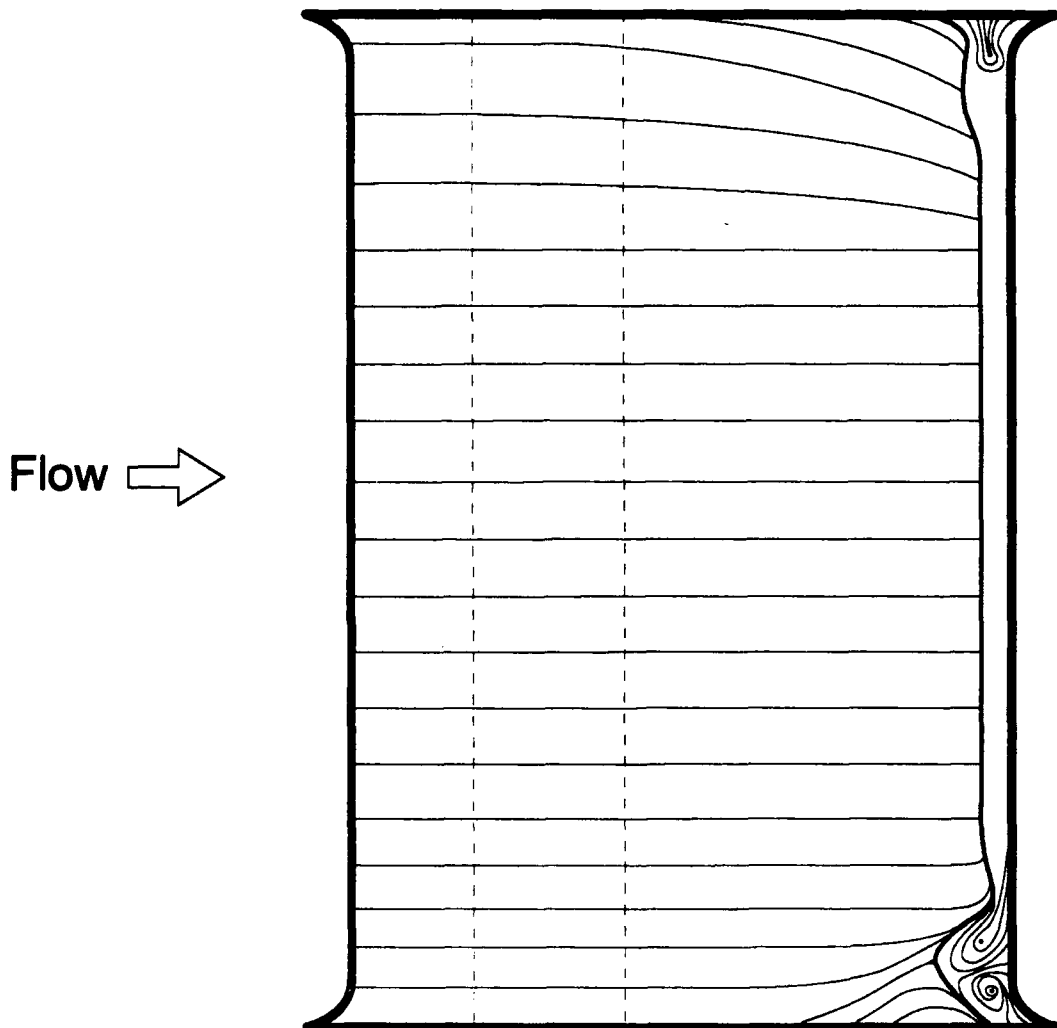


Figure 21. Schematic of Surface Flow Visualization on the IGV Suction Surface

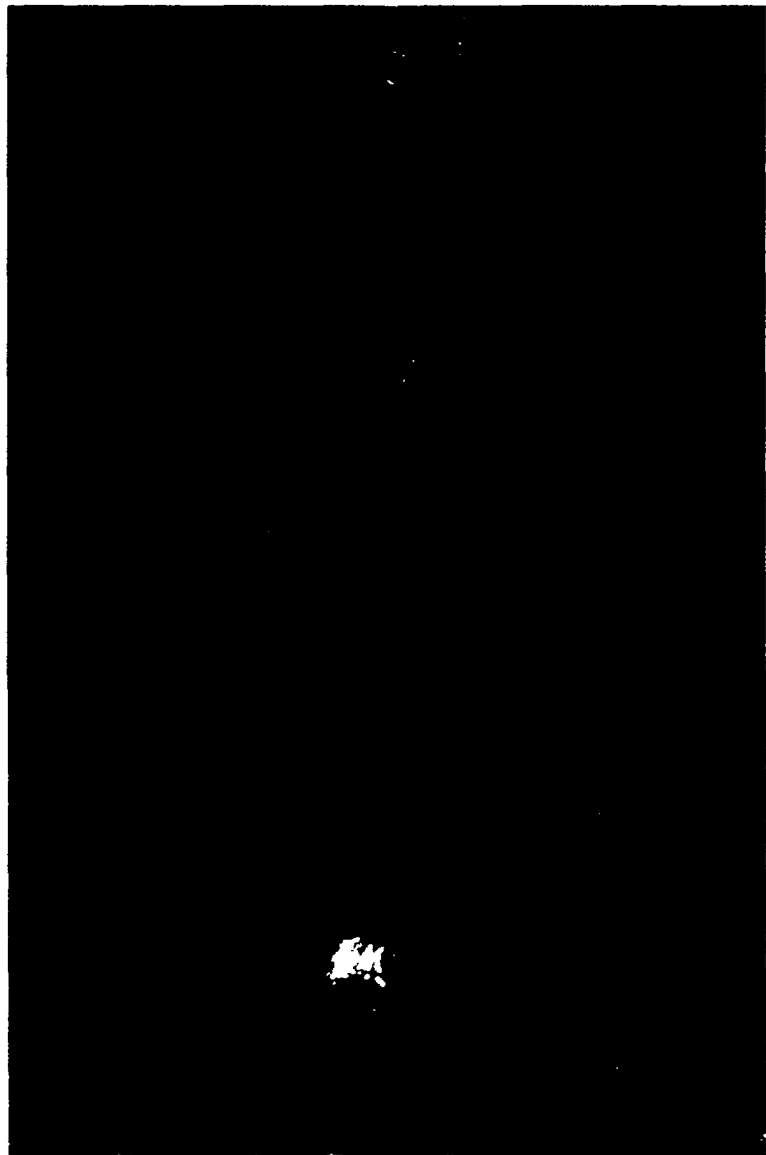


Figure 22. Photograph of the Surface Flow Visualization Showing the IGV Suction Surface Corner Separation

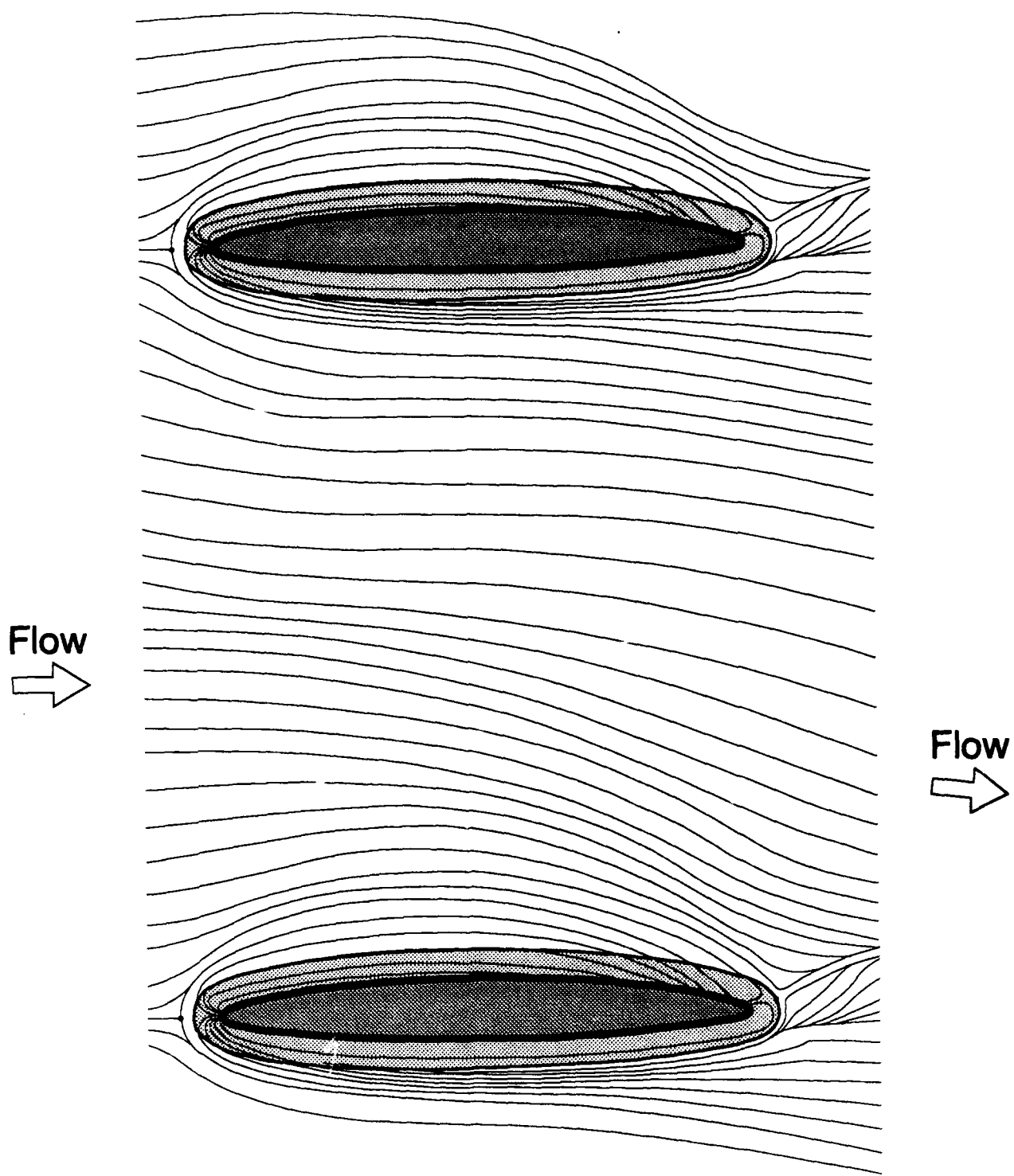


Figure 23. Schematic of Surface Flow Visualization on the IGV Casing Surface

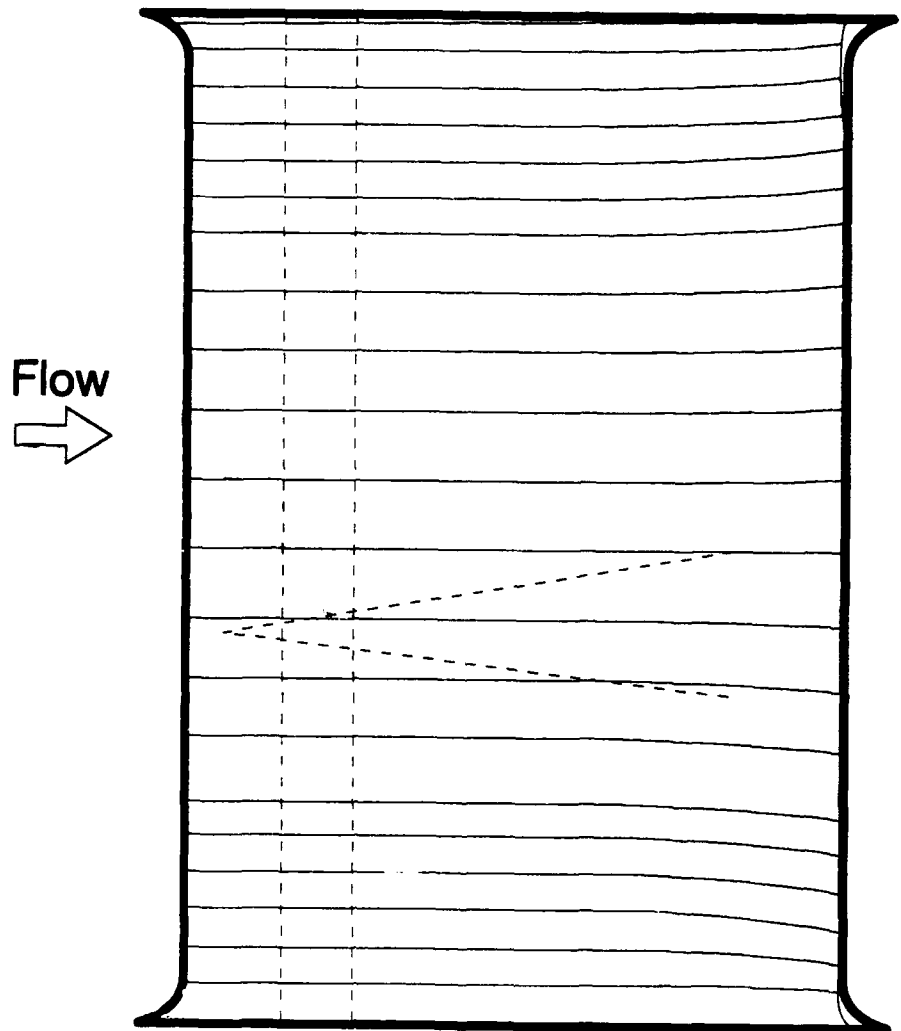


Figure 24. Schematic of Surface Flow Visualization on the IGV Pressure Surface

Flow
→

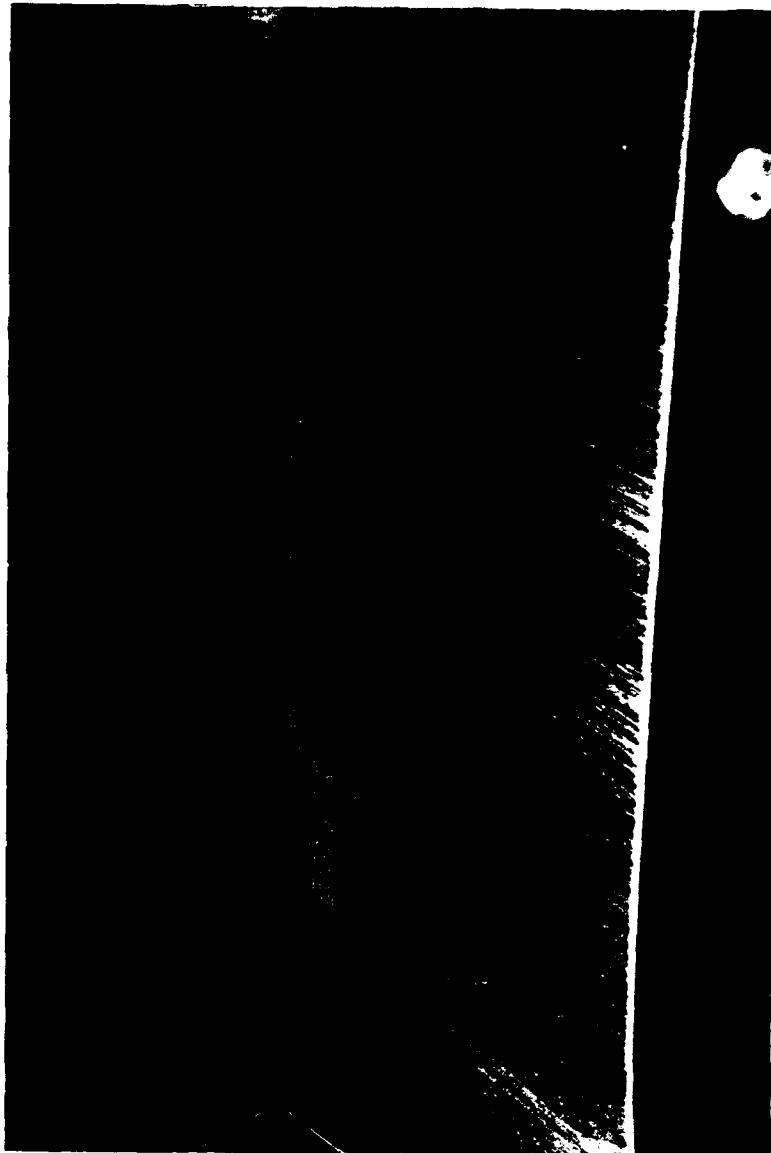


Figure 25. Photograph of the Surface Flow Visualization Showing the IGV Pressure Surface

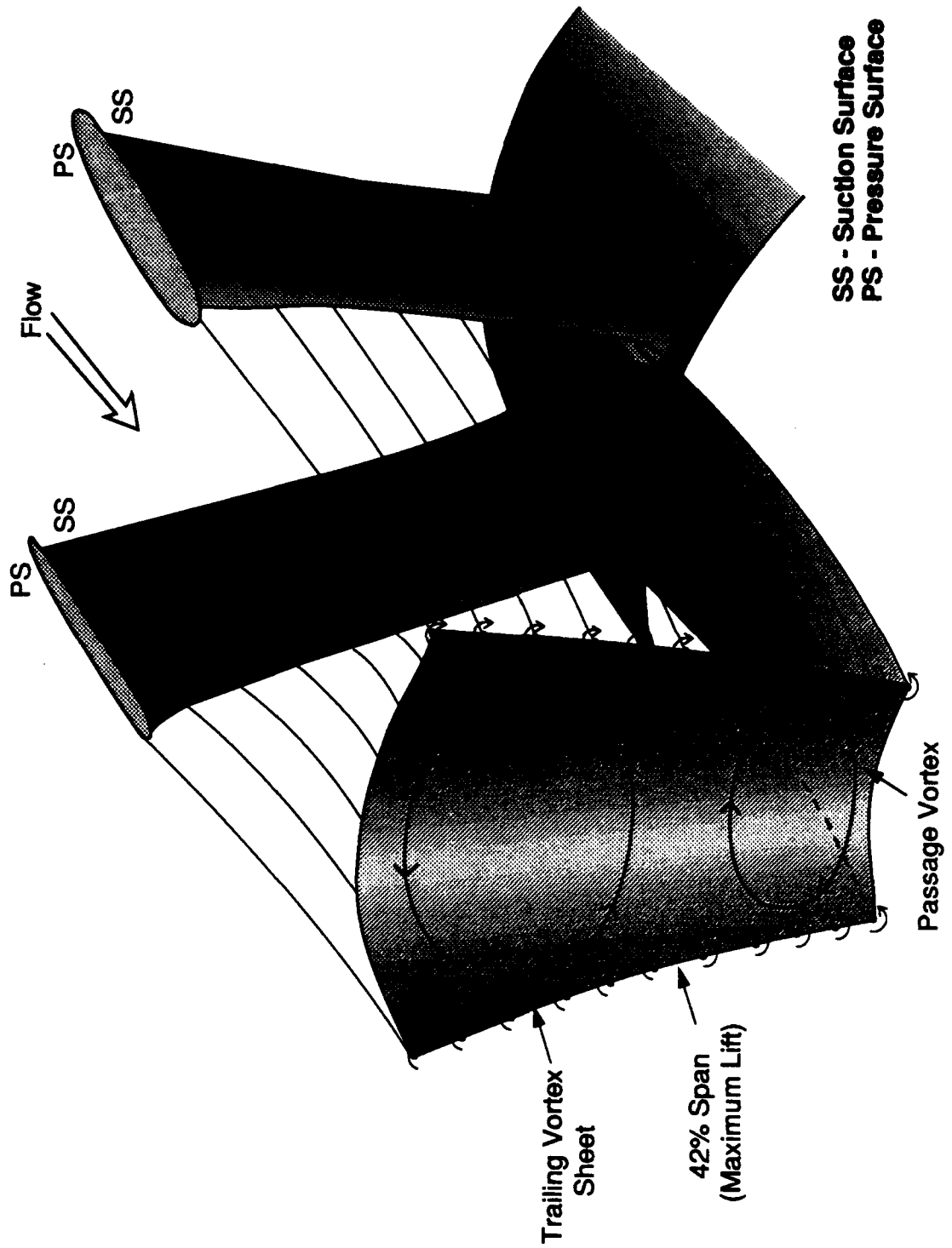


Figure 26. Schematic of IGV Secondary Flow: Passage Vortices and Trailing Vortex Sheets

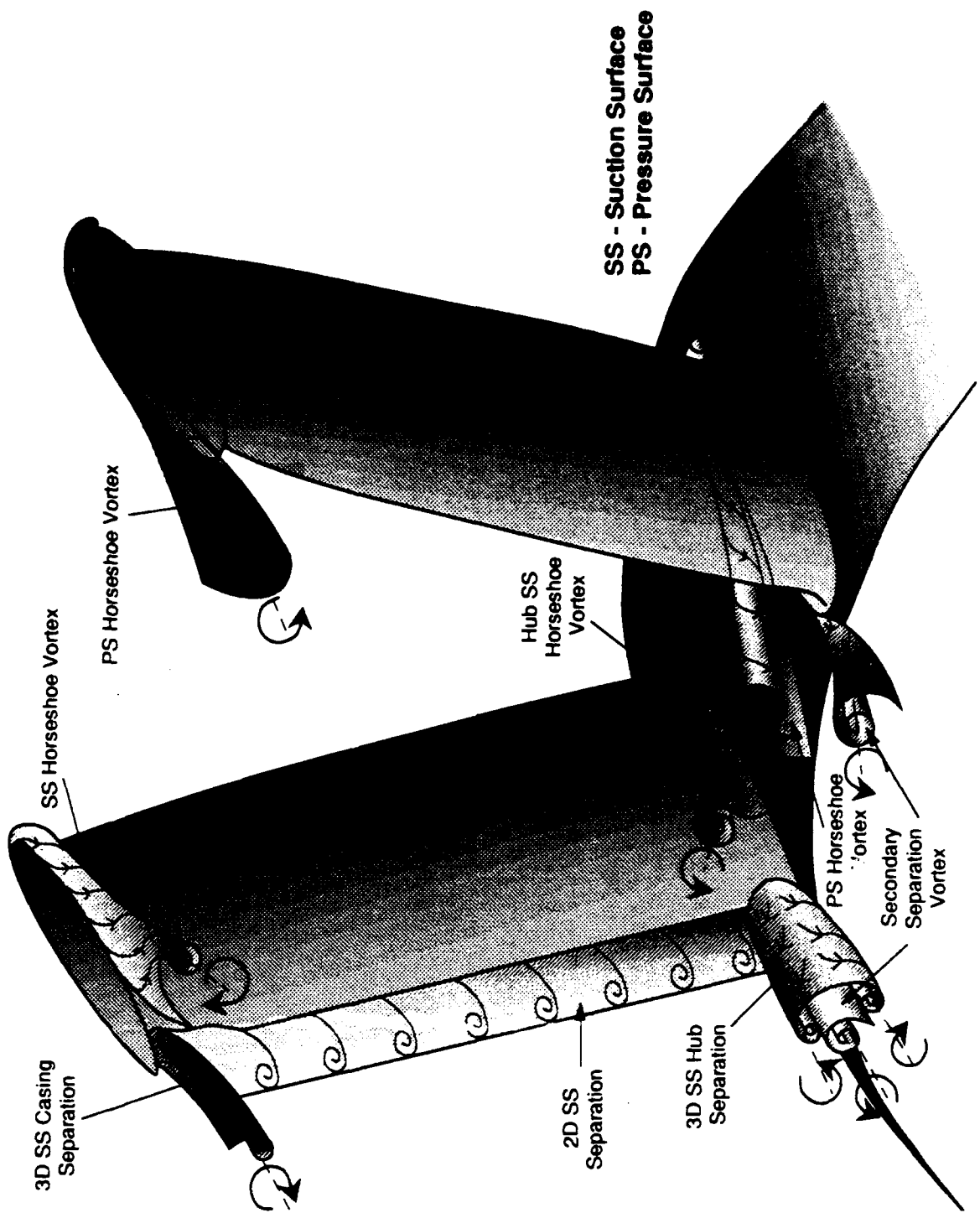


Figure 27. Schematic of IGV Secondary Flow: Interpretation of Surface Flow Visualization

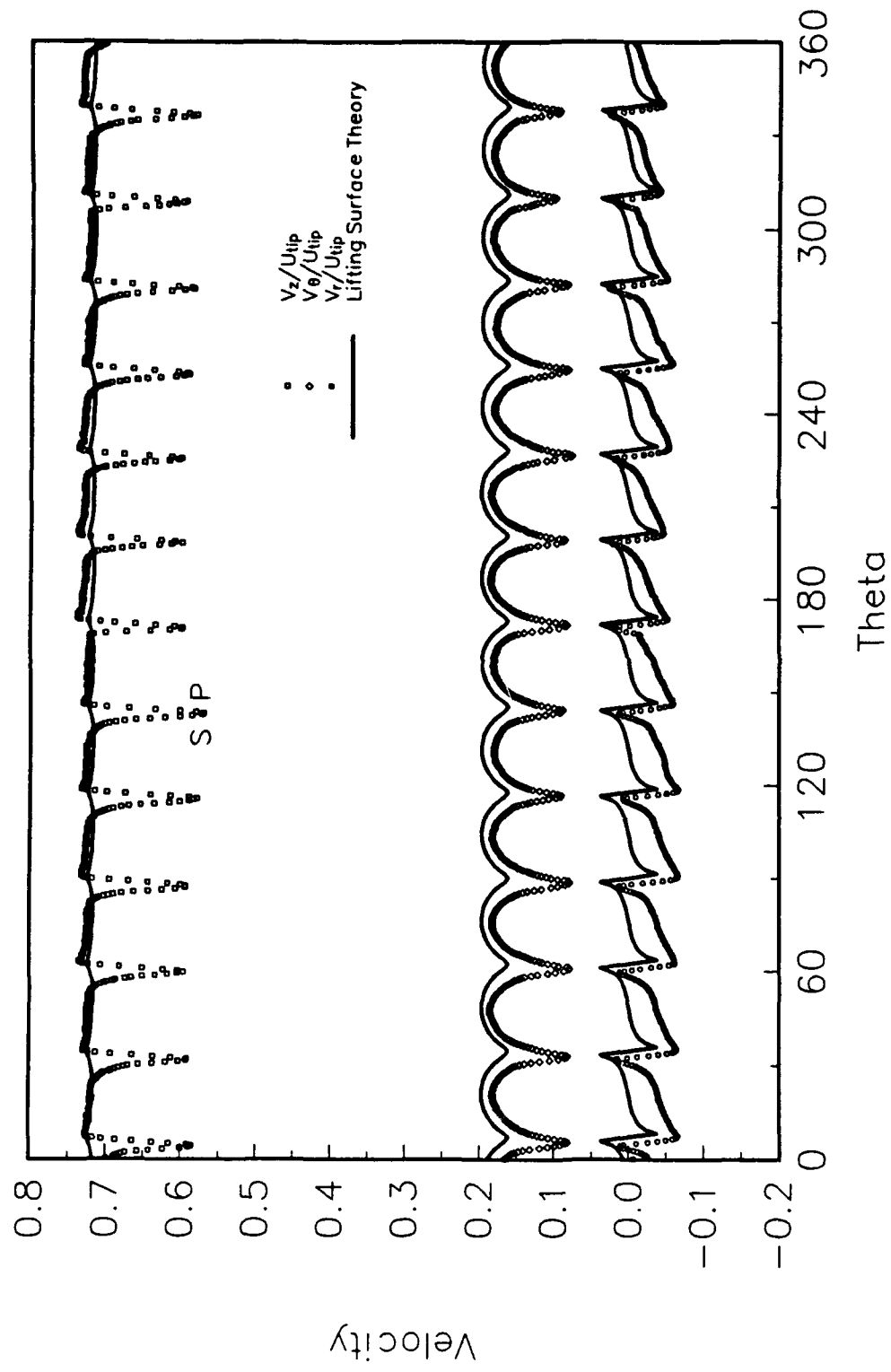


Figure 28. Circumferential Variation of Velocity Components 49.7% Chord Axially Downstream of the IGV Trailing Edge:
Five-Hole Probe Measurements and Lifting Surface Calculations; a) 4.8% Span

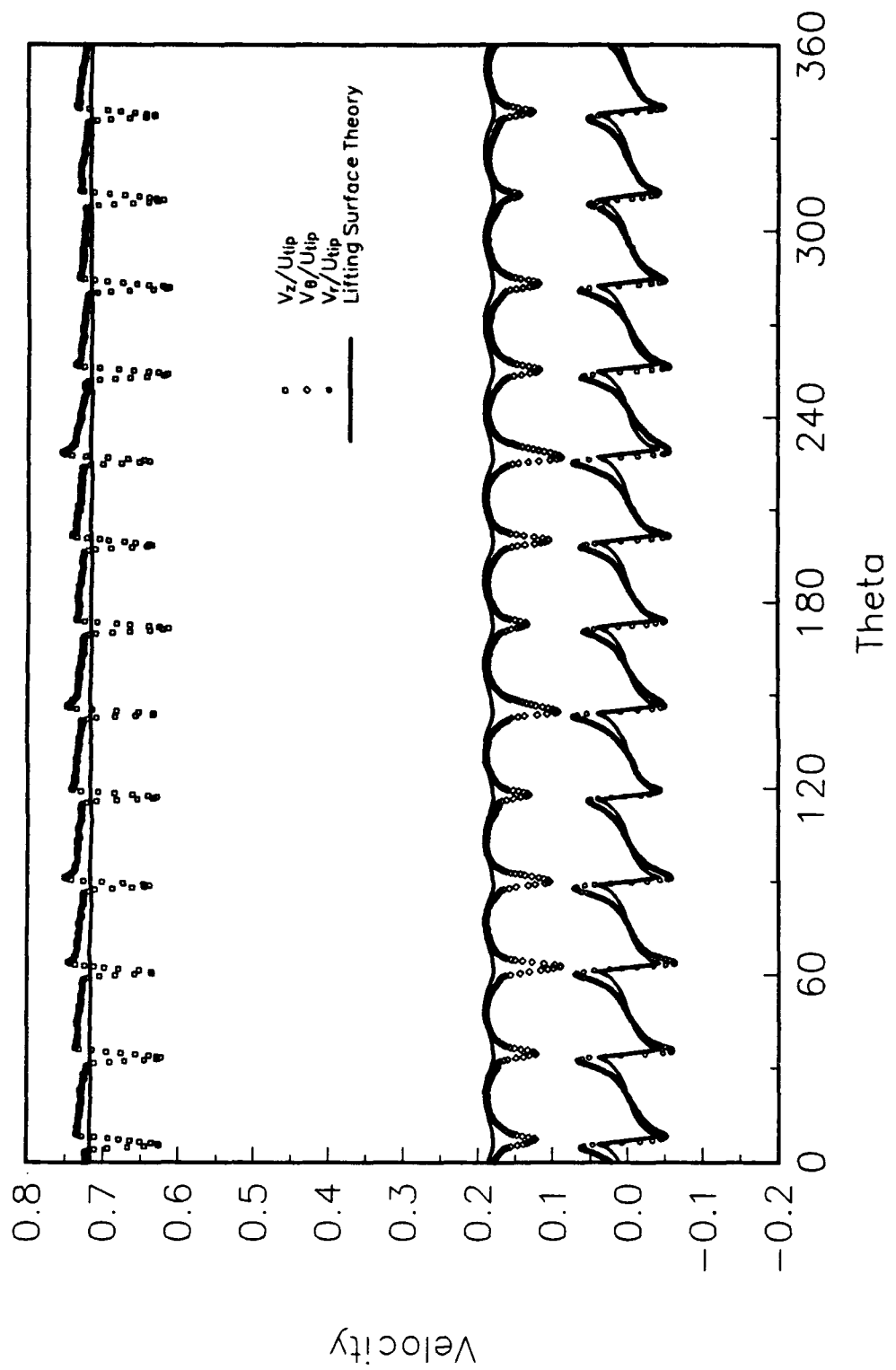


Figure 28. Circumferential Variation of Velocity Components 49.7% Chord Axially Downstream of the IGV Trailing Edge:
Five-Hole Probe Measurements and Lifting Surface Calculations; b) 9.5% Span

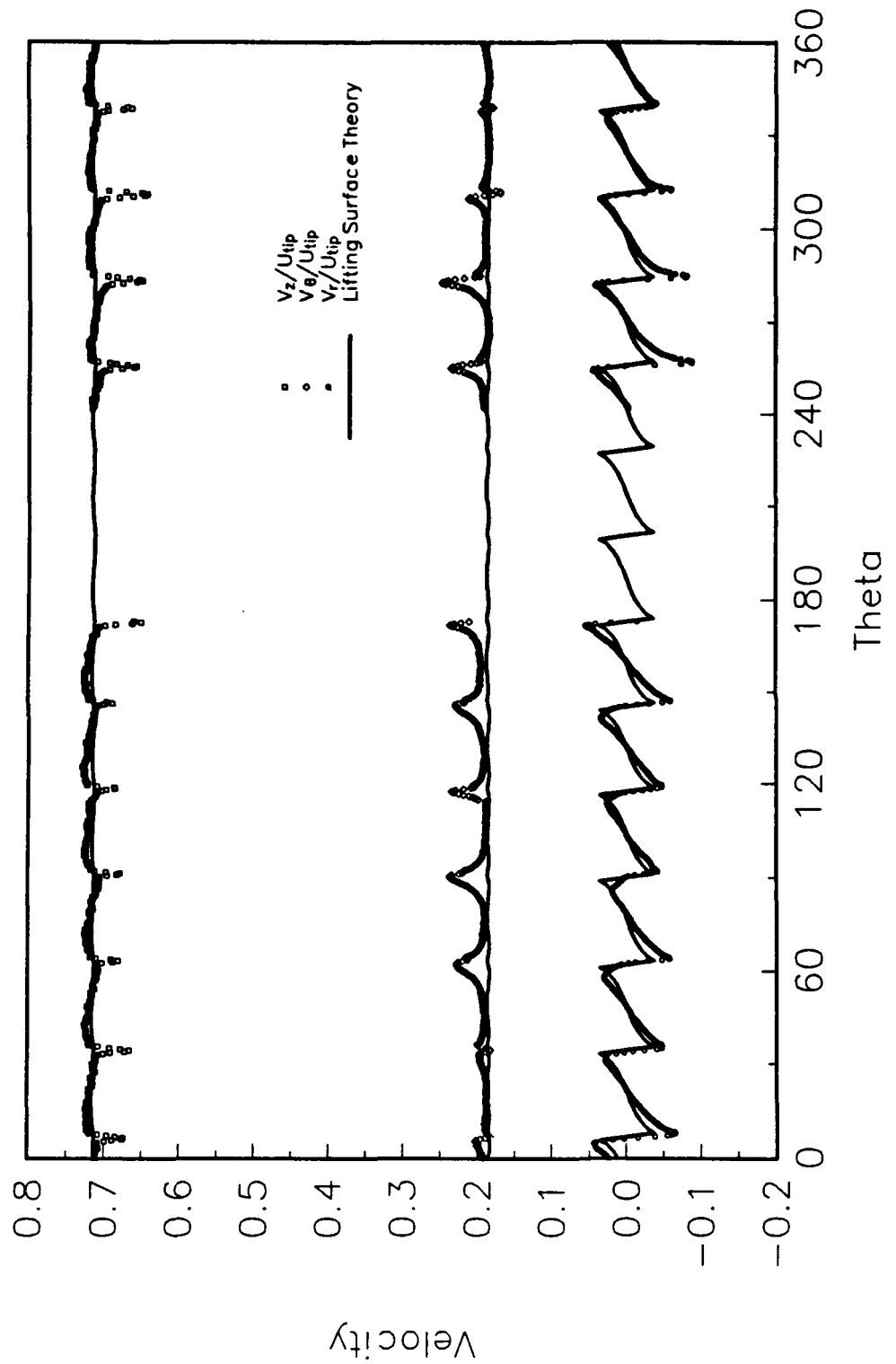


Figure 28. Circumferential Variation of Velocity Components 49.7% Chord Axially Downstream of the IGV Trailing Edge:
Five-Hole Probe Measurements and Lifting Surface Calculations; c) 19.0% Span

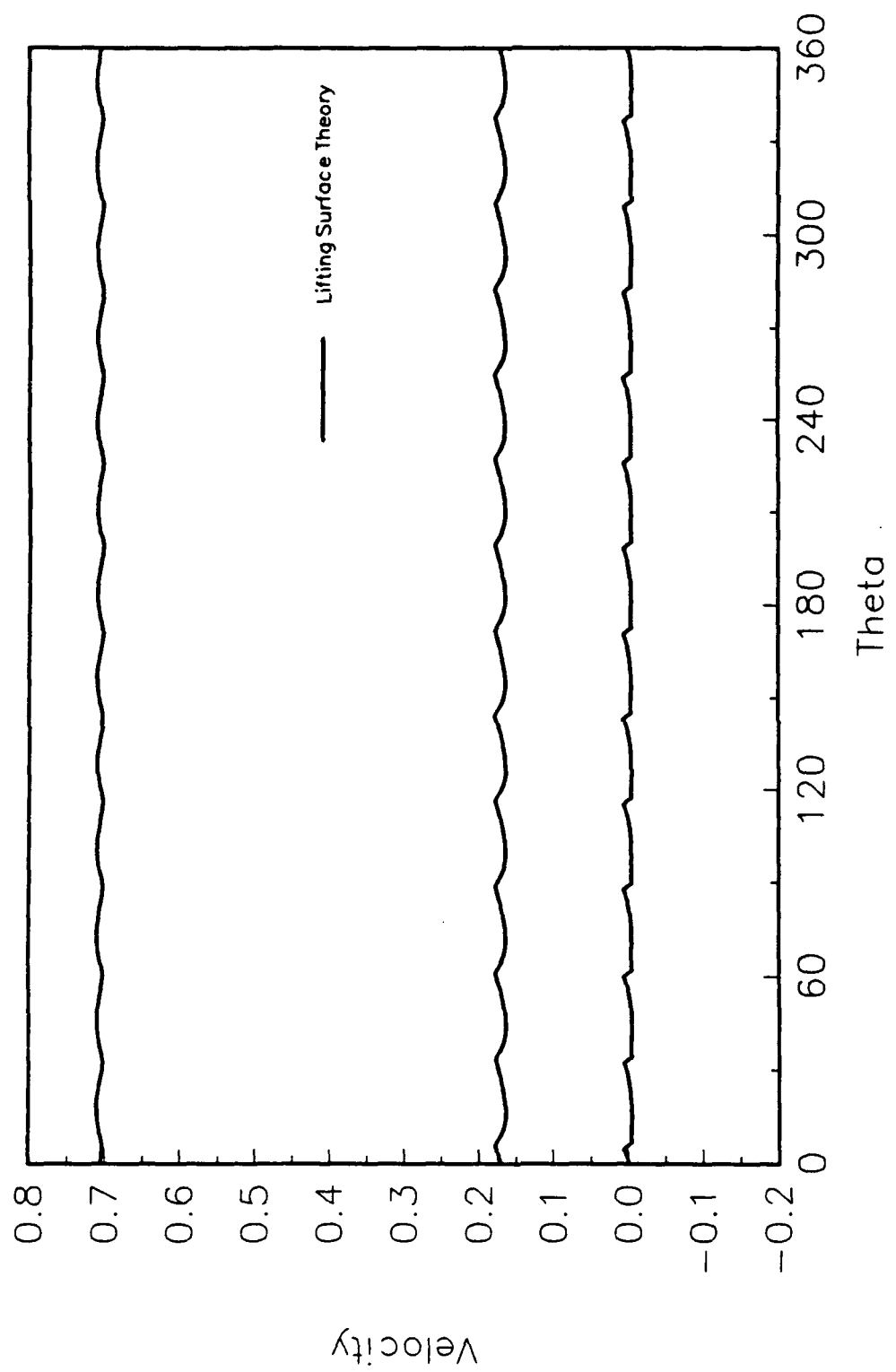


Figure 28. Circumferential Variation of Velocity Components 49.7 % Chord Axially Downstream of the IGV Trailing Edge:
Five-Hole Probe Measurements and Lifting Surface Calculations; d) 38.1 % Span

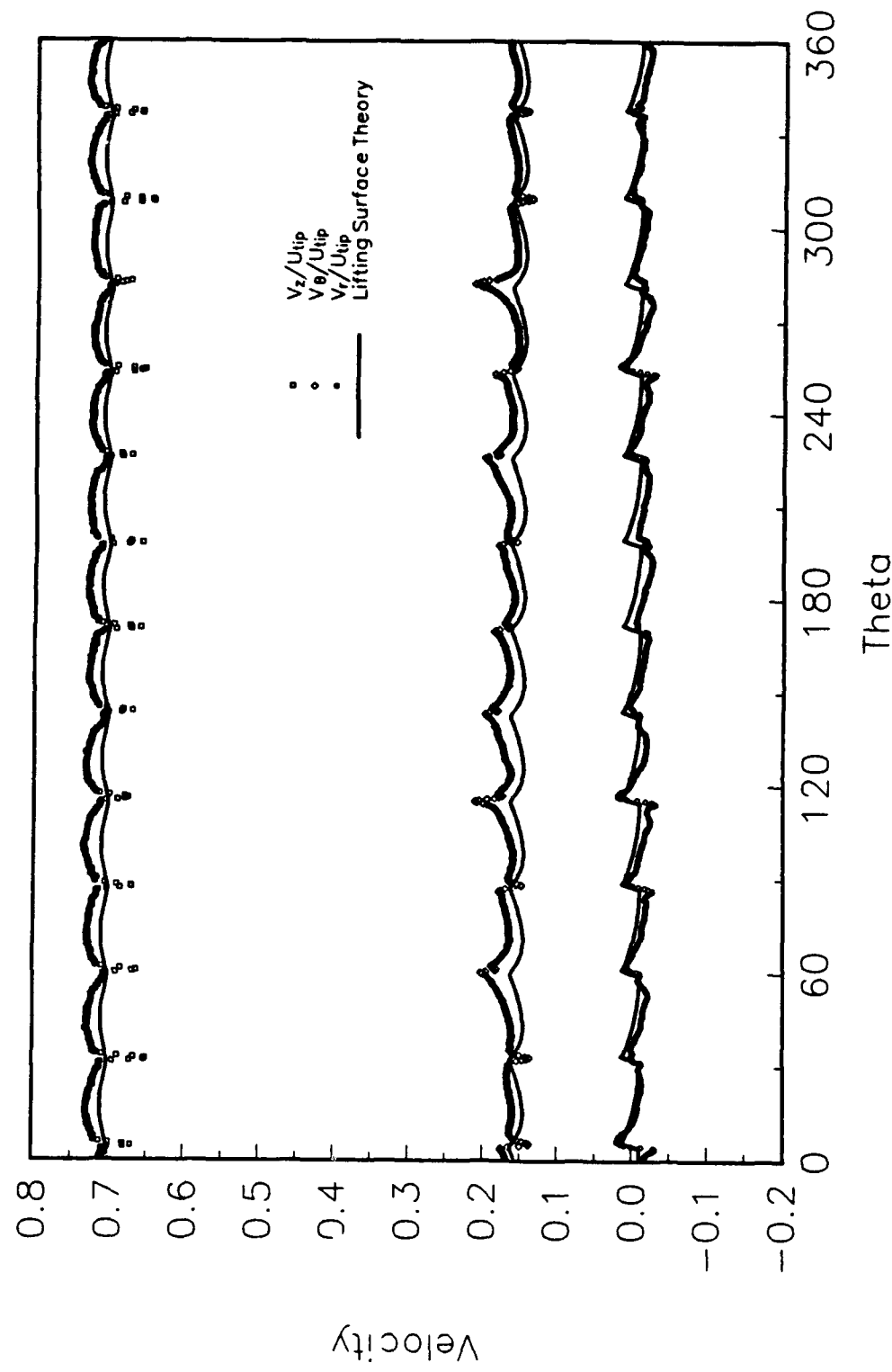


Figure 28. Circumferential Variation of Velocity Components 49.7% Chord Axially Downstream of the IGV Trailing Edge:
Five-Hole Probe Measurements and Lifting Surface Calculations; e) 52.4% Span

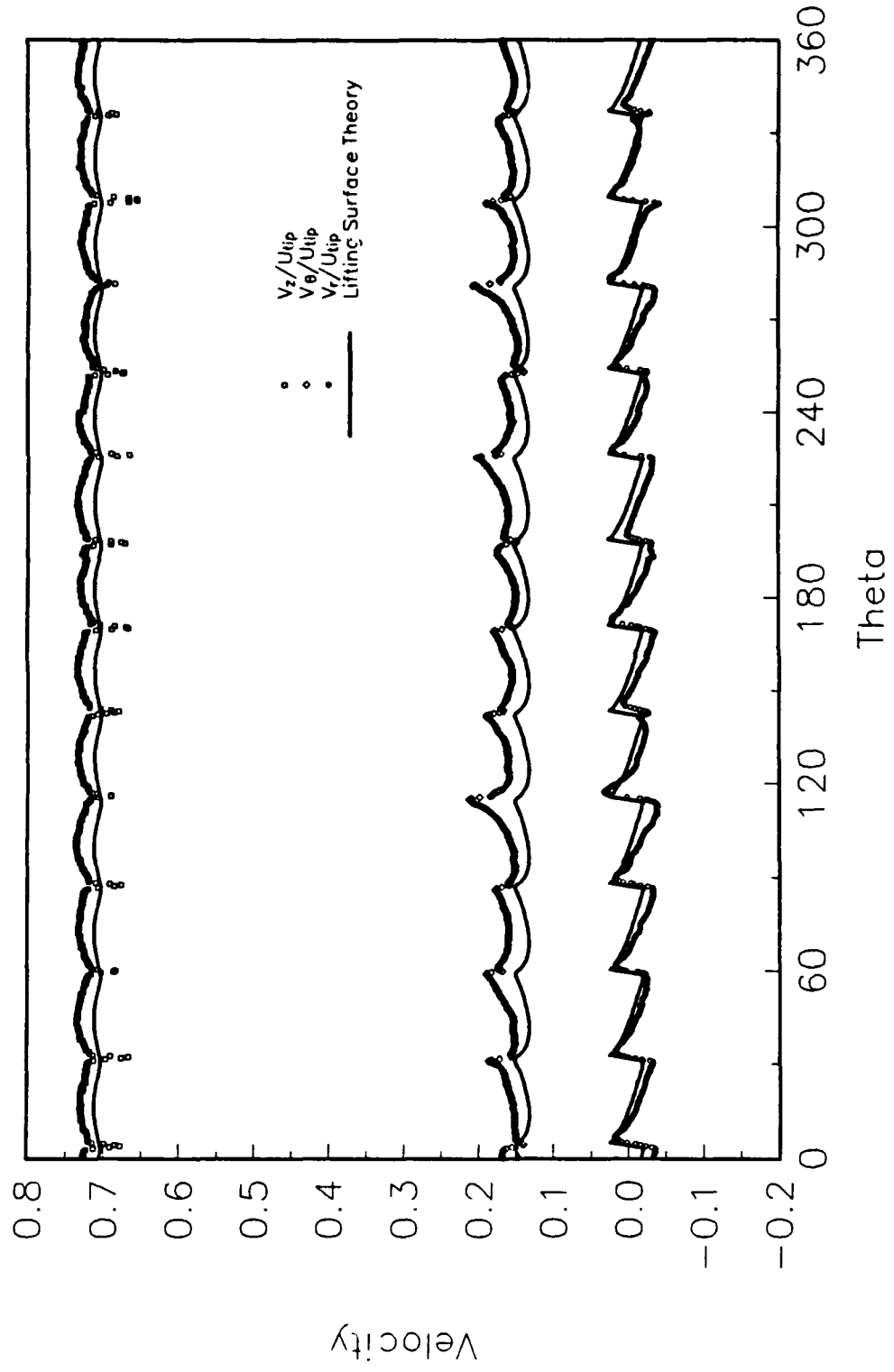


Figure 28. Circumferential Variation of Velocity Components 49.7 % Chord Axially Downstream of the IGV Trailing Edge:
Five-Hole Probe Measurements and Lifting Surface Calculations; δ 61.9% Span

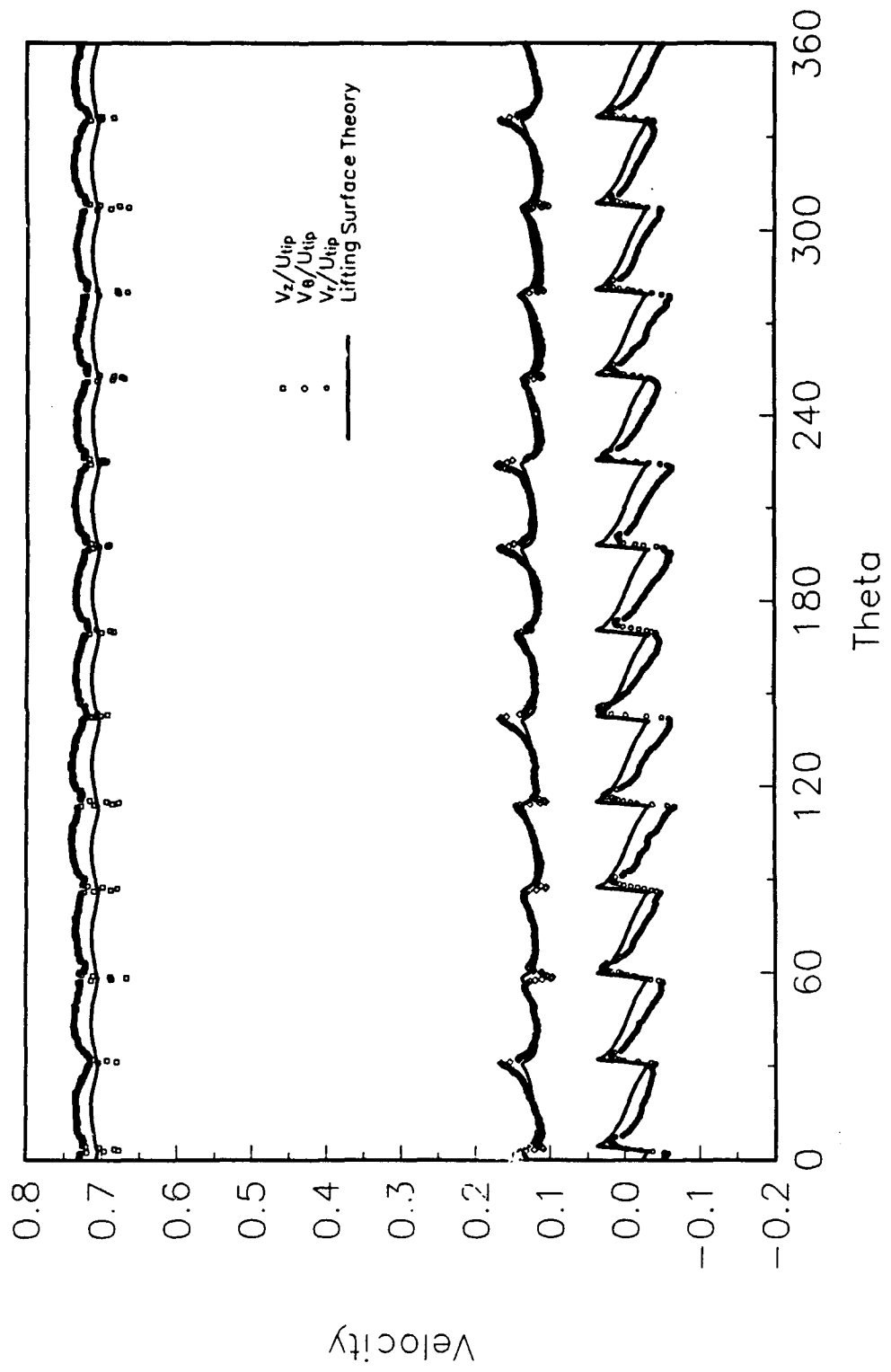


Figure 28. Circumferential Variation of Velocity Components 49.7% Chord Axially Downstream of the IGV Trailing Edge:
Five-Hole Probe Measurements and Lifting Surface Calculations; g) 71.4% Span

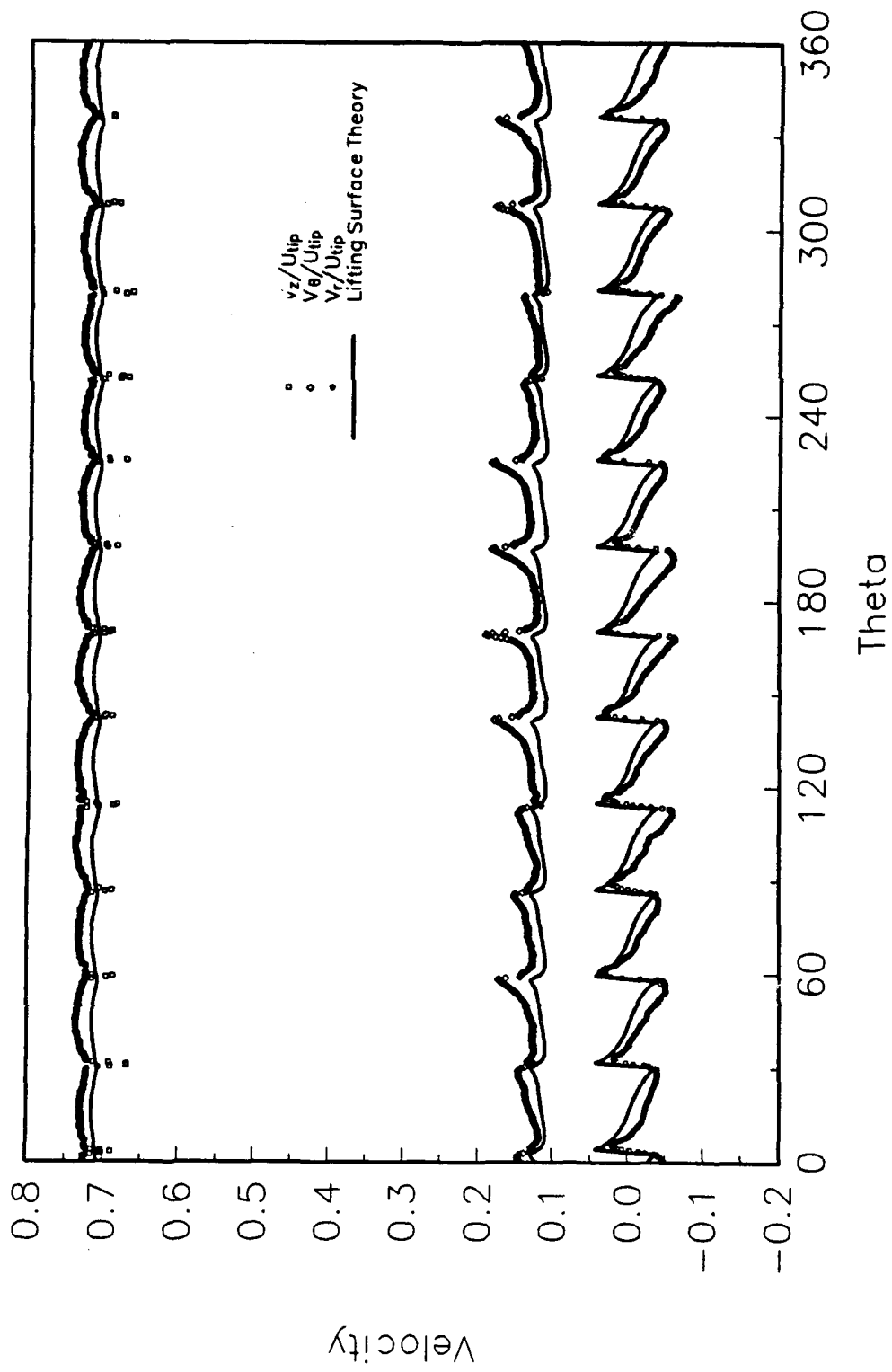


Figure 28. Circumferential Variation of Velocity Components 49.7% Chord Axially Downstream of the IGV Trailing Edge:
Five-Hole Probe Measurements and Lifting Surface Calculations; h) 76.2% Span

Figure 28.

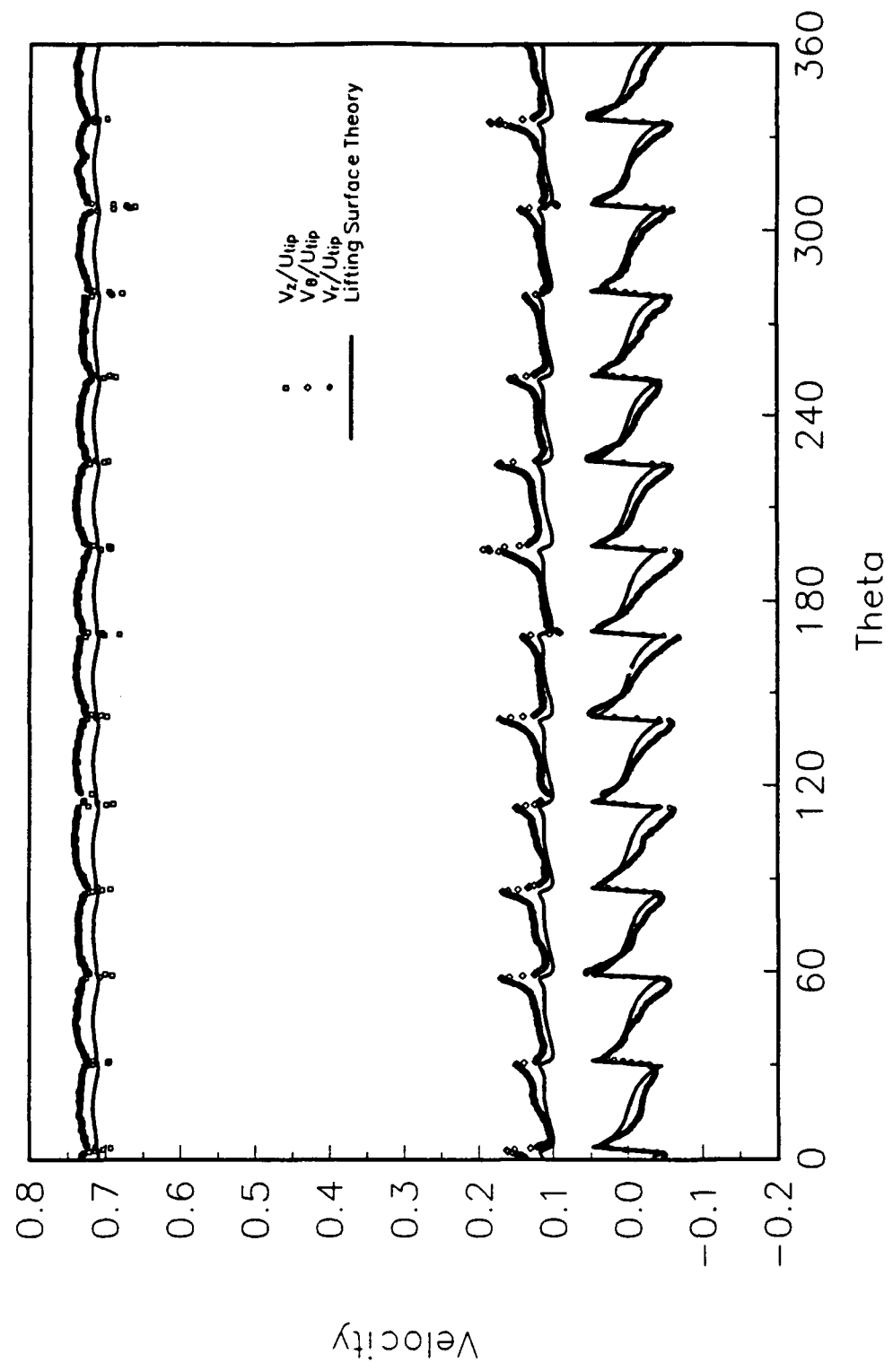


Figure 28. Circumferential Variation of Velocity Components 49.7% Chord Axially Downstream of the IGV Trailing Edge:
Five-Hole Probe Measurements and Lifting Surface Calculations; i) 81.0% Span

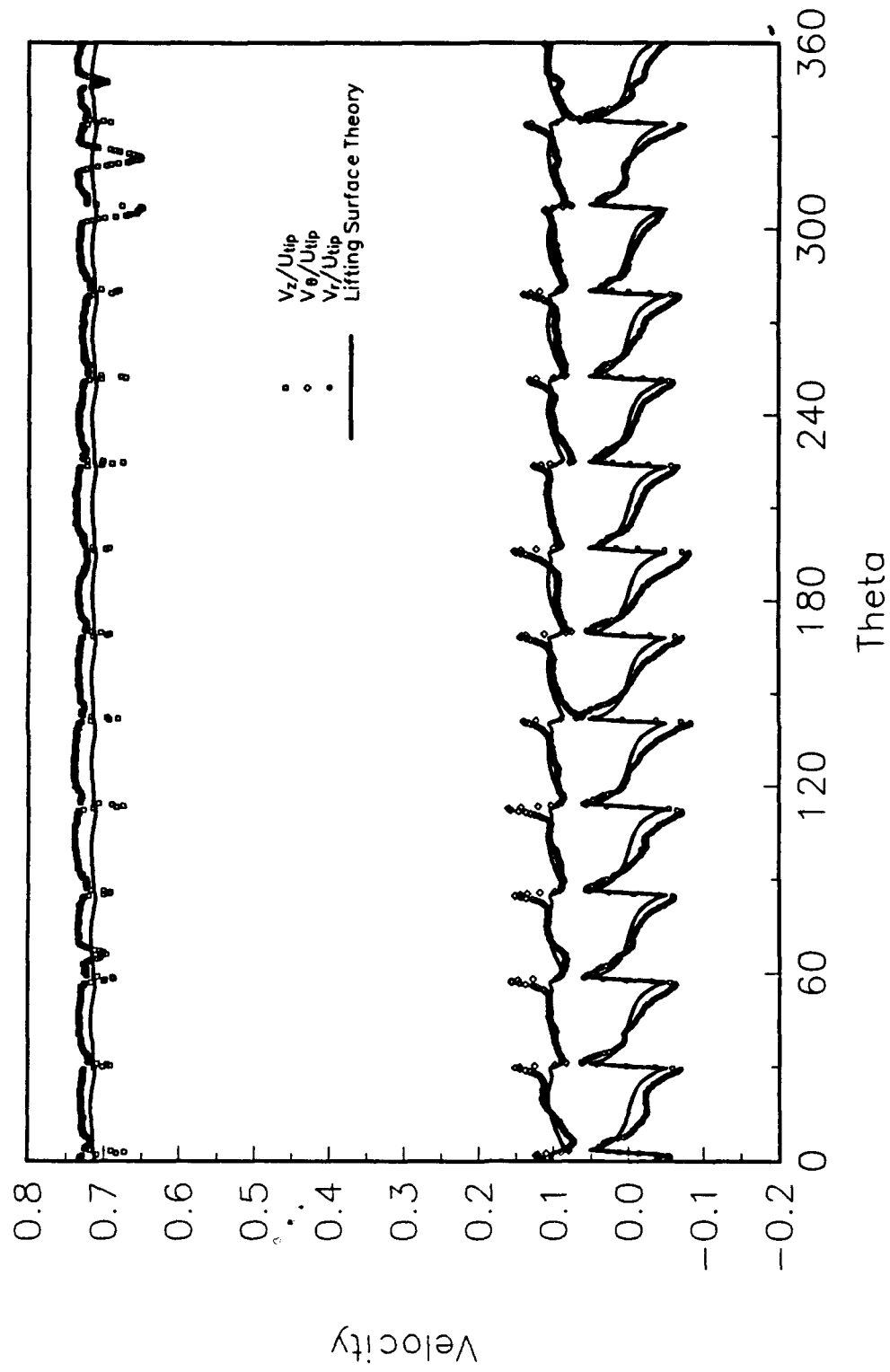


Figure 28. Circumferential Variation of Velocity Components 49.7% Chord Axially Downstream of the IGV Trailing Edge:
Five-Hole Probe Measurements and Lifting Surface Calculations; i) 85.7% Span

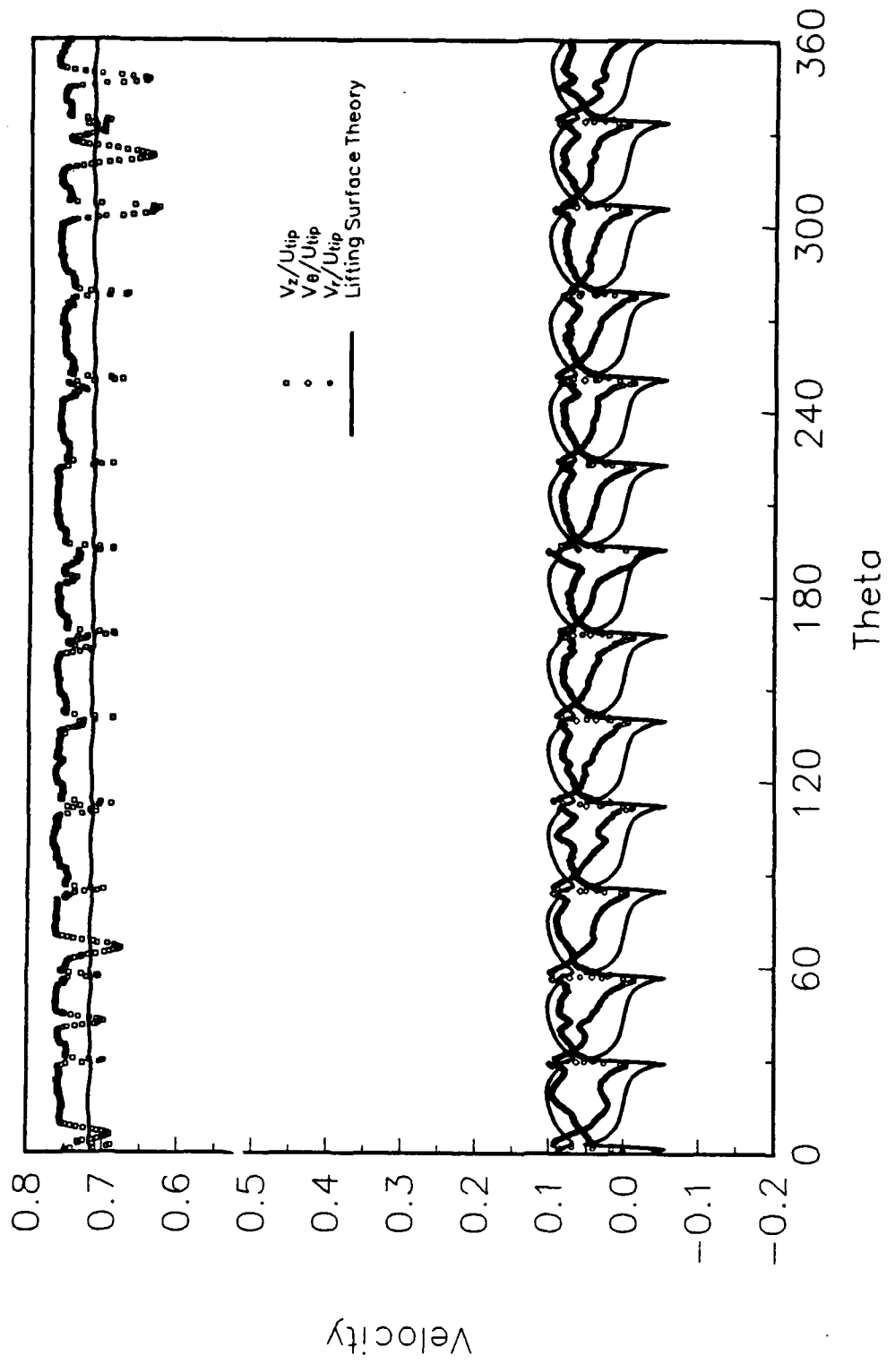


Figure 28. Circumferential Variation of Velocity Components 49.7% Chord Axially Downstream of the IGV Trailing Edge:
Five-Hole Probe Measurements and Lifting Surface Calculations; k) 90.5% Span

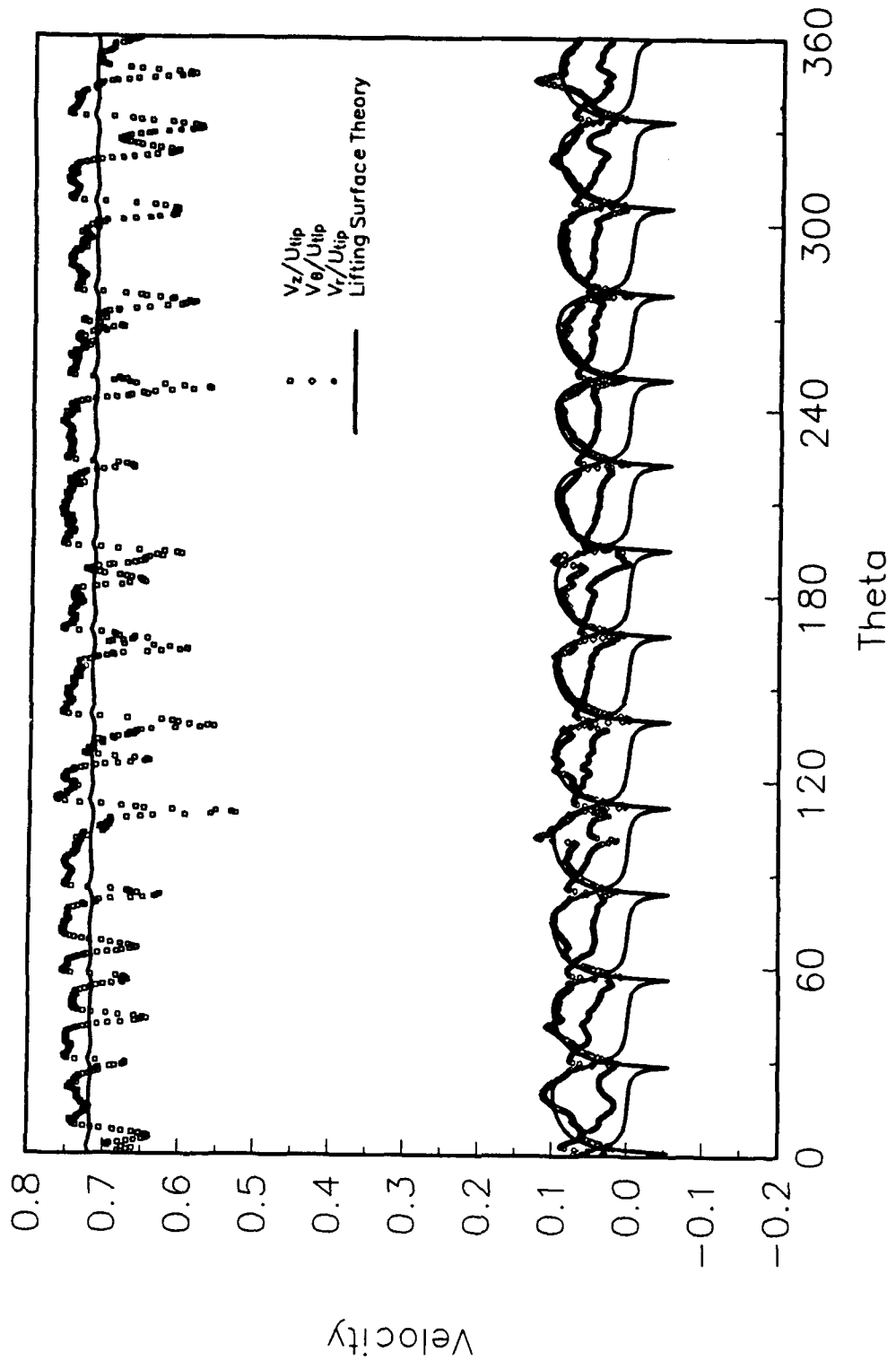


Figure 28. Circumferential Variation of Velocity Components 49.7 % Chord Axially Downstream of the IGV Trailing Edge:
Five-Hole Probe Measurements and Lifting Surface Calculations, 1) 95.2 % Span

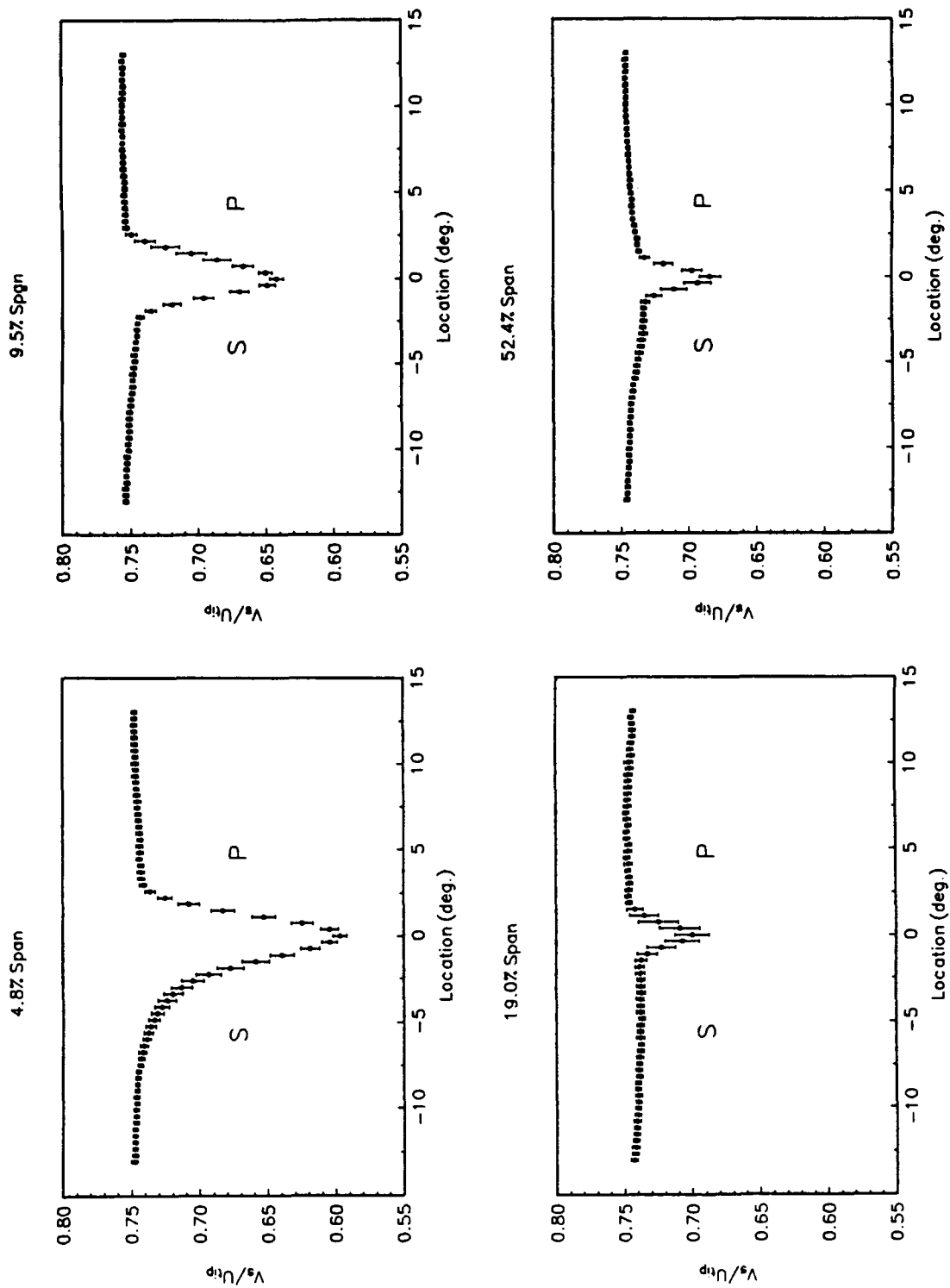


Figure 29. Passage-Averaged IGV Wakes Measured 49.7% Chord Axially Downstream of the IGV Trailing Edge with Five-Hole Probes: a) 4.8%, 9.5%, 19.0%, and 52.4% Span

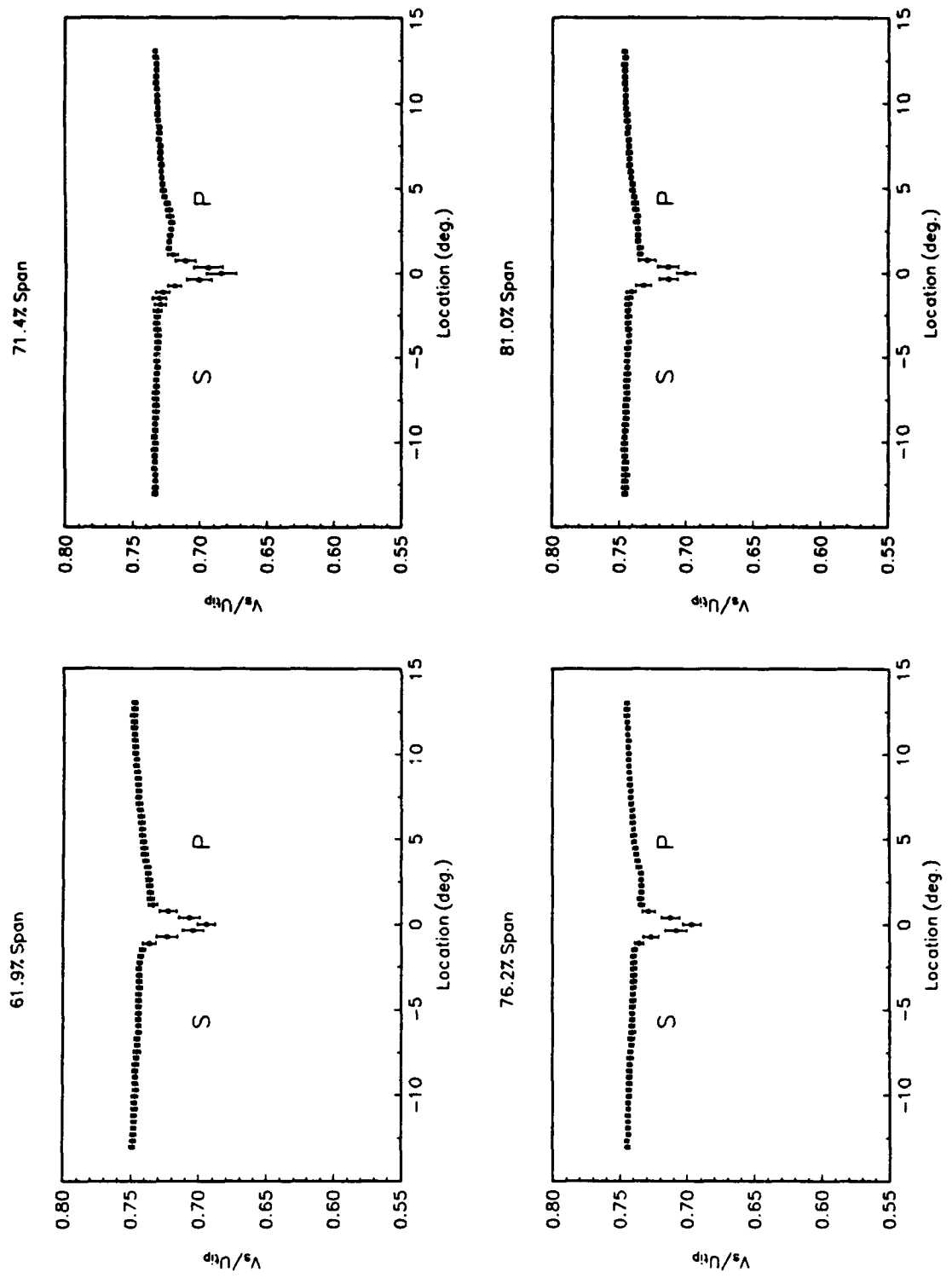


Figure 29. Passage-Averaged IGV Wakes Measured 49.7% Chord Axially Downstream of the IGV Trailing Edge with Five-Hole Probes: b) 61.9%, 71.4%, 76.2%, and 81.0% Span

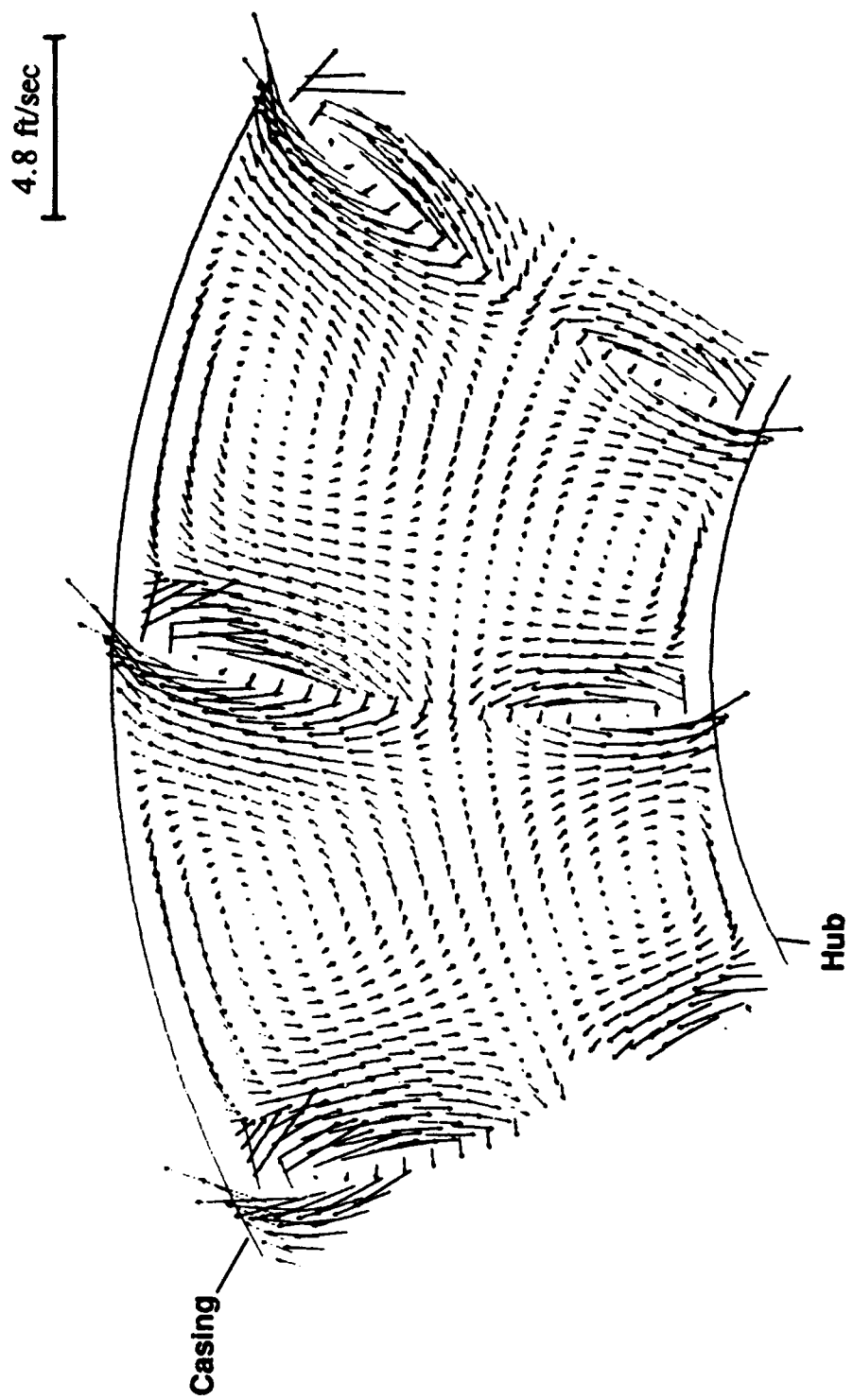


Figure 30. Secondary Velocity Vectors 49.7% Chord Axially Downstream of the IGV Trailing Edge:
a) Lifting Surface Theory Calculations

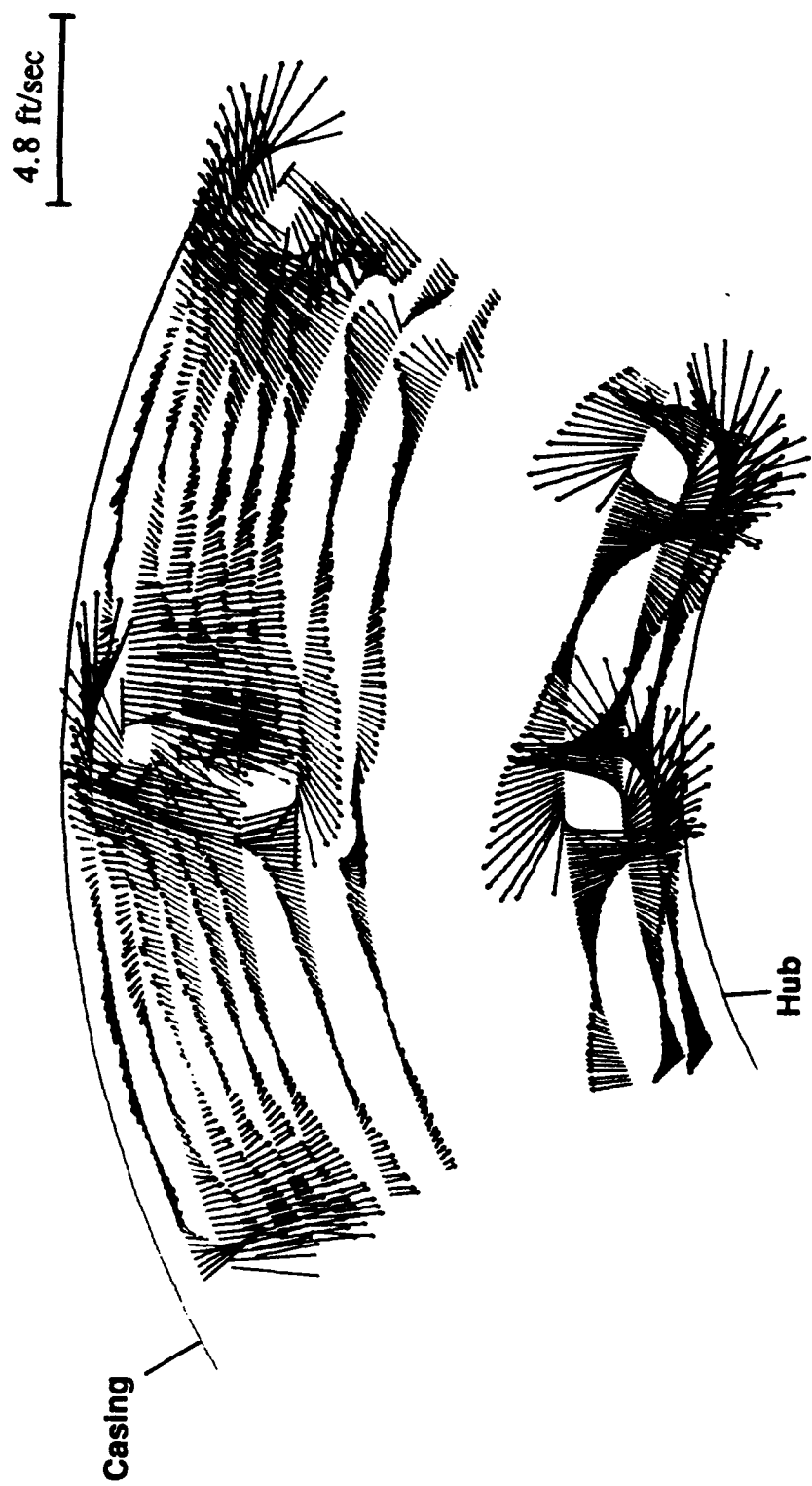


Figure 30. Secondary Velocity Vectors 49.7% Chord Axially Downstream of the IGV Trailing Edge:
b) Five-Hole Probe Rake Surveys

147

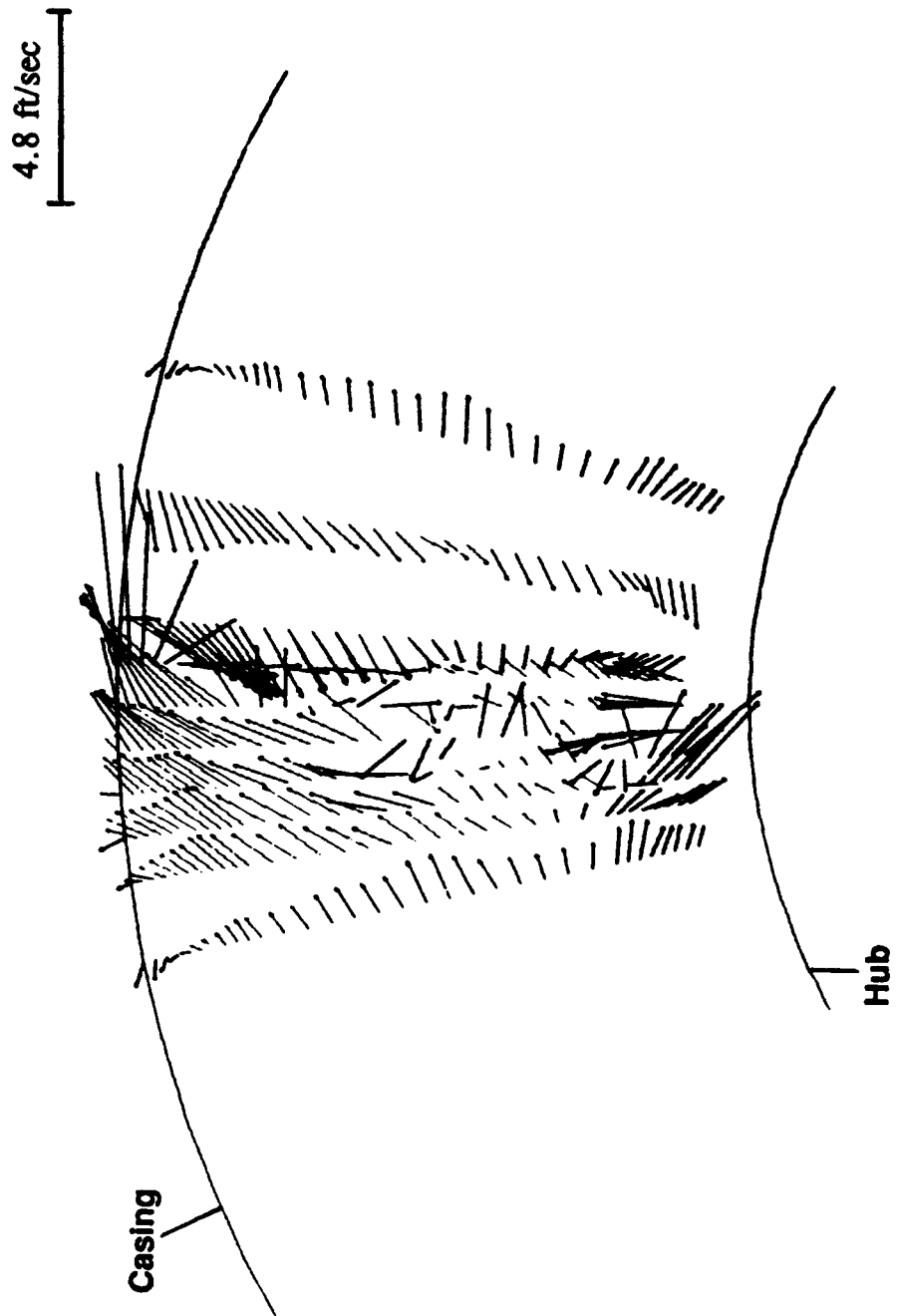


Figure 30. Secondary Velocity Vectors 49.7% Chord Axially Downstream of the IGV Trailing Edge:
c) Five-Hole Probe Radial Surveys

148

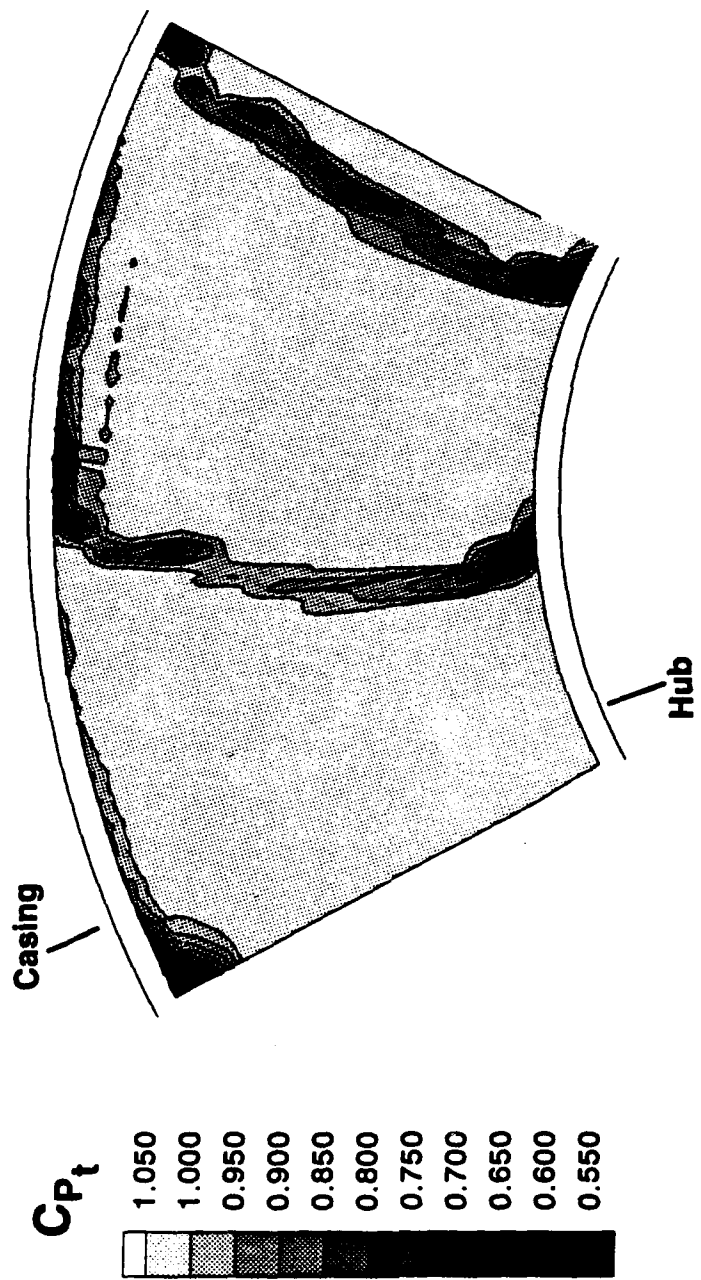


Figure 31. Total-Pressure Coefficient Contours Measured 49.7% Chord Axially Downstream of the IGV Trailing Edge with Five-Hole Probes

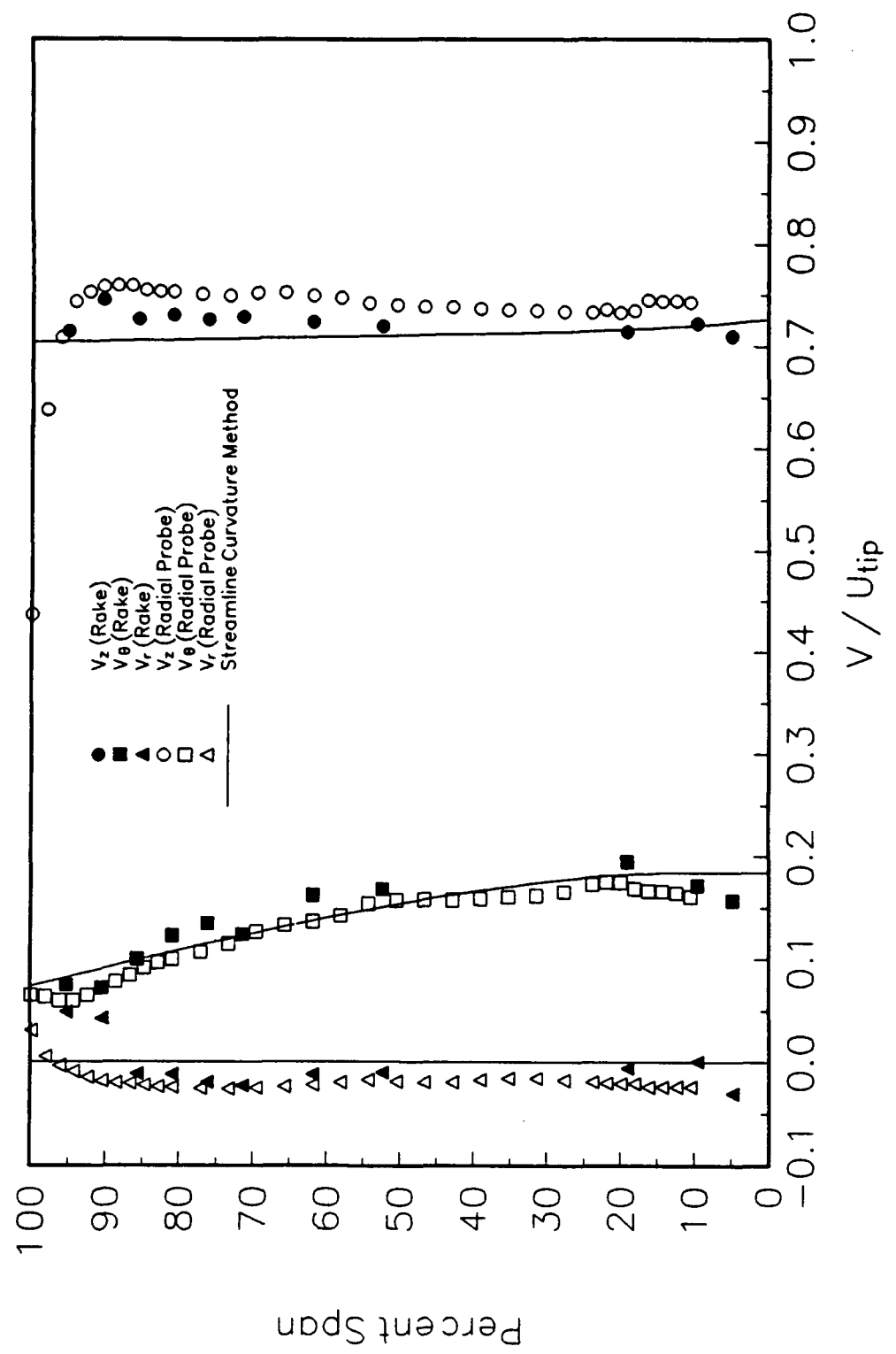


Figure 32. Circumferentially-Averaged Velocities Measured 49.7% Chord Axially Downstream of the IGV Trailing Edge With Five-Hole Probes

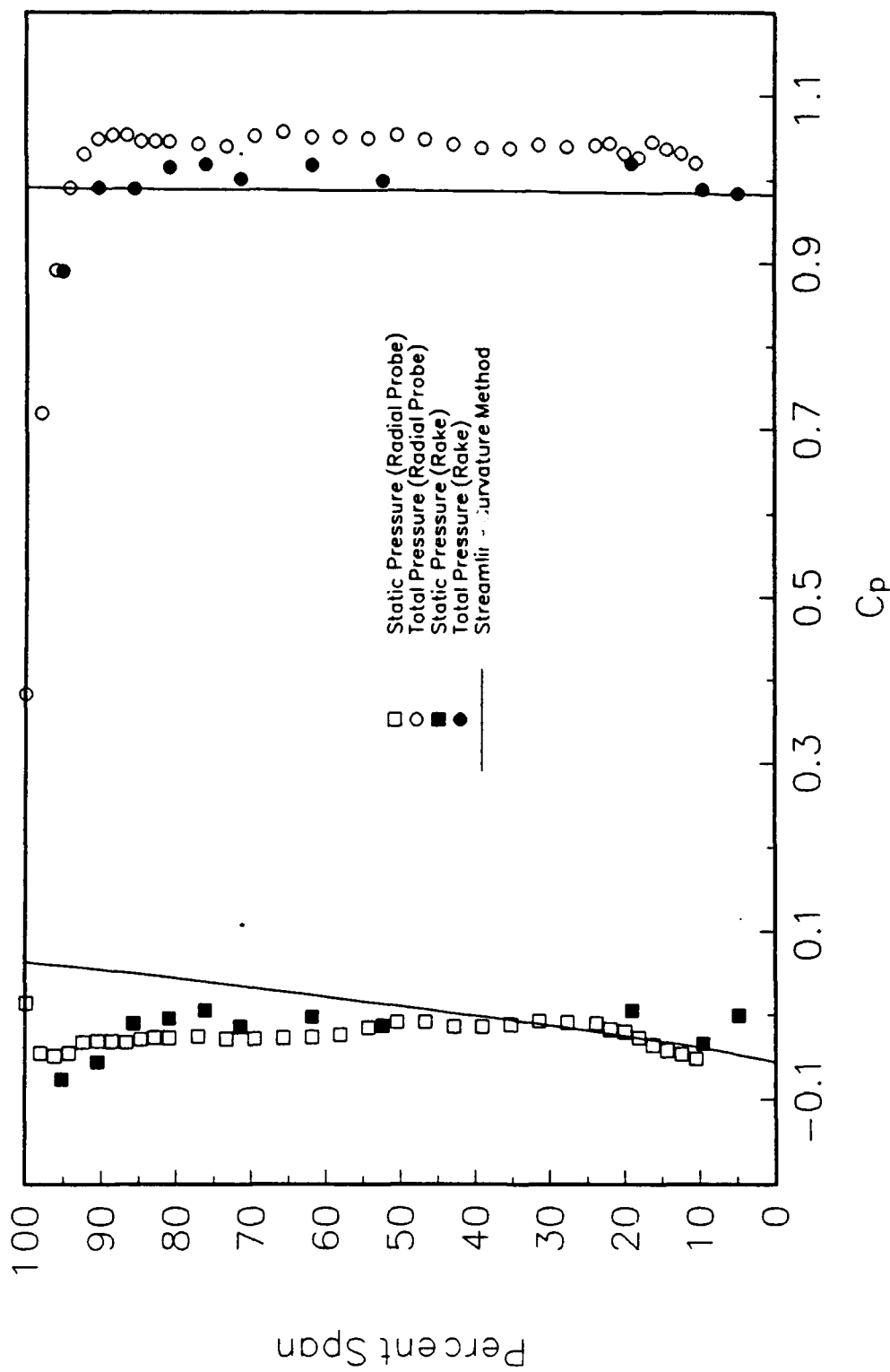


Figure 33. Circumferentially-Averaged Pressure Coefficients Measured 49.7% Chord Axially Downstream of the IGV Trailing Edge with Five-Hole Probes

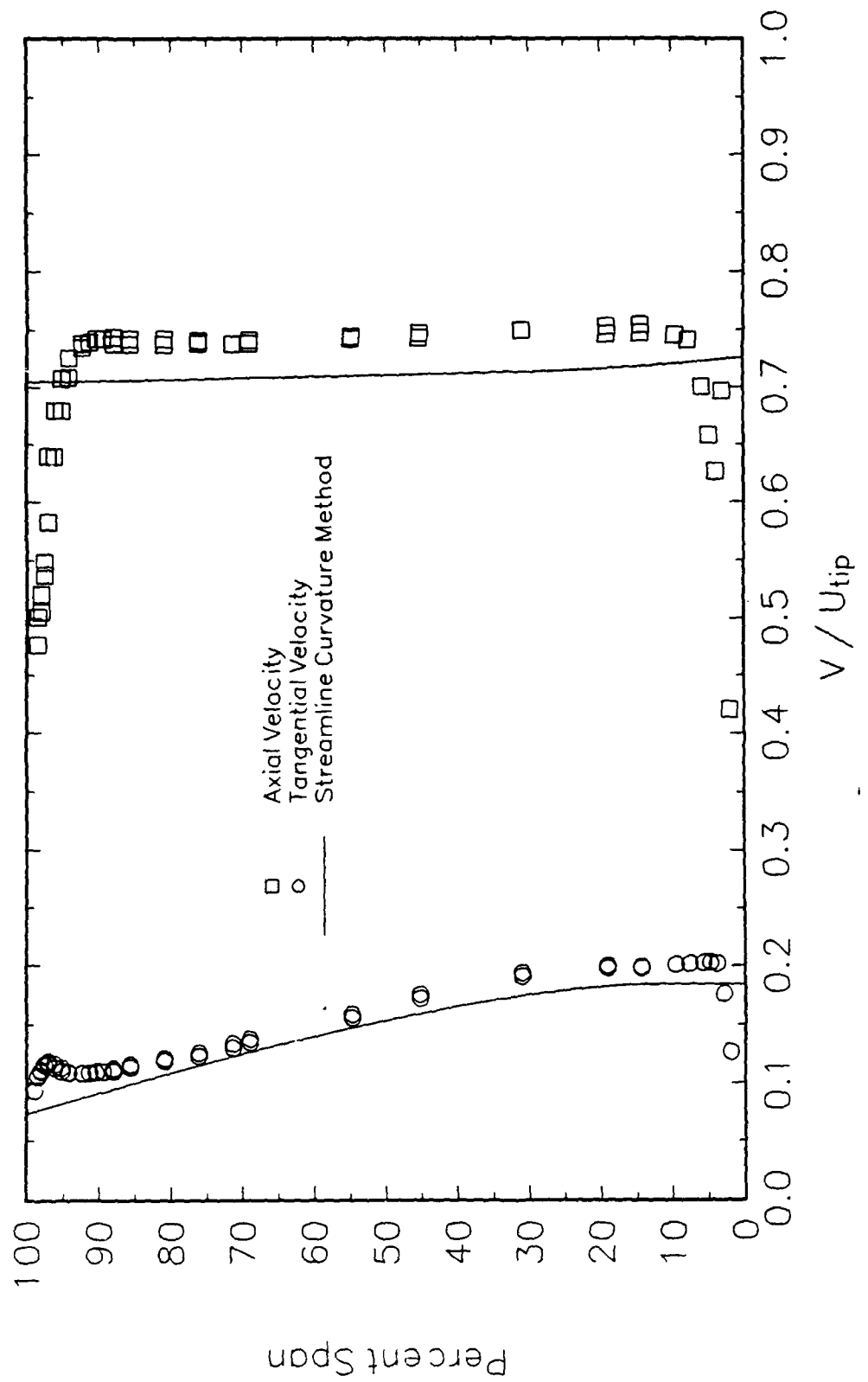


Figure 34. Circumferentially-Averaged Velocities Measured 88.5% Chord Axially Downstream of the IGV Trailing Edge with LDV

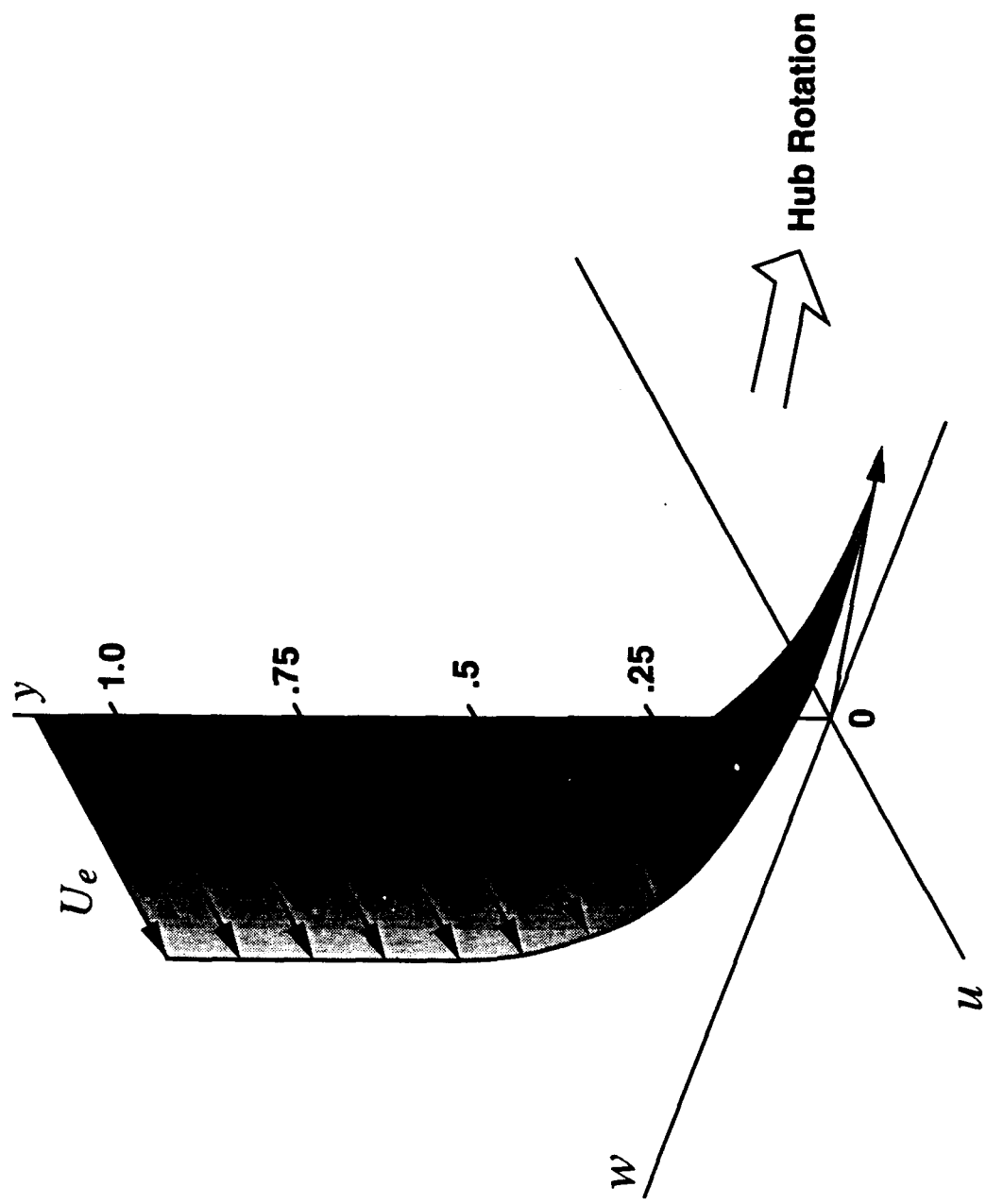


Figure 35. Skewed Boundary Layer Measured Above the Rotating Hub 88.5% Chord Axially Downstream of the IGV Trailing Edge with LDV

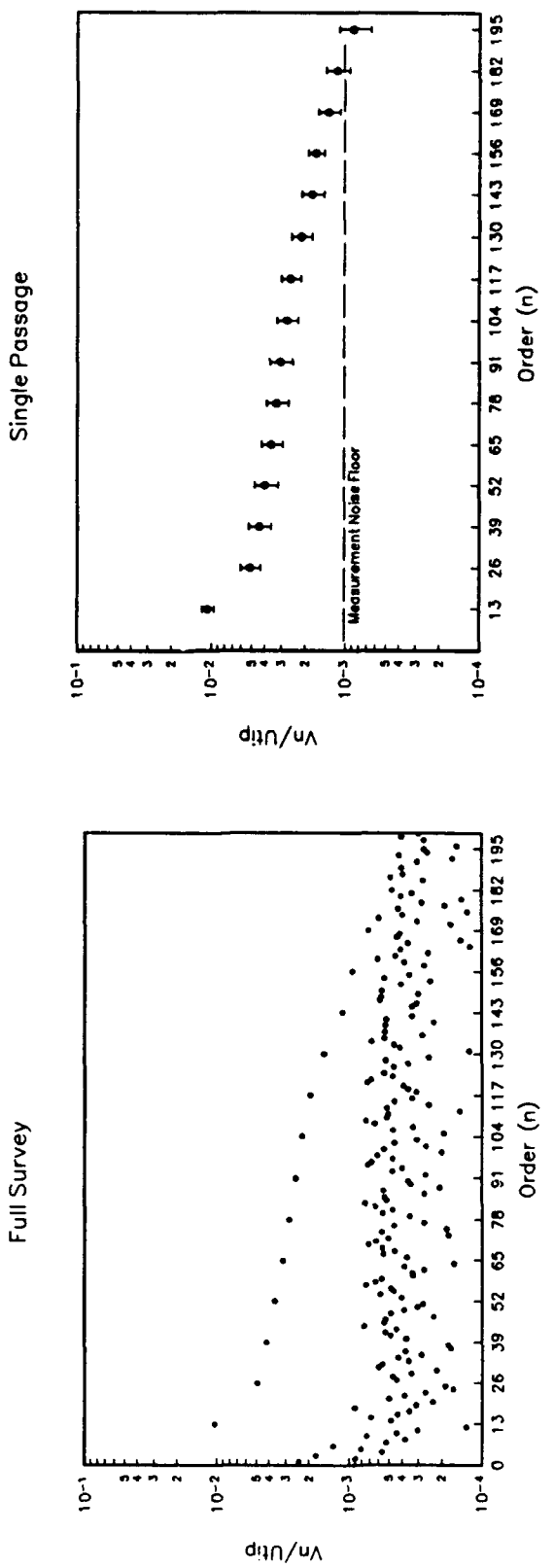


Figure 36. Comparison of Fourier Analysis Using a Full Circumferential Survey and Using a Combination of Individual Passages: Fourier Coefficients of Axial Velocity at 61.9% Span and 49.7% Chord Axially Downstream of the IGV Trailing Edge

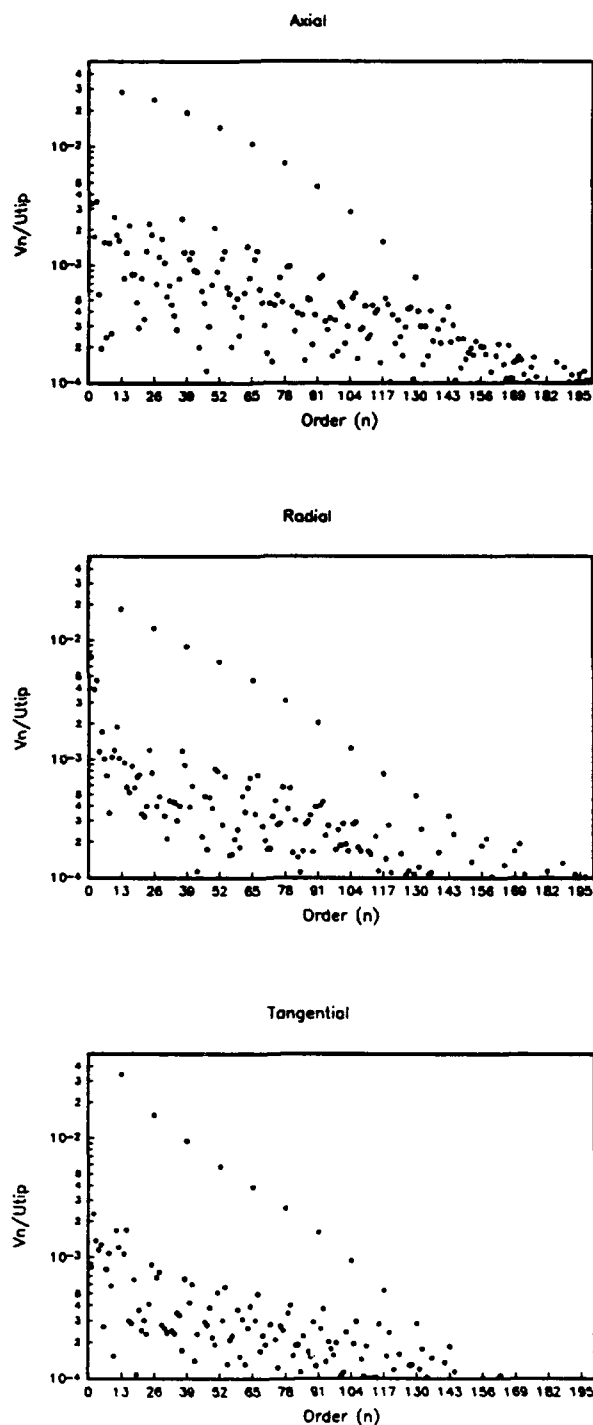


Figure 37. Fourier Coefficients of Velocity Components 49.7% Chord Axially Downstream of the IGV Trailing Edge: a) 4.8% Span

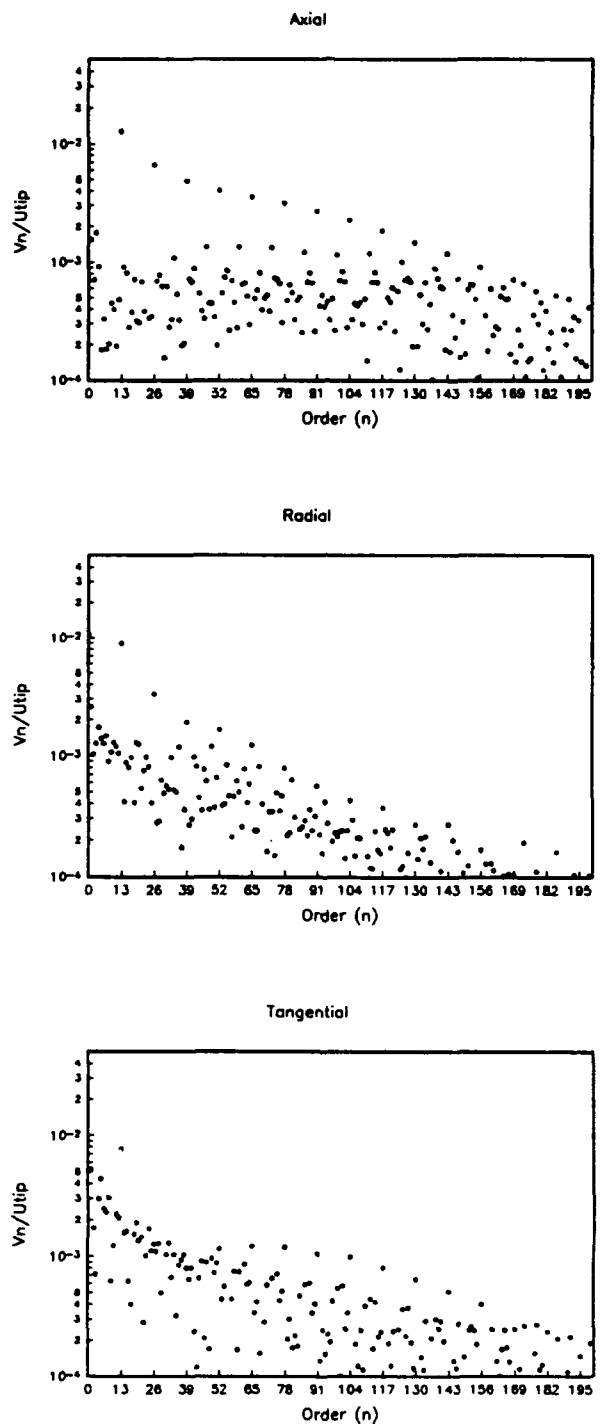


Figure 37. Fourier Coefficients of Velocity Components 49.7% Chord Axially Downstream of the IGV Trailing Edge: b) 52.4% Span

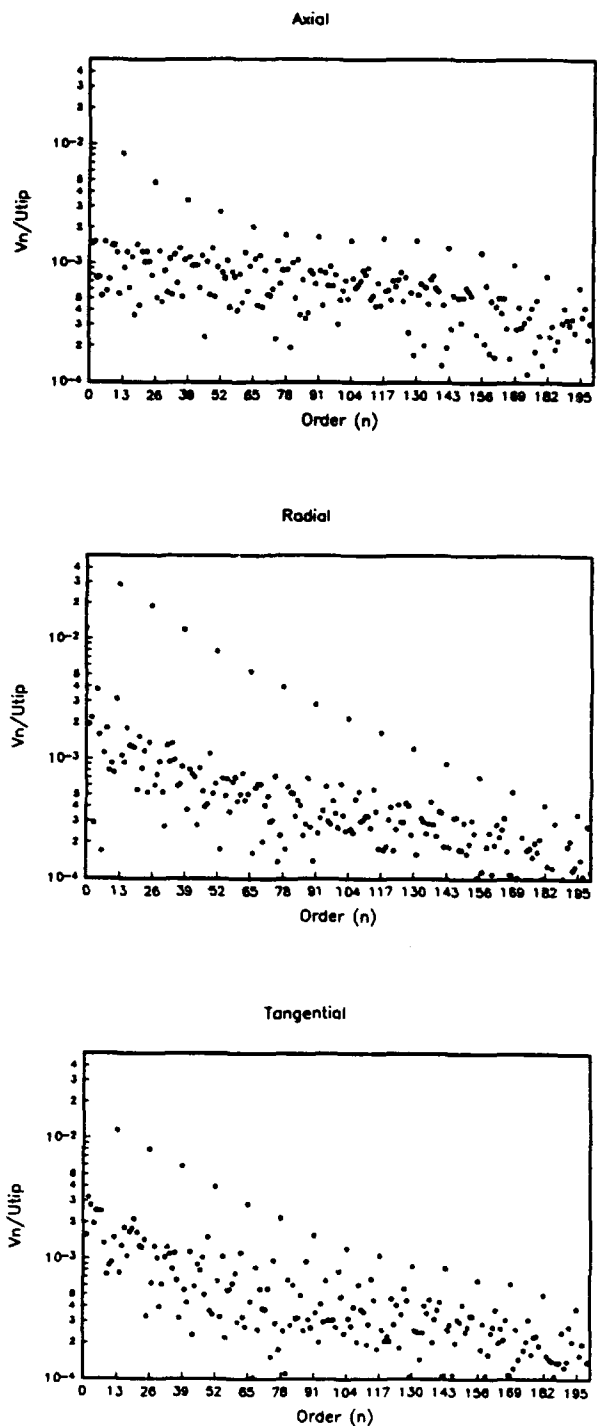


Figure 37. Fourier Coefficients of Velocity Components 49.7% Chord Axially Downstream of the IGV Trailing Edge: c) 81.0% Span

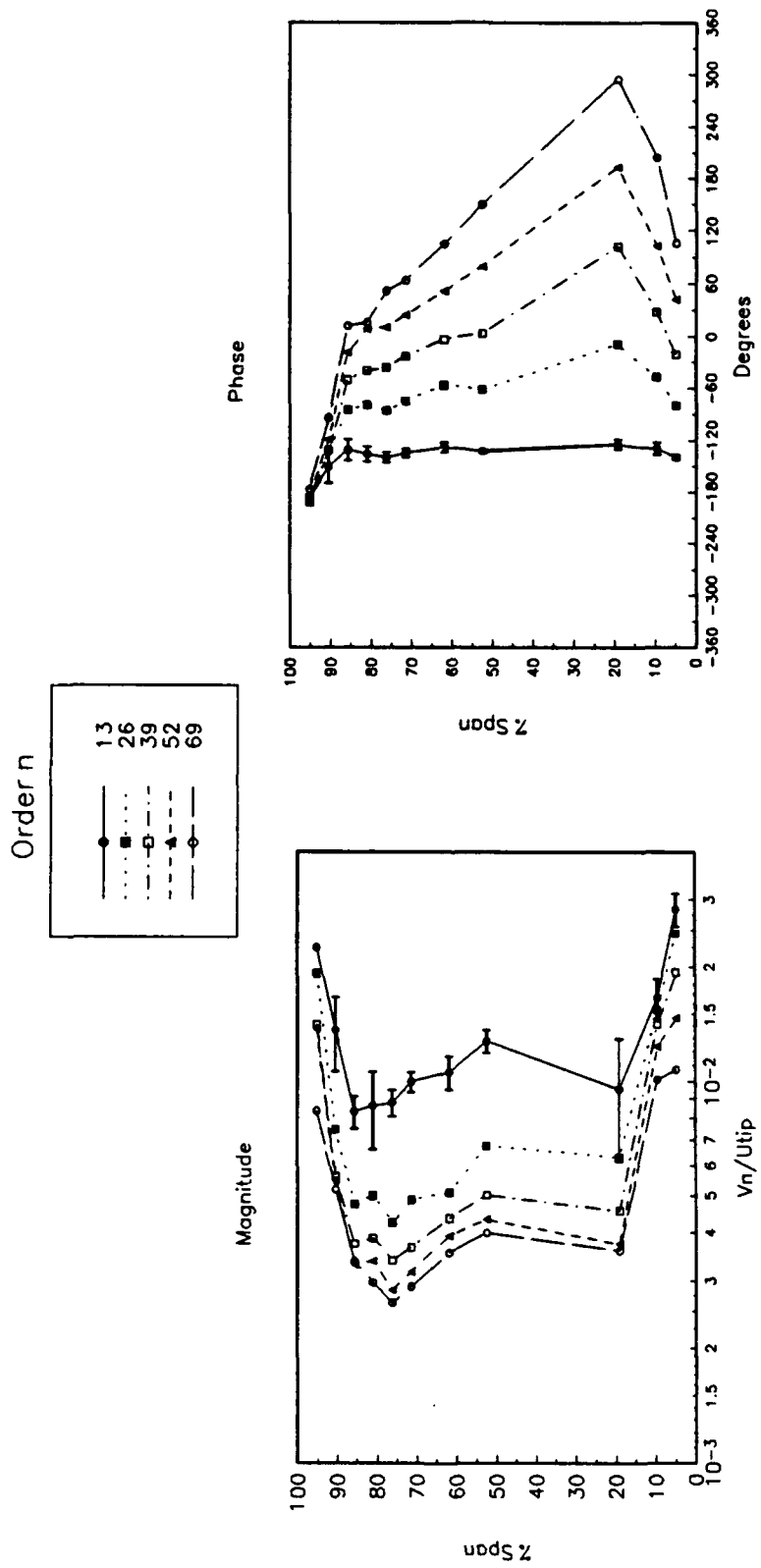


Figure 38. Spanwise Variation of Fourier Coefficients (Magnitude and Phase) 49.7% Chord Axially Downstream of the IGV Trailing Edge for the Harmonics of Order 13, 26, 39, 52, and 69: a) Axial Velocity

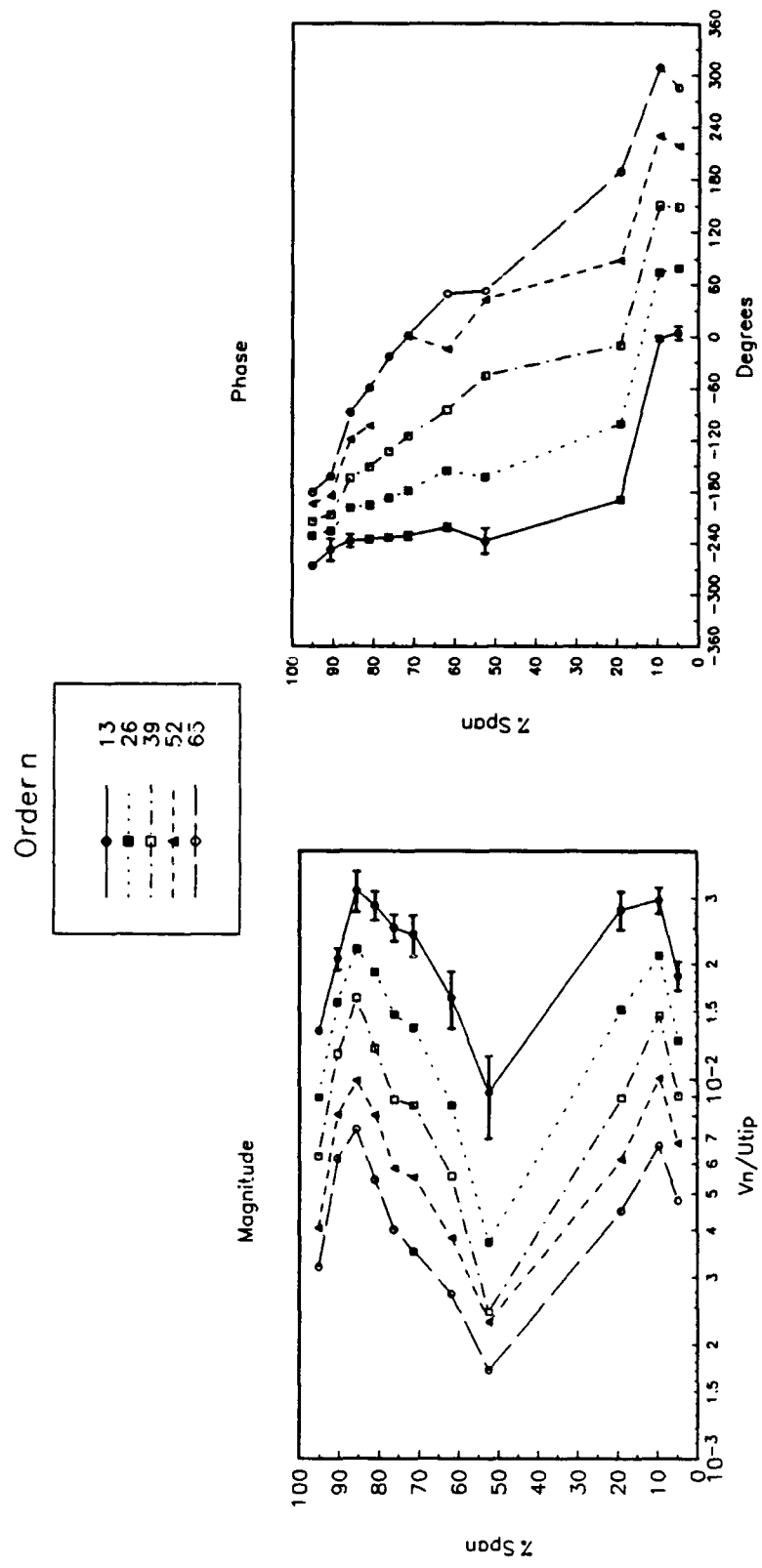


Figure 38. Spanwise Variation of Fourier Coefficients (Magnitude and Phase) 49.7% Chord Axially Downstream of the IGV Trailing Edge for the Harmonics of Order 13, 26, 39, 52, and 69: a) Radial Velocity

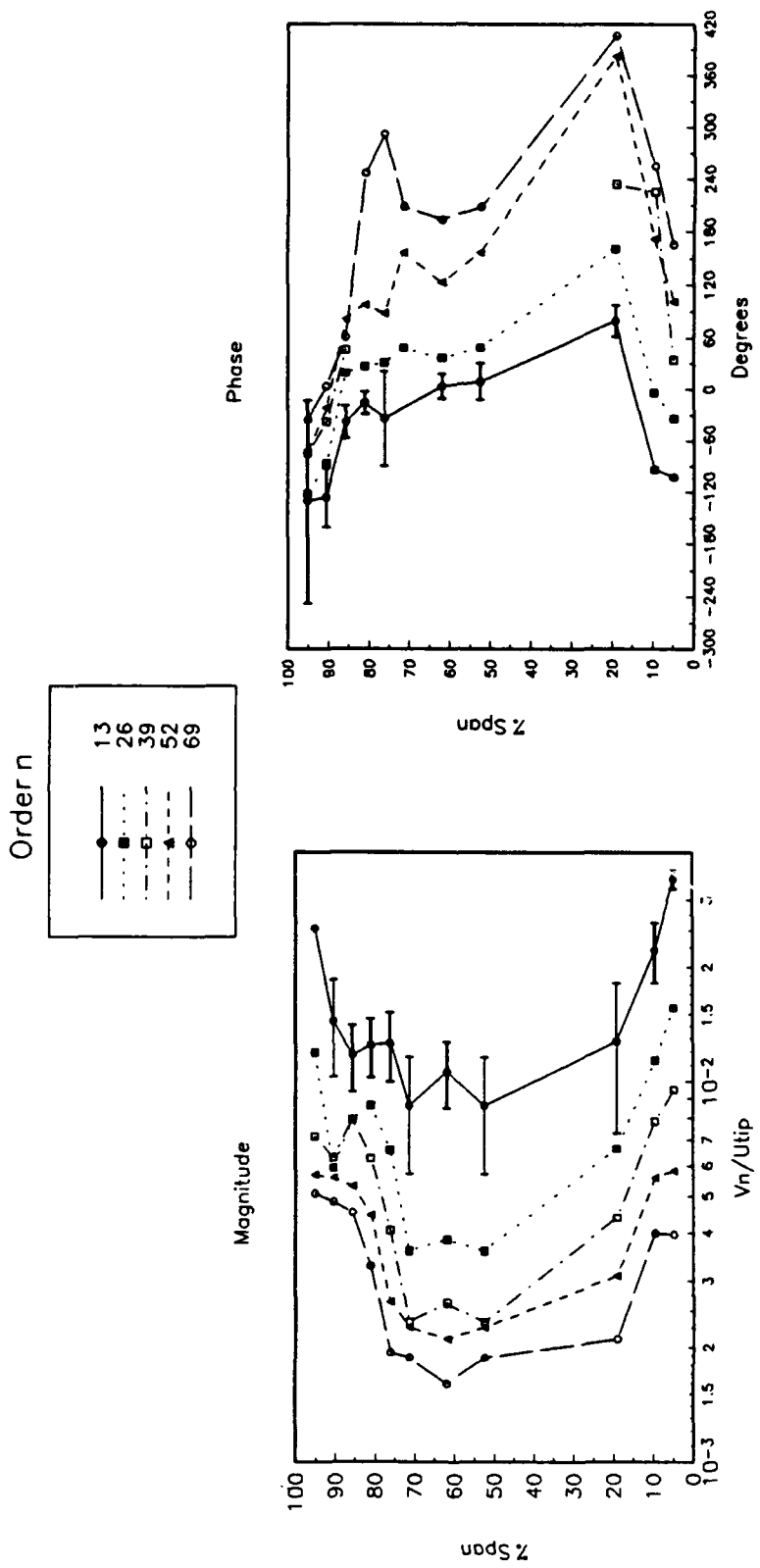


Figure 38. Spanwise Variation of Fourier Coefficients (Magnitude and Phase) 49.7% Chord Axially Downstream of the IGV Trailing Edge for the Harmonics of Order 13, 26, 39, 52, and 69: c) Tangential Velocity

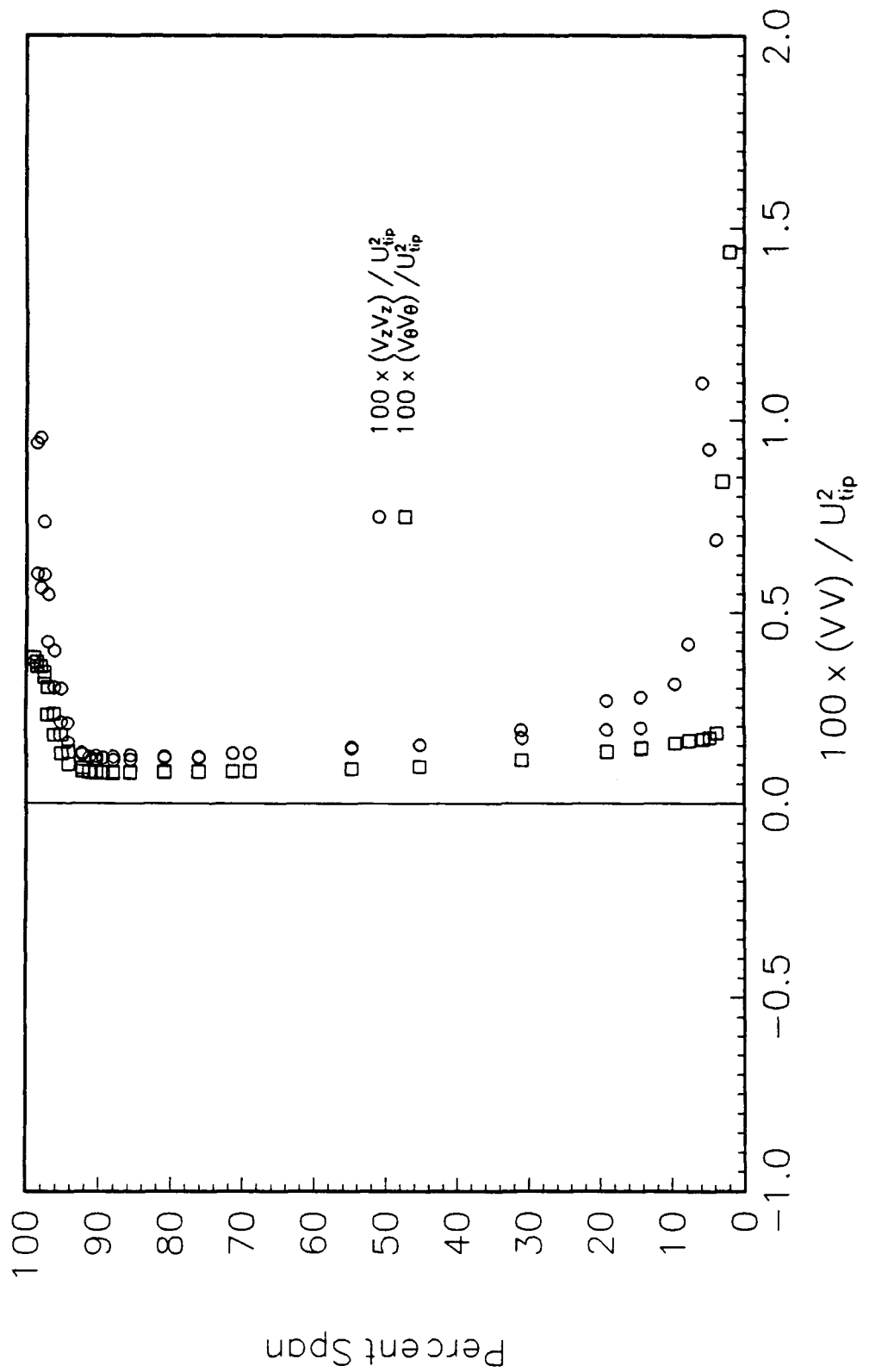


Figure 39. Overall Unsteady Velocity Correlations Measured 88.5% Chord Axially Downstream of the IGV Trailing Edge with LDV

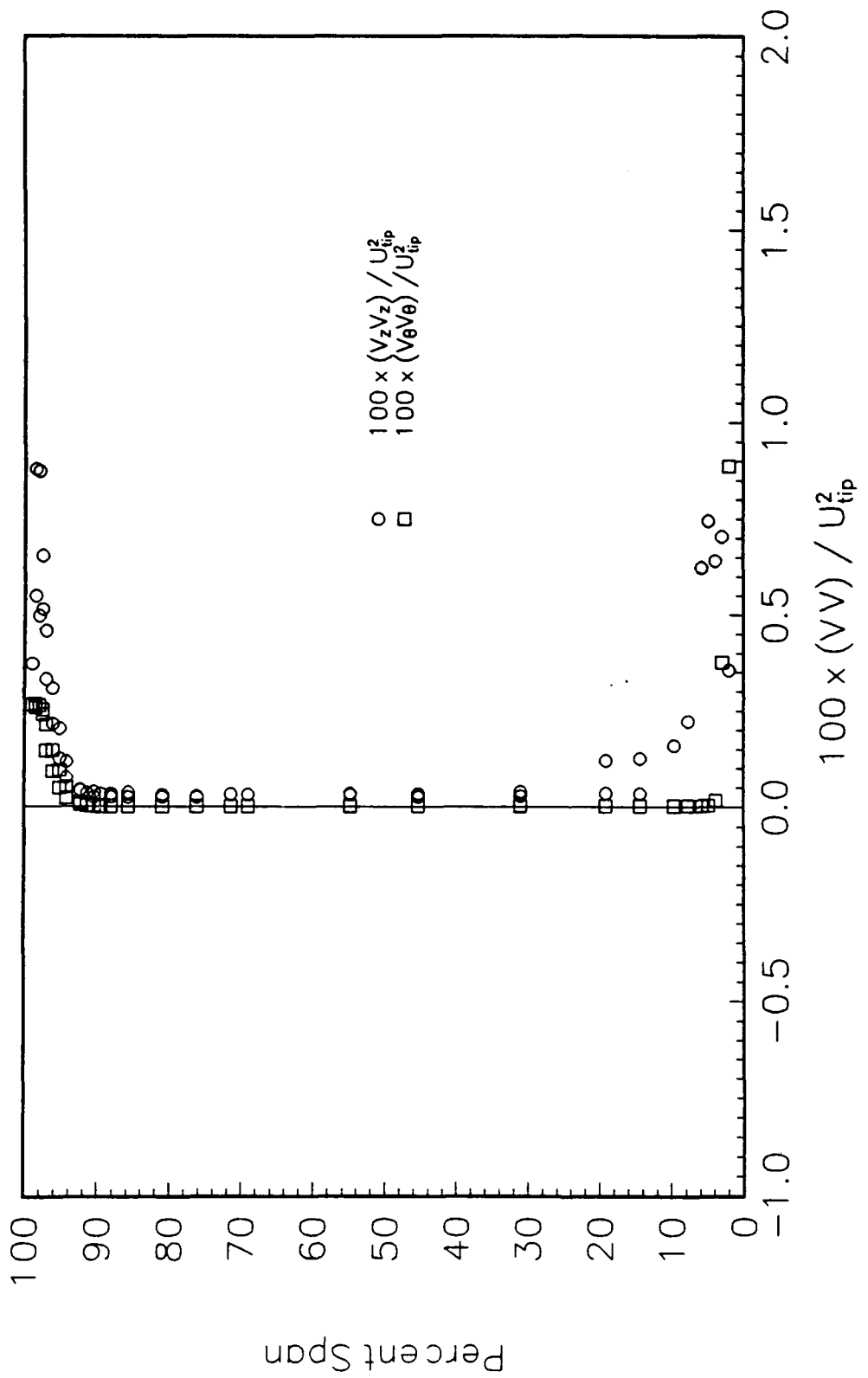


Figure 40. Nondeterministic Unsteady Velocity Correlations Measured 88.5% Chord Axially Downstream of the IGV Trailing Edge with LDV

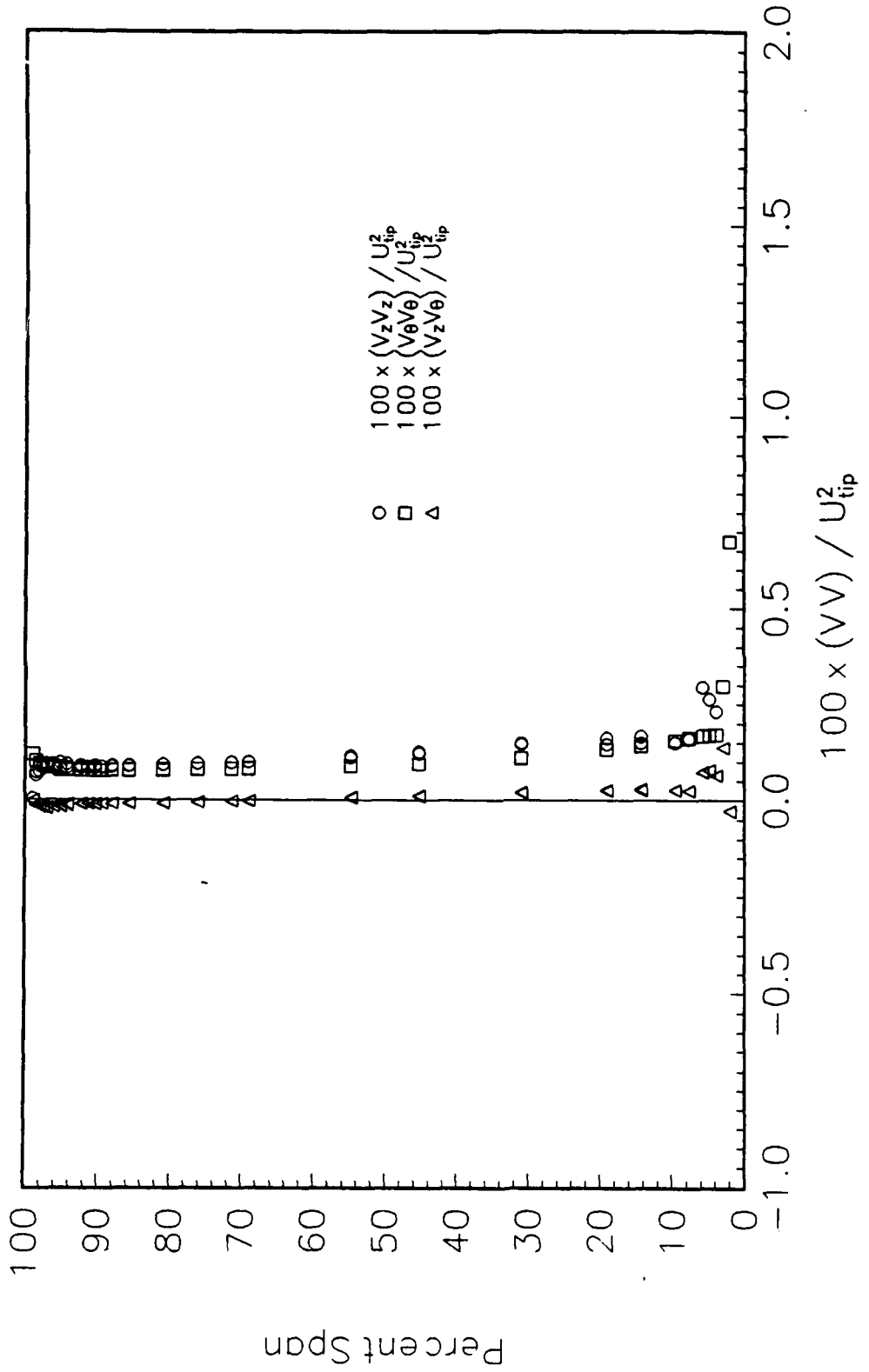


Figure 41. Deterministic Unsteady Velocity Correlations Measured 88.5% Chord Axially Downstream of the IGV Trailing Edge

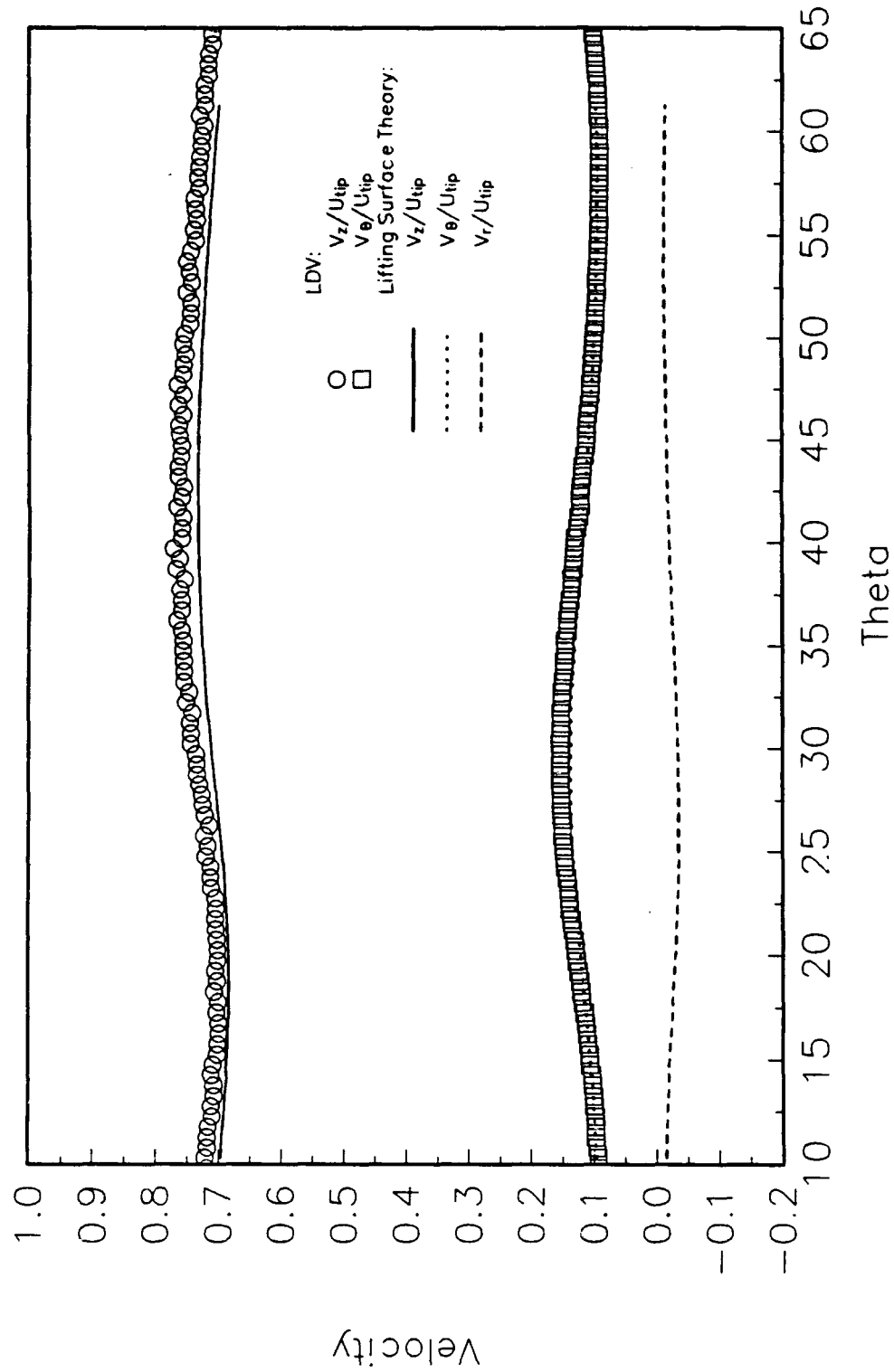


Figure 42. Unsteady Potential Flow Effect at 76.2% Span:
a) 28.0% Chord Axially Upstream of the Rotor Blade Leading Edge

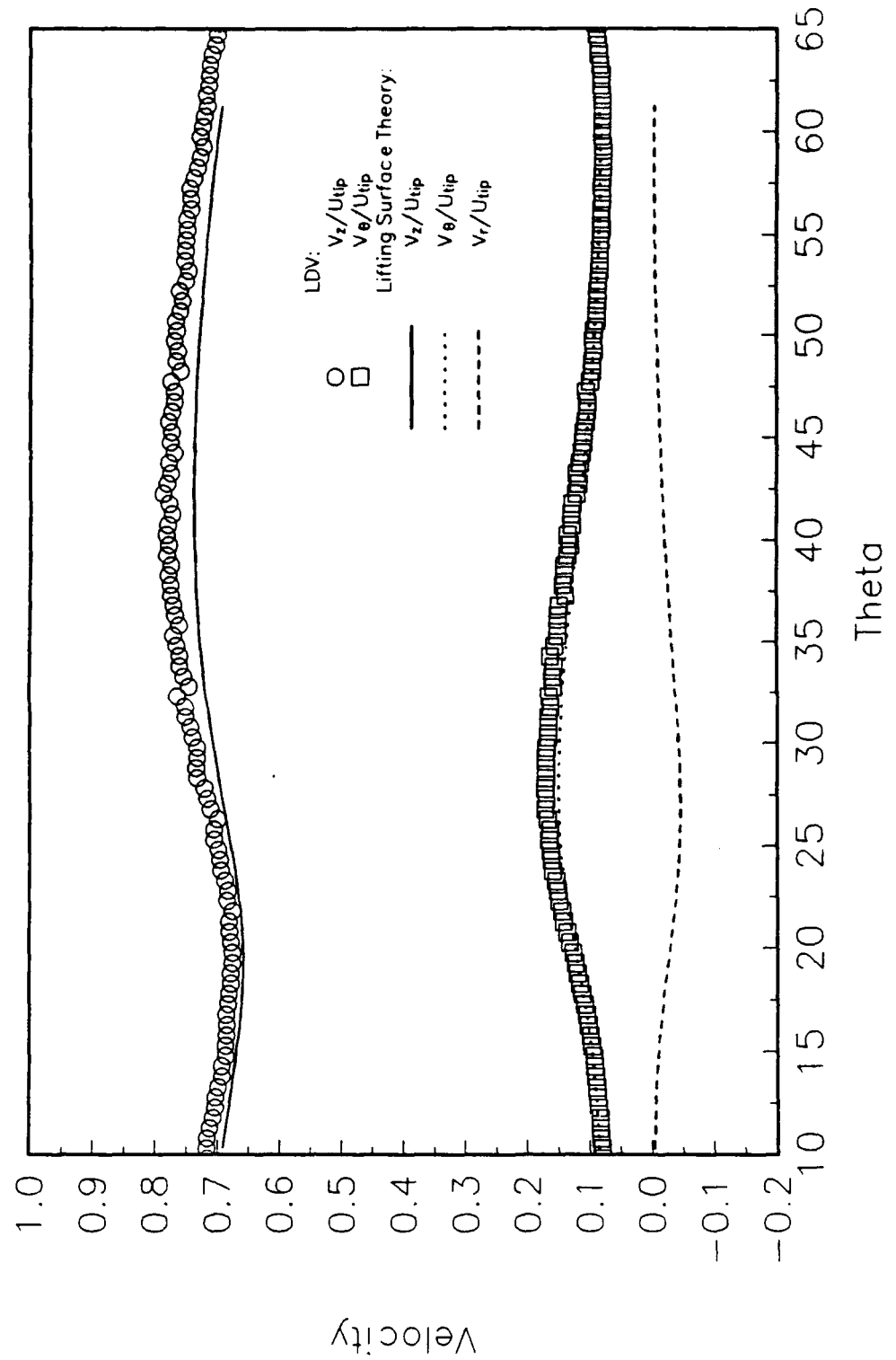


Figure 42. Unsteady Potential Flow Effect at 76.2% Span:
b) 18.7% Chord Axially Upstream of the Rotor Blade Leading Edge

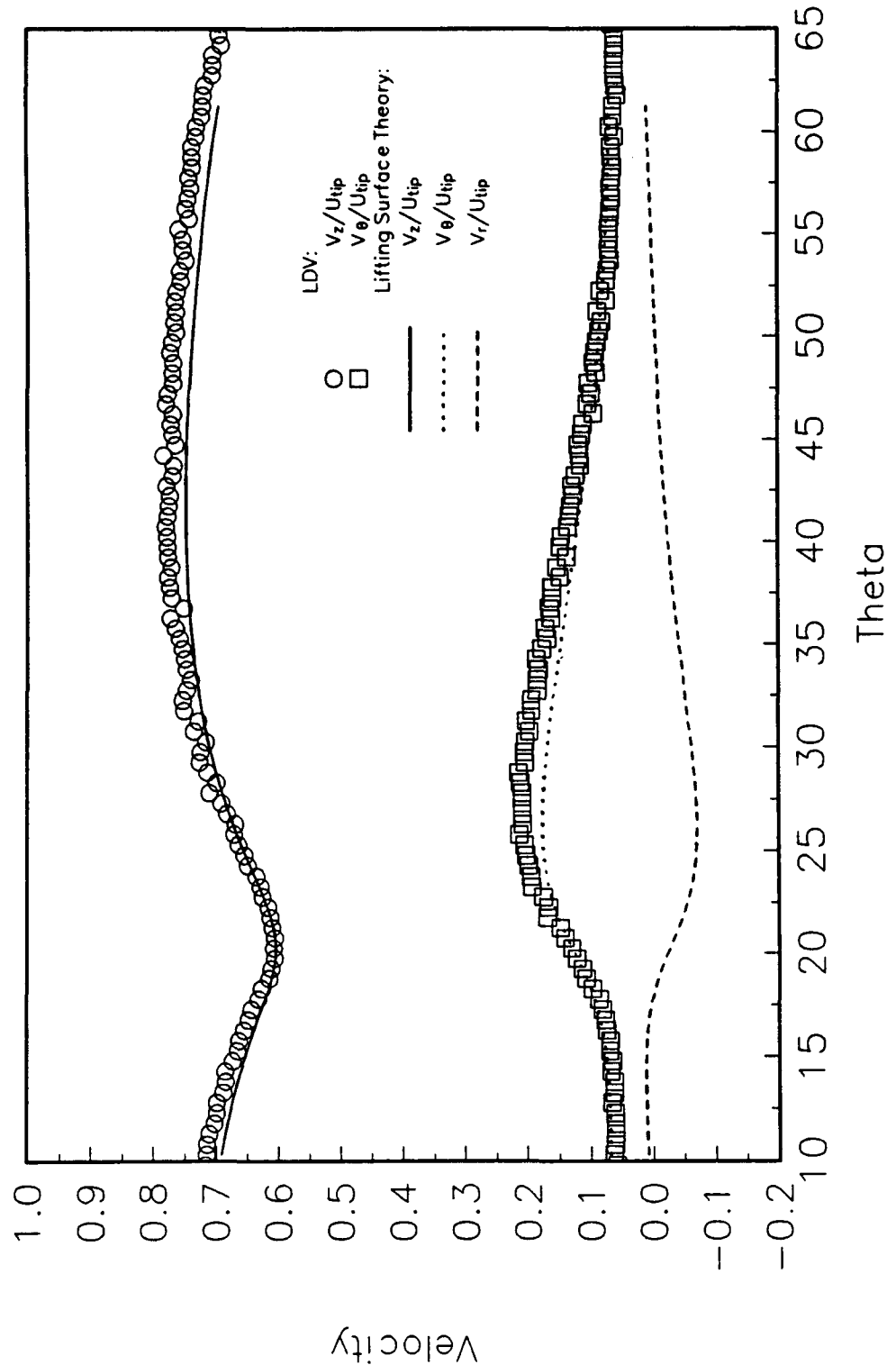


Figure 42. Unsteady Potential Flow Effect at 76.2% Span.
c) 9.4% Chord Axially Upstream of the Rotor Blade Leading Edge

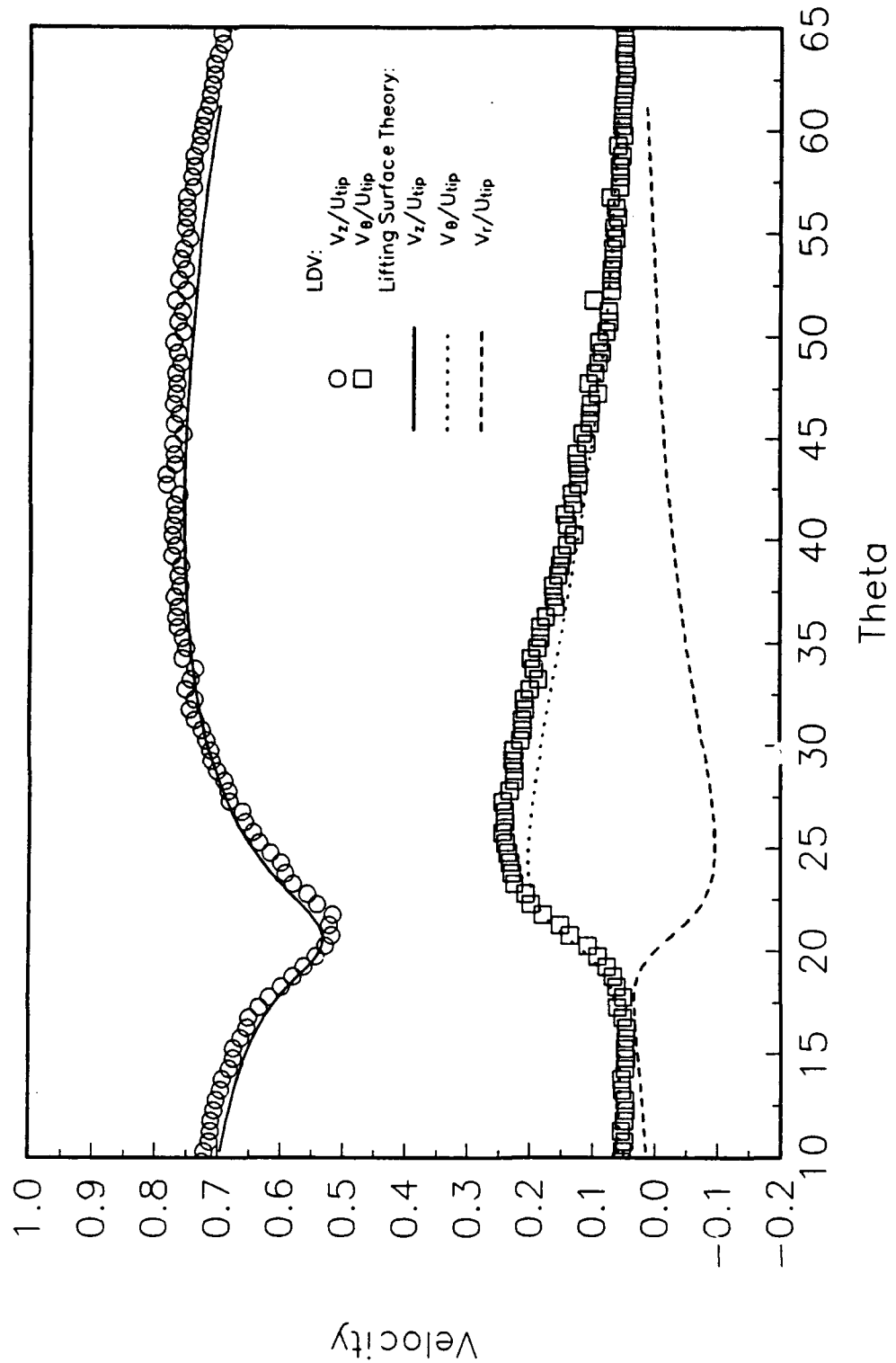


Figure 42. Unsteady Potential Flow Effect at 76.2% Span:
d) 4.7% Chord Axially Upstream of the Rotor Blade Leading Edge

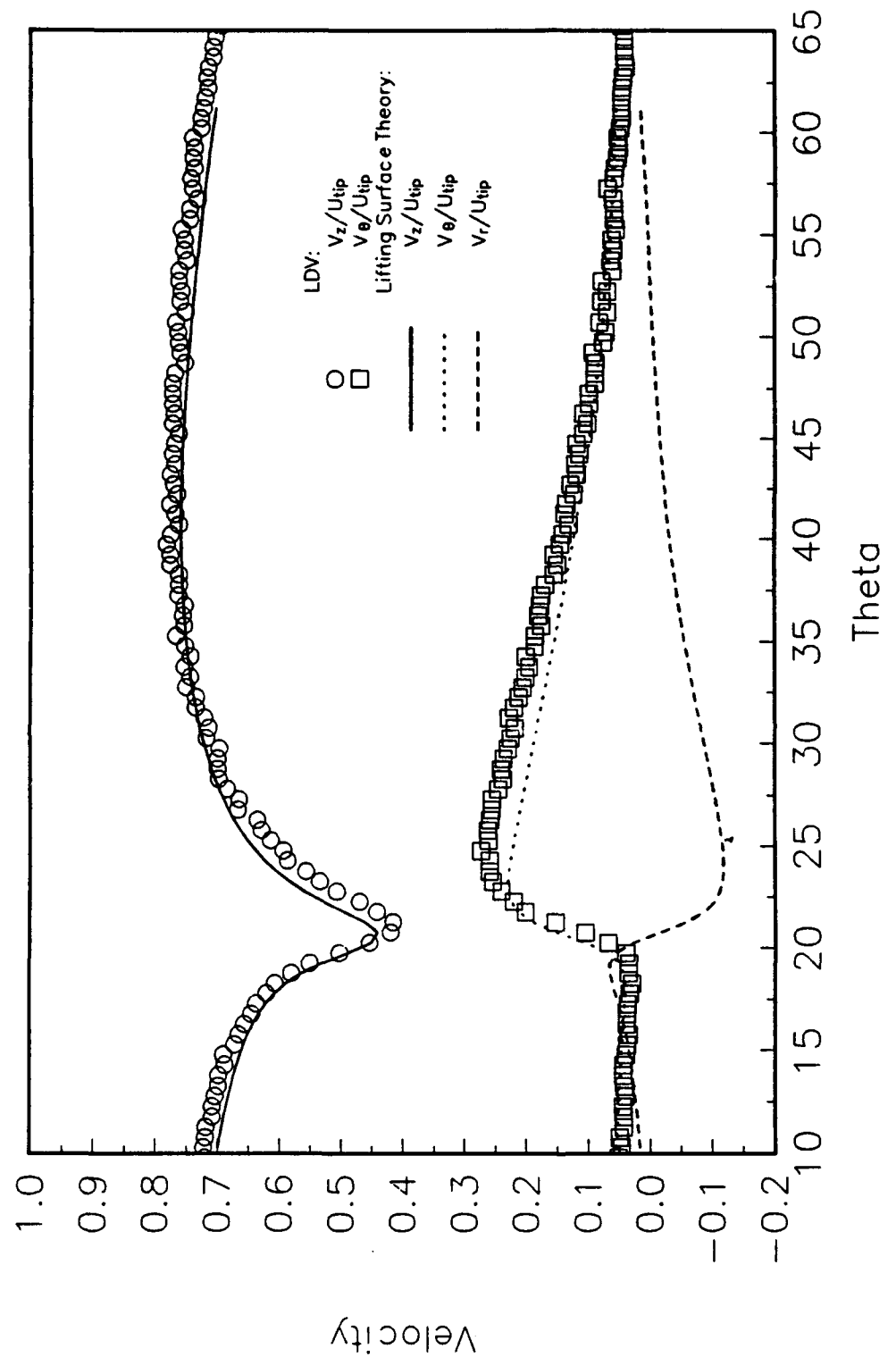


Figure 42. Unsteady Potential Flow Effect at 76.2% Span:
e) 2.3% Chord Axially Upstream of the Rotor Blade Leading Edge

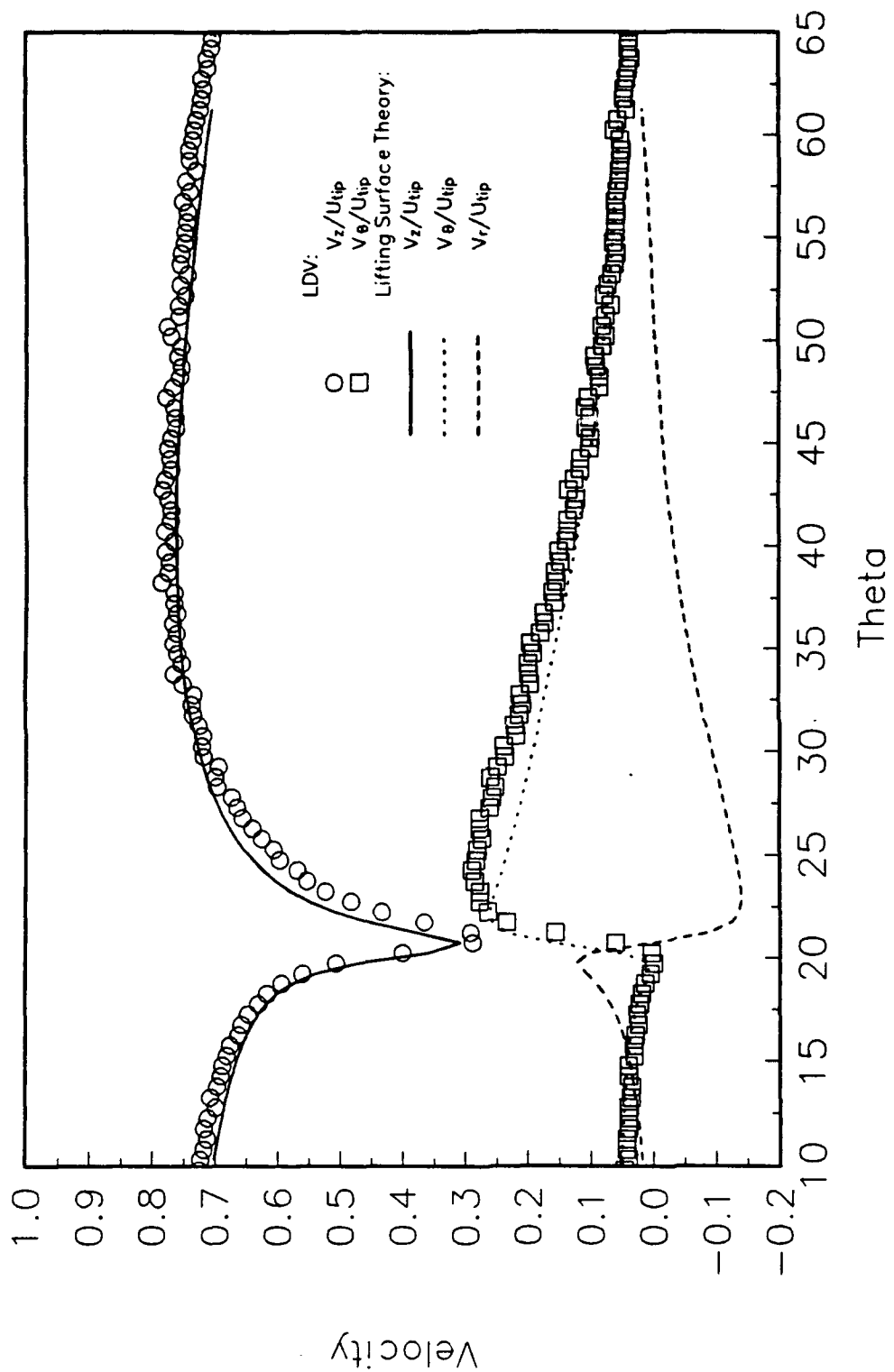


Figure 42. Unsteady Potential Flow Effect at 76.2% Span:
 Ω 0.9% Chord Axially Upstream of the Rotor Blade Leading Edge

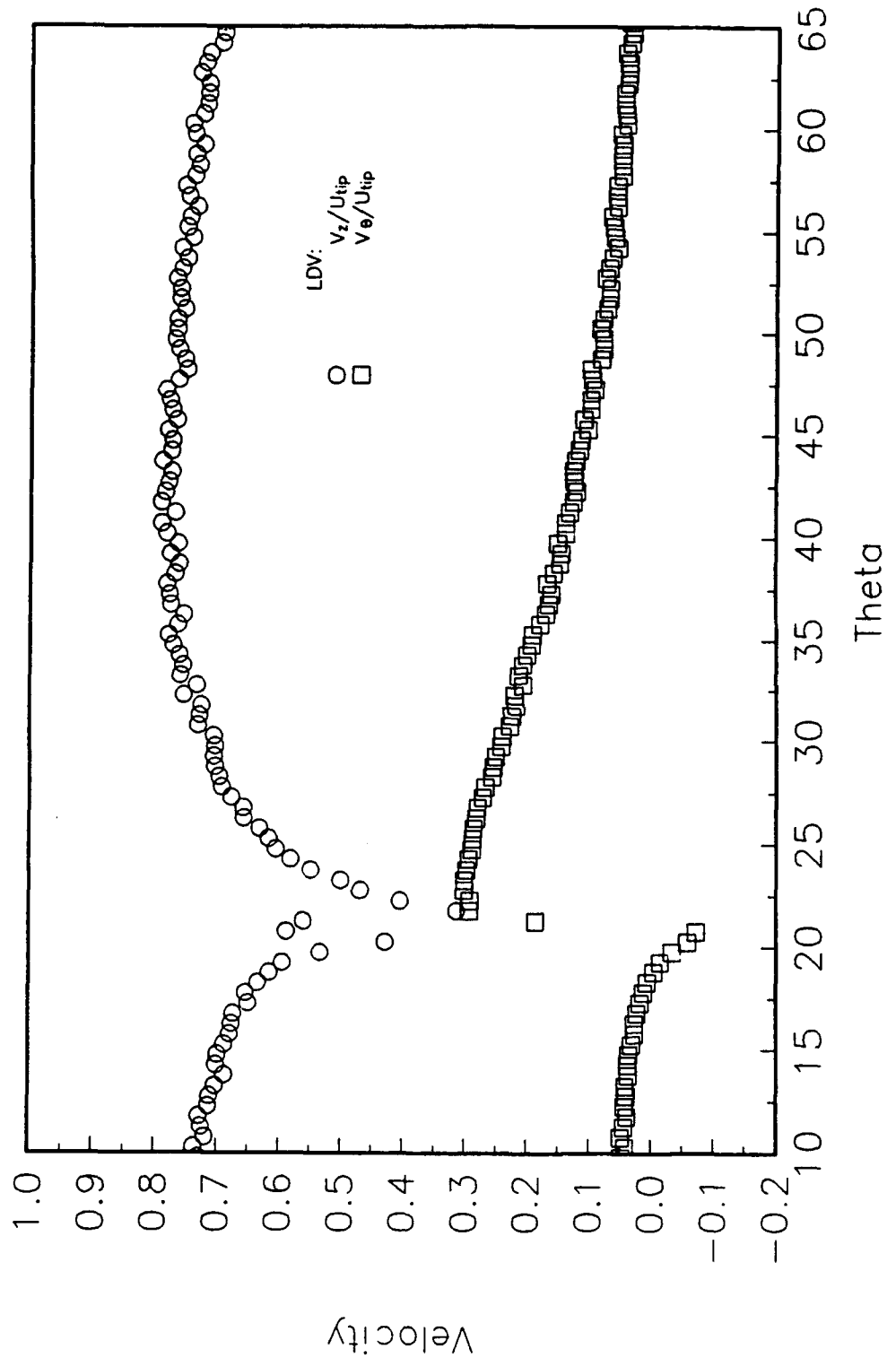


Figure 42. Unsteady Potential Flow Effect at 76.2% Span:
g) at the Rotor Blade Leading Edge

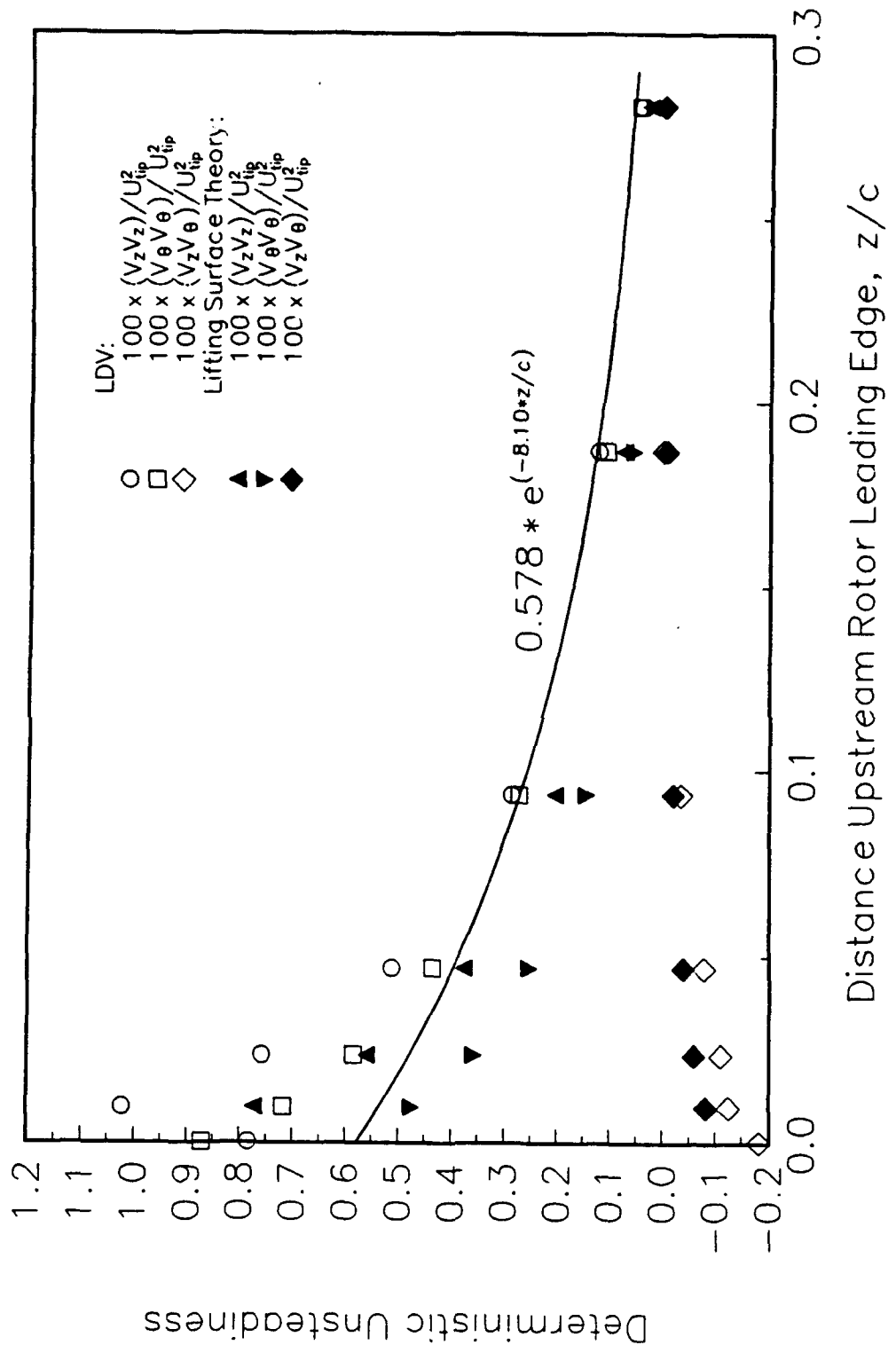


Figure 43. Decay of Deterministic Unsteady Velocity Correlations at 76.2% Chord

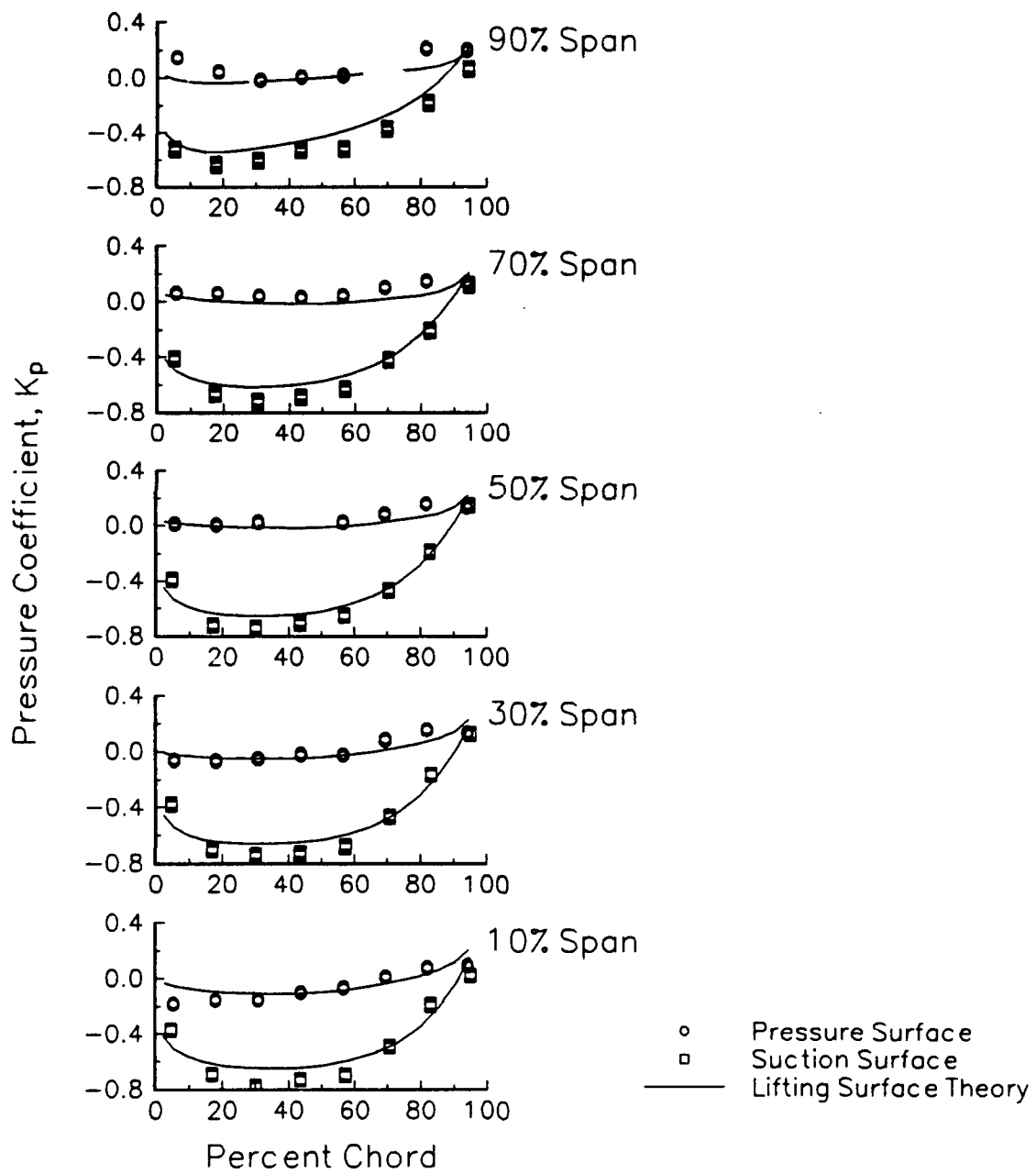


Figure 44. Rotor Blade Static-Pressure Distribution

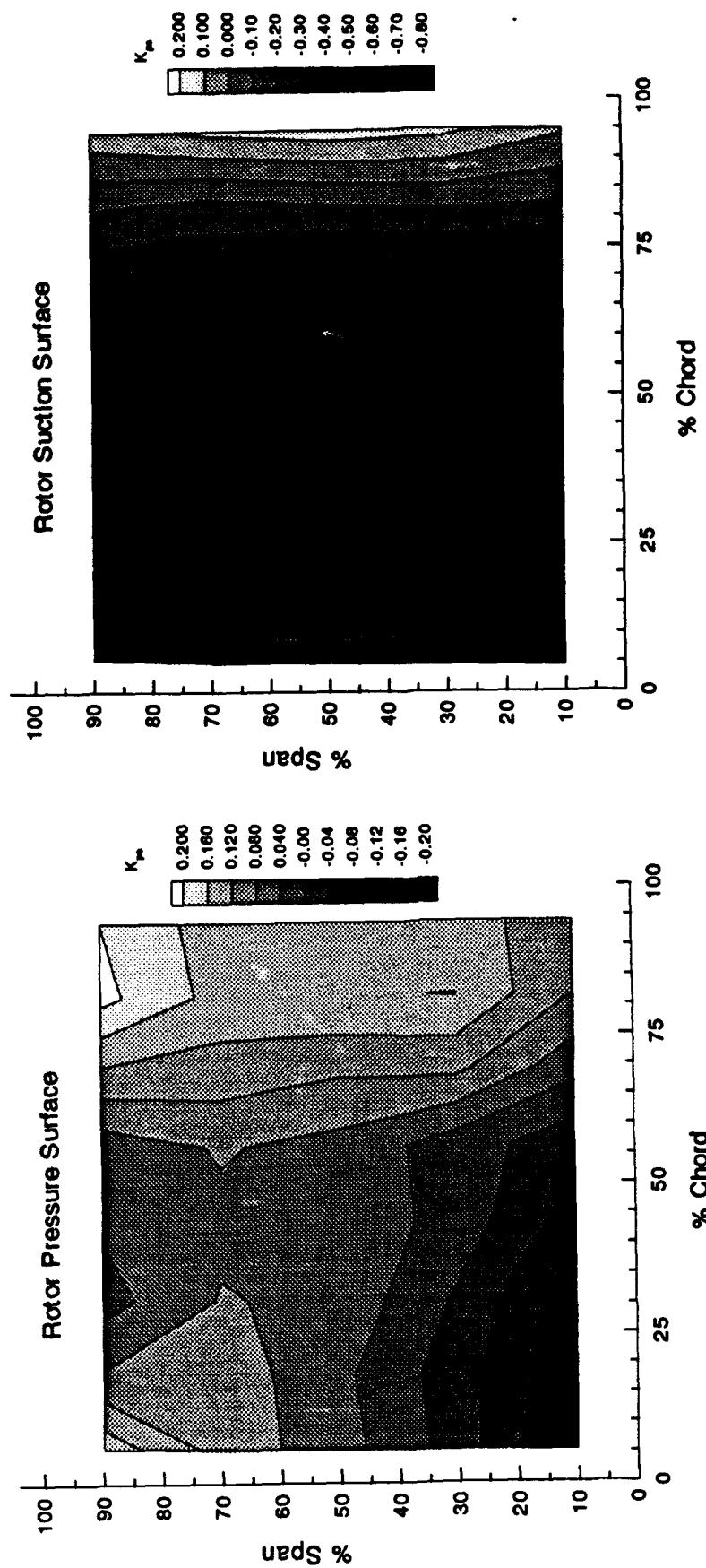


Figure 45. Rotor Blade Static-Pressure Contours

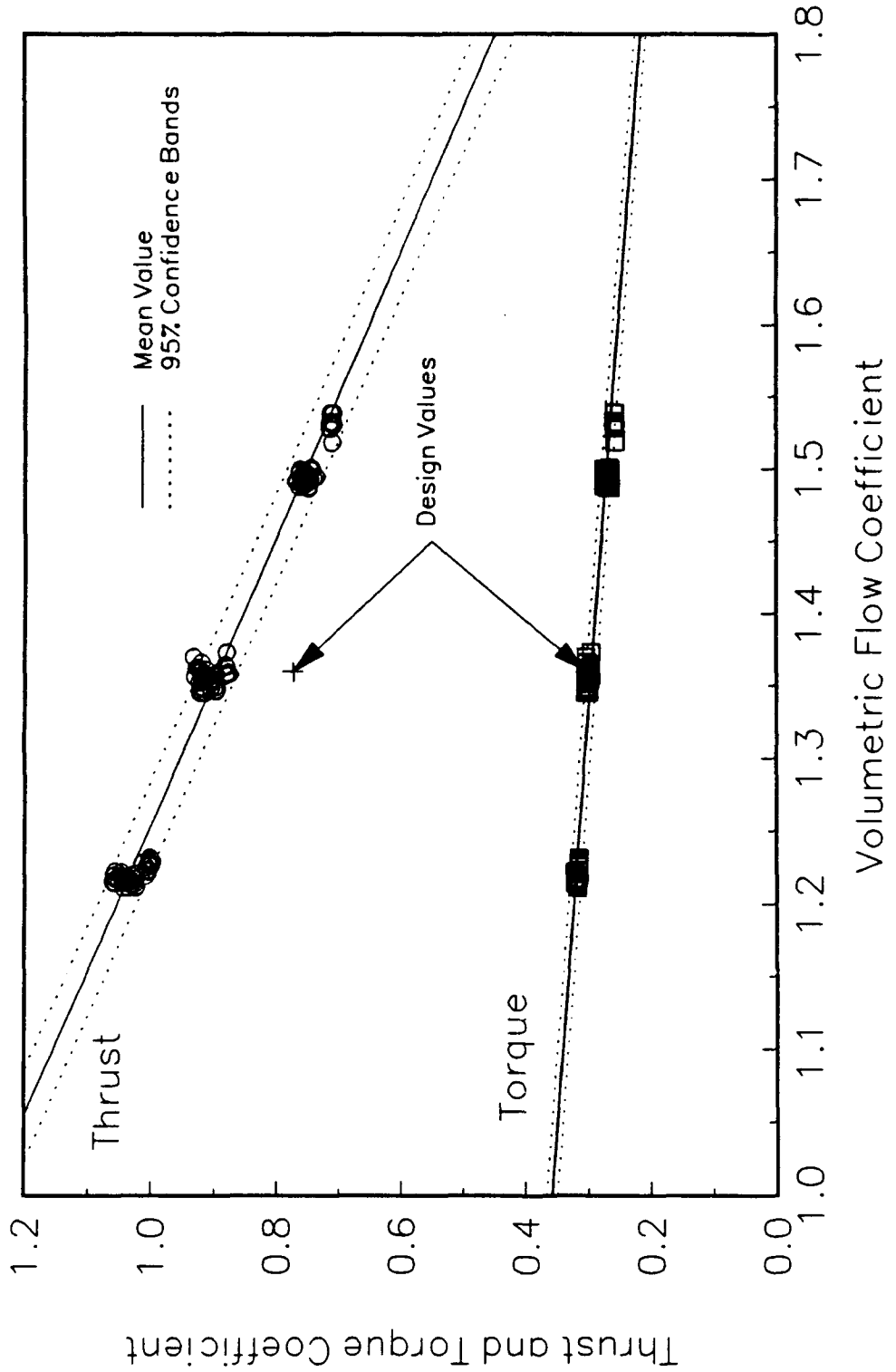


Figure 46. Variation of Rotor Shaft Thrust and Torque with Volumetric Flow Coefficient

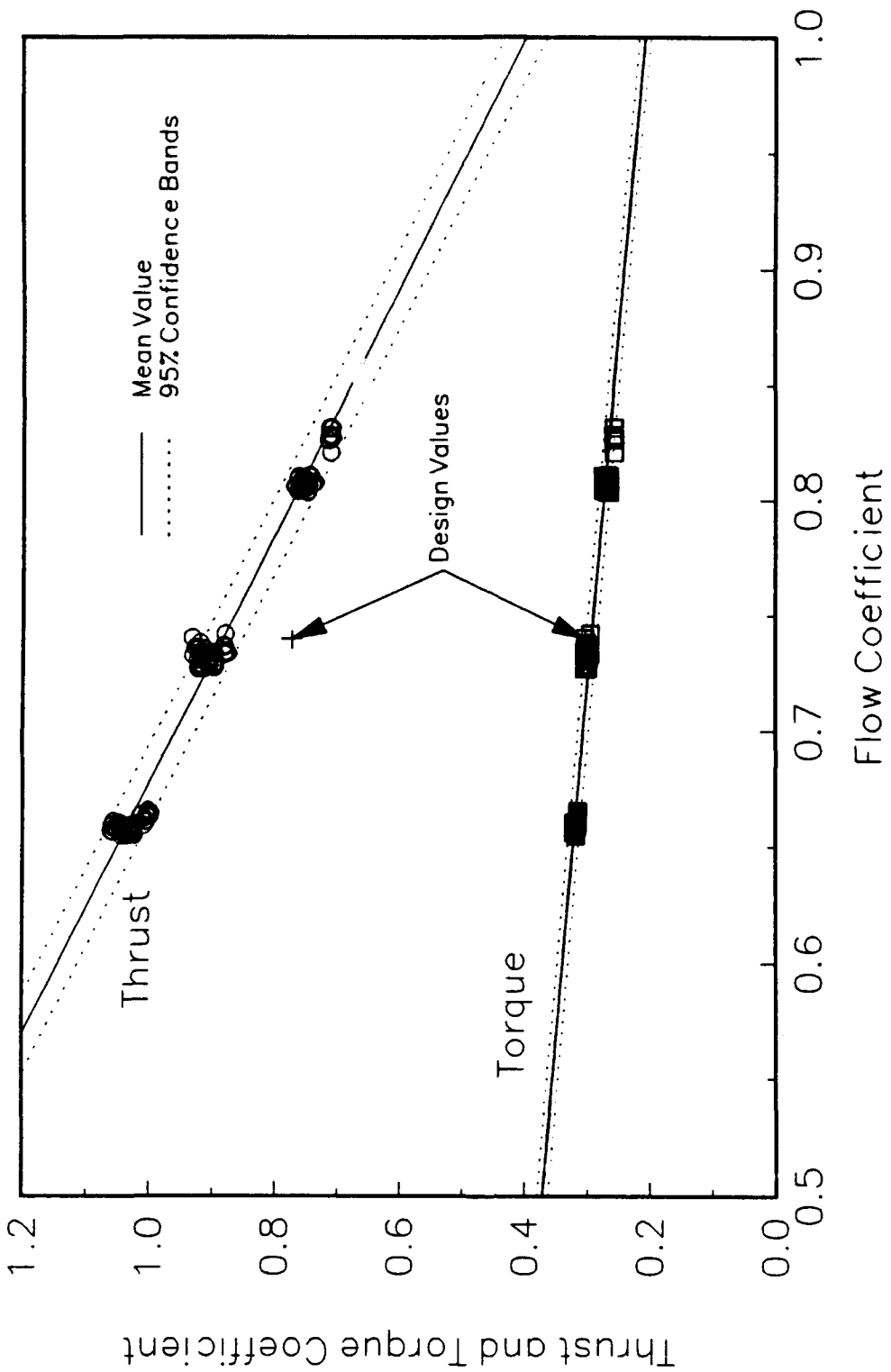


Figure 47. Variation of Rotor Shaft Thrust and Torque with Flow Coefficient

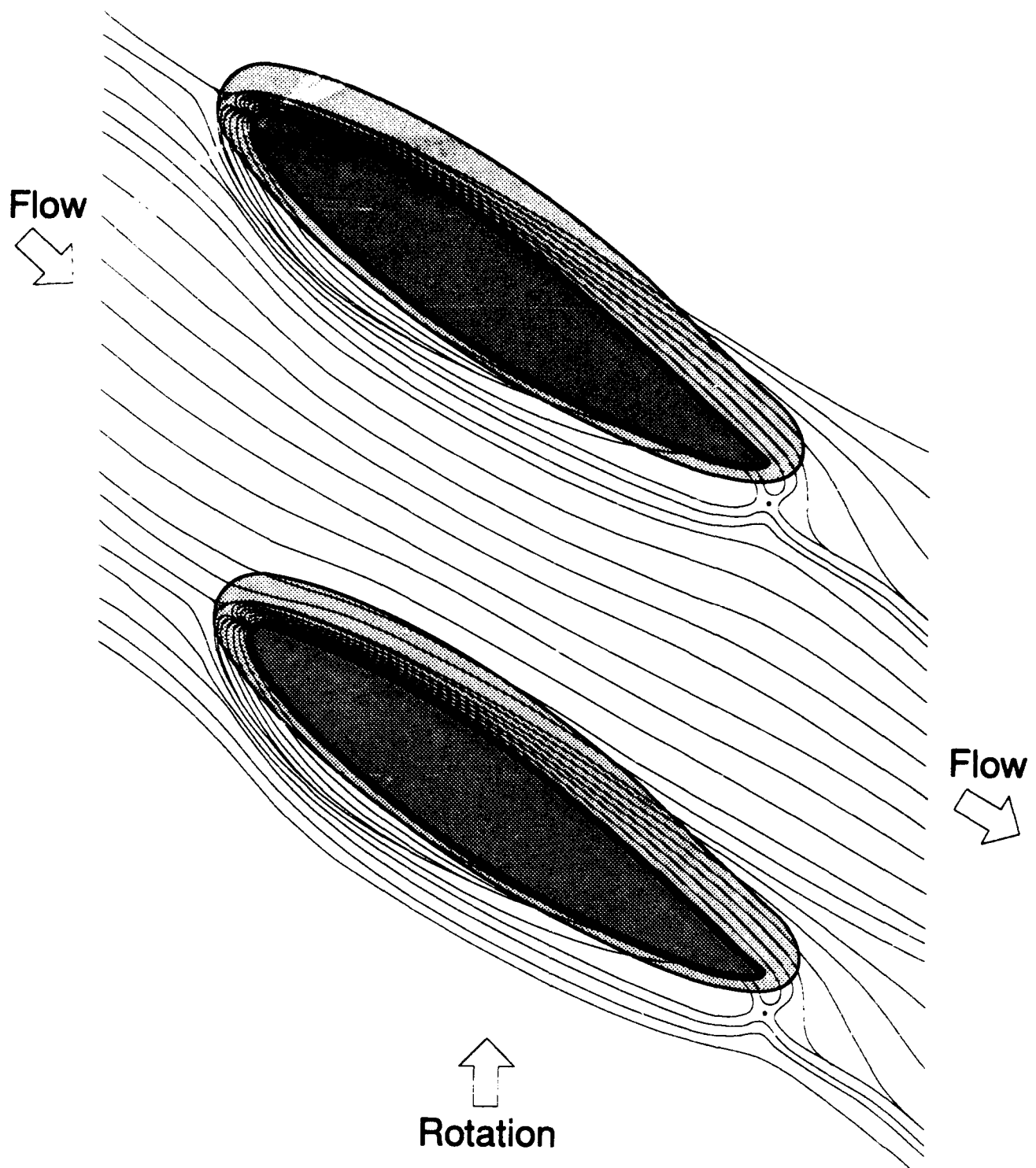


Figure 48. Schematic of Surface Flow Visualization on the Rotor Blade Hub Surface

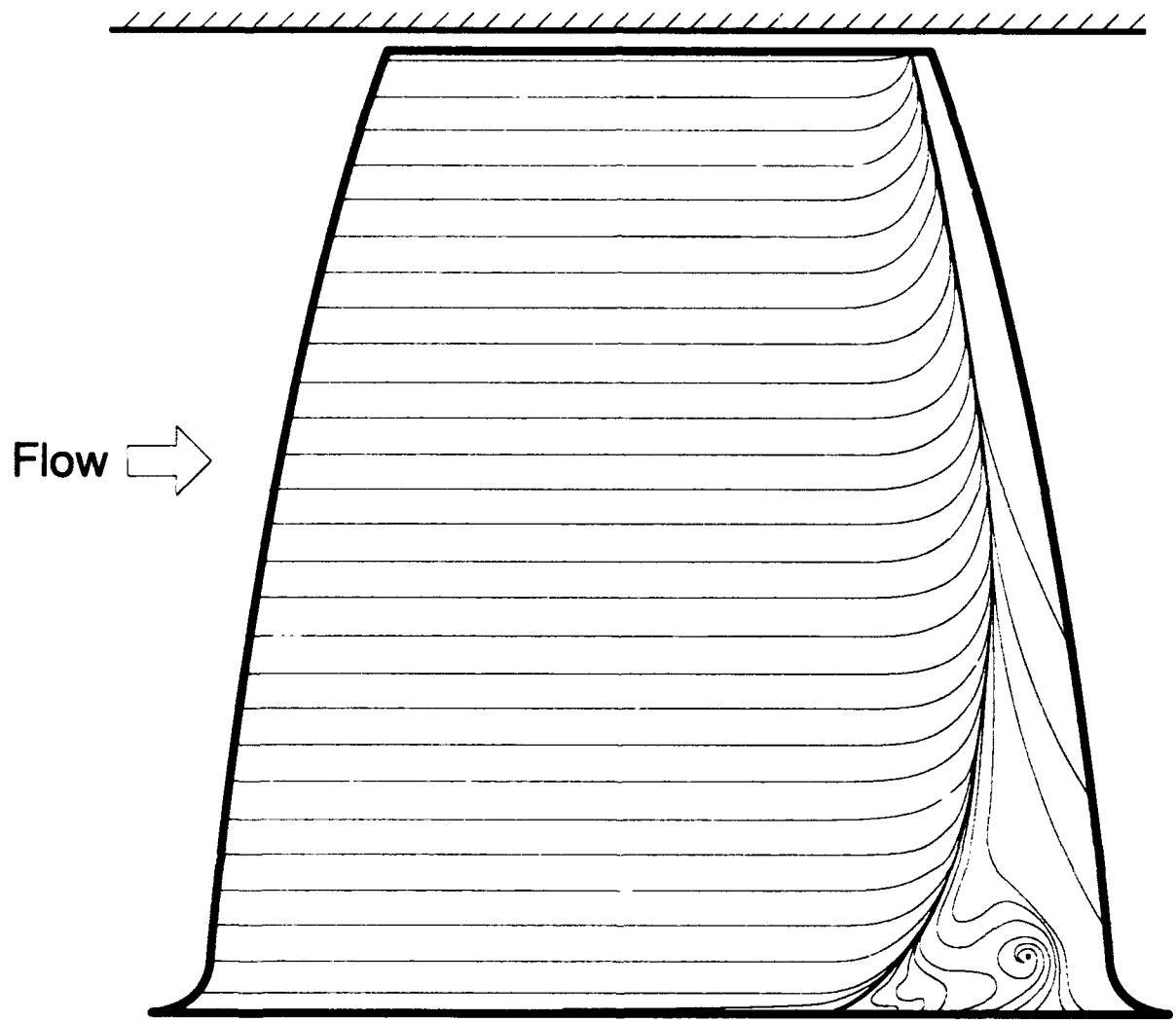


Figure 49. Schematic of Surface Flow Visualization on the Rotor Blade Suction Surface

Flow 

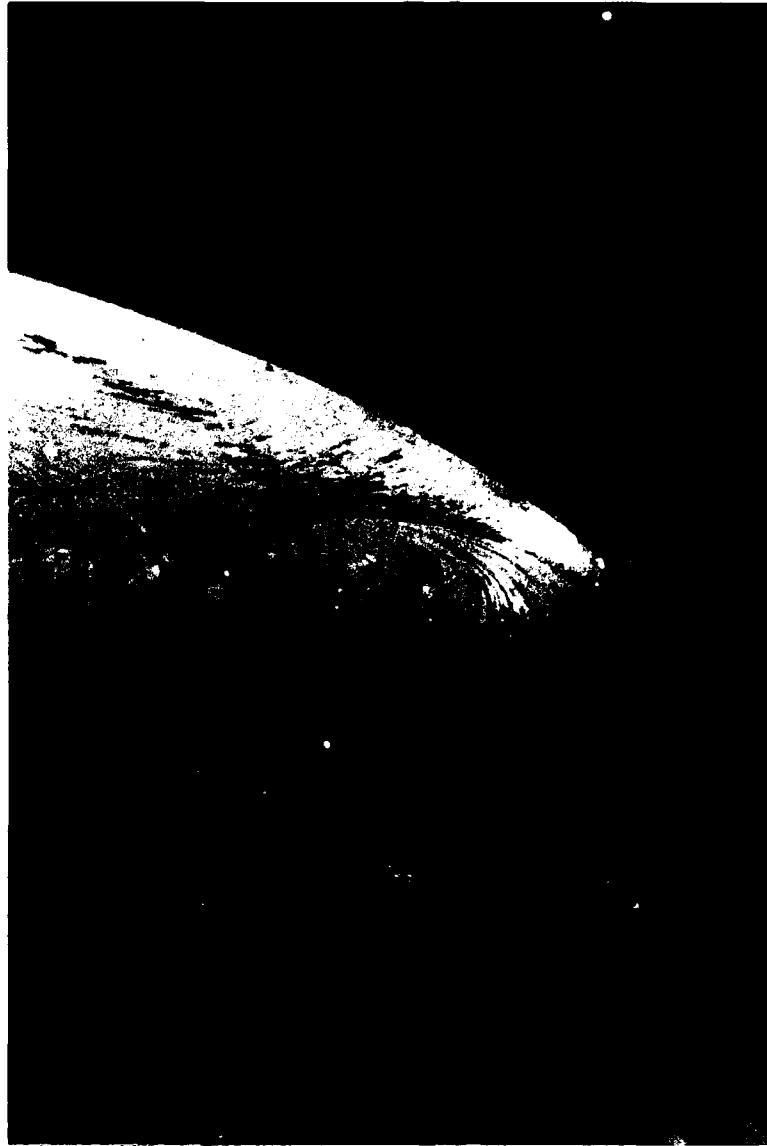


Figure 50. Photograph of the Surface Flow Visualization Showing the Rotor Blade Suction Surface Corner Separation

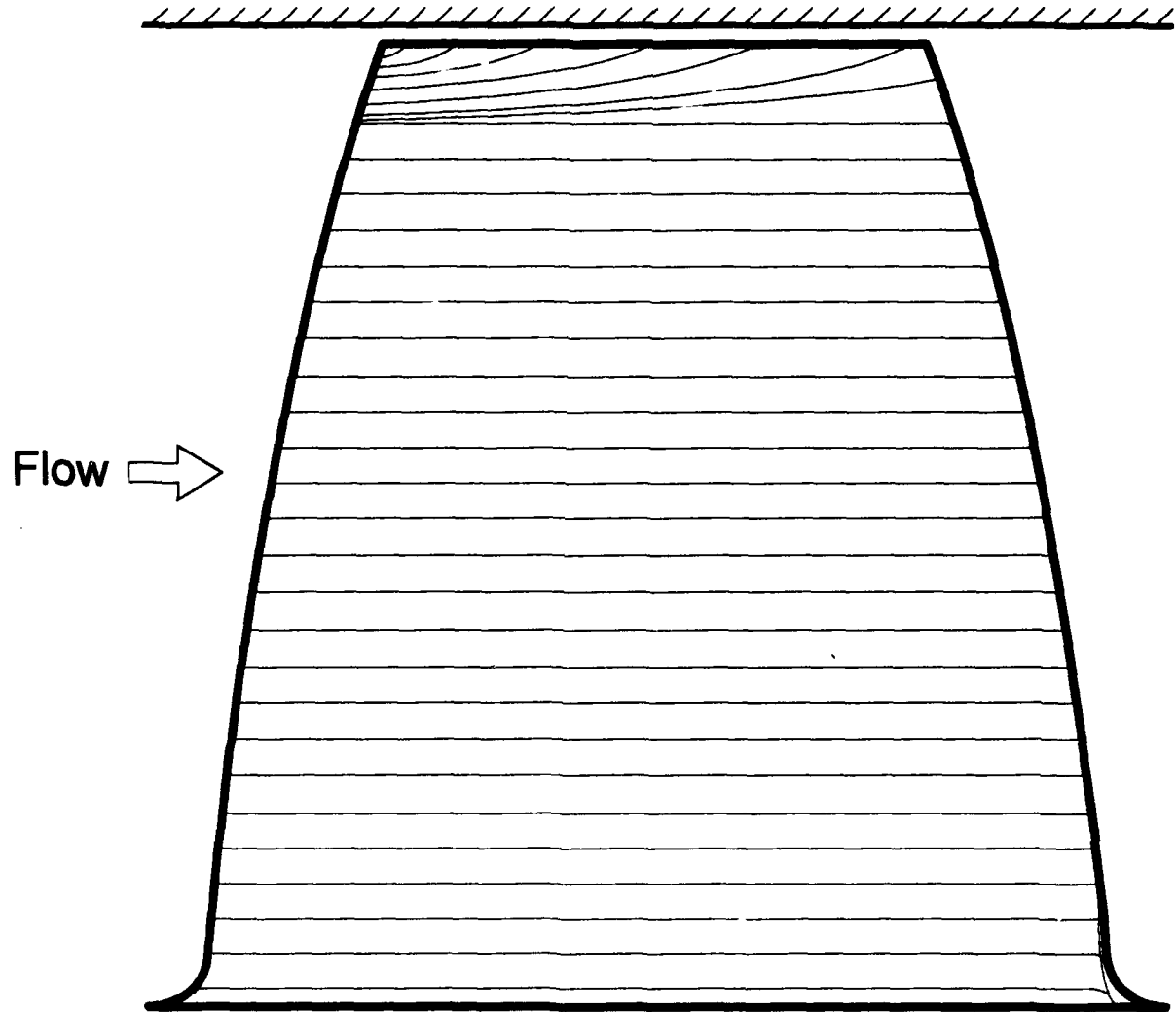


Figure 51. Schematic of Surface Flow Visualization on the Rotor Blade Pressure Surface

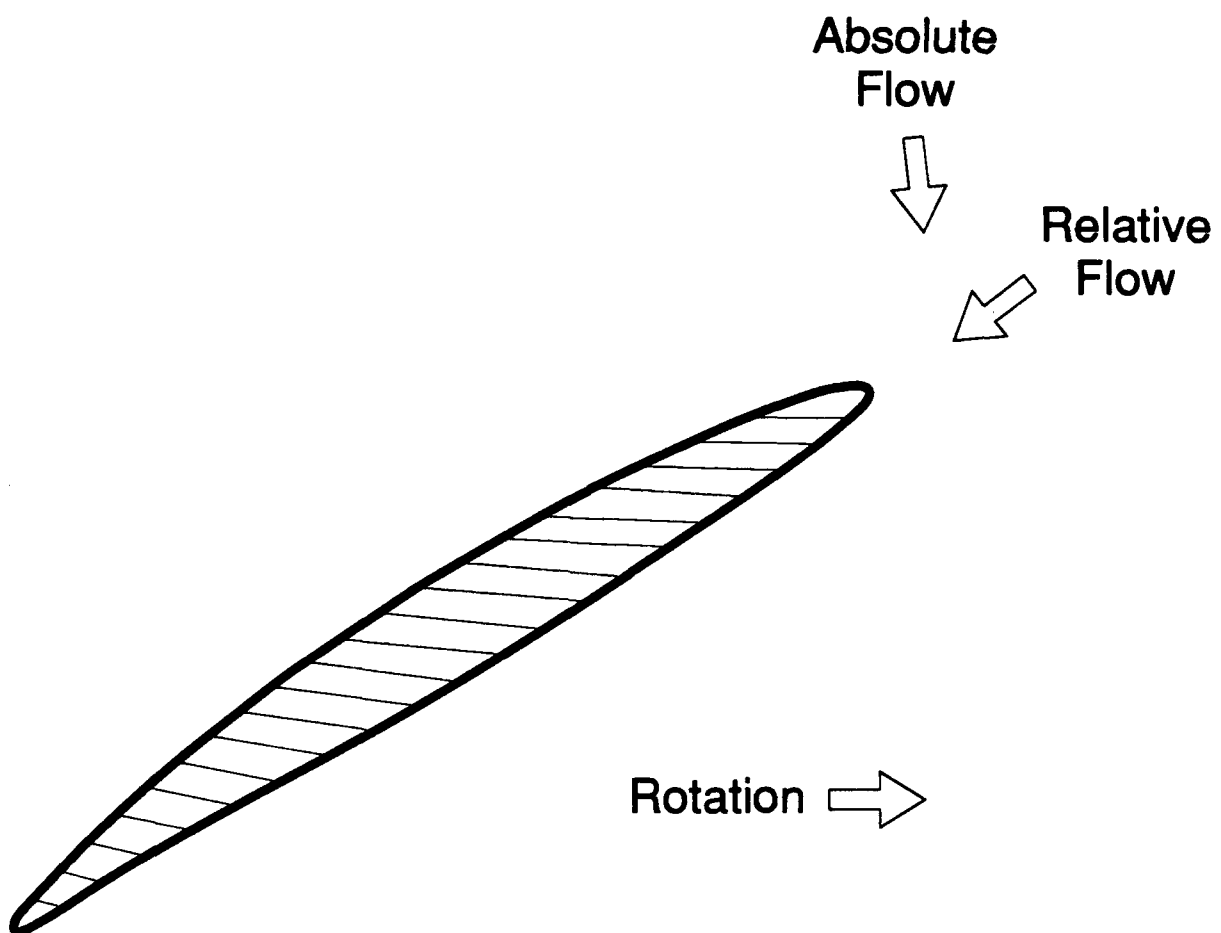


Figure 52. Schematic of Surface Flow Visualization on the Rotor Blade Tip Section

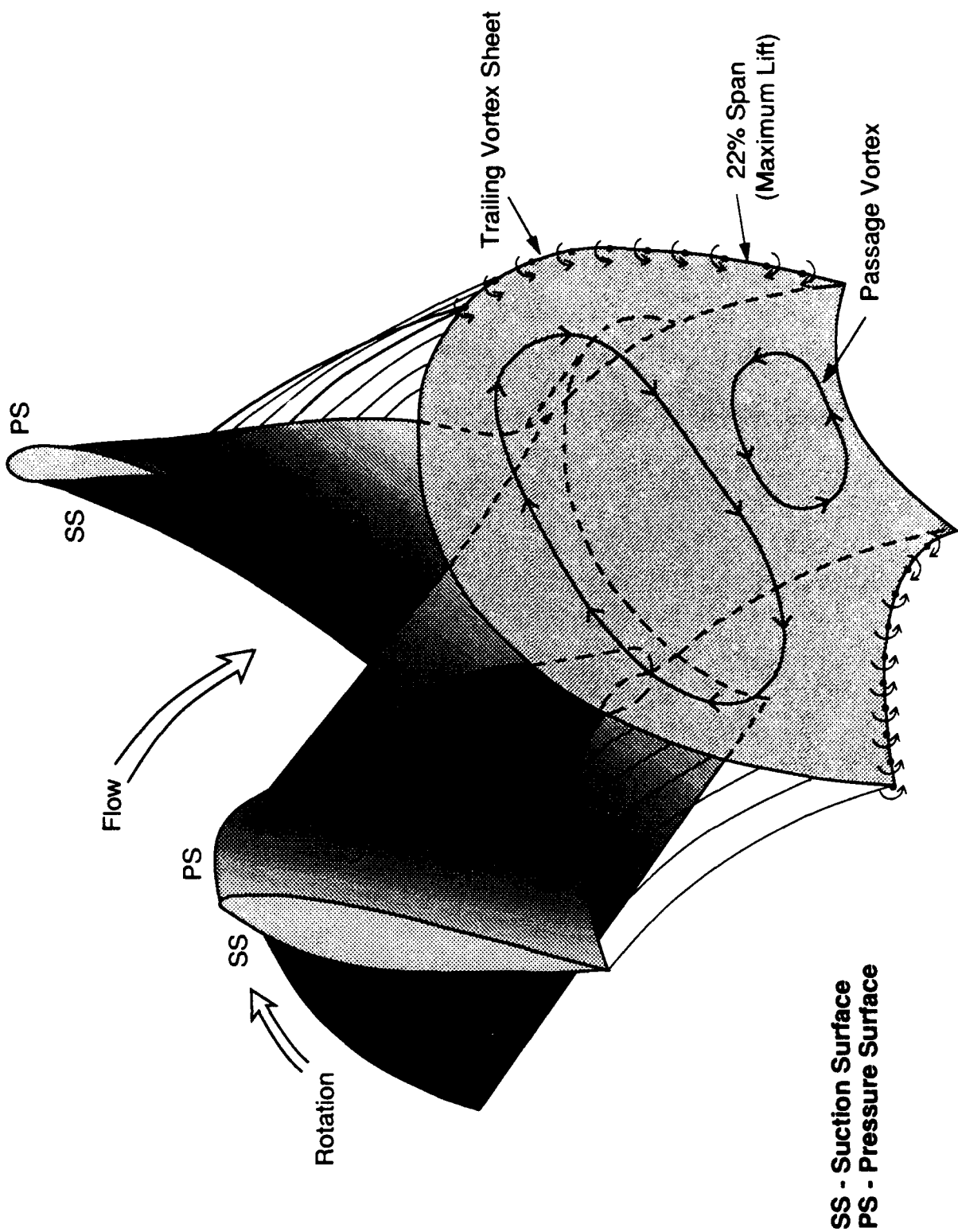


Figure 53. Schematic of Rotor Blade Secondary Flow: Interpretation of Surface Flow Visualization

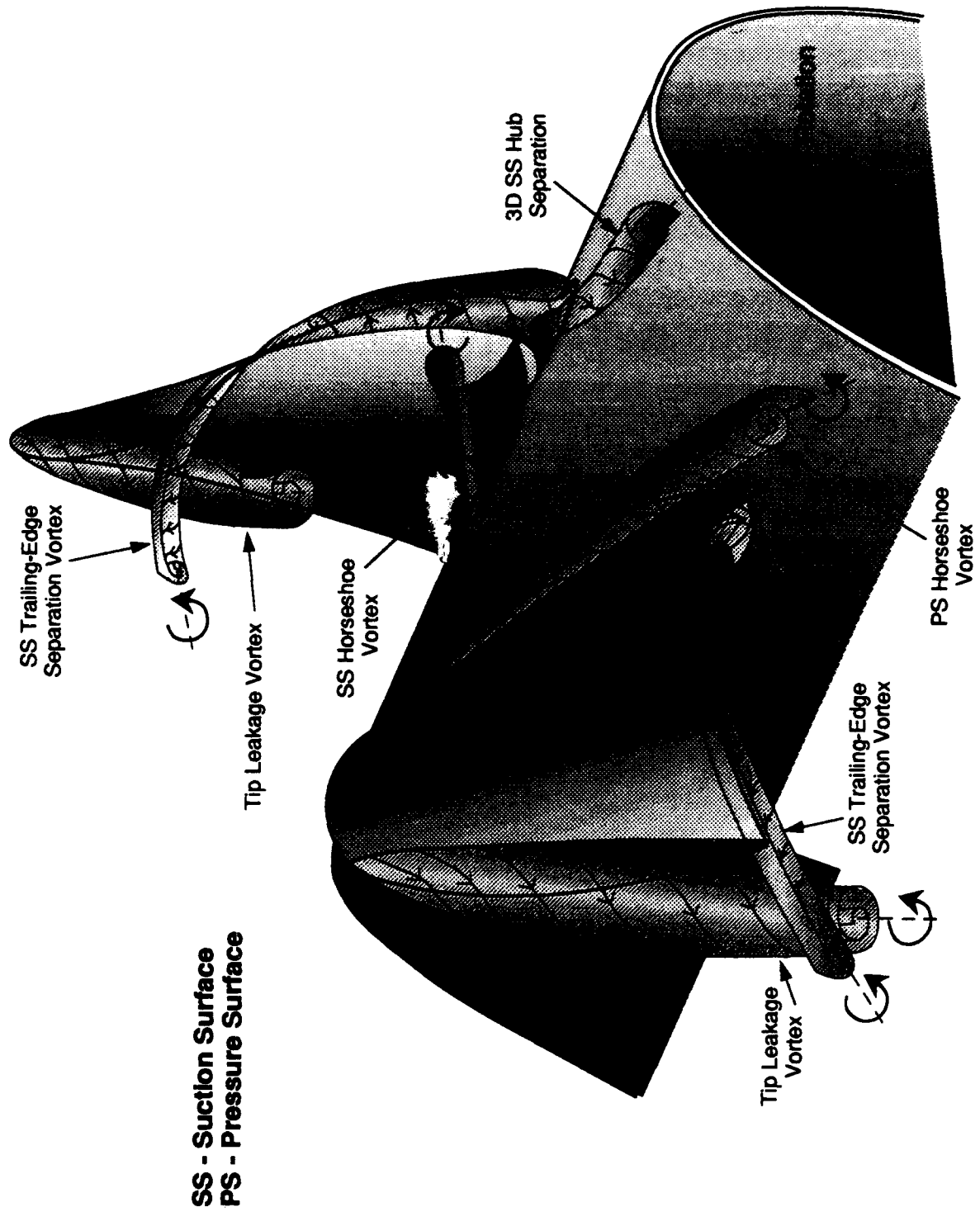


Figure 54. Schematic of Rotor Blade Secondary Flow: Passage Vortices and Trailing Vortex Sheets

Figure 54.

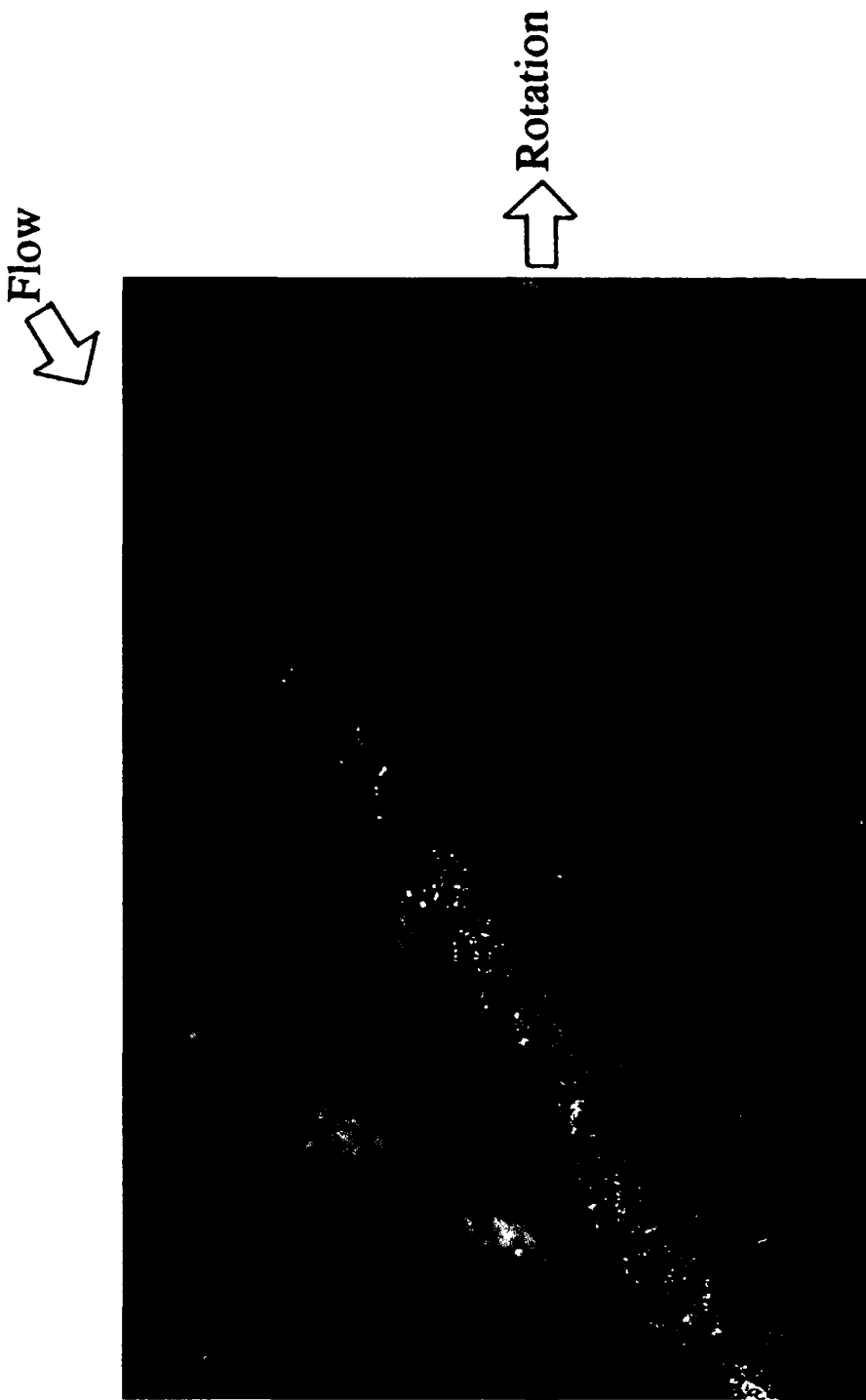


Figure 55. Photograph of a Cavitating Rotor Tip Leakage Vortex and a Cavitating Trailing-Edge Separation Vortex Near a Rotor Blade Tip Section (Farrell [1989])

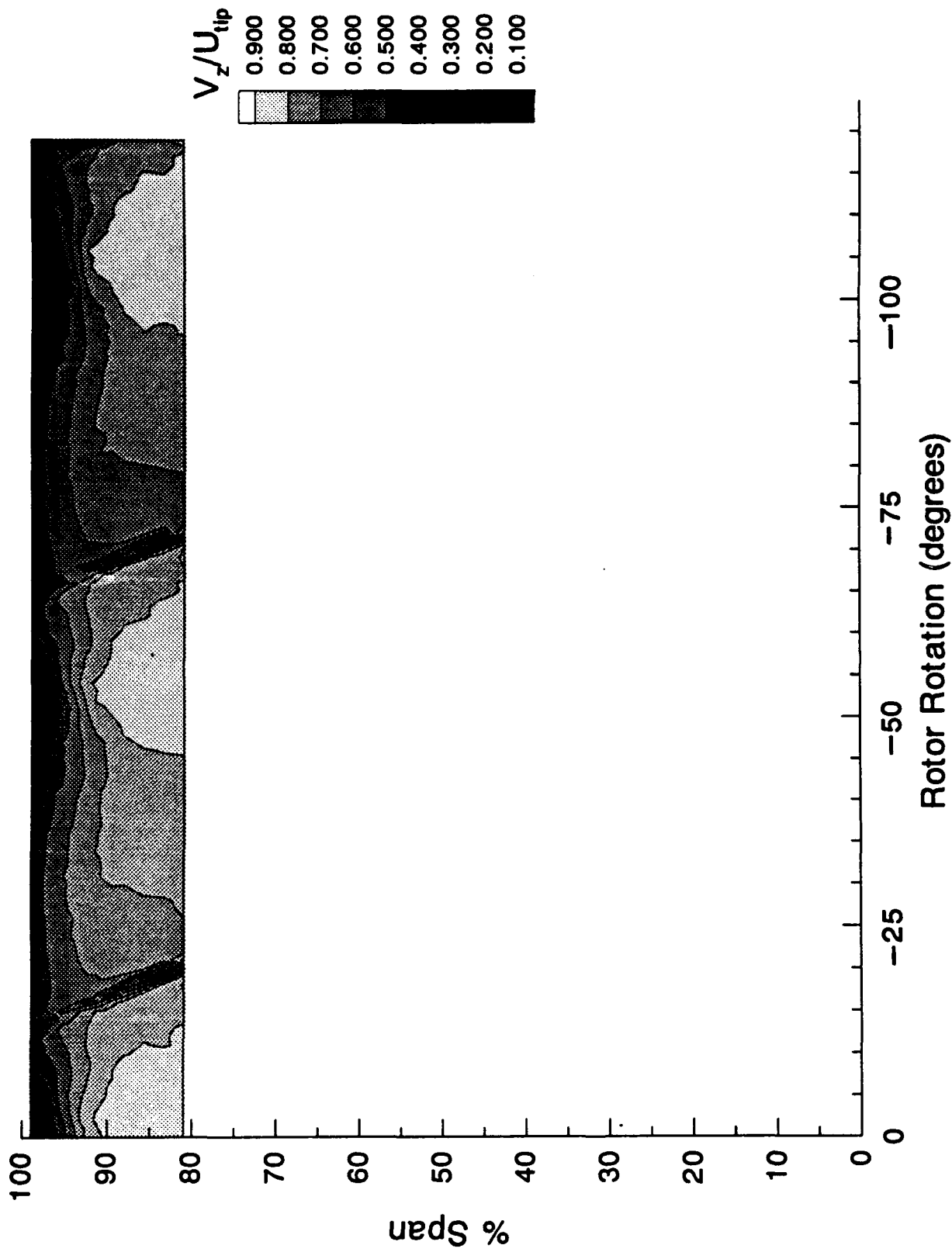


Figure 56. Axial Velocity Contours of LDV Measurements:
a) 4.8% Chord Axially Downstream of the Rotor Tip Trailing Edge

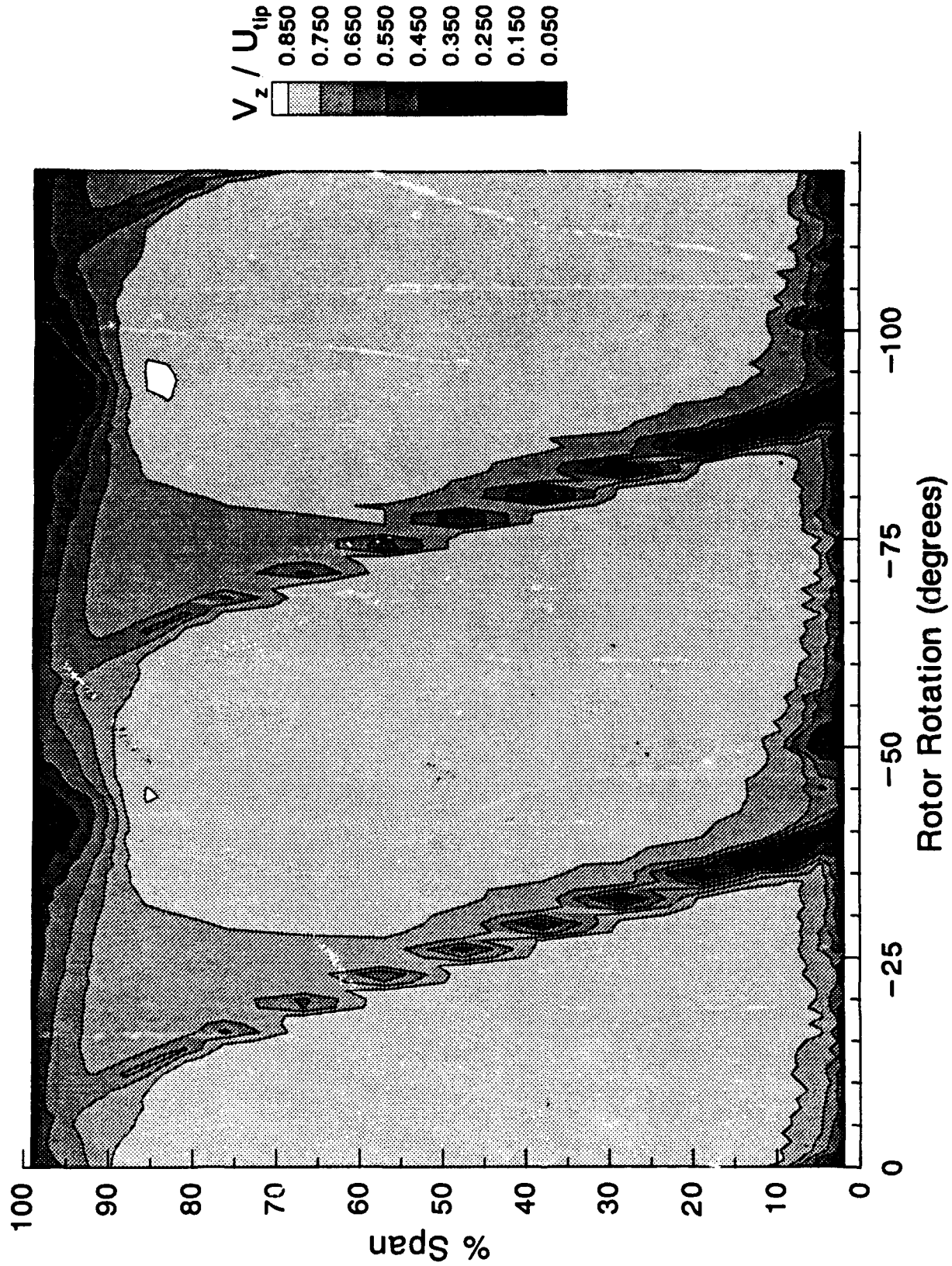


Figure 56. Axial Velocity Contours of LDV Measurements:
b) 21.4% Chord Axially Downstream of the Rotor Tip Trailing Edge

185

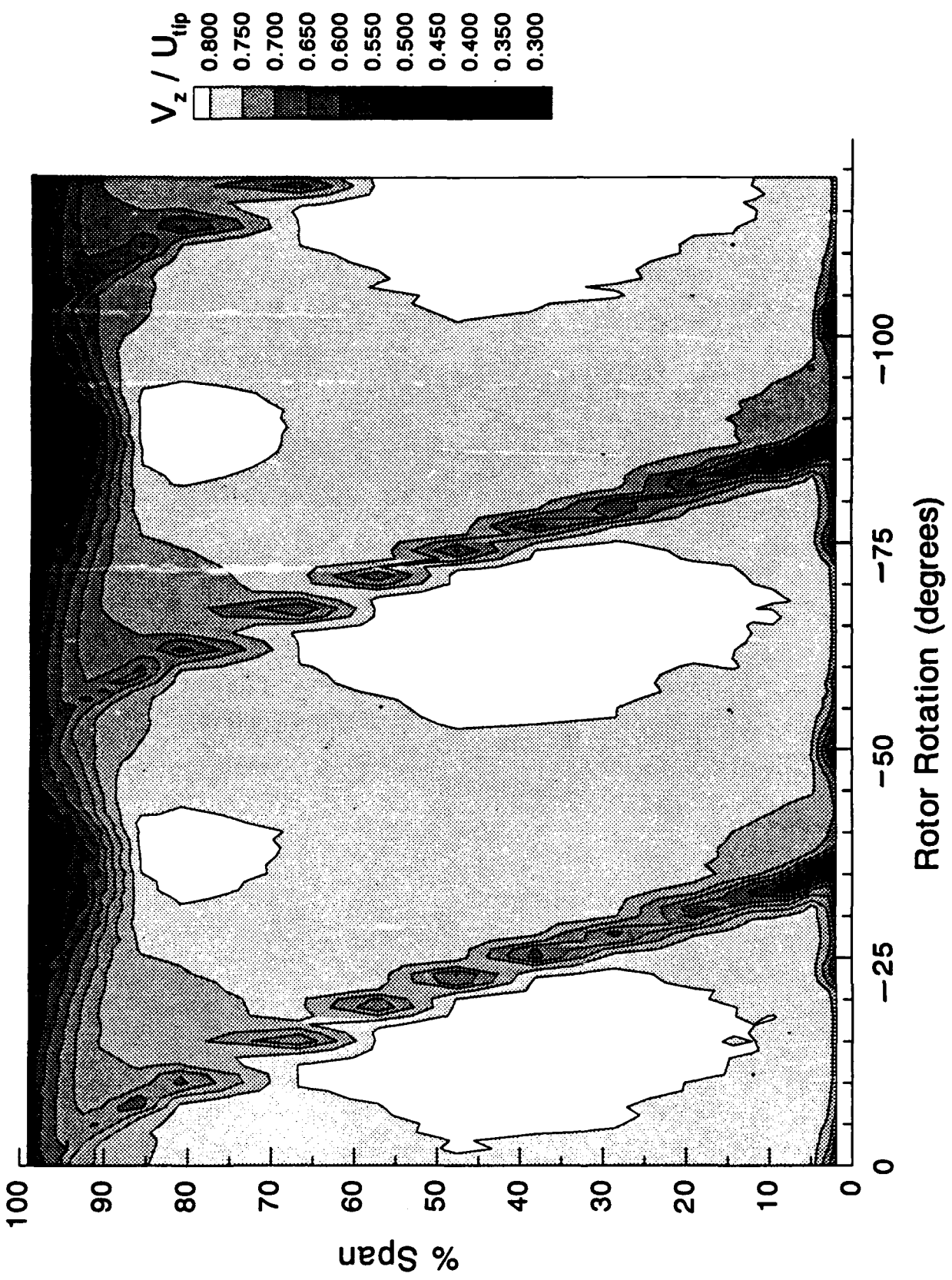


Figure 56. Axial Velocity Contours of LDV Measurements:
c) 32.2% Chord Axially Downstream of the Rotor Tip Trailing Edge

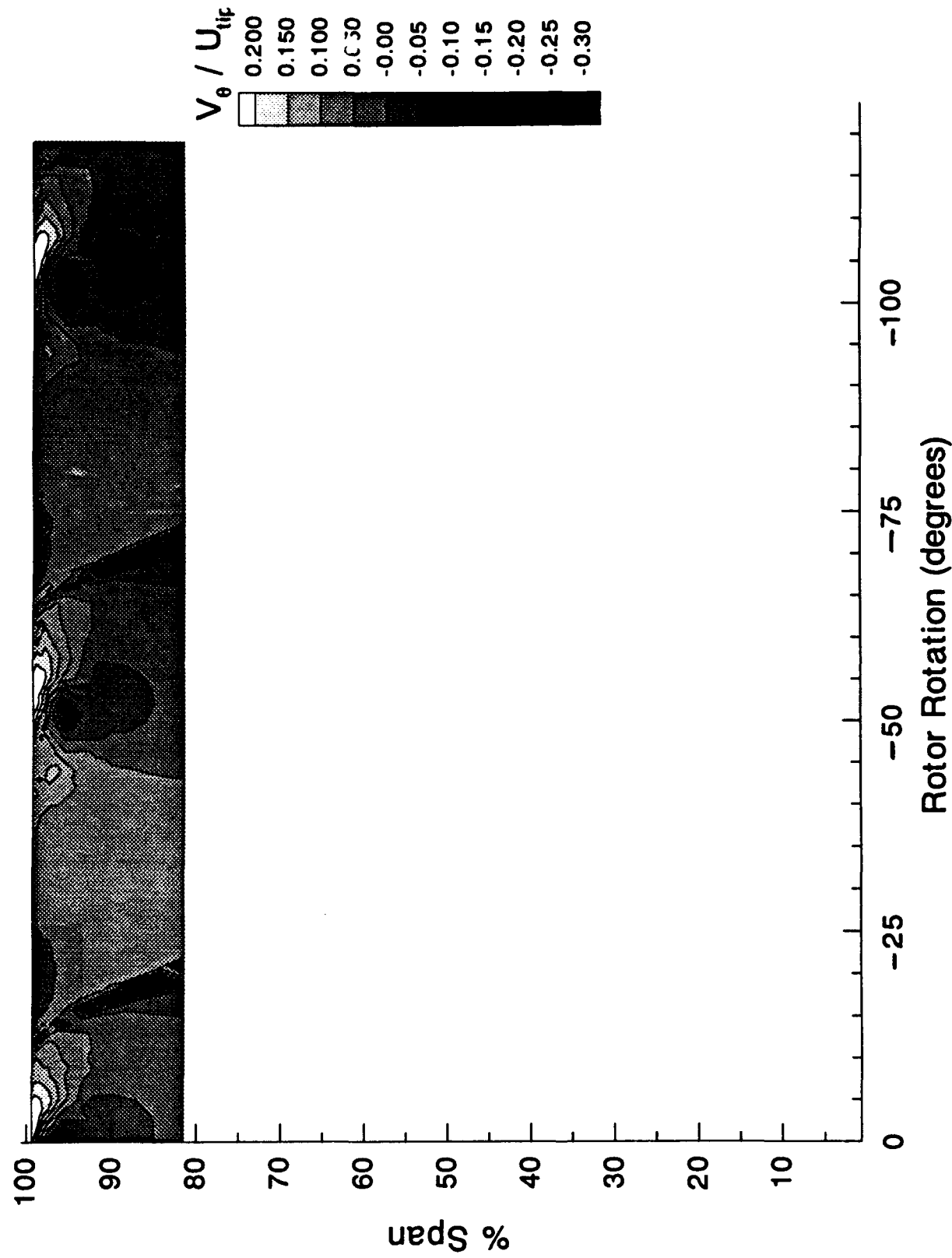


Figure 57. Tangential Velocity Contours of LDV Measurements:
a) 4.8% Chord Axially Downstream of the Rotor Tip Trailing Edge

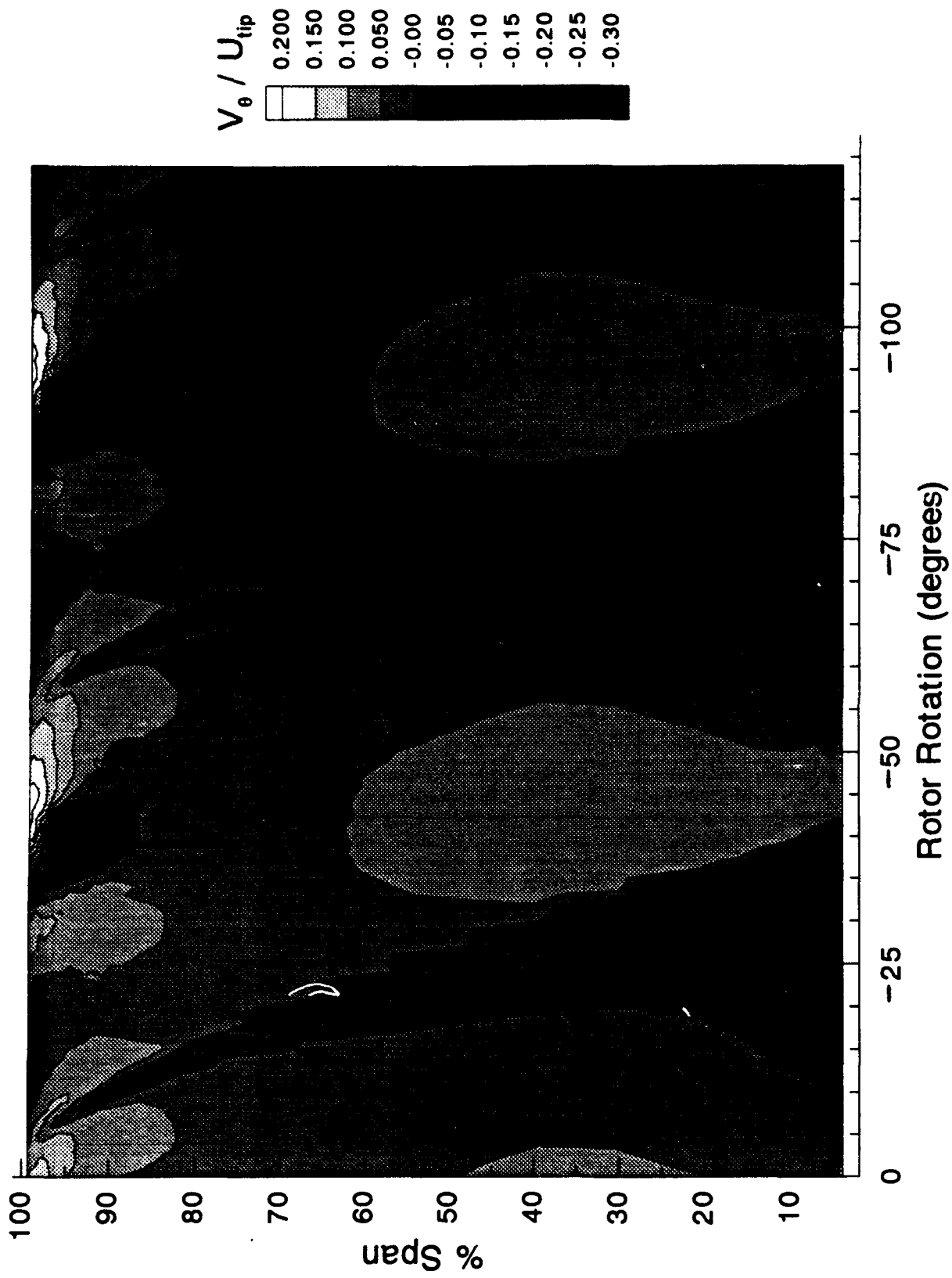


Figure 57. Tangential Velocity Contours of LDV Measurements:
b) 21.4% Chord Axially Downstream of the Rotor Tip Trailing Edge

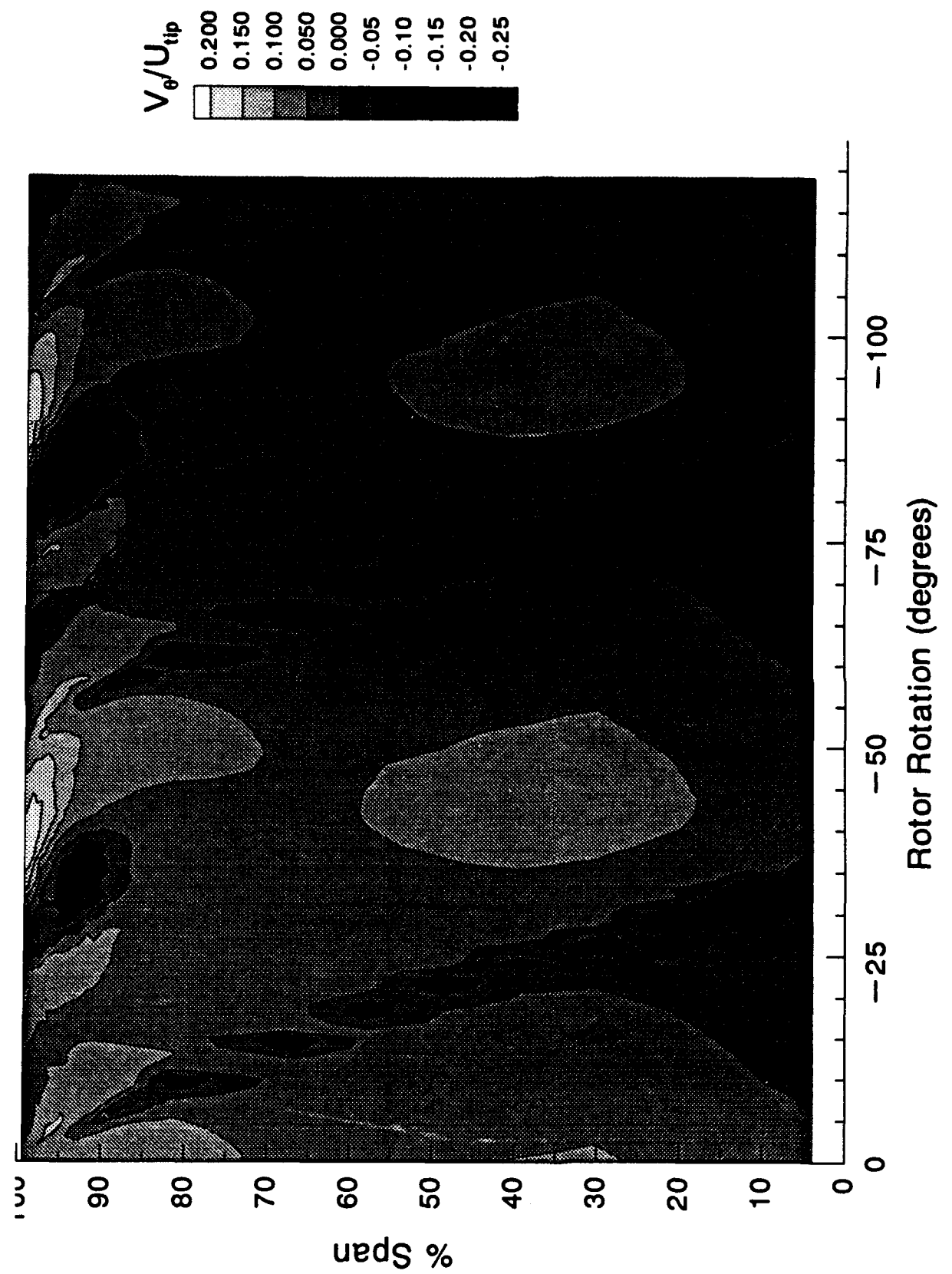
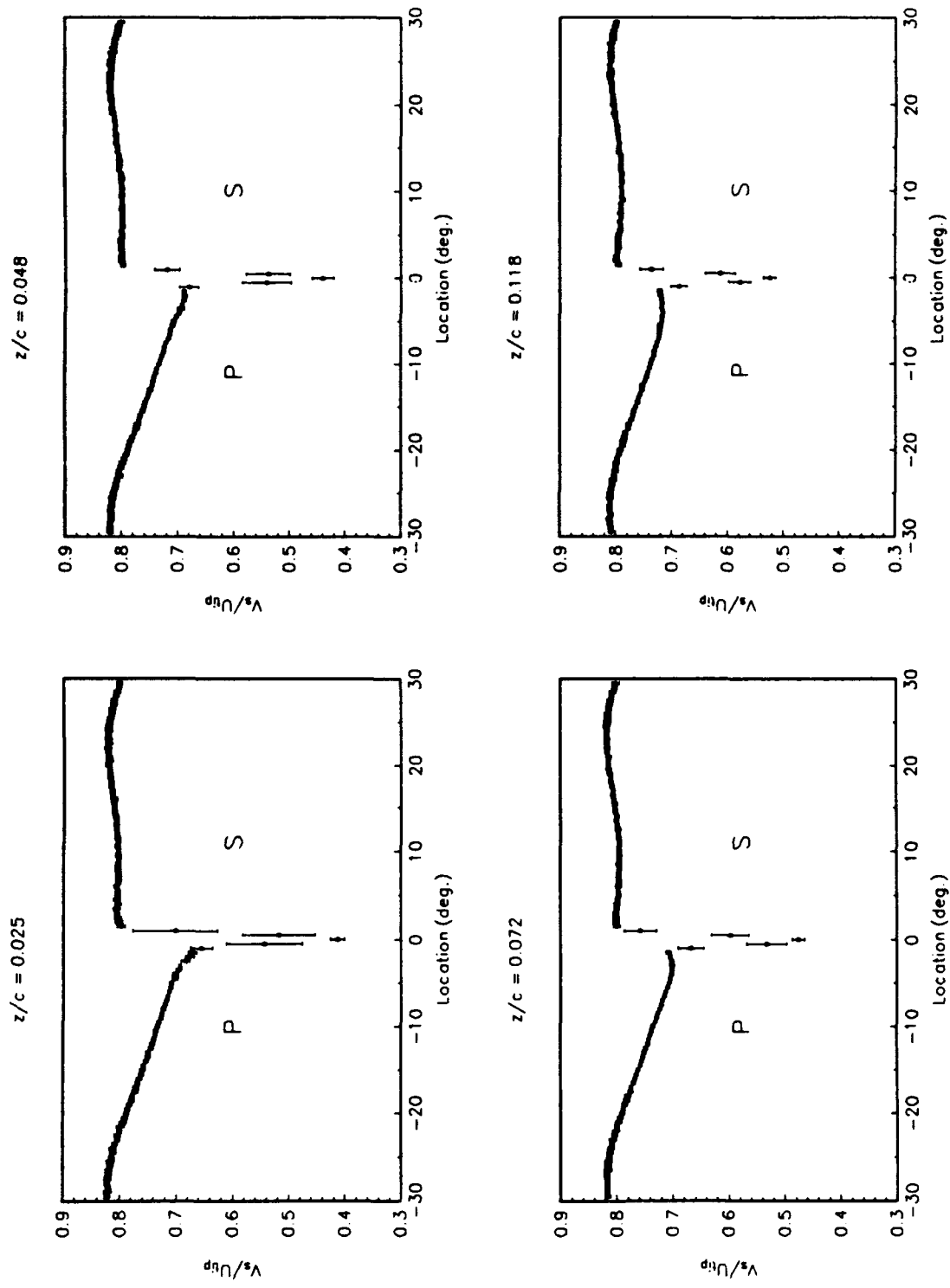
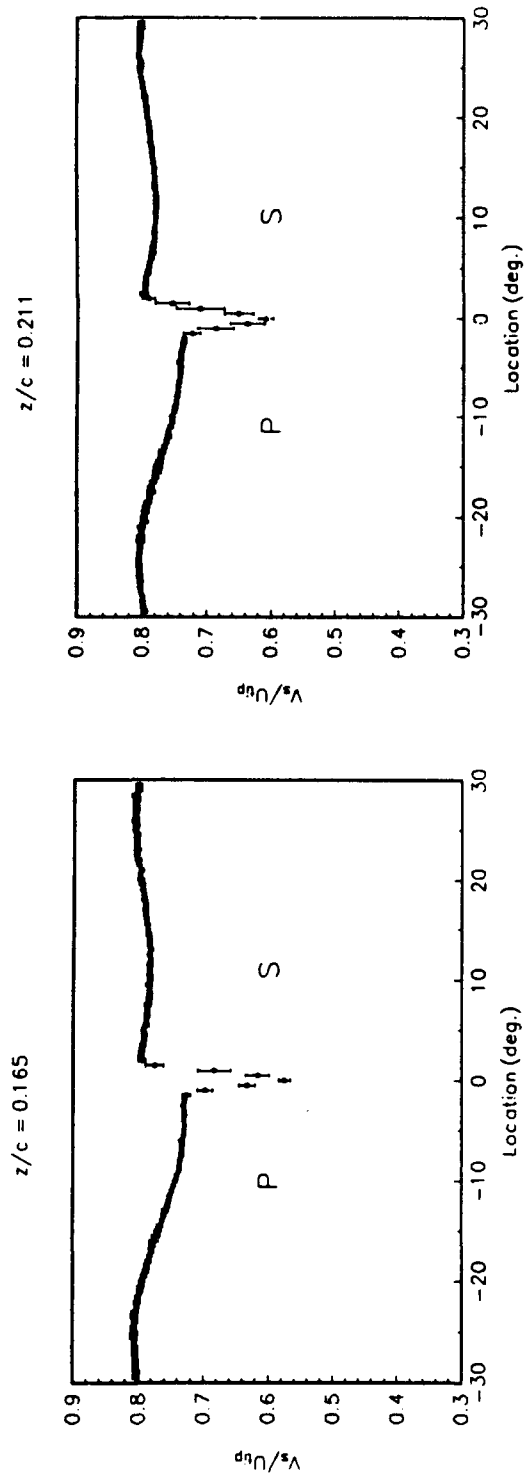


Figure 57. Tangential Velocity Contours of LDV Measurements:
c) 32.2% Chord Axially Downstream of the Rotor Tip Trailing Edge



**Figure 58. Passage-Averaged Rotor Blade Wakes from LDV Measurements at 76.2% Span:
a) 2.5%, 4.8%, 7.2%, and 11.8% Chord Axially Downstream of the Rotor Blade Trailing Edge**



$z/c = 0.165$

191

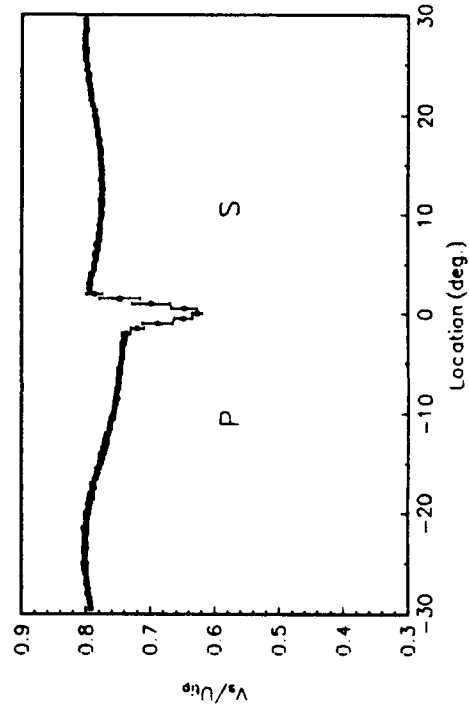
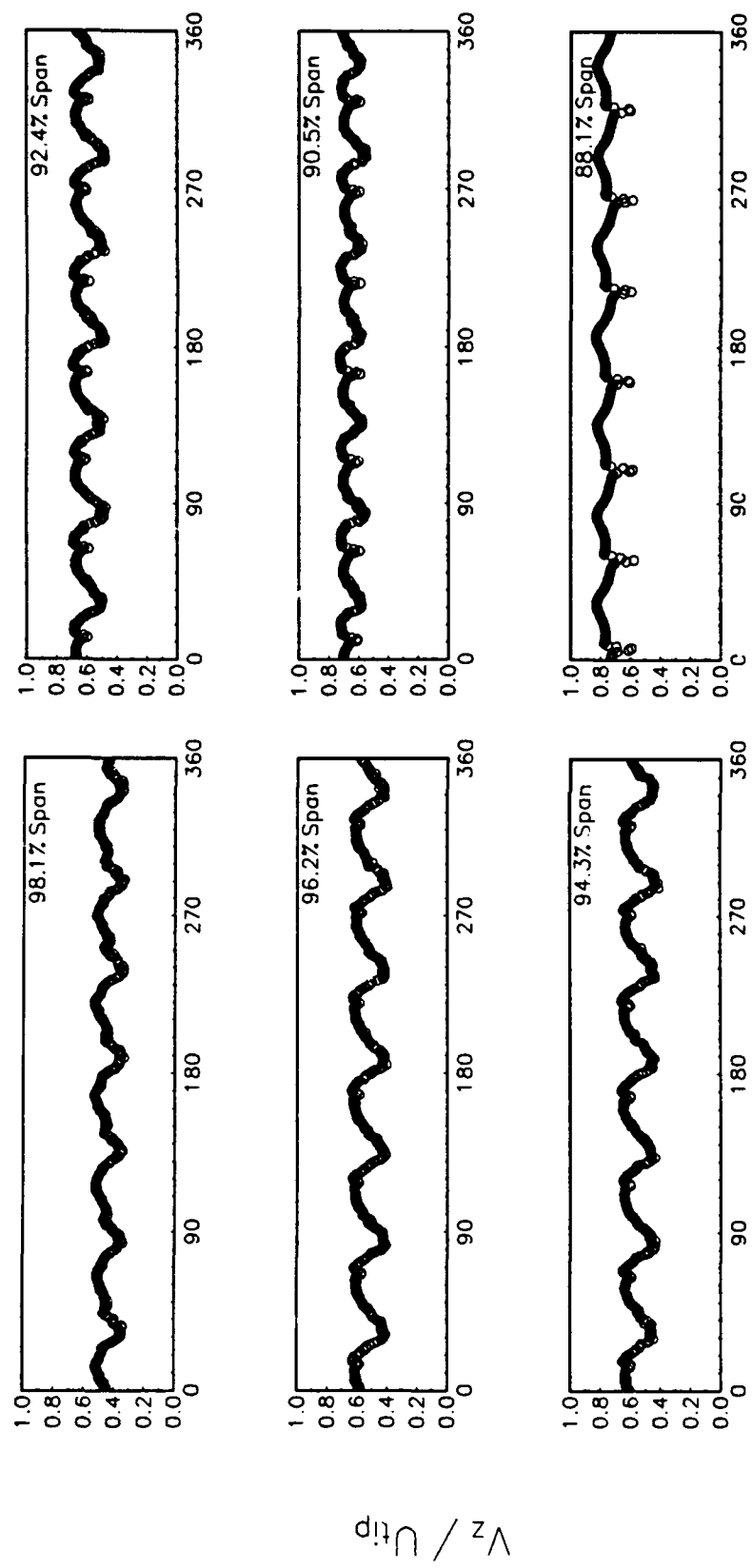


Figure 58. Passage-Averaged Rotor Blade Wakes from LDV Measurements at 76.2% Span:
b) 16.5%, 21.1%, and 24.6% Chord Axially Downstream of the Rotor Blade Trailing Edge



Rotor Rotation (degrees)

Figure 59. Circumferential Variation of the Axial Velocity Measured 32.2% Chord Axially Downstream of the Rotor Tip Trailing Edge with LDV

Rotor Rotation (degrees)

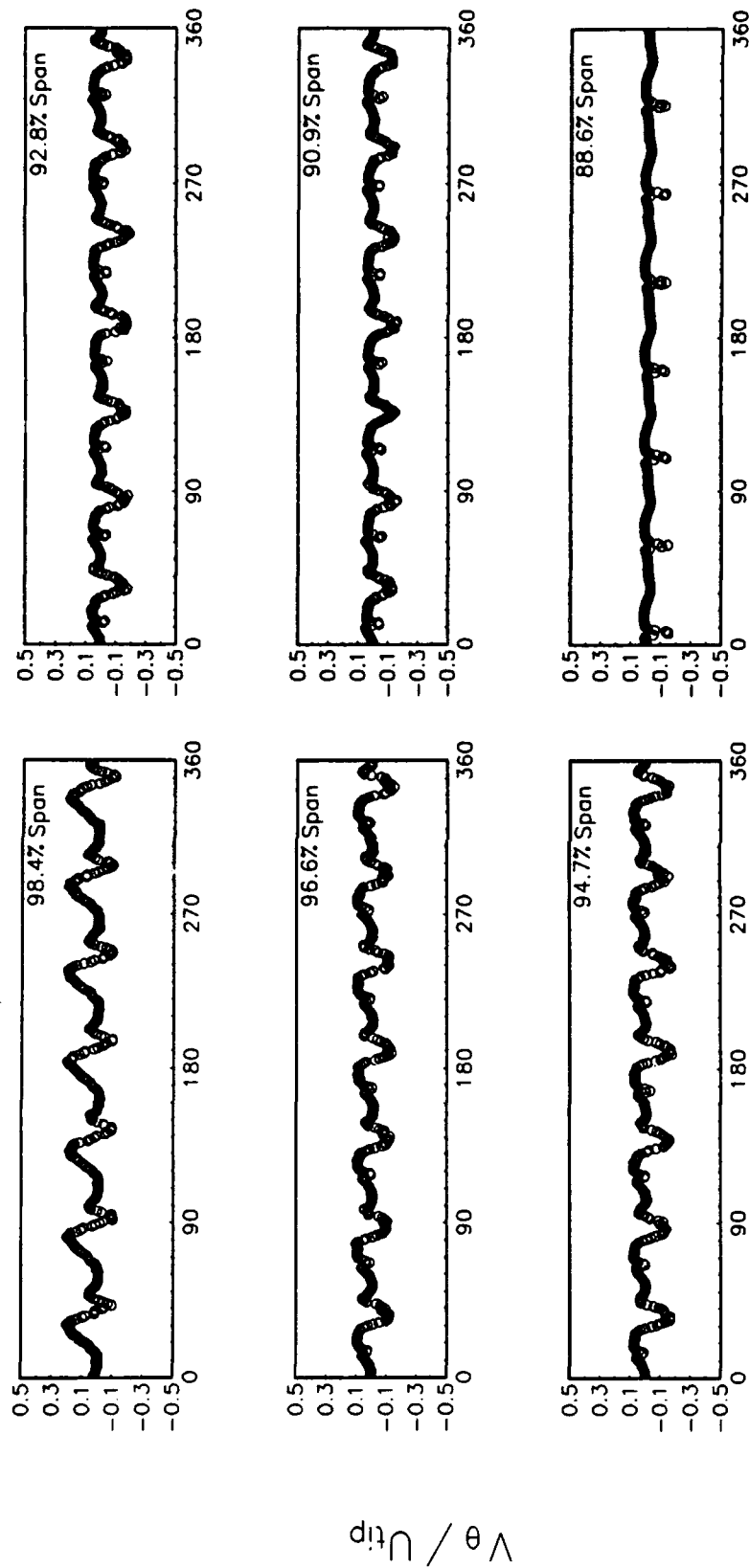
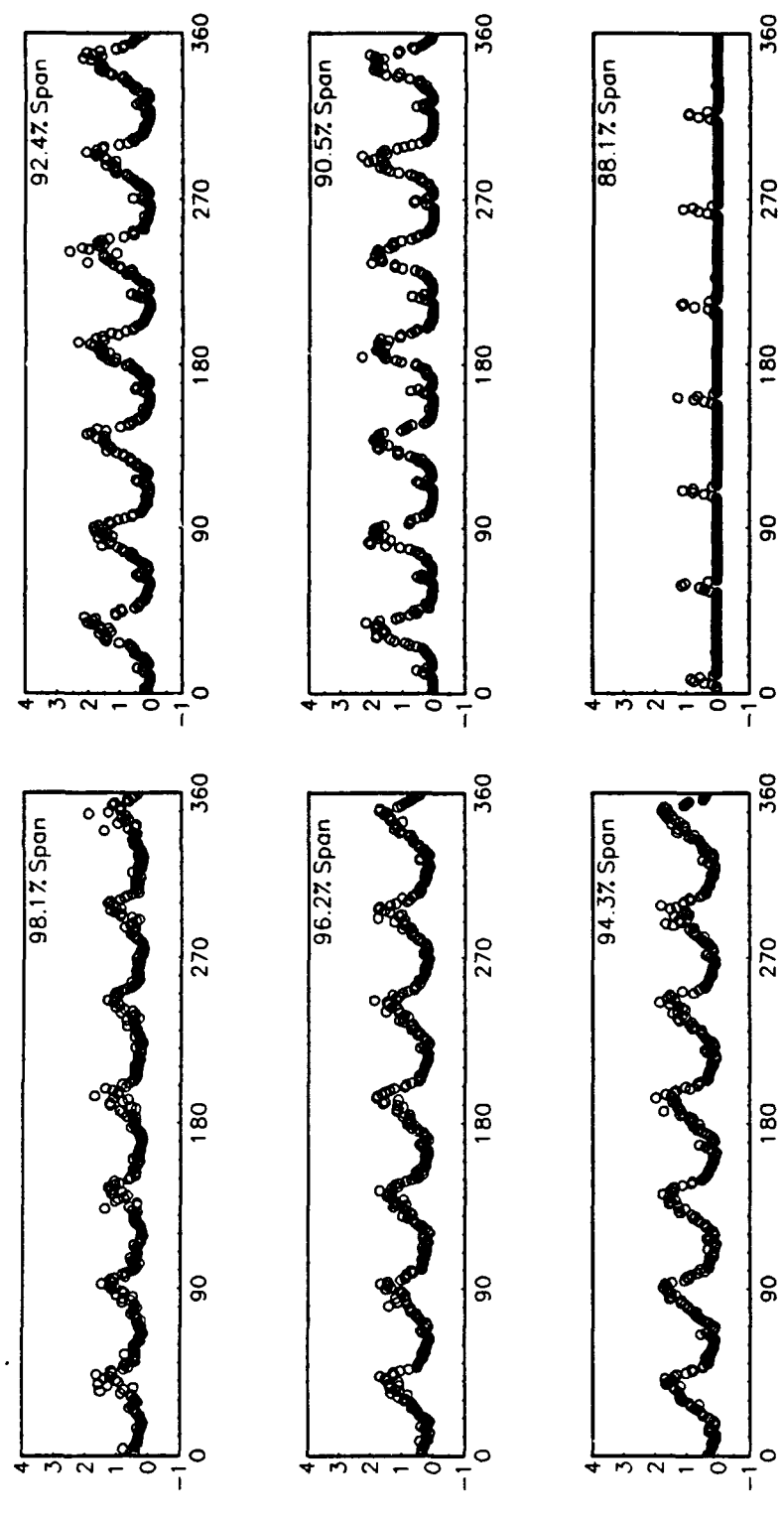


Figure 60. Circumferential Variation of the Tangential Velocity Measured 32.2% Chord Axially Downstream of the Rotor Tip Trailing Edge with LDV



Rotor Rotation (degrees)

Figure 61. Circumferential Variation of the Axial Nondeterministic Unsteady Velocity Correlation
Measured 32.2% Chord Axially Downstream of the Rotor Tip Trailing Edge with LDV

Rotor Rotation (degrees)

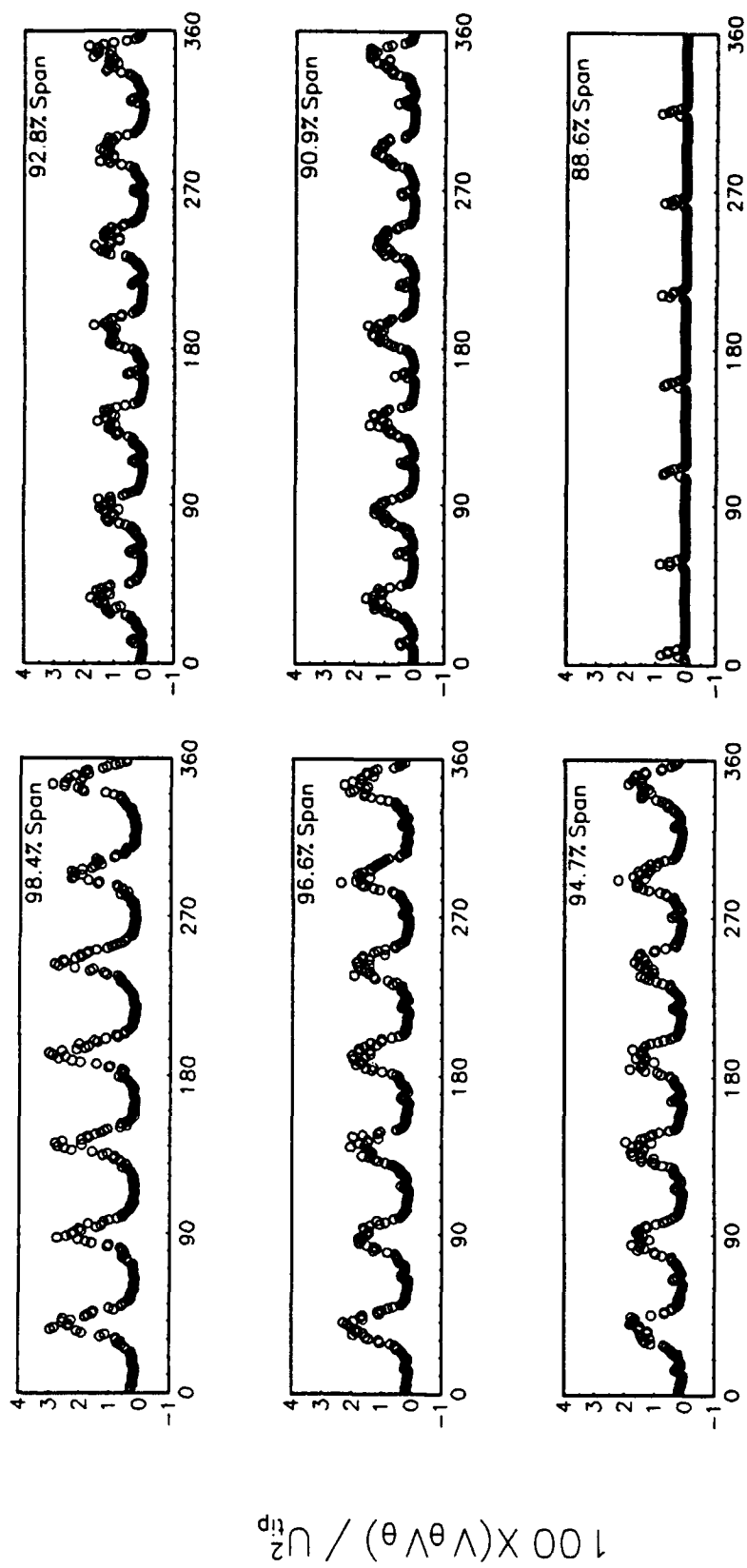


Figure 62. Circumferential Variation of the Tangential Nondeterministic Unsteady Velocity Correlation Measured 32.2% Chord Axially Downstream of the Rotor Tip Trailing Edge with LDV

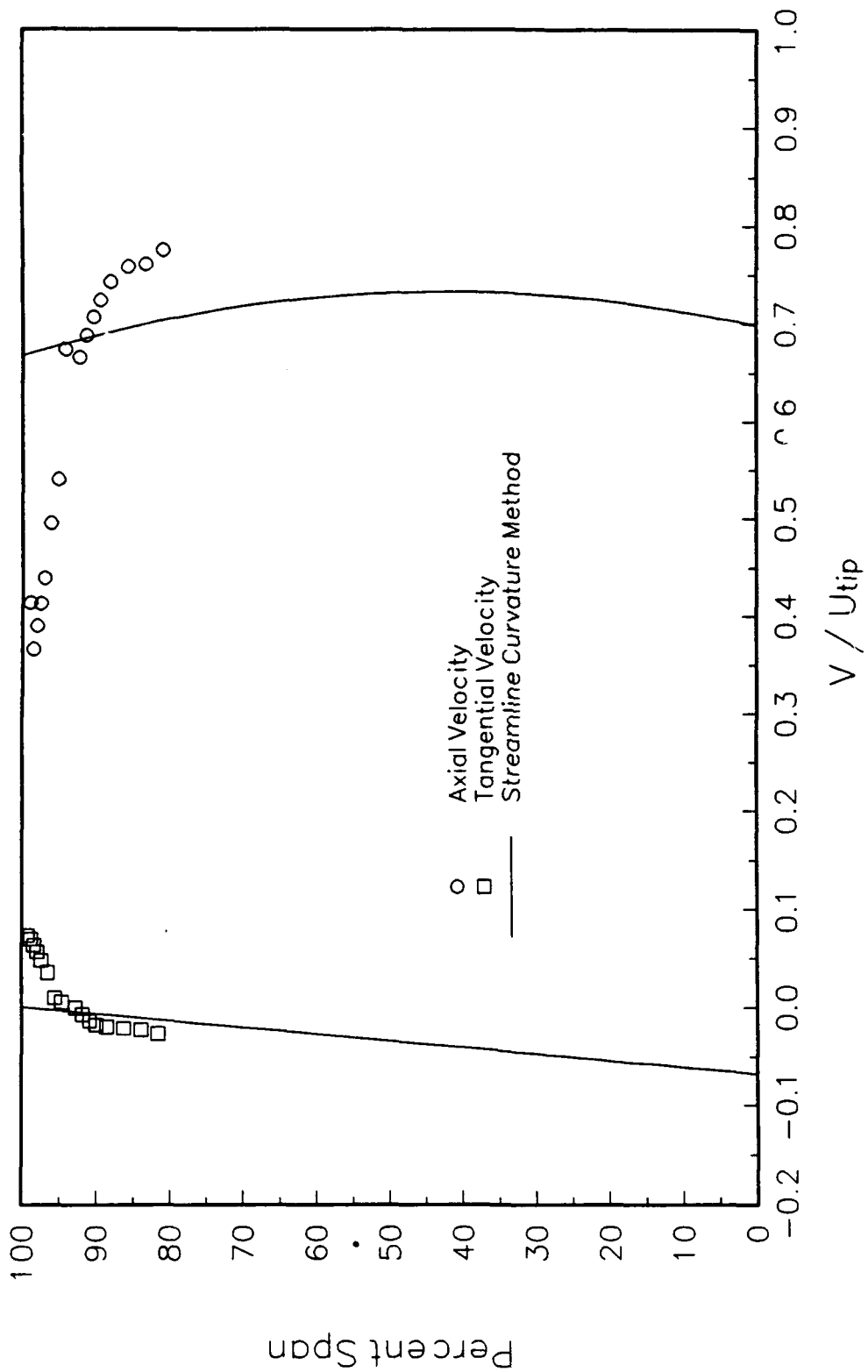


Figure 63. Circumferentially-Averaged Velocities Measured with LDV:
a) 4.8% Chord Axially Downstream of the Rotor Tip Trailing Edge

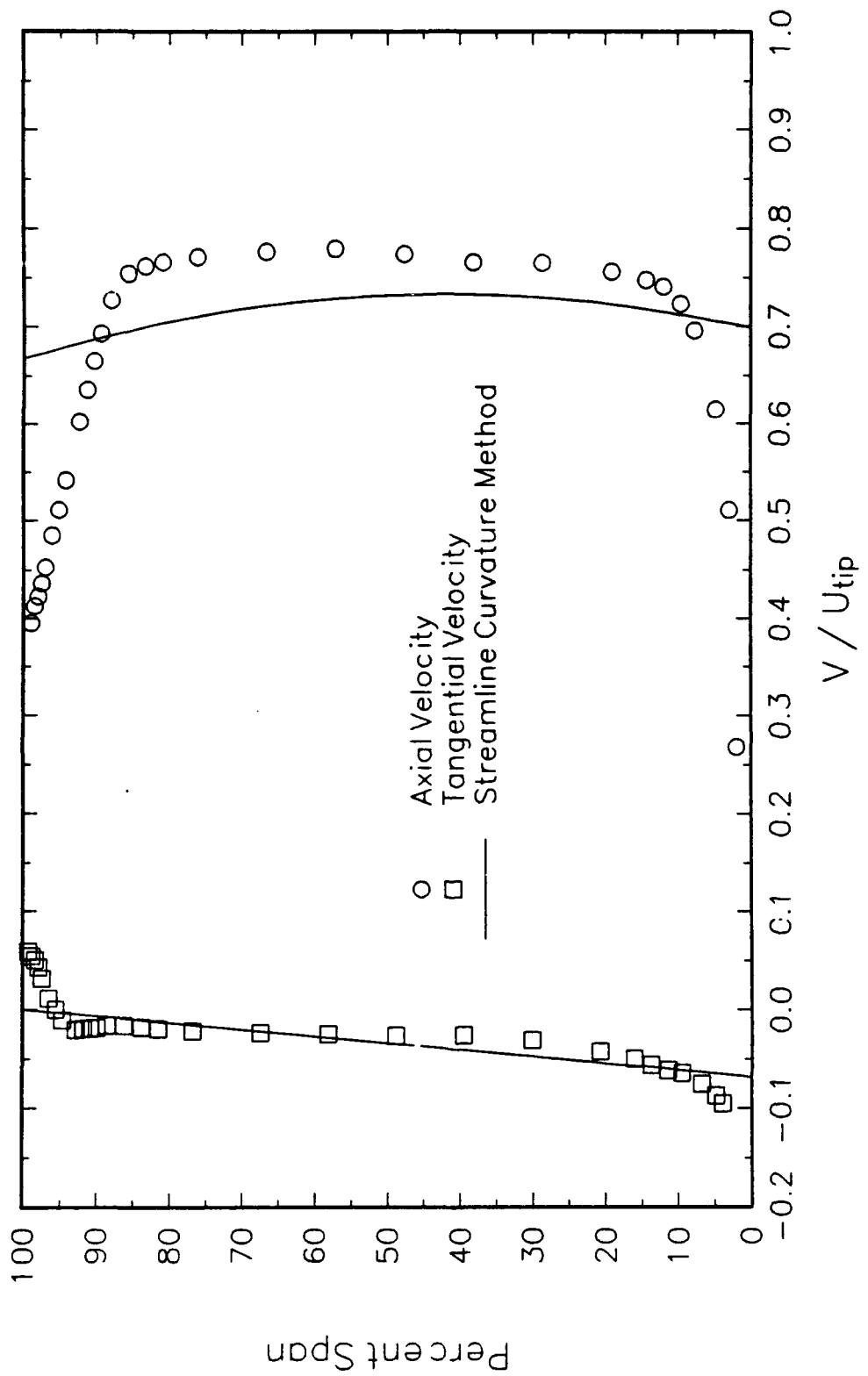


Figure 63. Circumferentially-Averaged Velocities Measured with LDV:
b) 21.4% Chord Axially Downstream of the Rotor Tip Trailing Edge

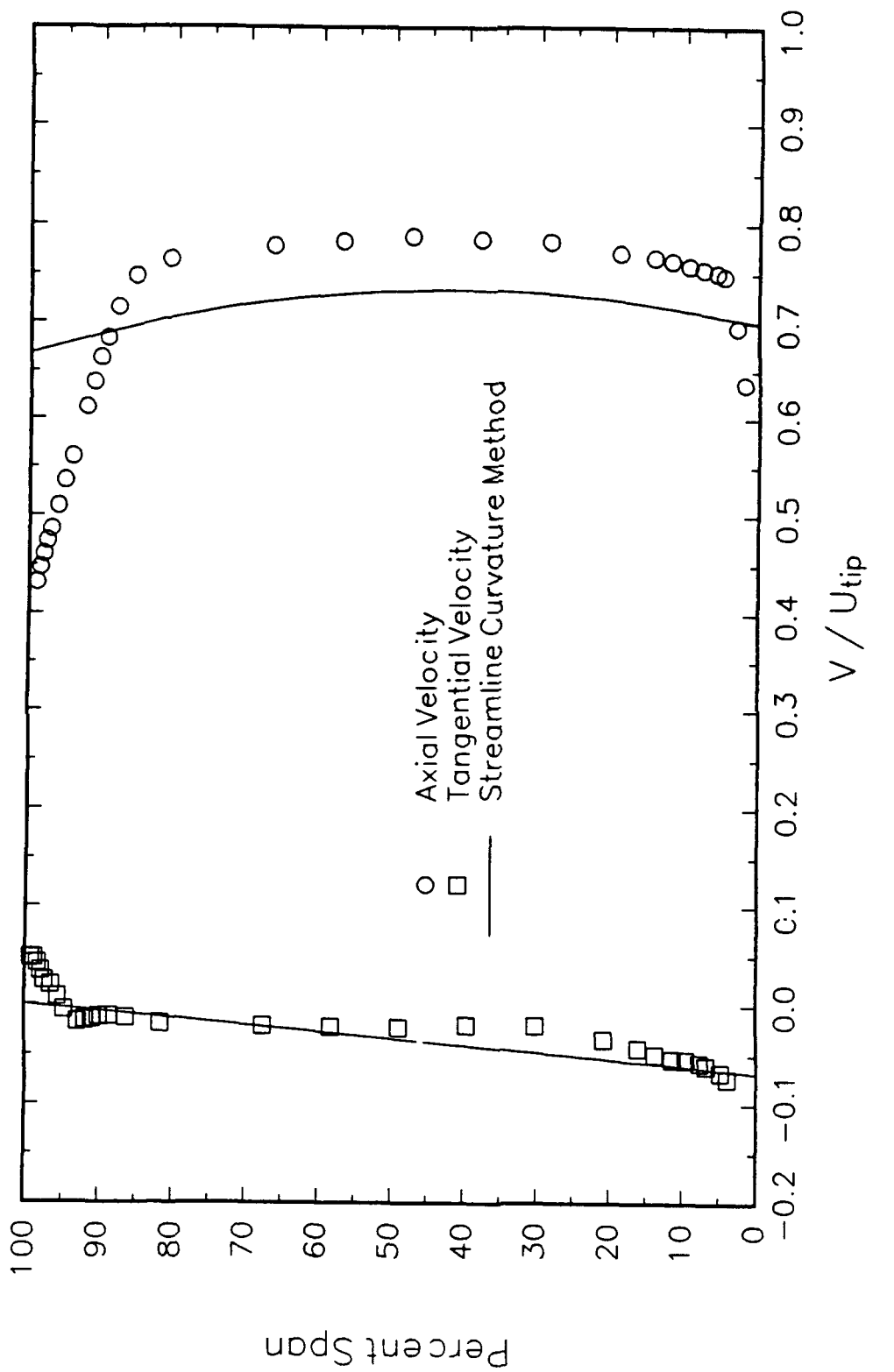


Figure 63. Circumferentially-Averaged Velocities Measured with LDV:
c) 32.2% Chord Axially Downstream of the Rotor Tip Trailing Edge

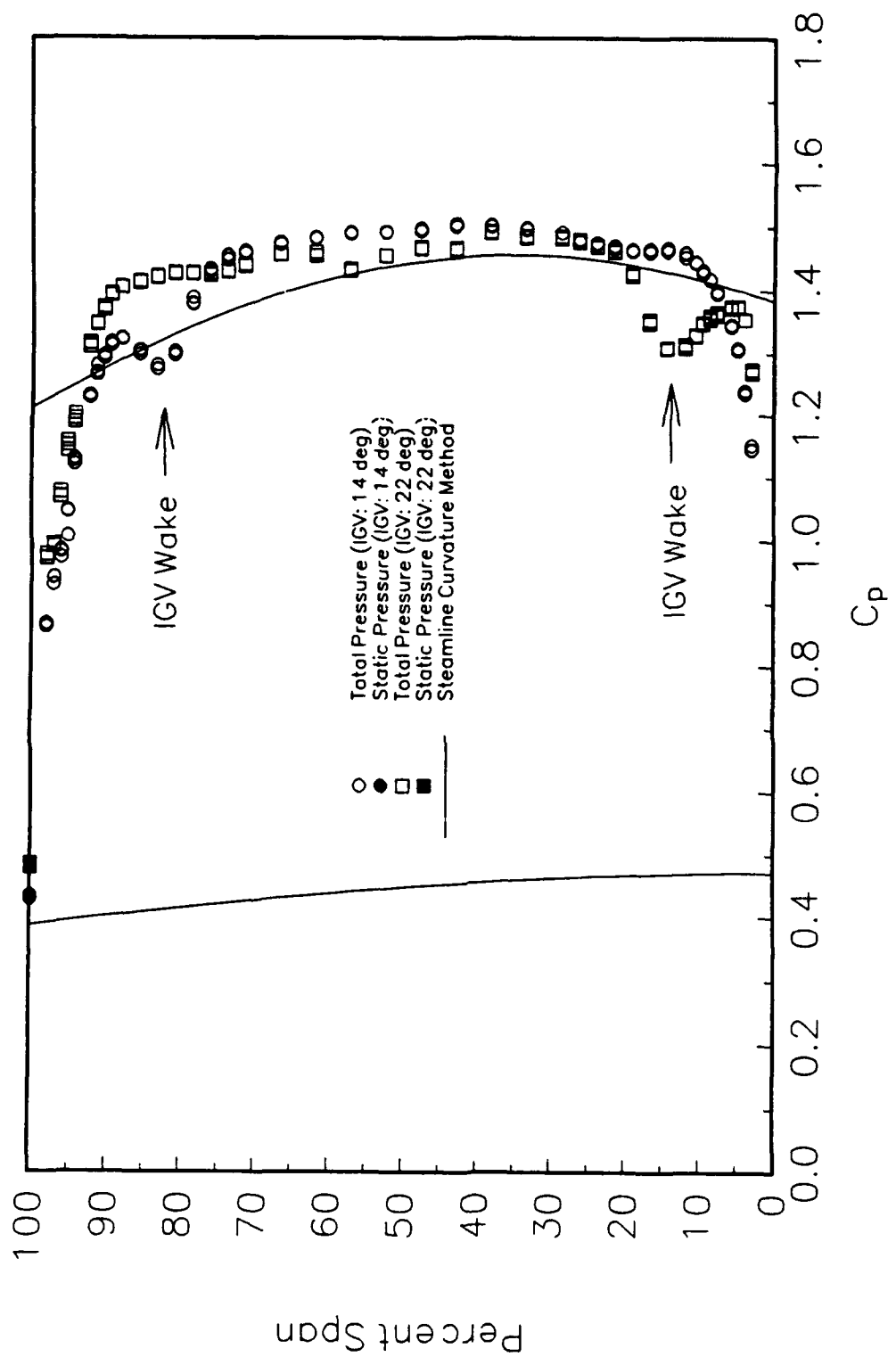


Figure 64. Spanwise Variation of Total-Pressure Coefficients 32.2% Chord Axially Downstream of the Rotor Tip Trailing Edge (at Two IGV Index Locations)

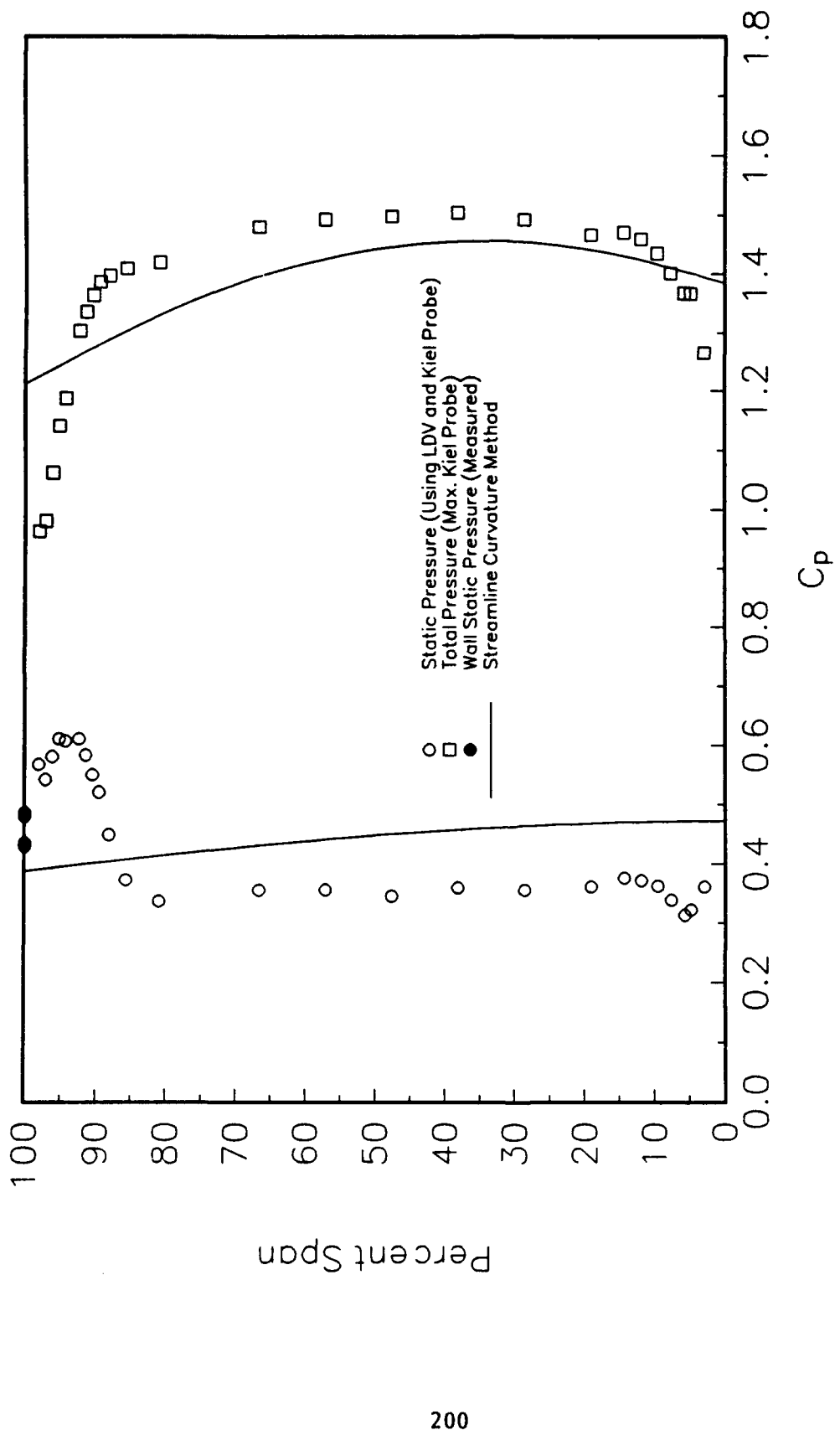


Figure 65. Estimated Spanwise Variation of Total- and Static-Pressure Coefficients 32.2% Chord Axially Downstream of the Rotor Tip Trailing Edge (without the Presence of an IGV Wake)

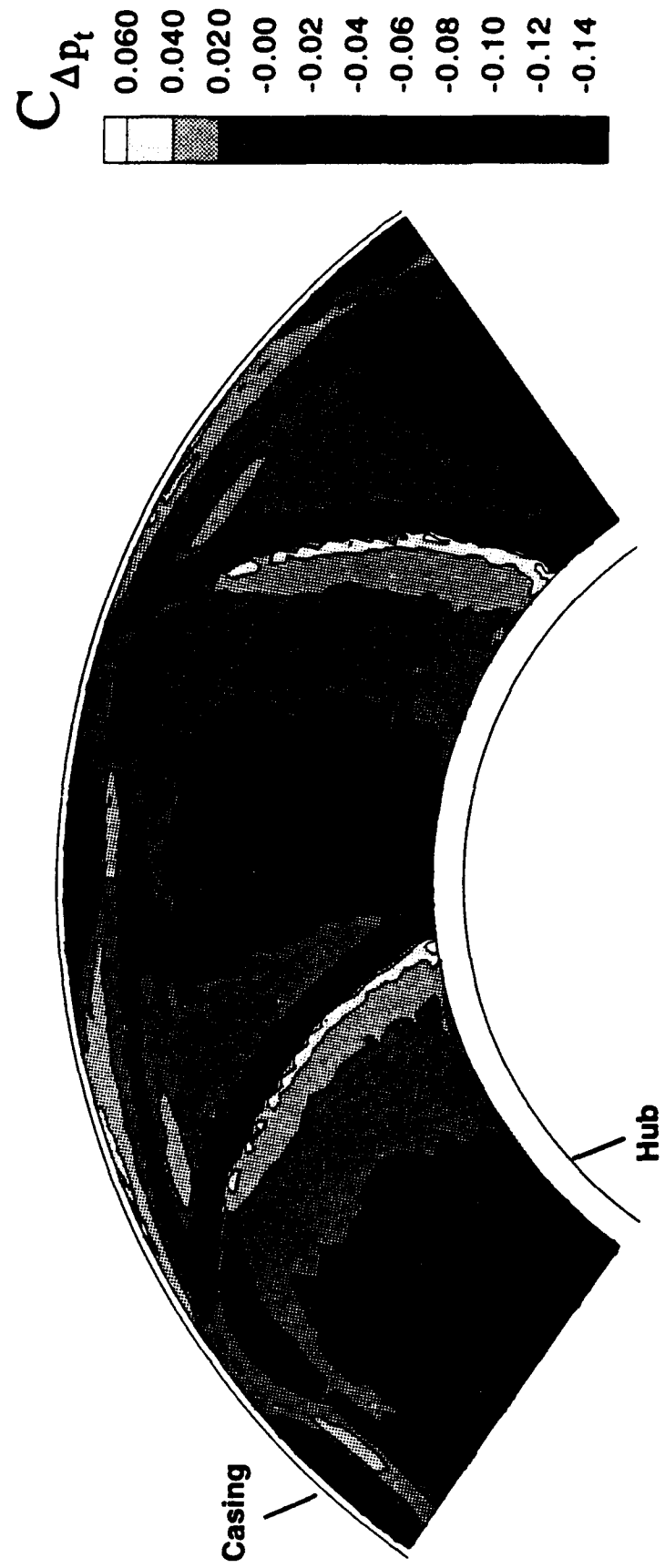


Figure 66. Contours of the Total-Pressure Variation Coefficient Measured with the Fast-Response, Total-Pressure Probe 32.2% Chord Axially Downstream of the Rotor Tip Trailing Edge

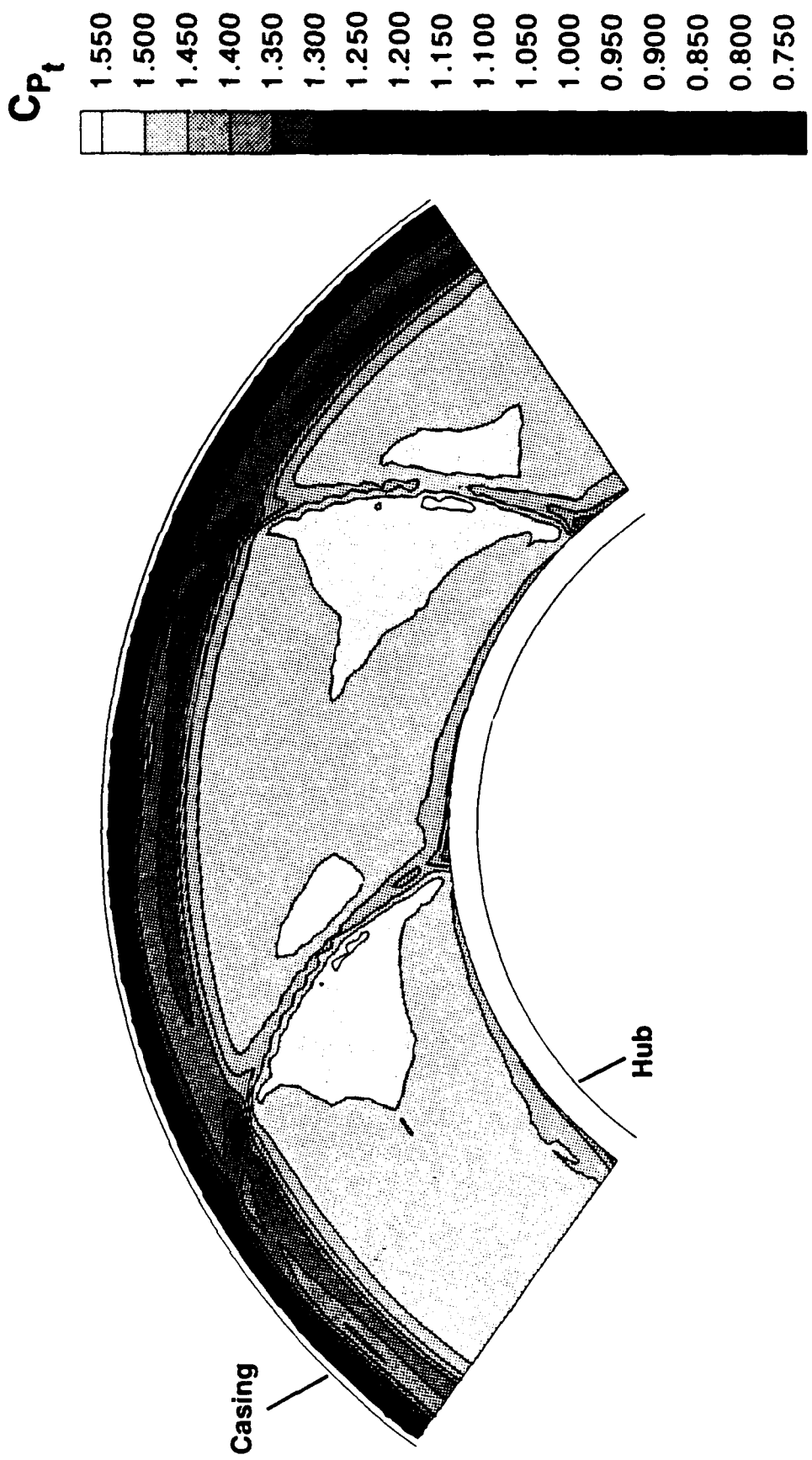


Figure 67. Contours of the Total-Pressure Coefficient Measured with the Fast-Response, Total-Pressure Probe 32.2% Chord Axially Downstream of the Rotor Tip Trailing Edge

202

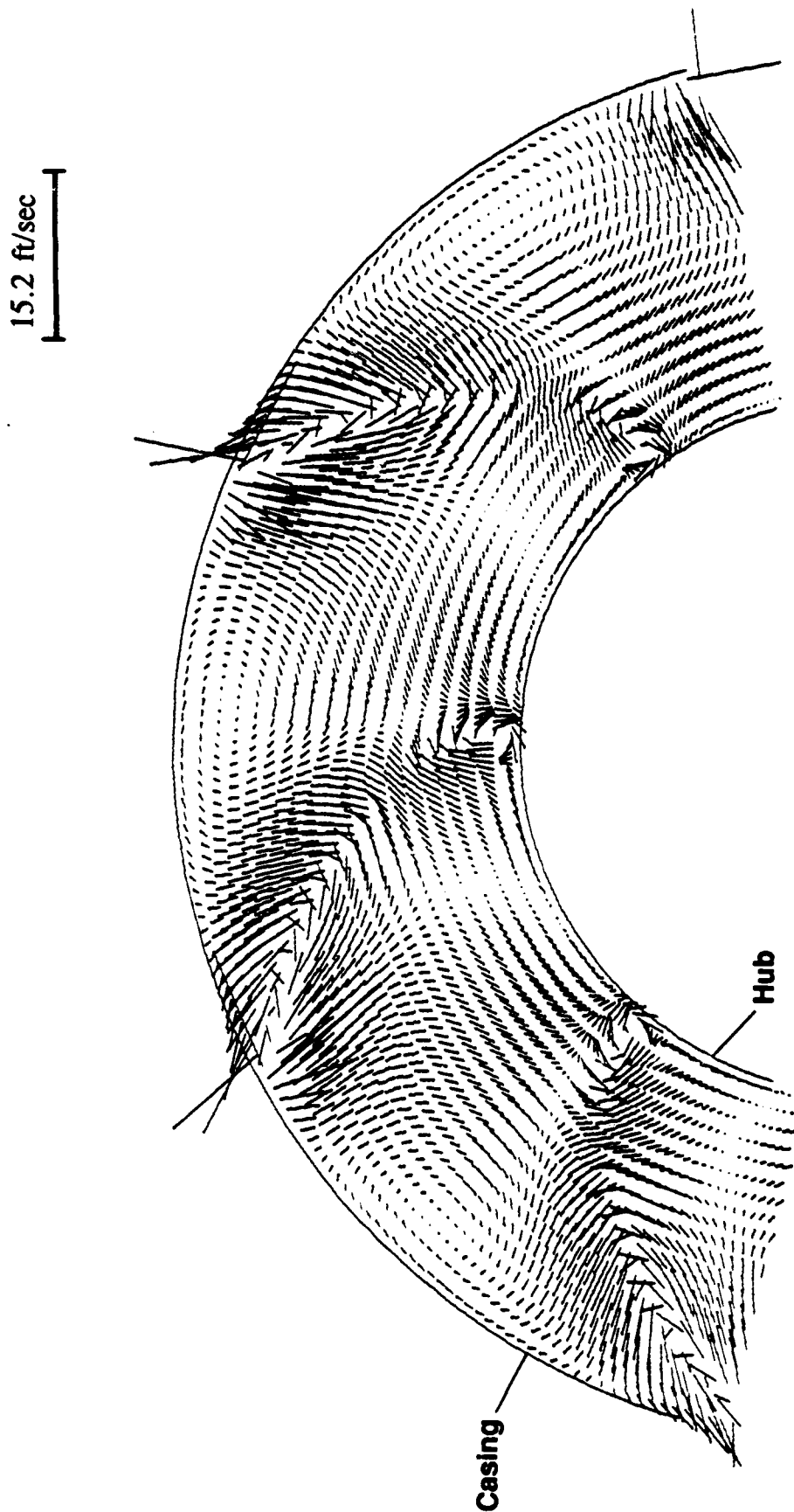


Figure 68. Secondary Velocity Vectors Calculated 32.2% Chord Axially Downstream of the Rotor Tip Trailing Edge with Lifting Surface Theory

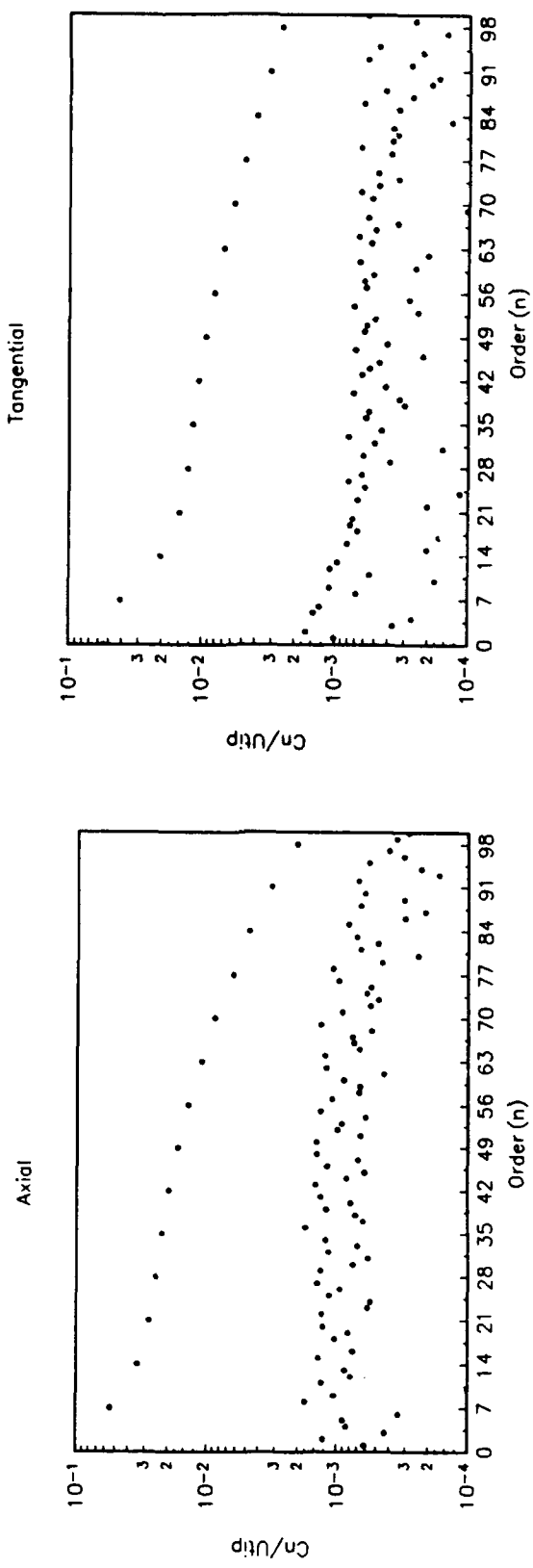


Figure 69. Fourier Coefficients of Velocity Components 32.2% Chord Axially Downstream of the Rotor Tip Trailing Edge: a) 9.5% Span

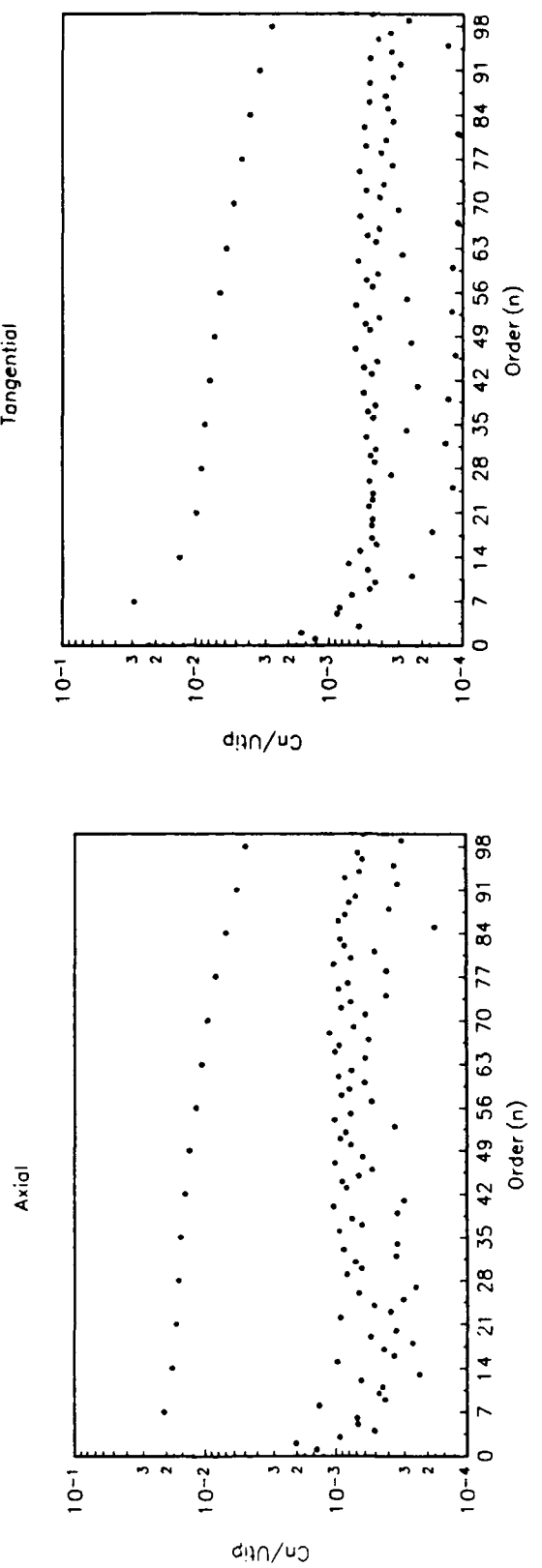


Figure 69. Fourier Coefficients of Velocity Components 32.2% Chord Axially Downstream
of the Rotor Tip Trailing Edge: b) 57.1% Span

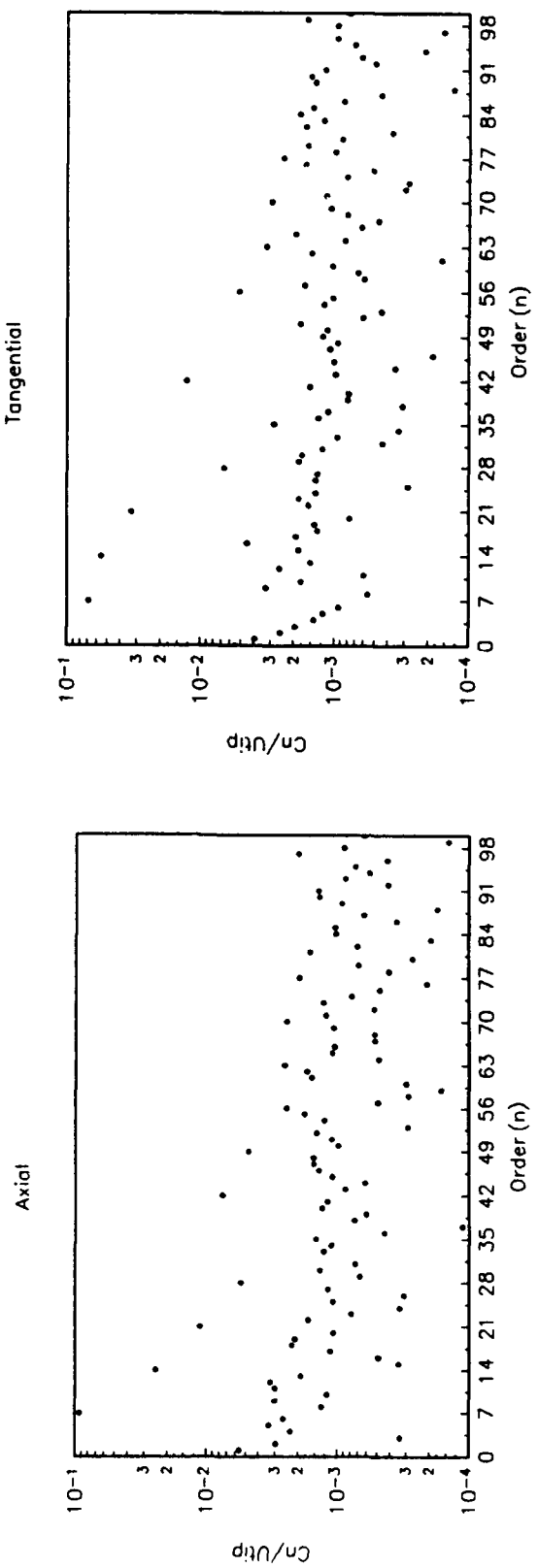


Figure 69. Fourier Coefficients of Velocity Components 32.2% Chord Axially Downstream of the Rotor Tip Trailing Edge: c) 94.3% Span

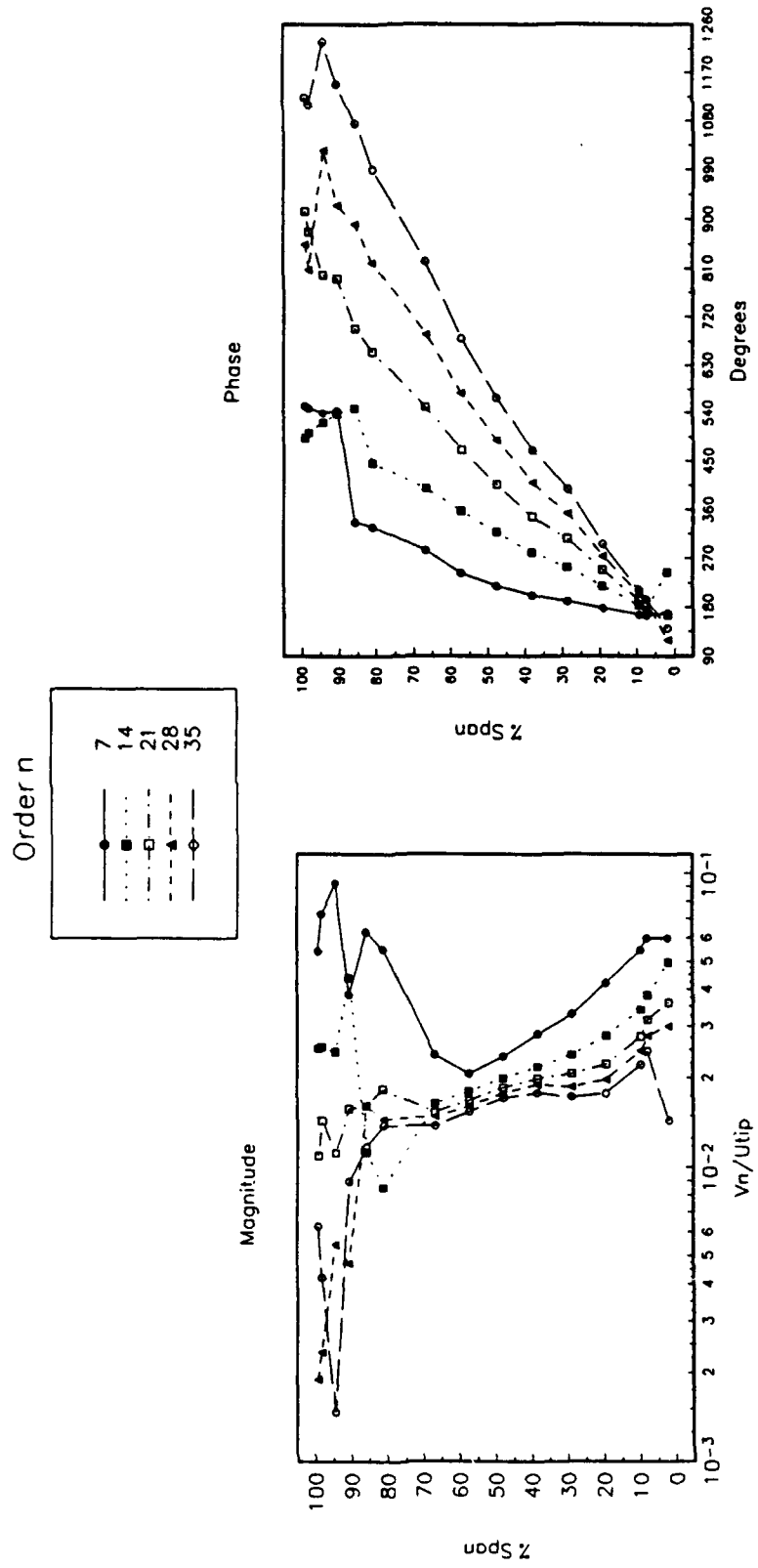


Figure 70. Spanwise Variation of Fourier Coefficients (Magnitude and Phase) 32.2% Chord Axially Downstream of the Rotor Tip Trailing Edge for the Harmonics of Order 7, 14, 21, 28, and 35: a) Axial Velocity

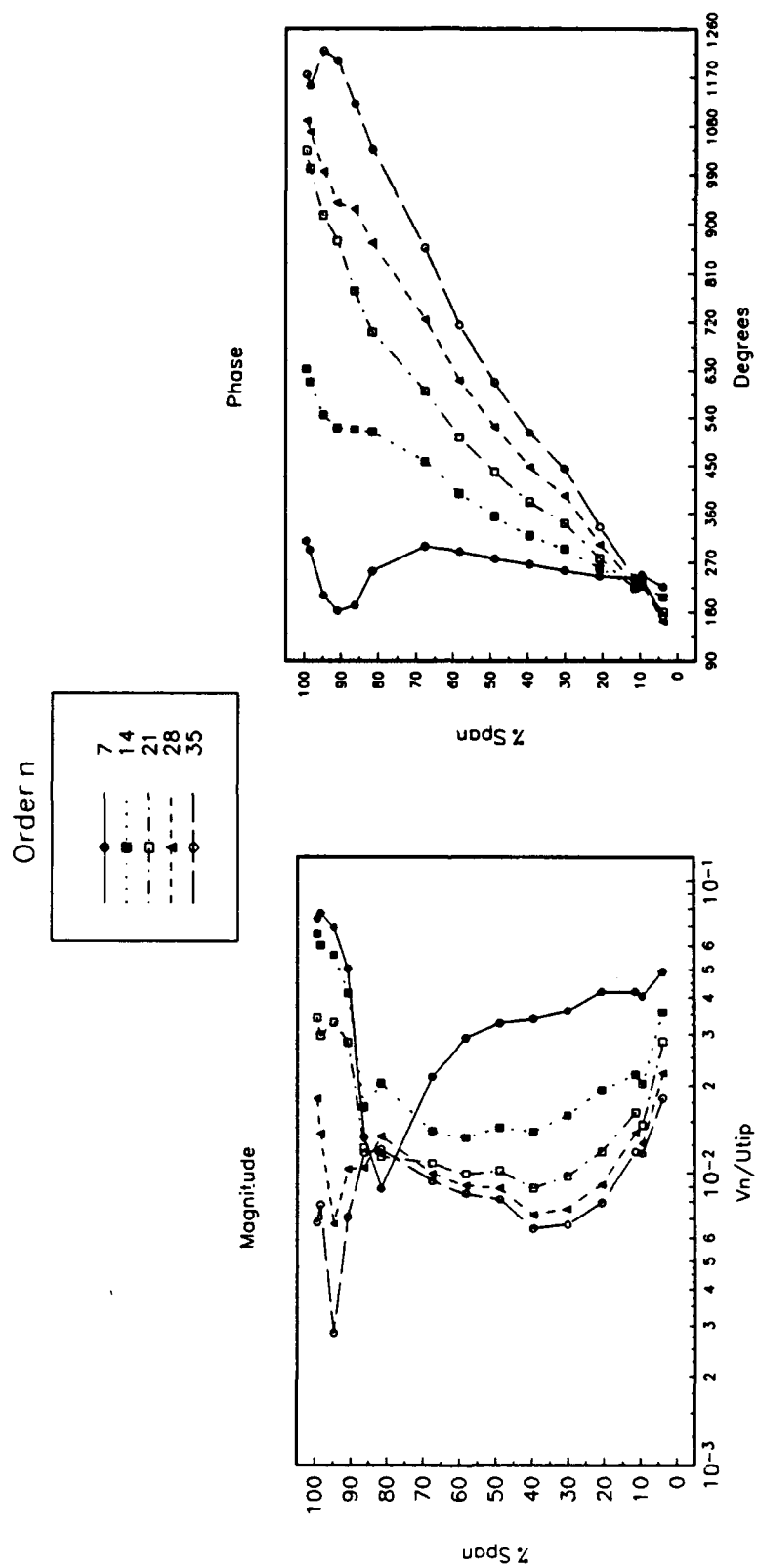


Figure 70. Spanwise Variation of Fourier Coefficients (Magnitude and Phase) 32.2% Chord Axially Downstream of the Rotor Tip Trailing Edge for the Harmonics of Order 7, 14, 21, 28, and 35: a) Tangential Velocity

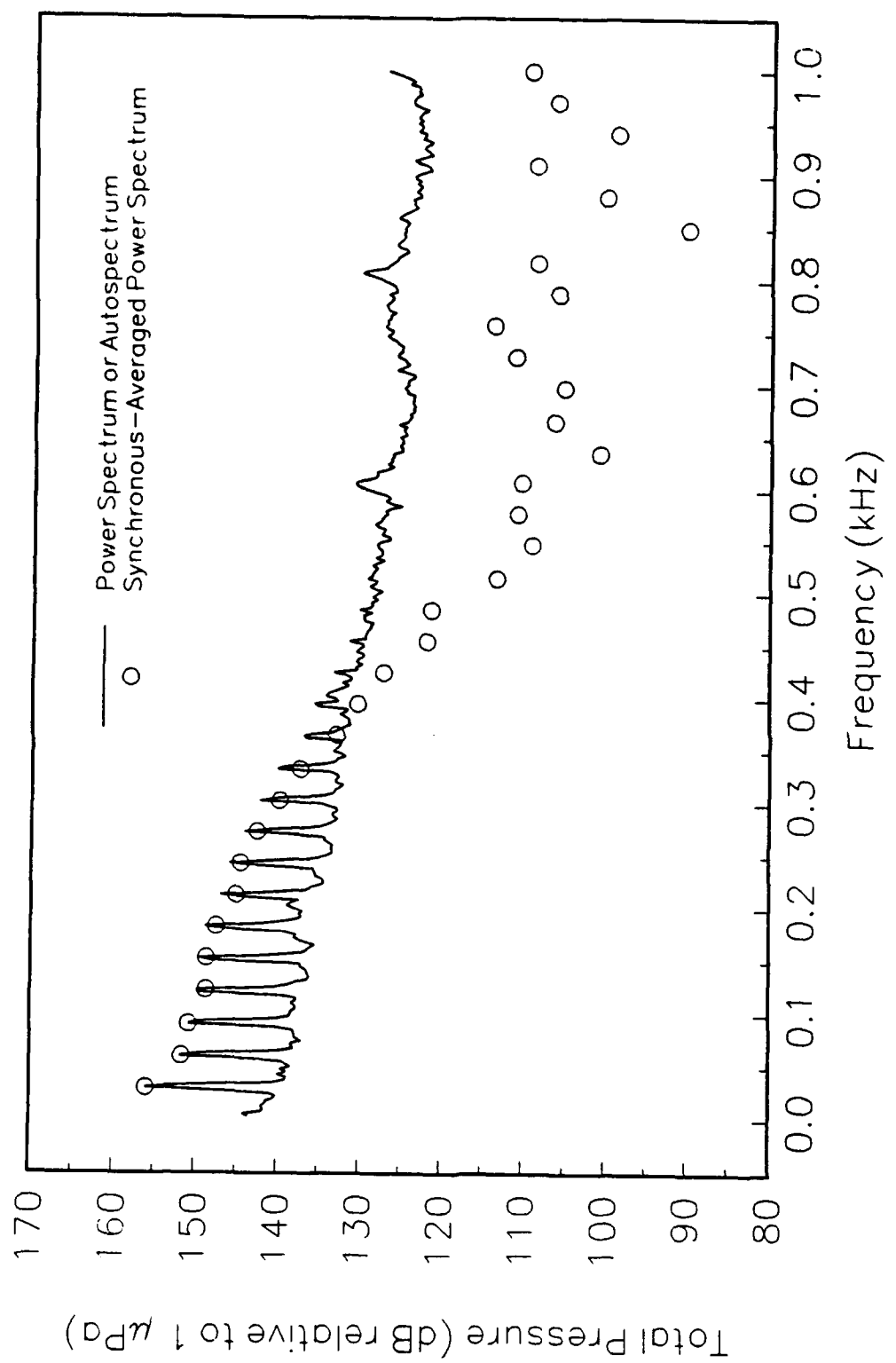


Figure 71. Power Spectra of the Total-Pressure Measurements 32.2% Chord Axially Downstream of the Rotor Tip Trailing Edge: a) 9.5% Span

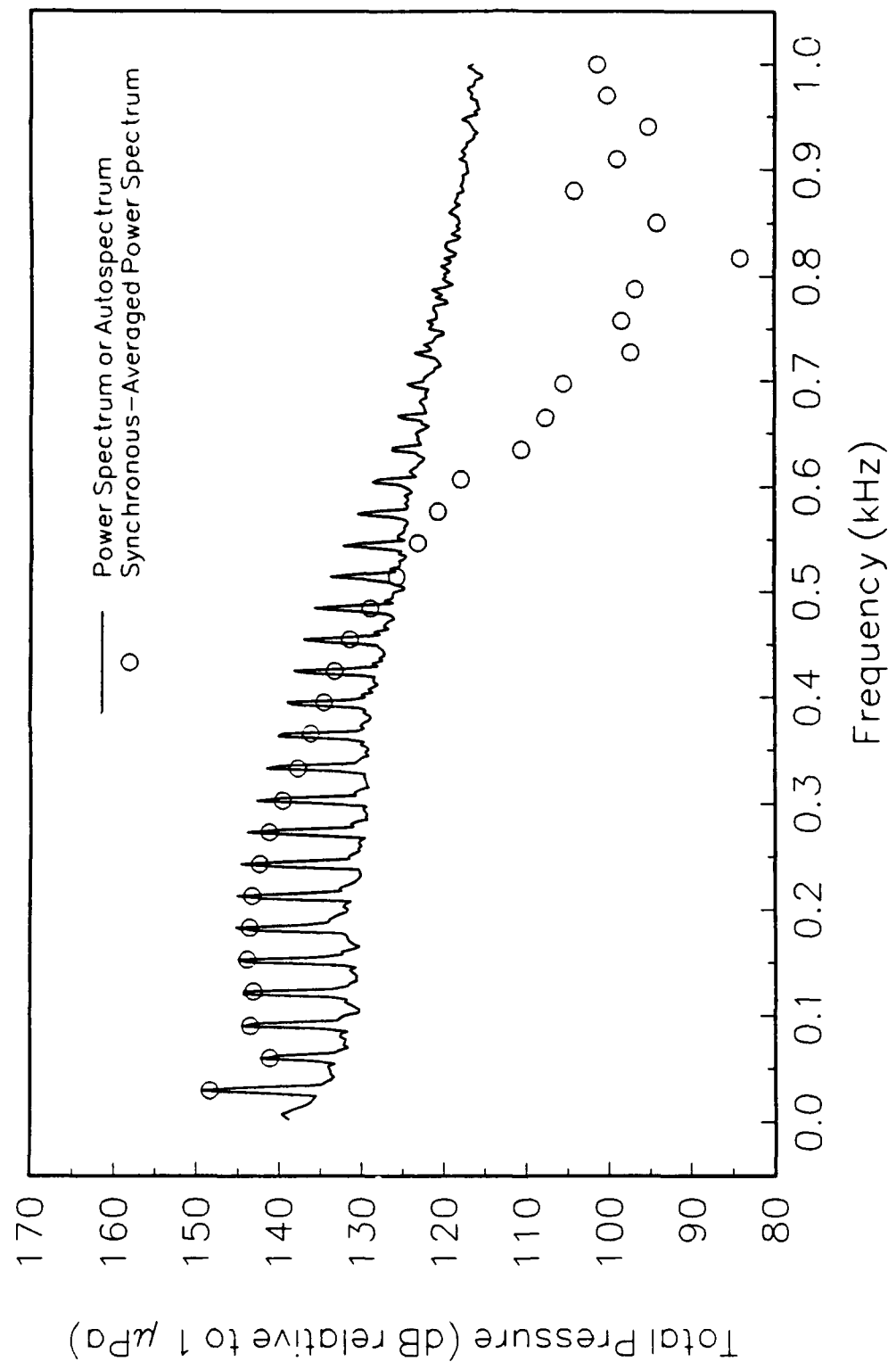


Figure 71. Power Spectra of the Total-Pressure Measurements 32.2% Chord Axially Downstream of the Rotor Tip Trailing Edge: b) 57.1% Span

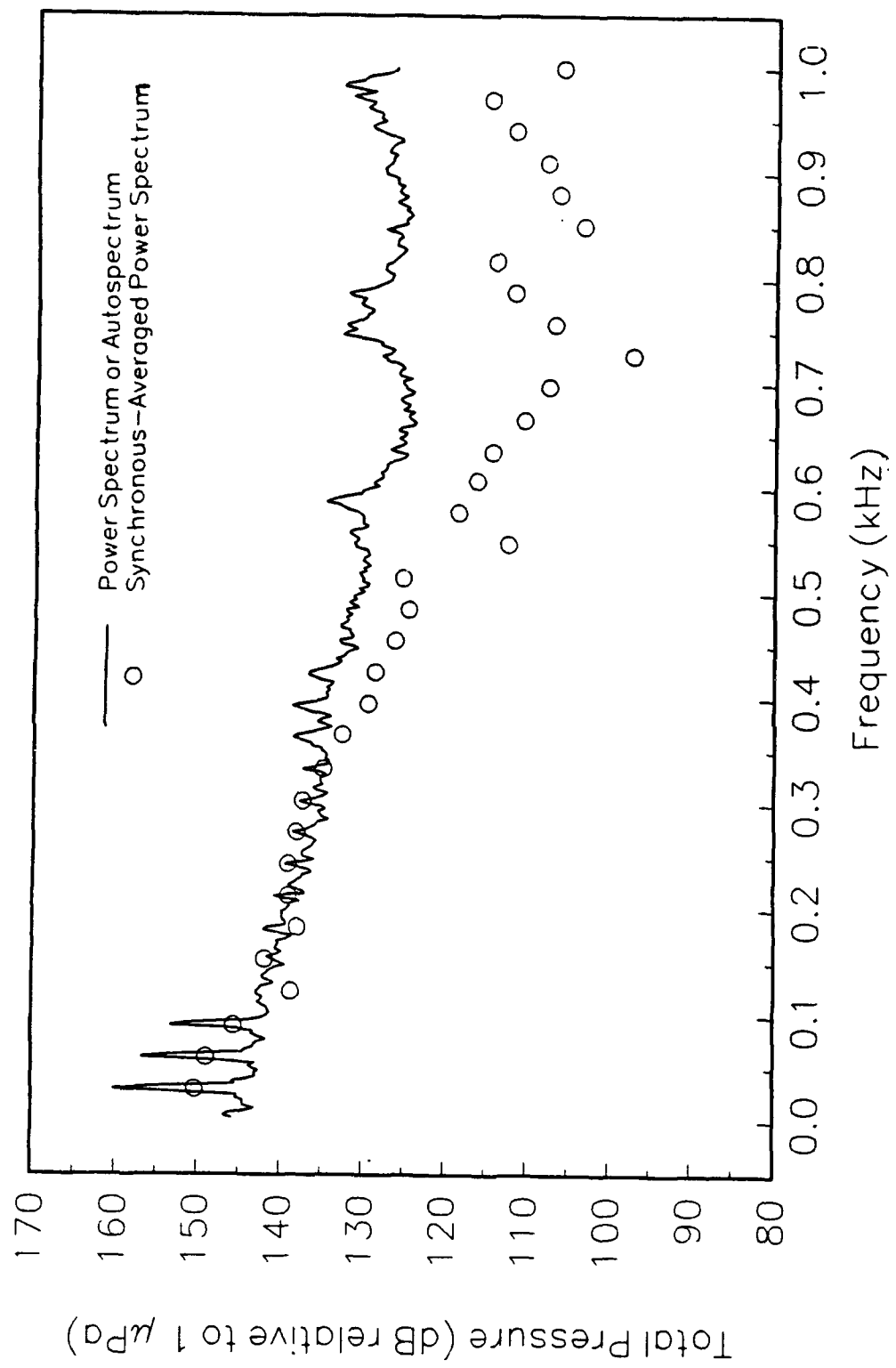


Figure 71. Power Spectra of the Total-Pressure Measurements 32.2% Chord Axially Downstream
 of the Rotor Tip Trailing Edge: c) 94.3% Span

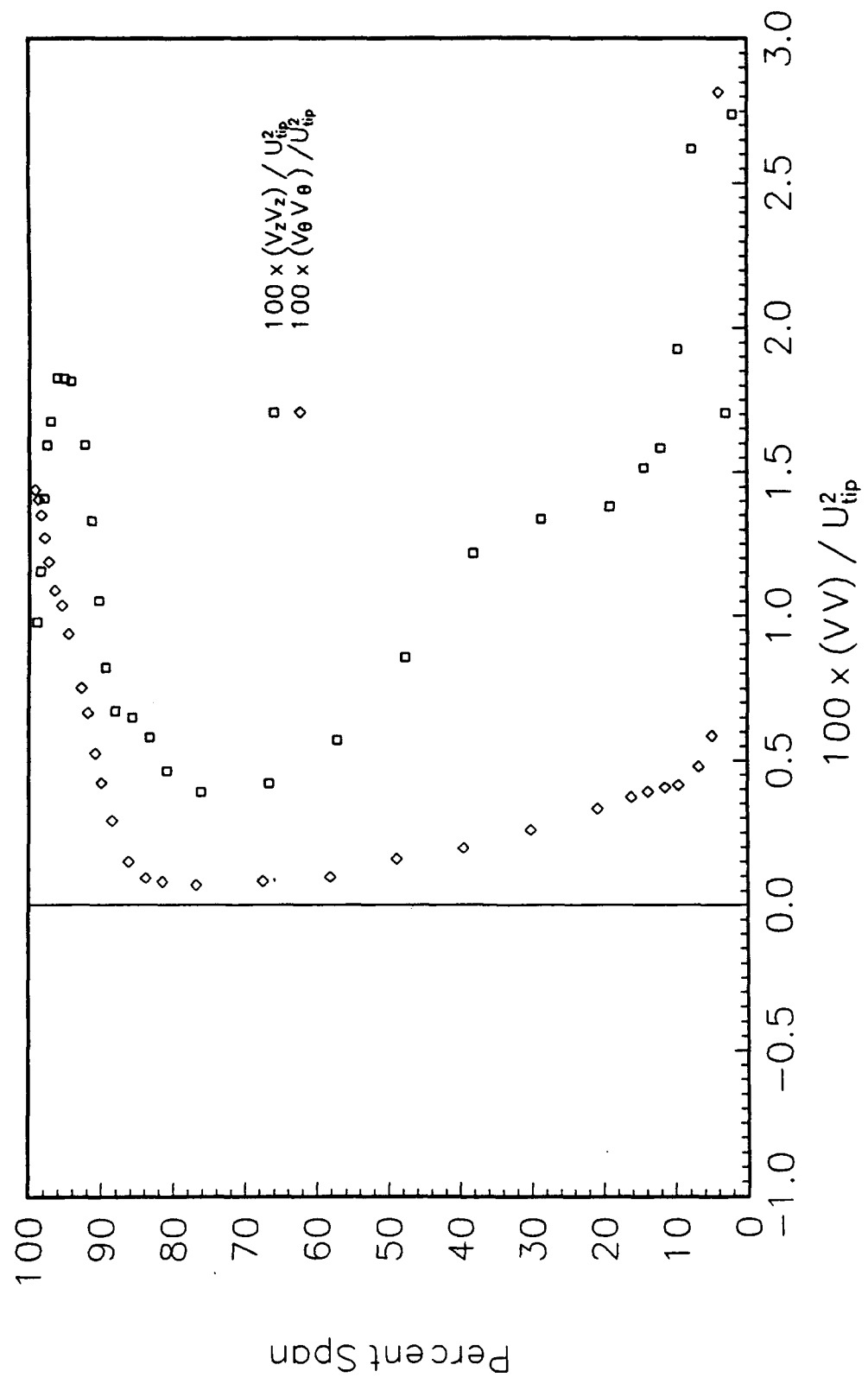


Figure 72. Overall Unsteady Velocity Correlations Measured with LDV:
a) 21.4% Chord Axially Downstream of the Rotor Tip Trailing Edge

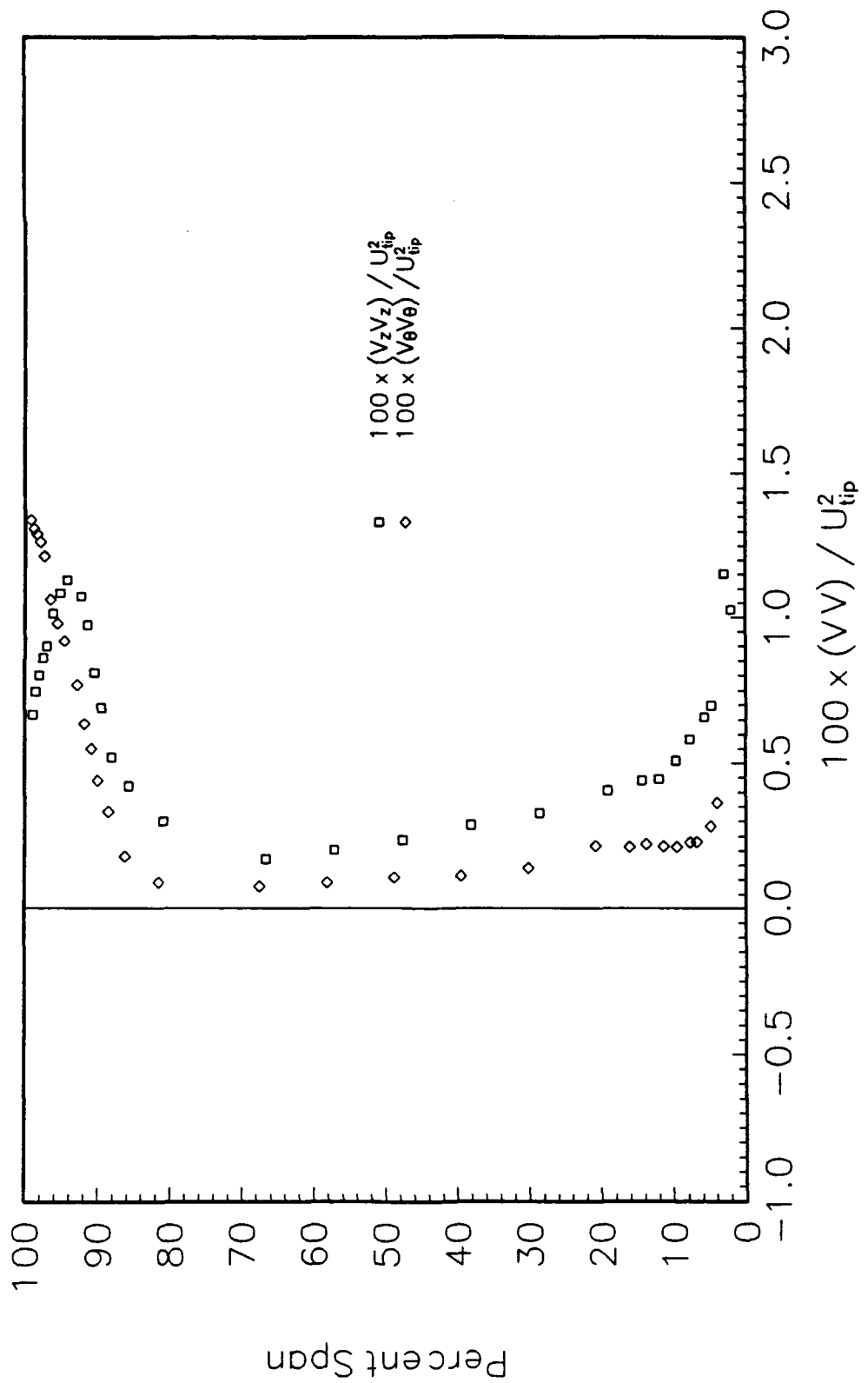


Figure 72. Overall Unsteady Velocity Correlations Measured with LDV:
b) 32.2% Chord Axially Downstream of the Rotor Tip Trailing Edge

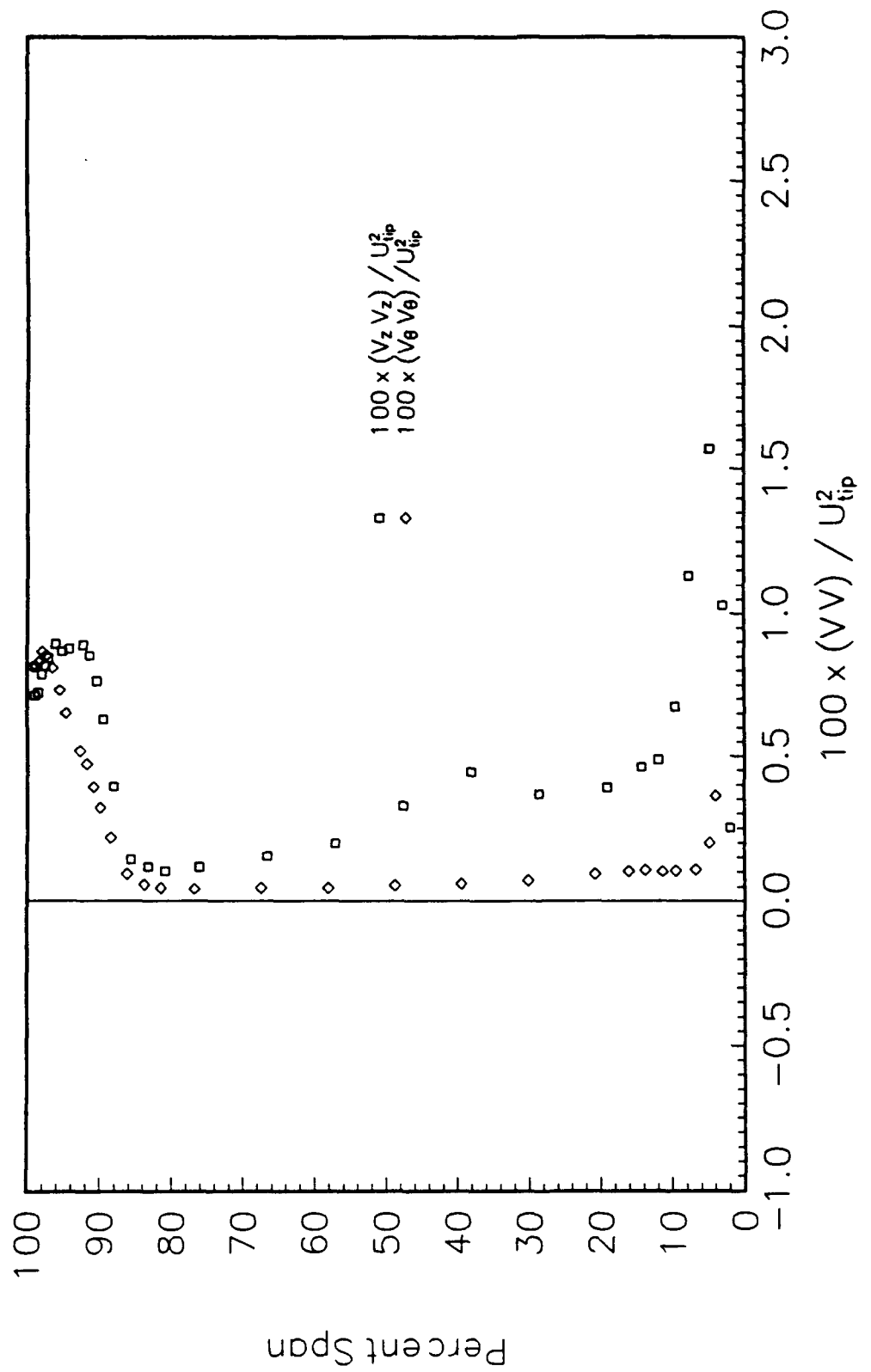


Figure 73. Nondeterministic Unsteady Velocity Correlations Measured with LDV:
a) 21.4% Chord Axially Downstream of the Rotor Tip Trailing Edge

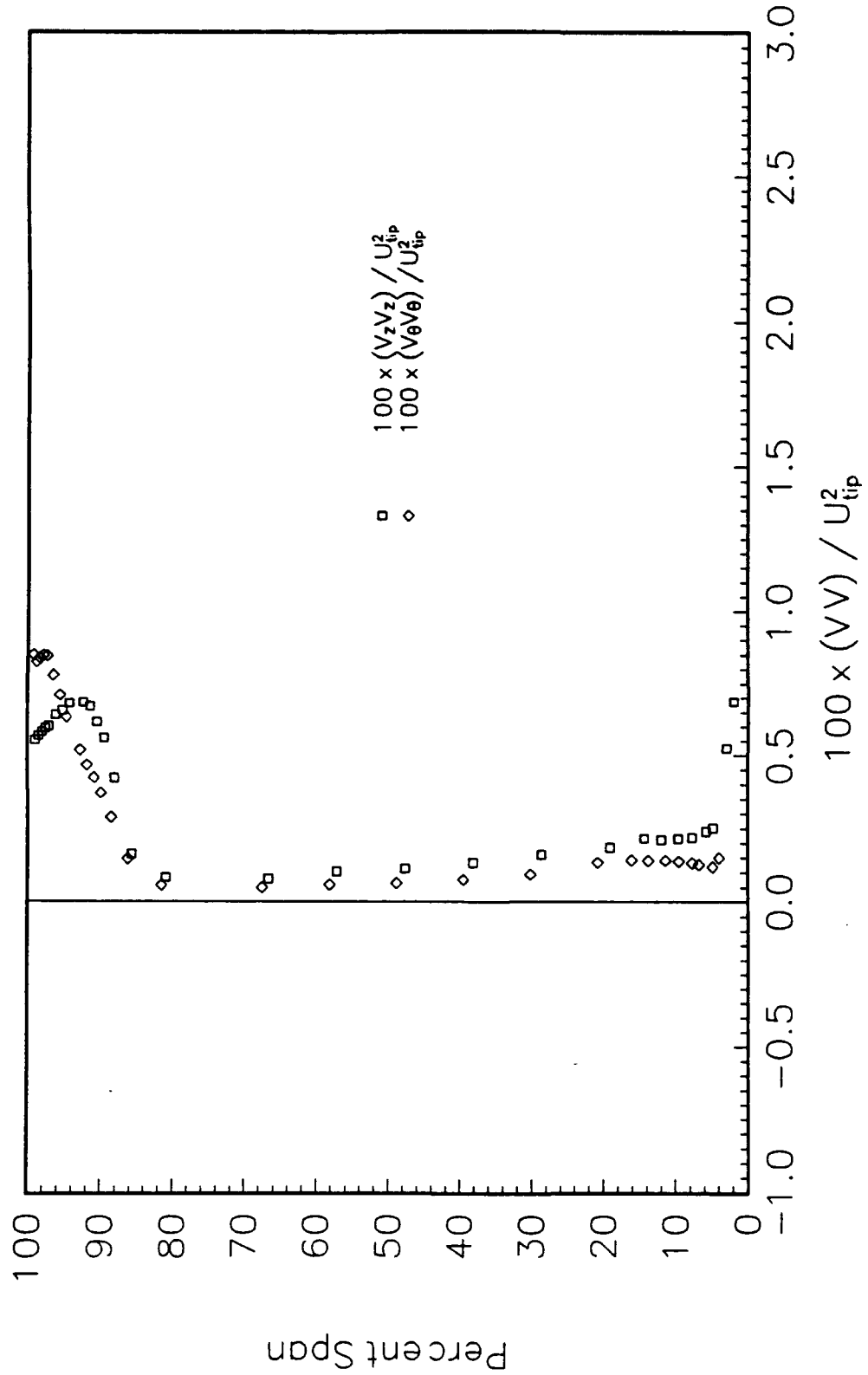


Figure 73. Nondeterministic Unsteady Velocity Correlations Measured with LDV:
b) 32.2% Chord Axially Downstream of the Rotor Tip Trailing Edge

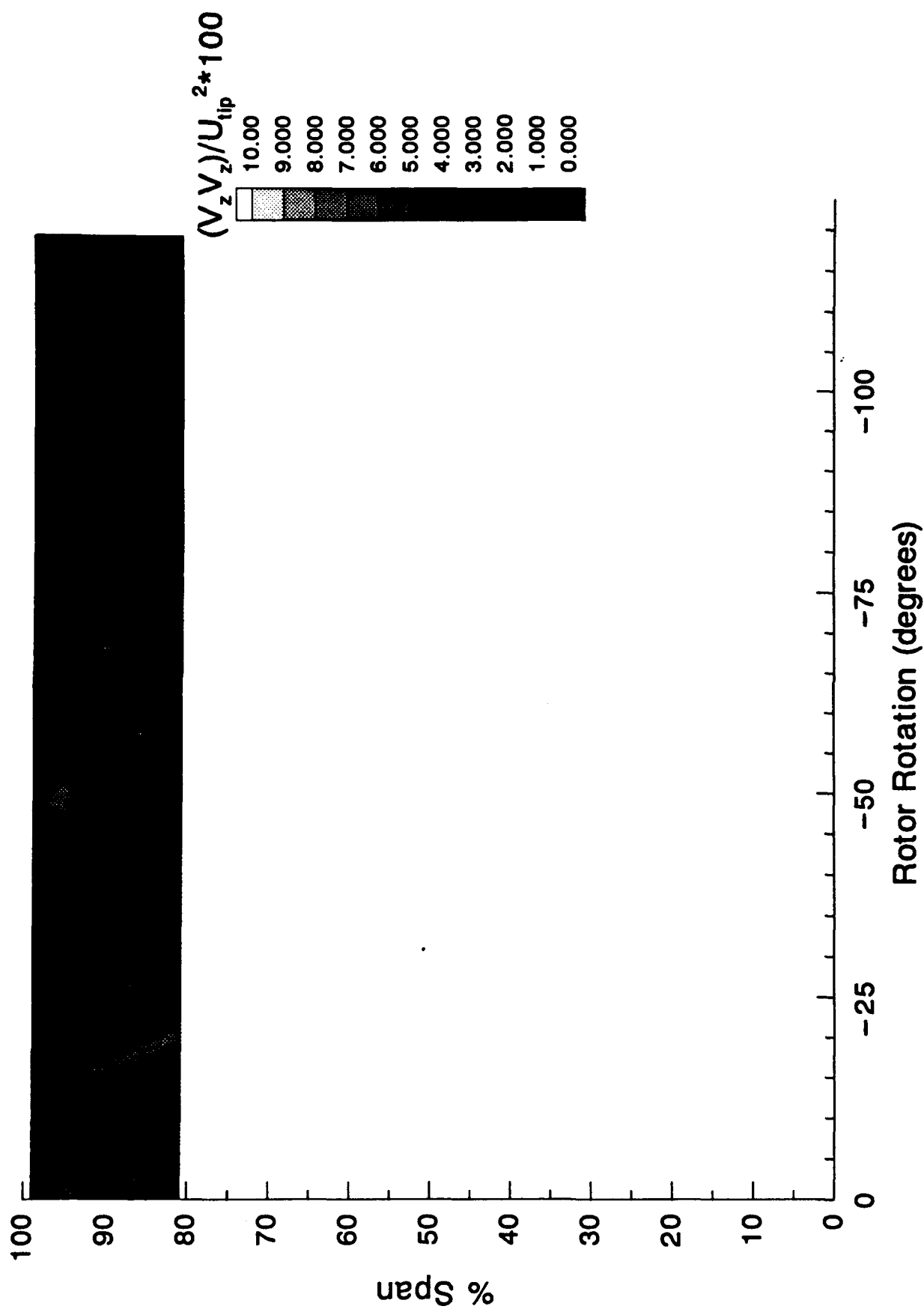


Figure 74. Nondeterministic Axial Velocity Correlation Contours of LDV Measurements:
a) 4.8% Chord Axially Downstream of the Rotor Tip Trailing Edge

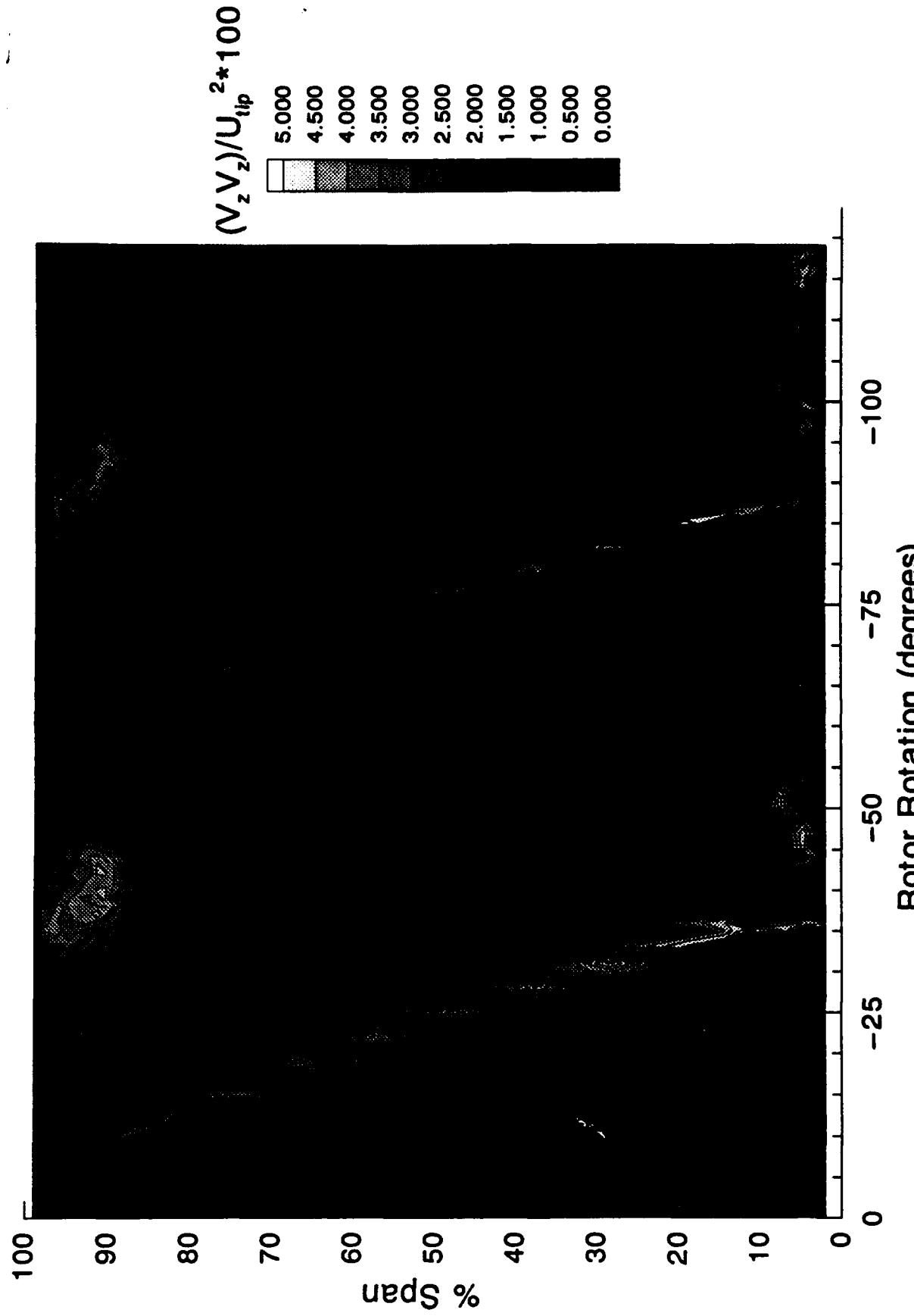


Figure 74. Nondeterministic Axial Velocity Correlation Contours of LDV Measurements:
b) 21.4% Chord Axially Downstream of the Rotor Tip Trailing Edge

217

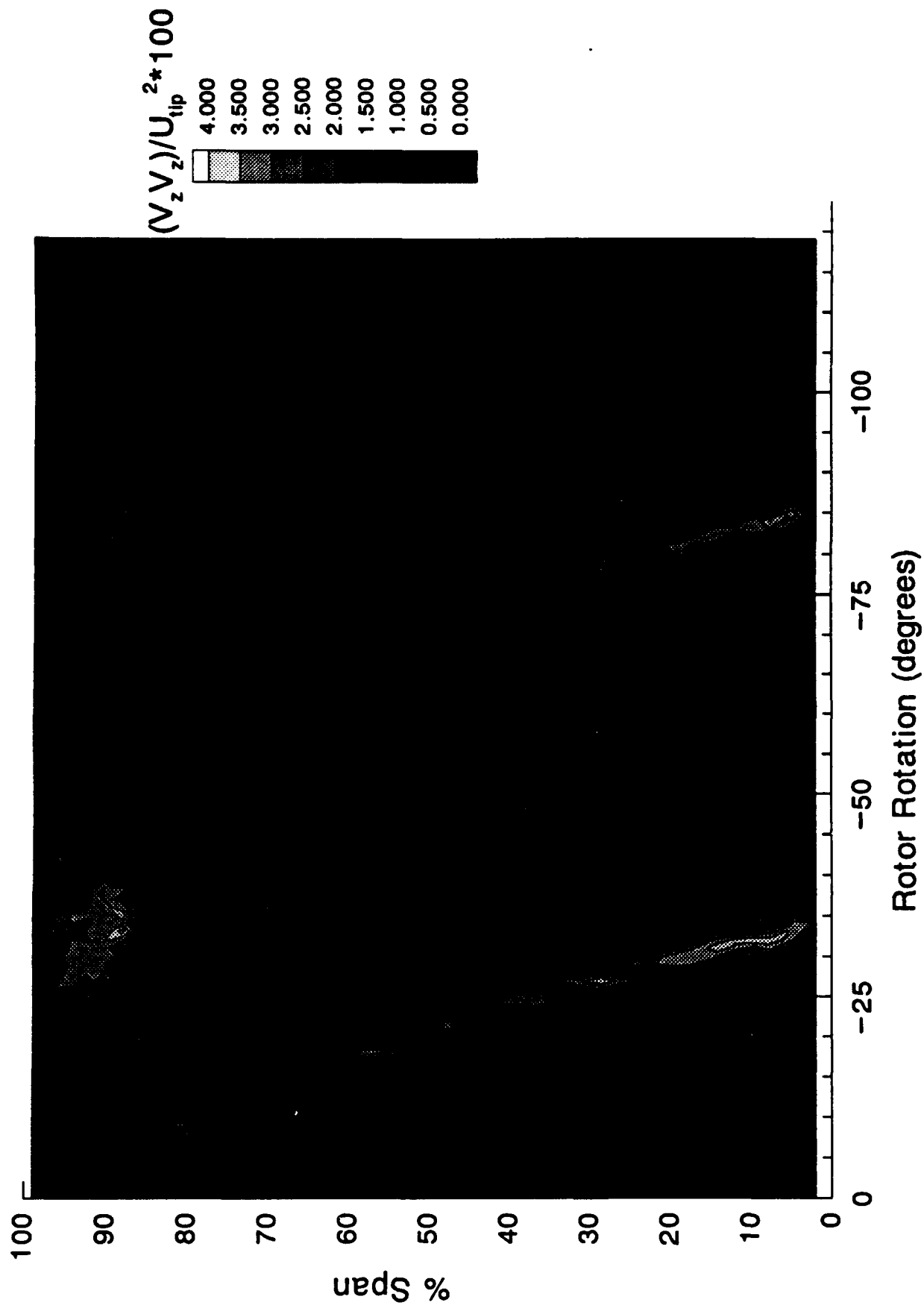


Figure 74. Nondeterministic Axial Velocity Correlation Contours of LDV Measurements:
c) 32.2% Chord Axially Downstream of the Rotor Tip Trailing Edge

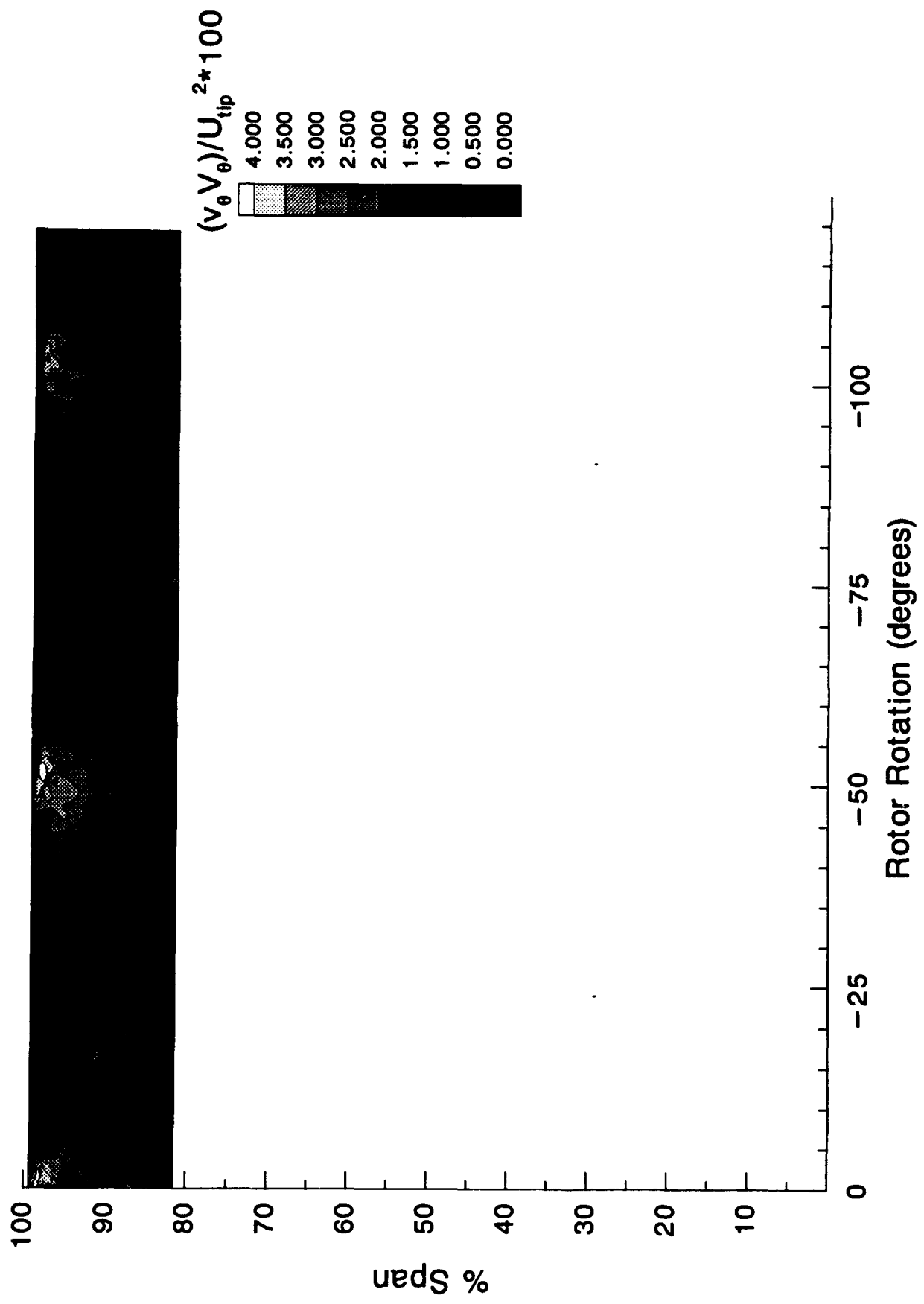


Figure 75. Nondeterministic Tangential Velocity Correlation Contours of LDV Measurements:
a) 4.8% Chord Axially Downstream of the Rotor Tip Trailing Edge

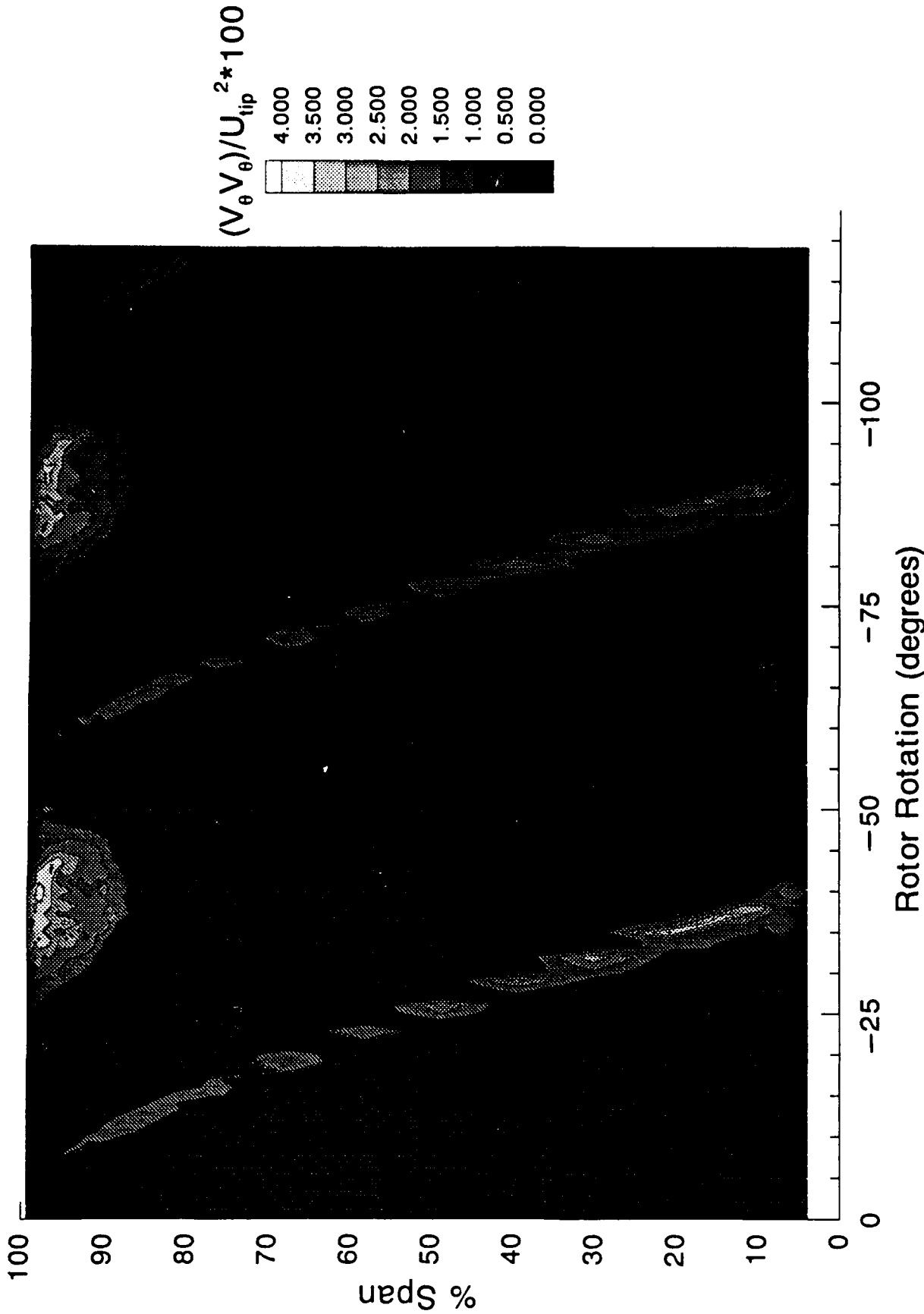


Figure 75. Nondeterministic Tangential Velocity Correlation Contours of LDV Measurements:
 b) 21.4% Chord Axially Downstream of the Rotor Tip Trailing Edge

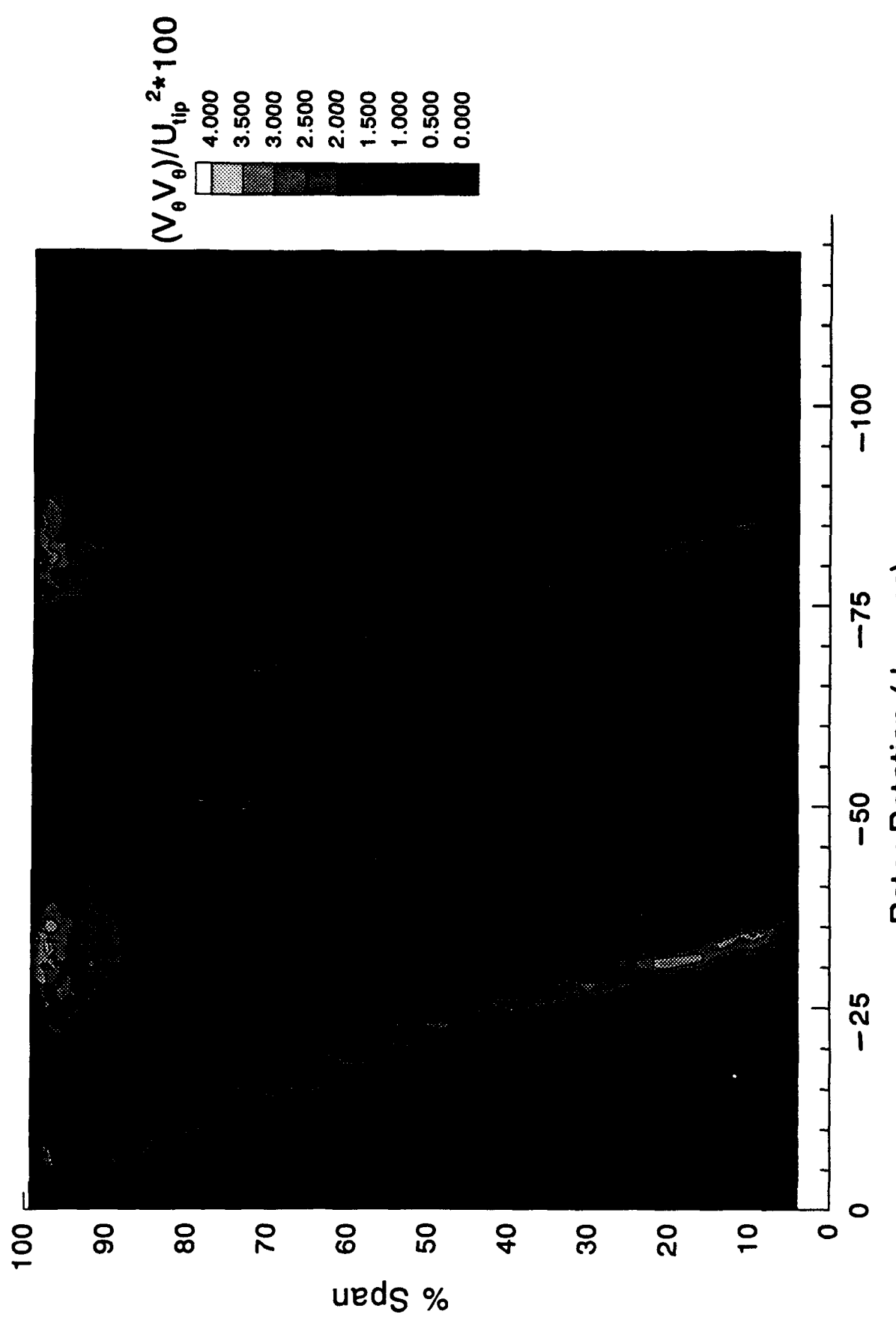


Figure 75. Nondeterministic Tangential Velocity Correlation Contours of LDV Measurements:
 c) 32.2% Chord Axially Downstream of the Rotor Tip Trailing Edge

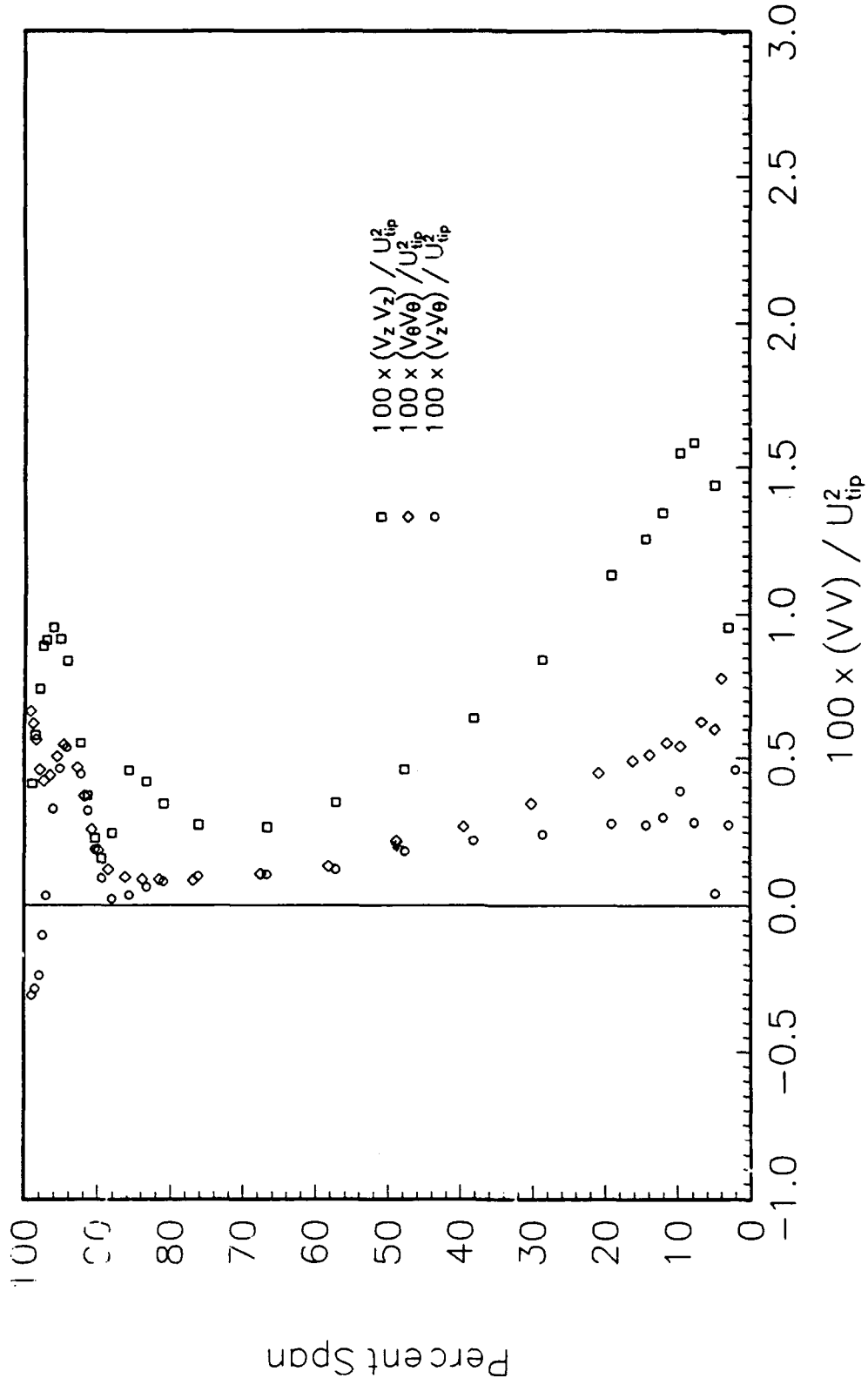


Figure 76. Deterministic Unsteady Velocity Correlations Measured with LDV:
a) 21.4% Chord Axially Downstream of the Rotor Tip Trailing Edge

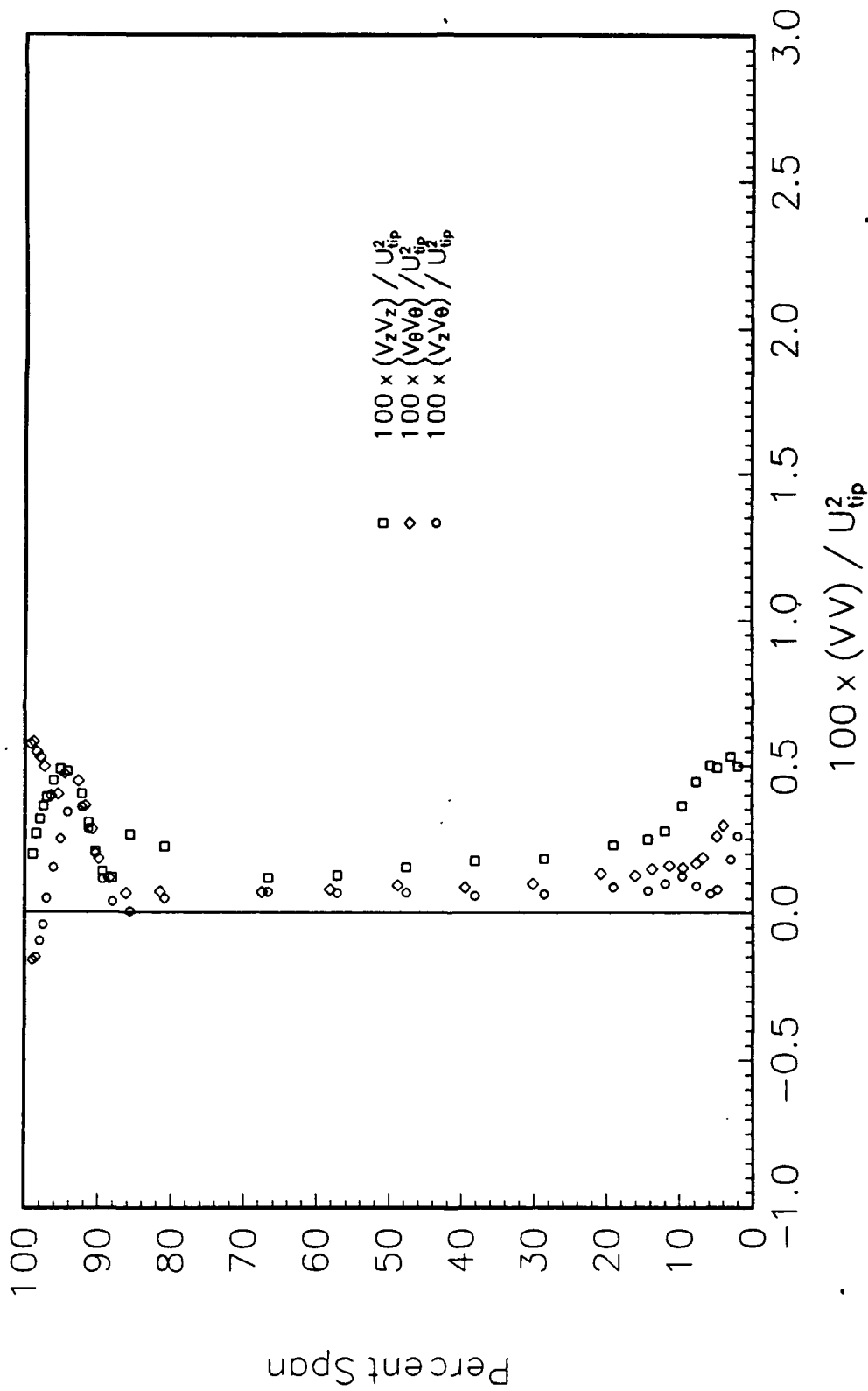


Figure 76. Deterministic Unsteady Velocity Correlations Measured with LDV:
b) 32.2% Chord Axially Downstream of the Rotor Tip Trailing Edge

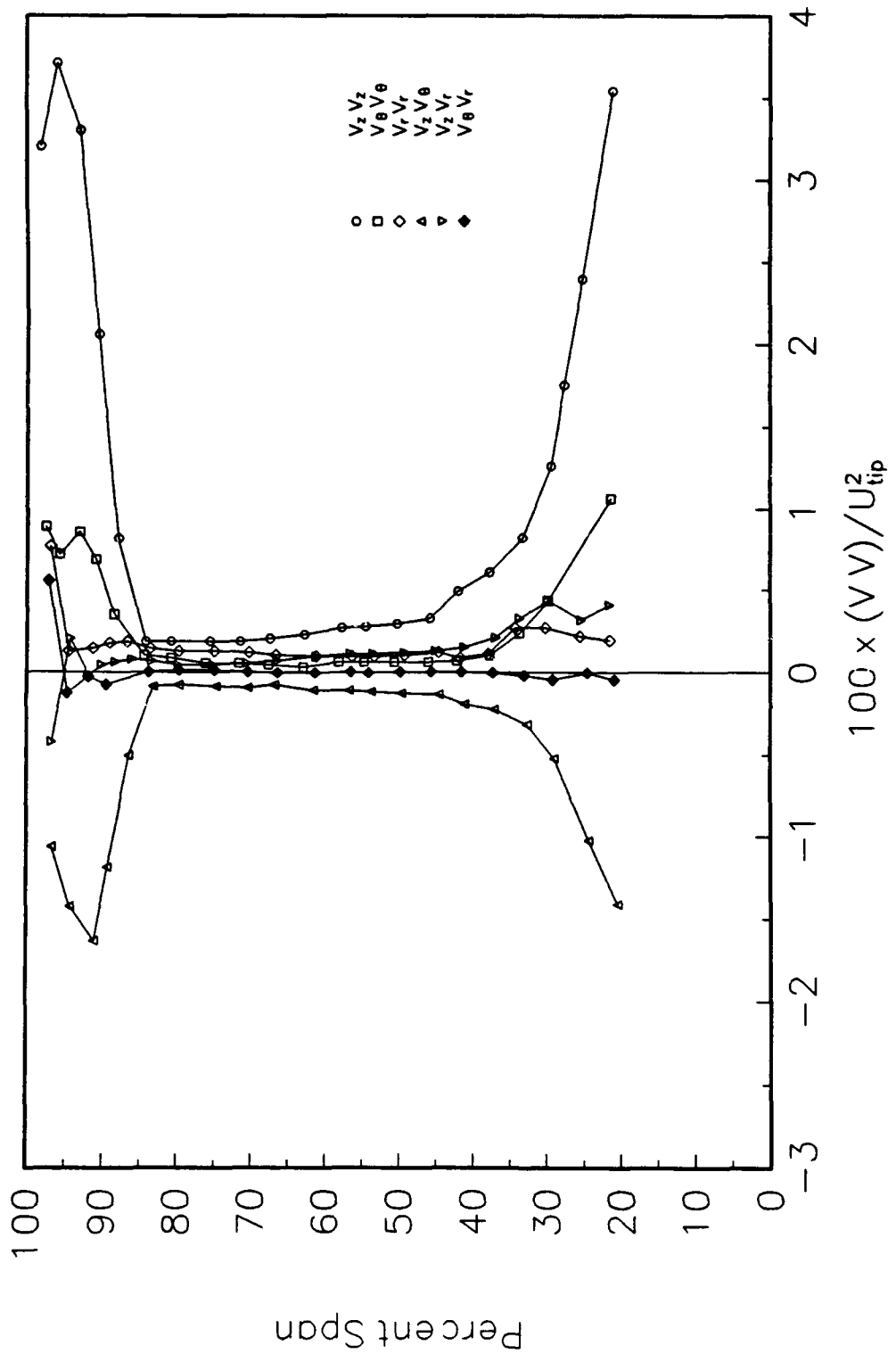


Figure 77. Deterministic Unsteady Velocity Correlations Downstream of a Rotor (Dring, Joslyn, and Hardin [1980]):
a) $\phi = 0.77$ and 10% Chord Axially Downstream of the Rotor Blade Trailing Edge

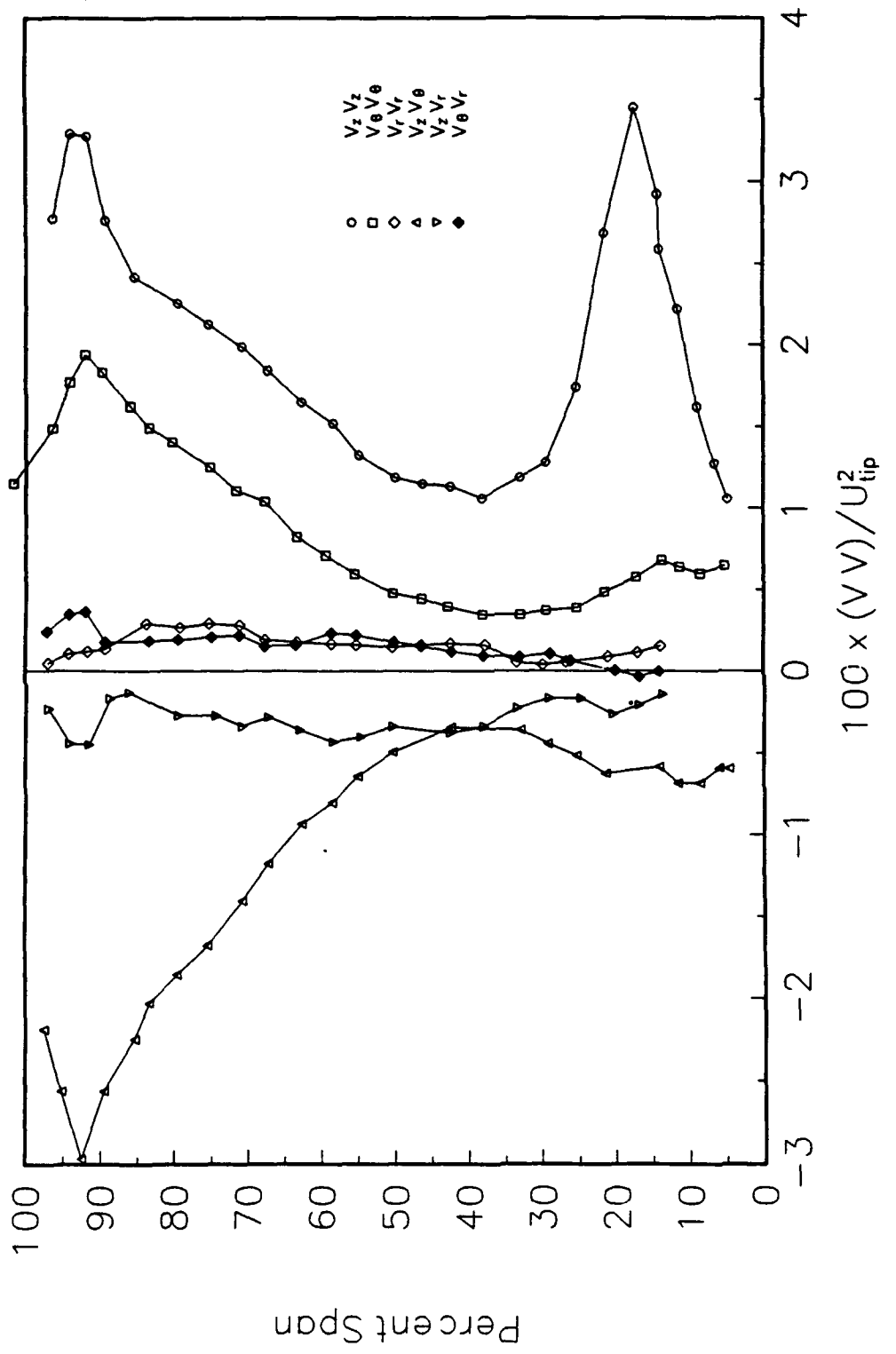


Figure 77. Deterministic Unsteady Velocity Correlations Downstream of a Rotor (Dring, Joslyn, and Hardin [1980]):
 b) $\phi = 0.59$ and 10% Chord Axially Downstream of the Rotor Blade Trailing Edge

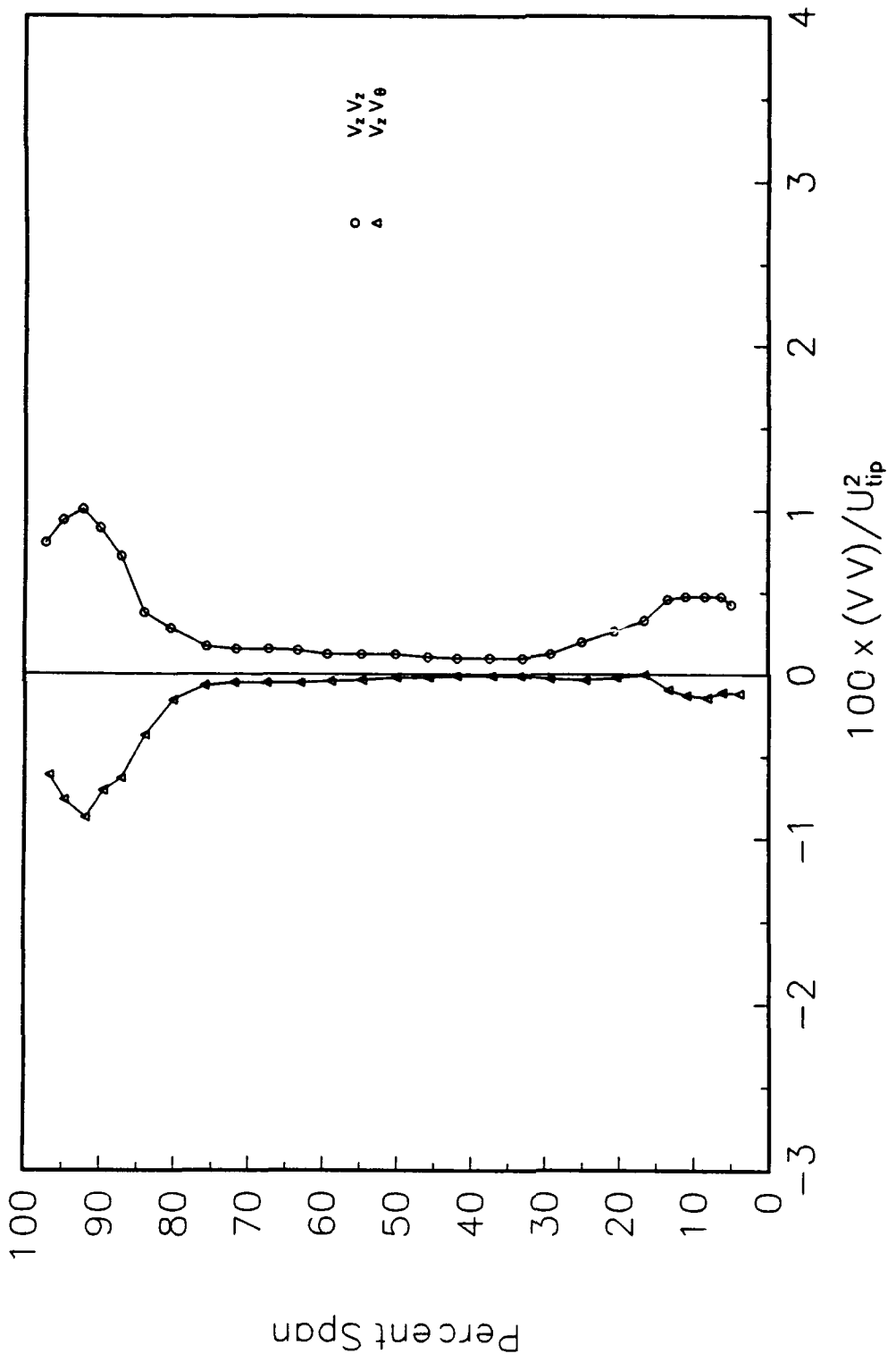


Figure 77. Deterministic Unsteady Velocity Correlations Downstream of a Rotor (Dring, Joslyn, and Hardin [1980]):
c) $\phi = 0.59$ and 50% Chord Axially Downstream of the Rotor Blade Trailing Edge

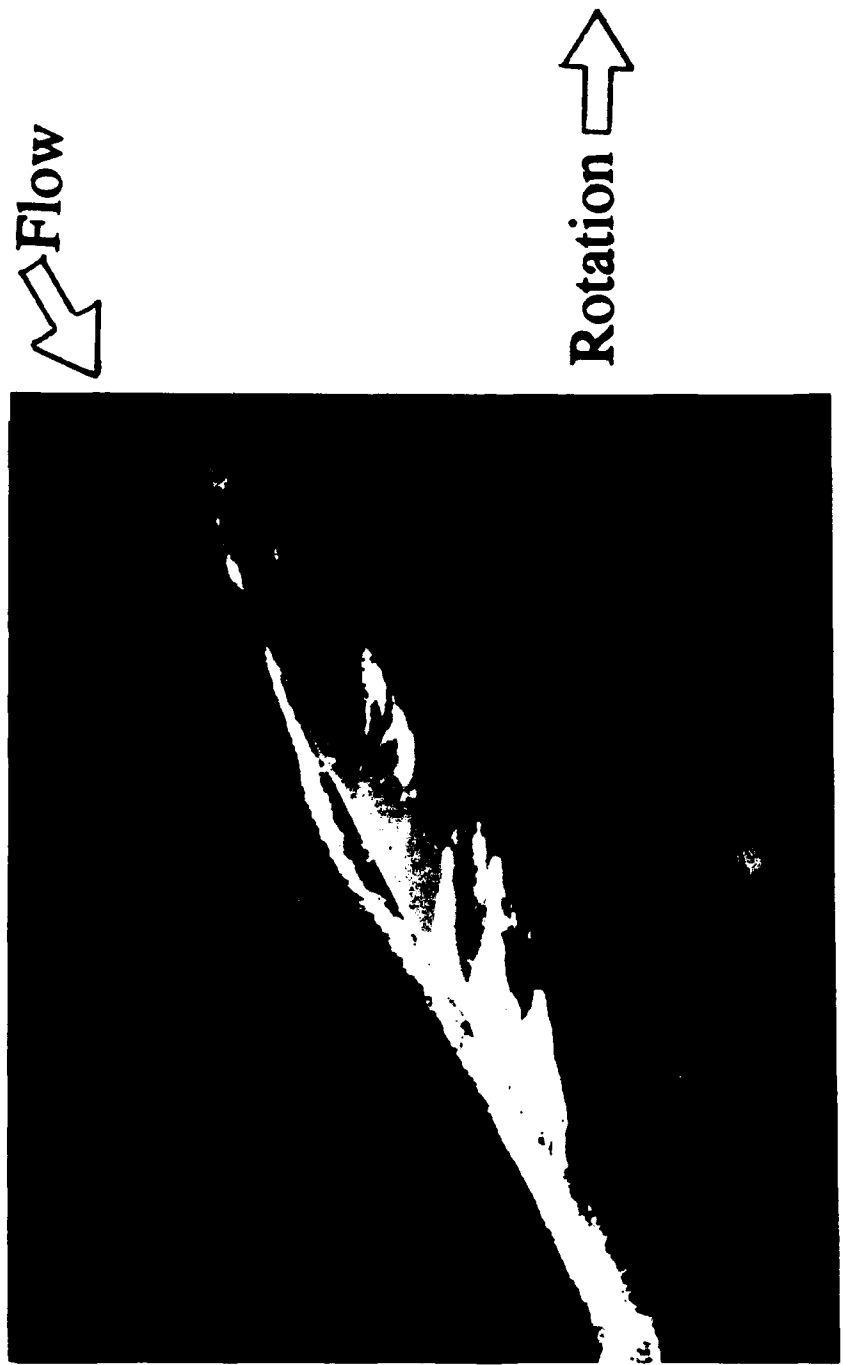


Figure 78. Photograph of a Cavitating Rotor Tip Leakage Vortex Emanating from Near the Leading Edge

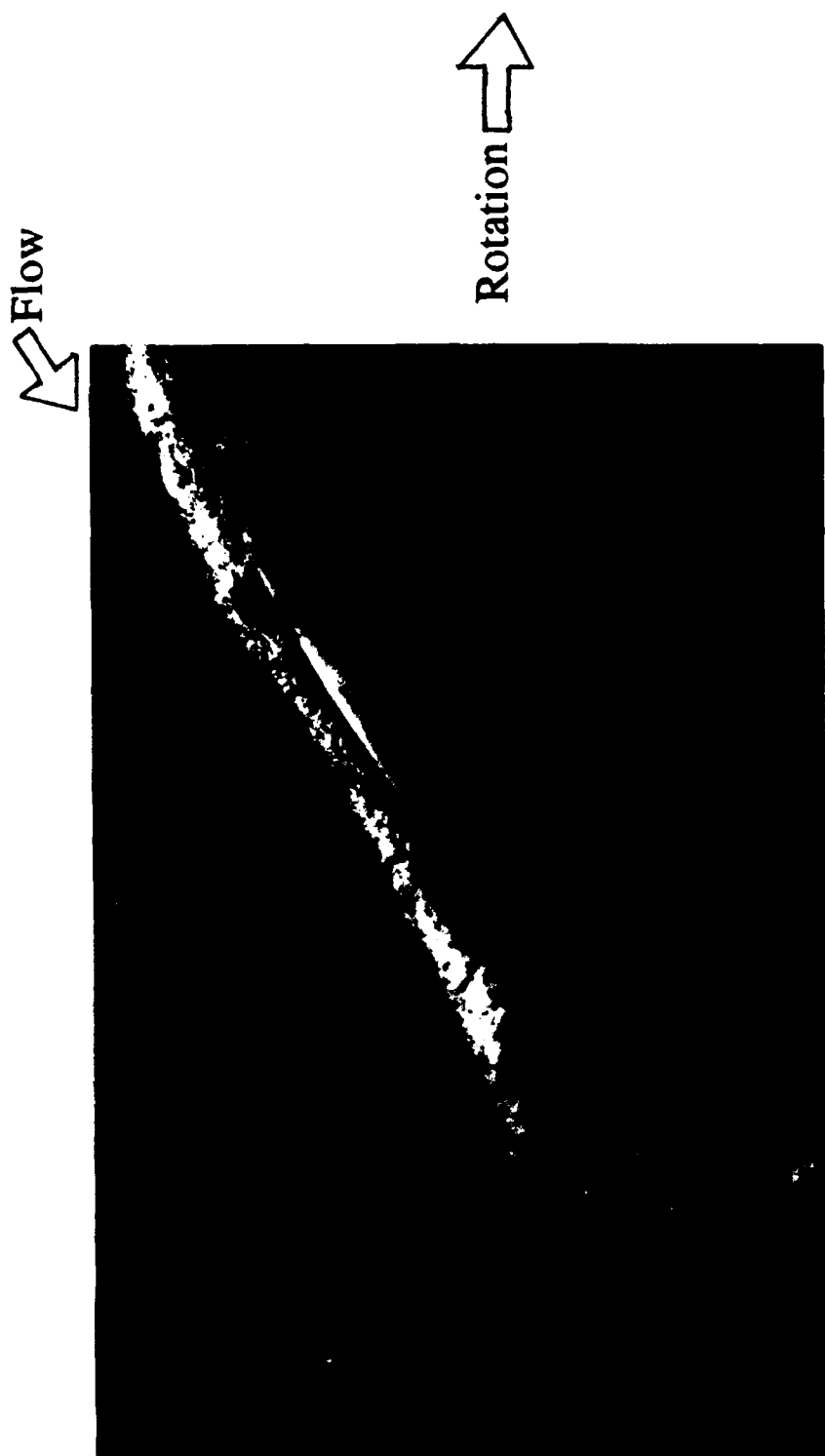
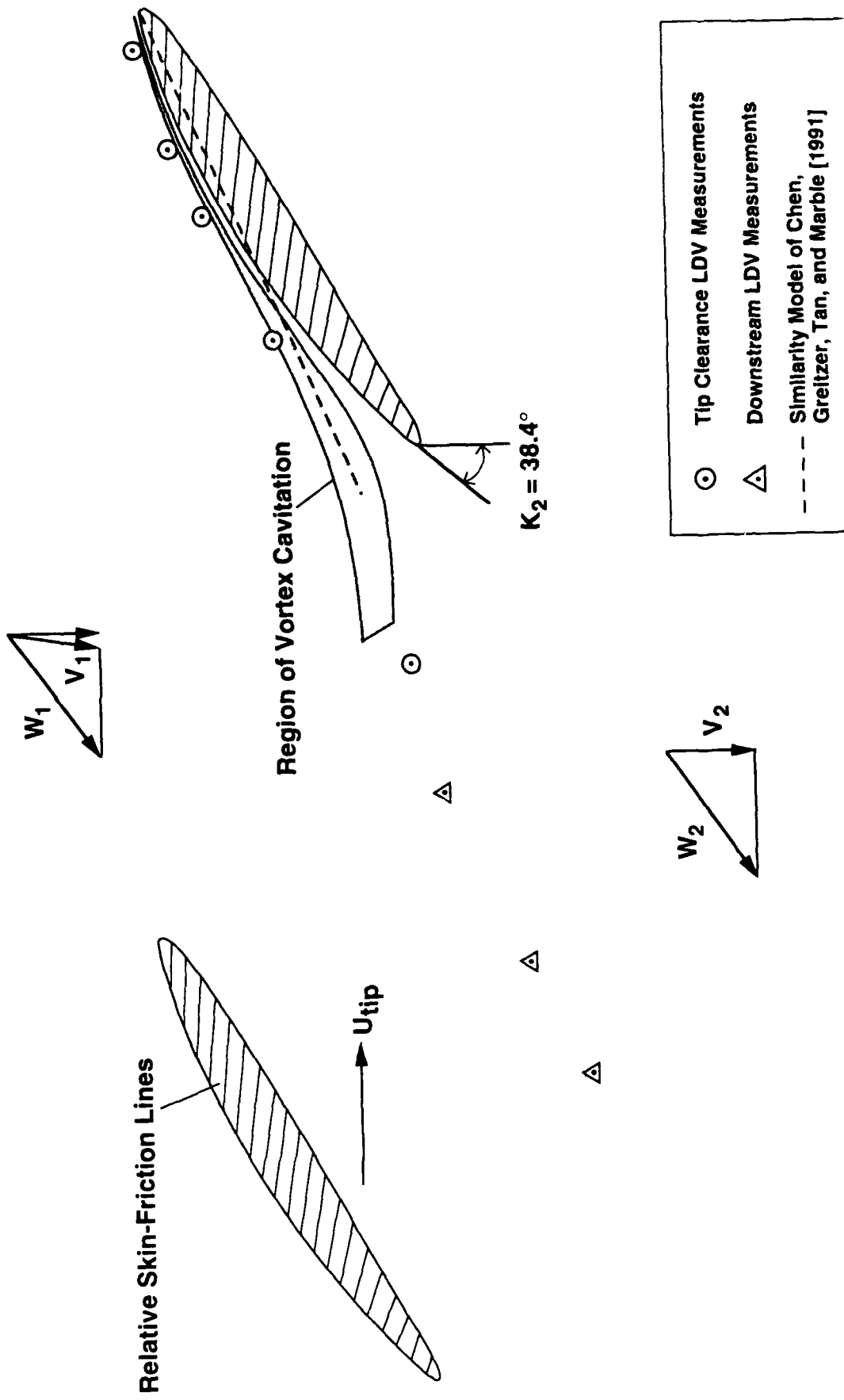


Figure 79.

Photograph of a Cavitating Rotor Tip Leakage Vortex Near the Trailing Edge



WCZ-303.01.mdf

Figure 80.

Schematic of the Relative Skin-Friction Lines Across the Rotor Blade Tip Section and the Position of the Rotor Tip Leakage Vortex in the Blade-to-Blade Plane, as Determined from Cavitation, from LDV data, and from the similarity model of Chen, Greitzer, Tan, and Marble [1991].

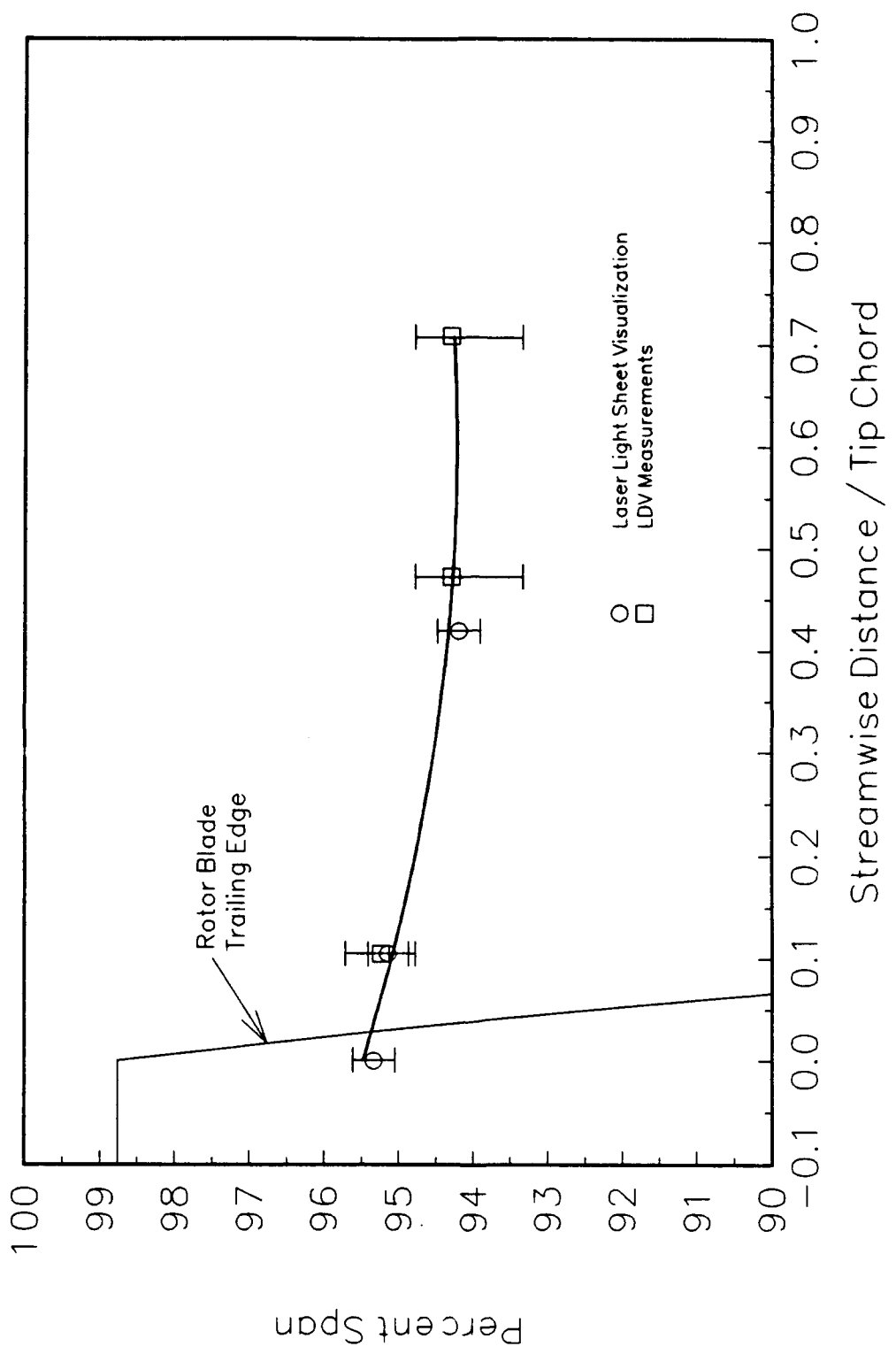


Figure 81. Spanwise Position of the Core of the Rotor Tip Leakage Vortex



Figure 82. Photograph of a Cavitating Rotor Tip Leakage Vortex with Vortex Kinking

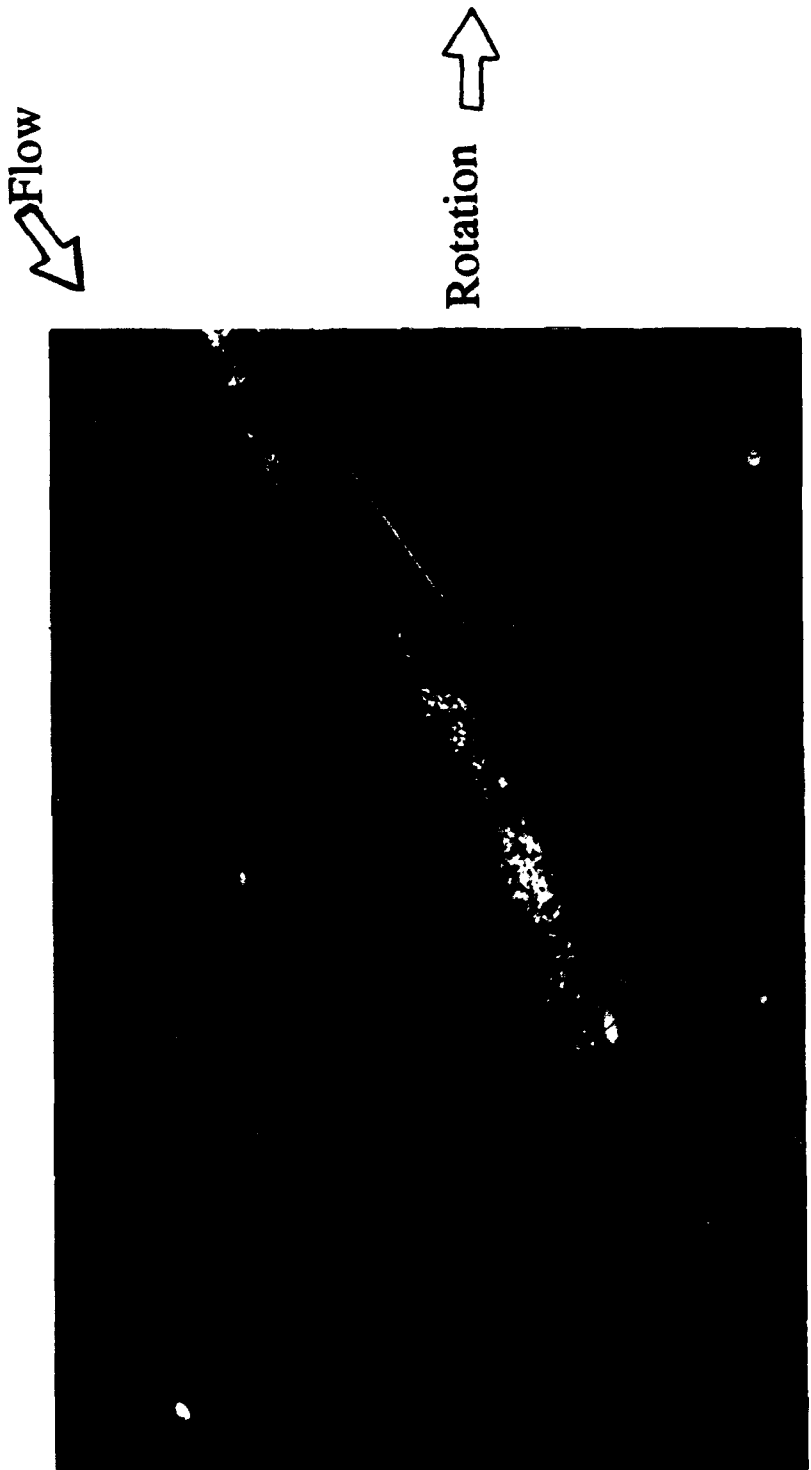


Figure 83. Photograph of a Cavitating Rotor Tip Leakage Vortex with a Streamwise Gap of Noncavitating Flow

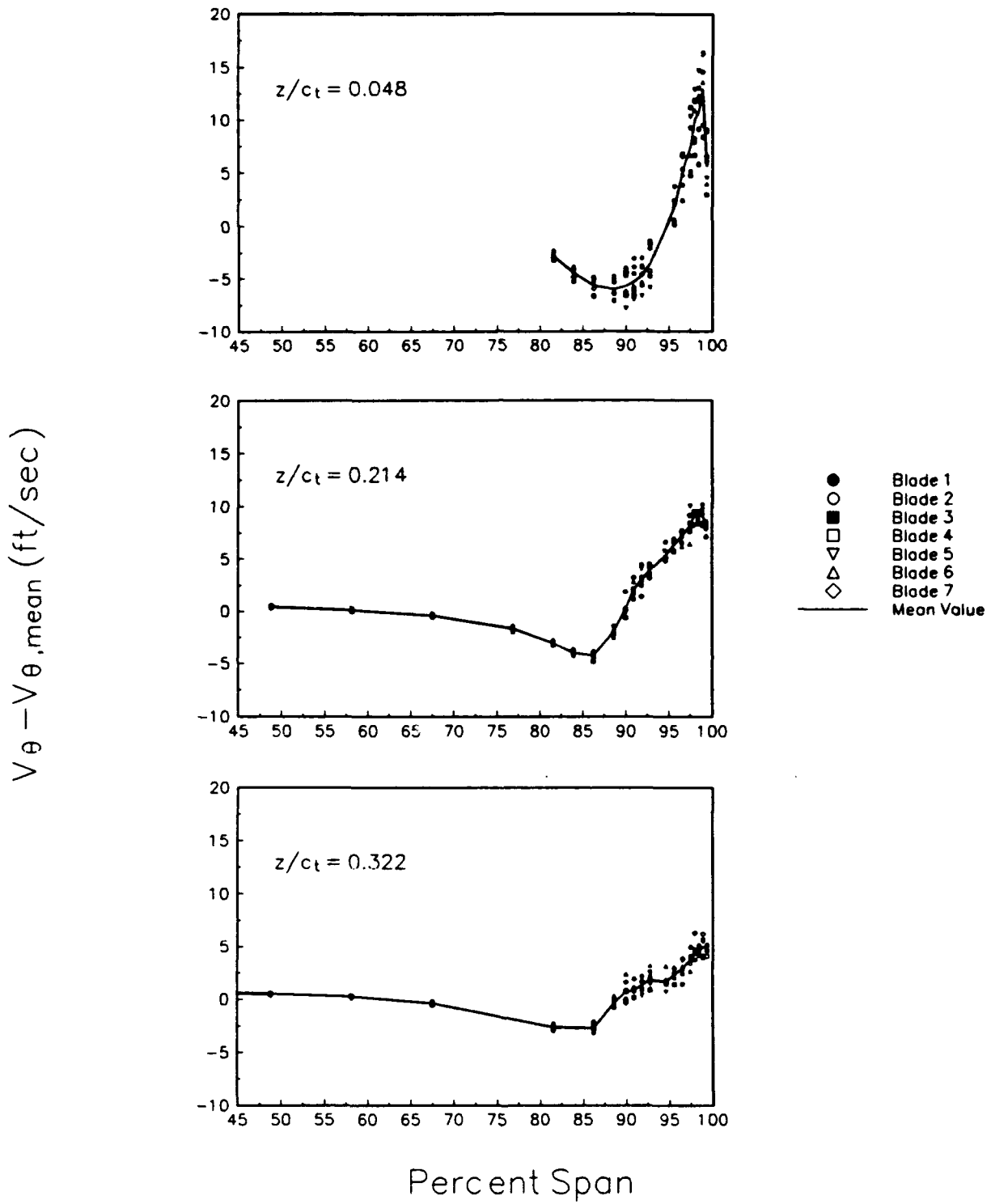


Figure 84. Vortex Tangential Velocity Distributions for the Rotor Tip Leakage Vortices Measured 4.8%, 21.4%, and 32.2% Chord Axially Downstream of the Rotor Tip Trailing Edge

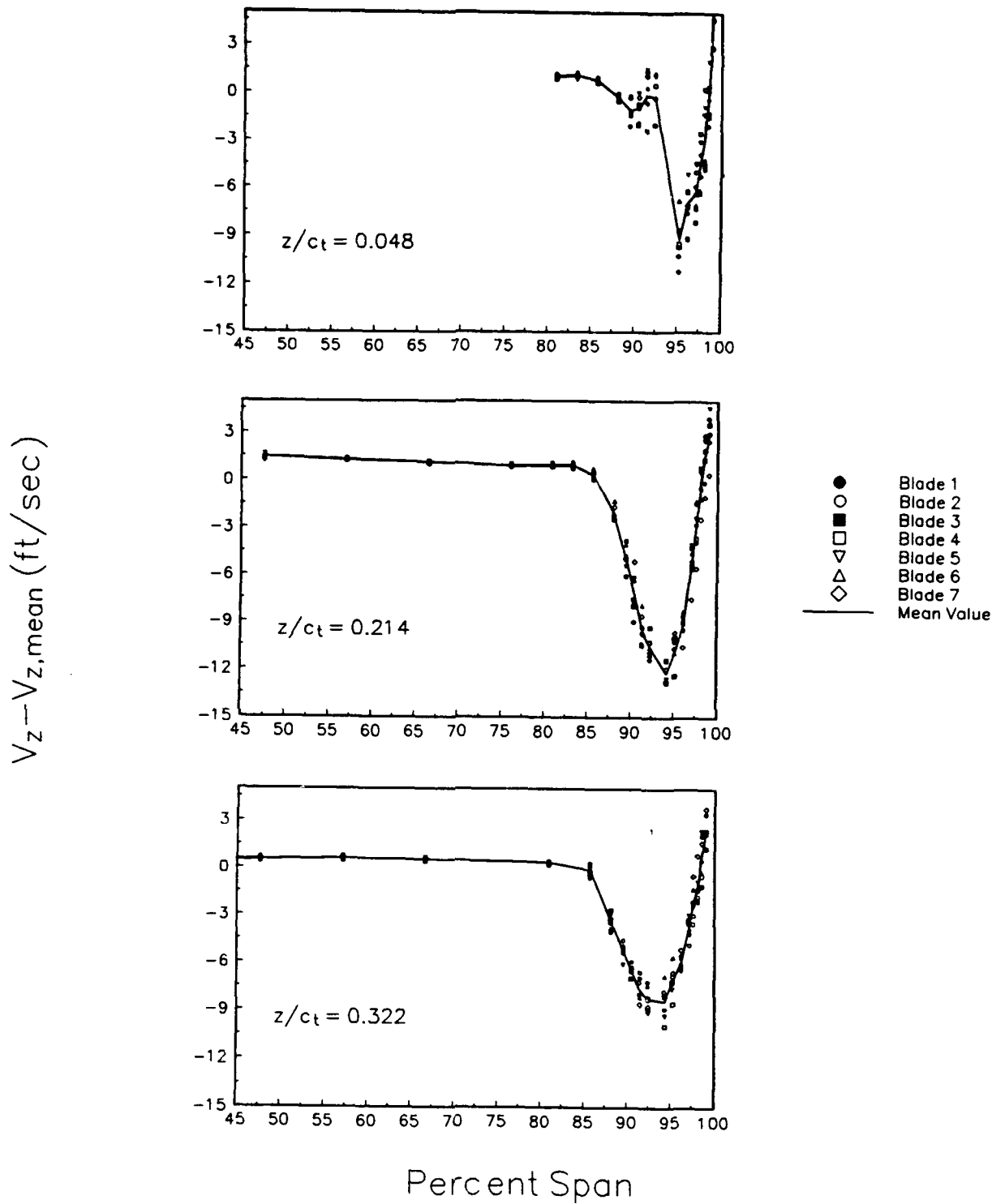


Figure 85. Vortex Axial Velocity Distributions for the Rotor Tip Leakage Vortices Measured 4.8%, 21.4%, and 32.2% Chord Axially Downstream of the Rotor Tip Trailing Edge

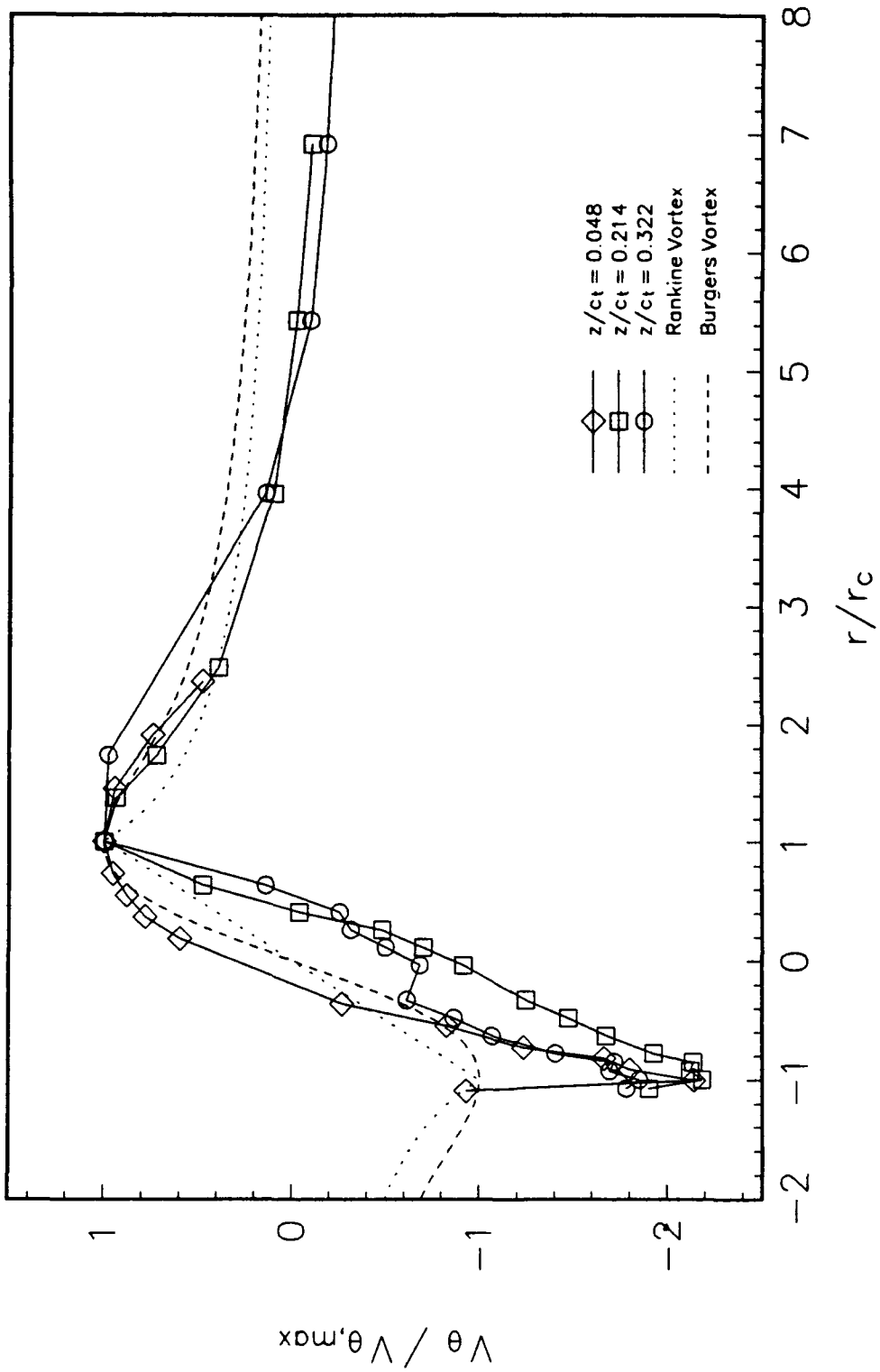


Figure 86. Nondimensional Tangential Velocity Distributions for the Rotor Tip
Leakage Vortices--Measurements and Ideal Formulations

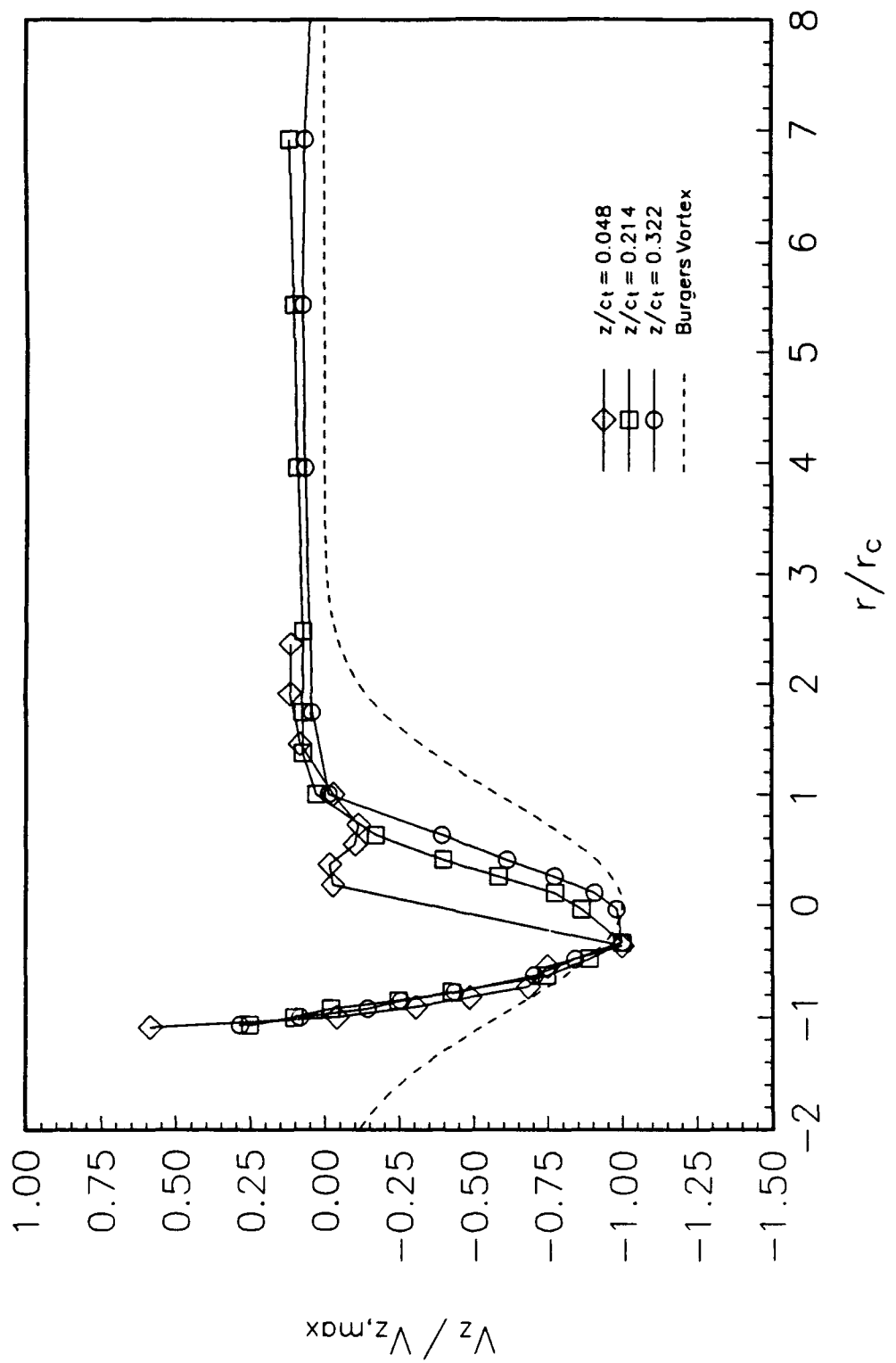


Figure 87. Nondimensional Axial Velocity Distributions for the Rotor Tip Leakage Vortices—Measurements and Ideal Formulations

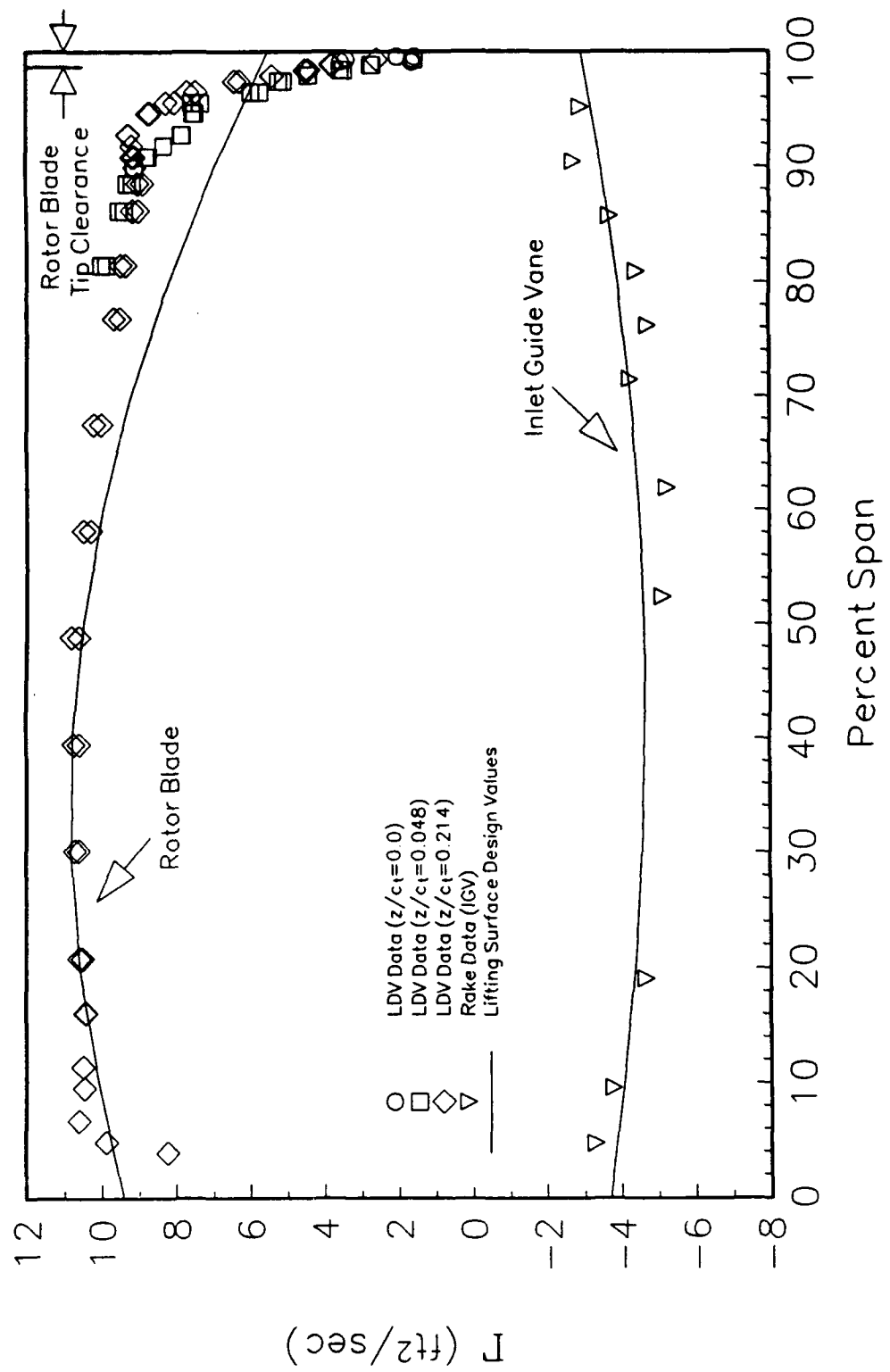


Figure 88. Spanwise Distribution of Circulation on the Inlet Guide Vanes and Rotor Blades

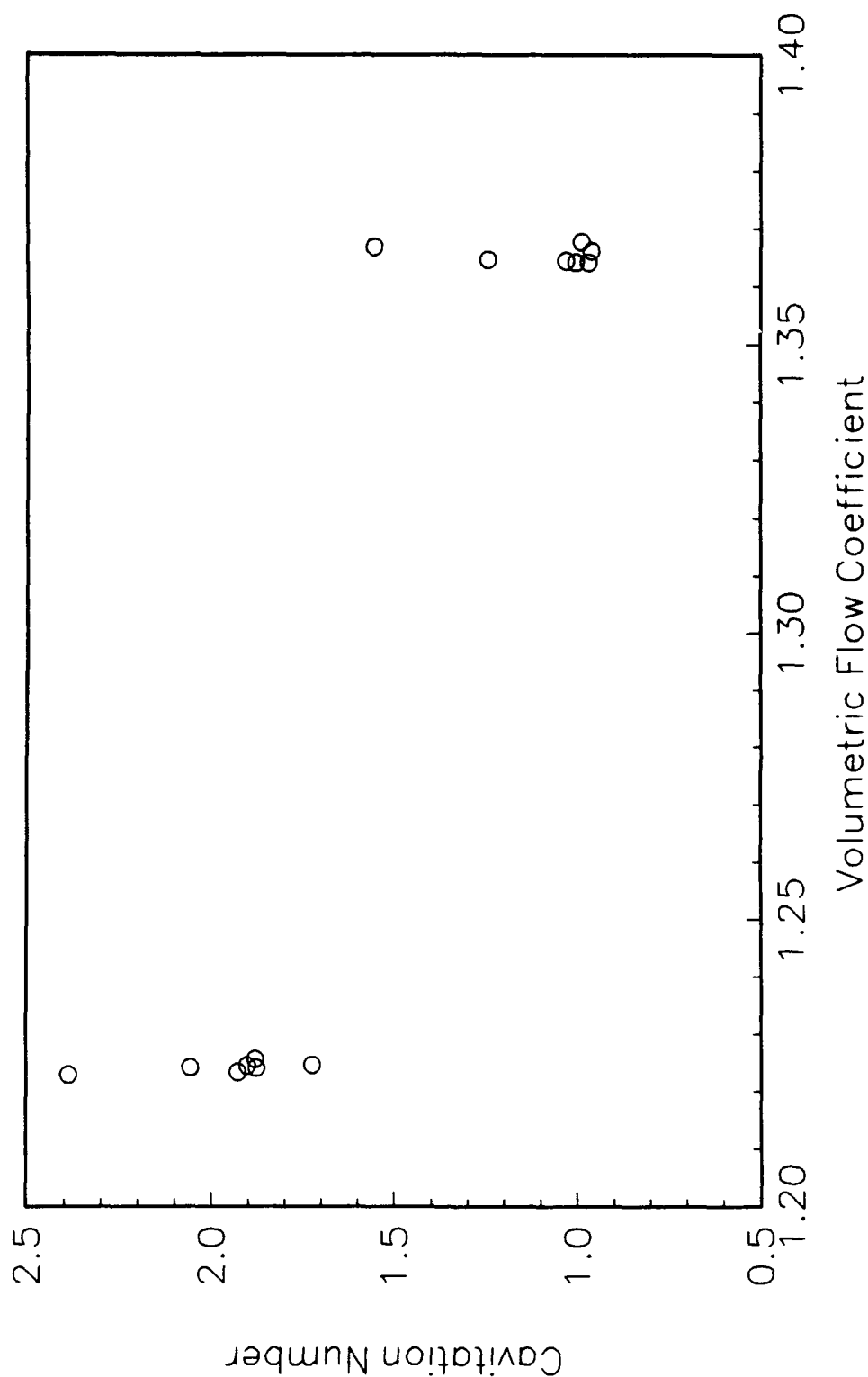


Figure 89. Cavitation Inception at Volumetric Flow Coefficients of 1.36 and 1.22

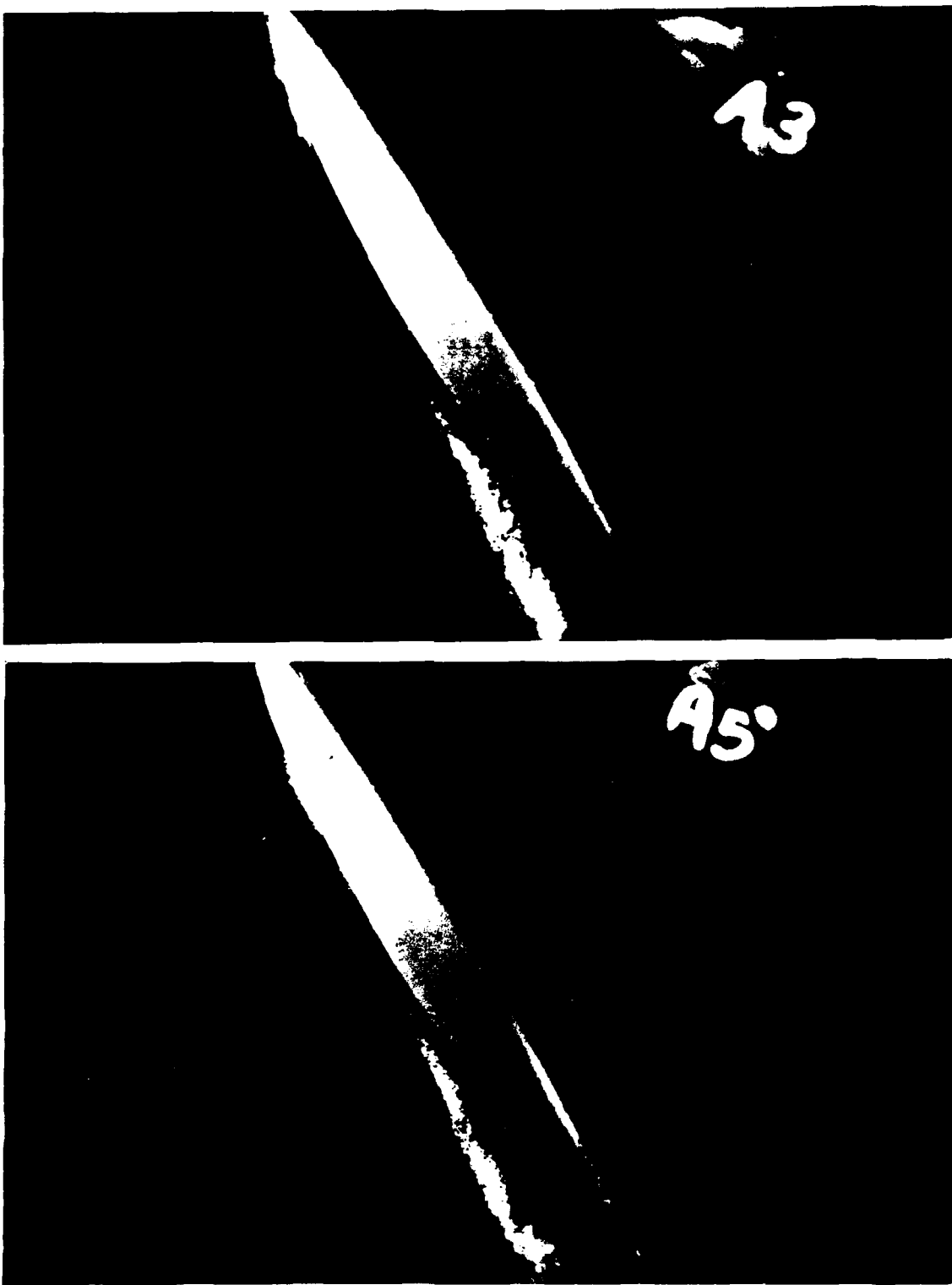


Figure 90. Photographs of a Rotor Blade with Vortex Cavitation ($\sigma=0.99$) and a Rotor Blade with Vortex and Gap Cavitation ($\sigma=1.55$)

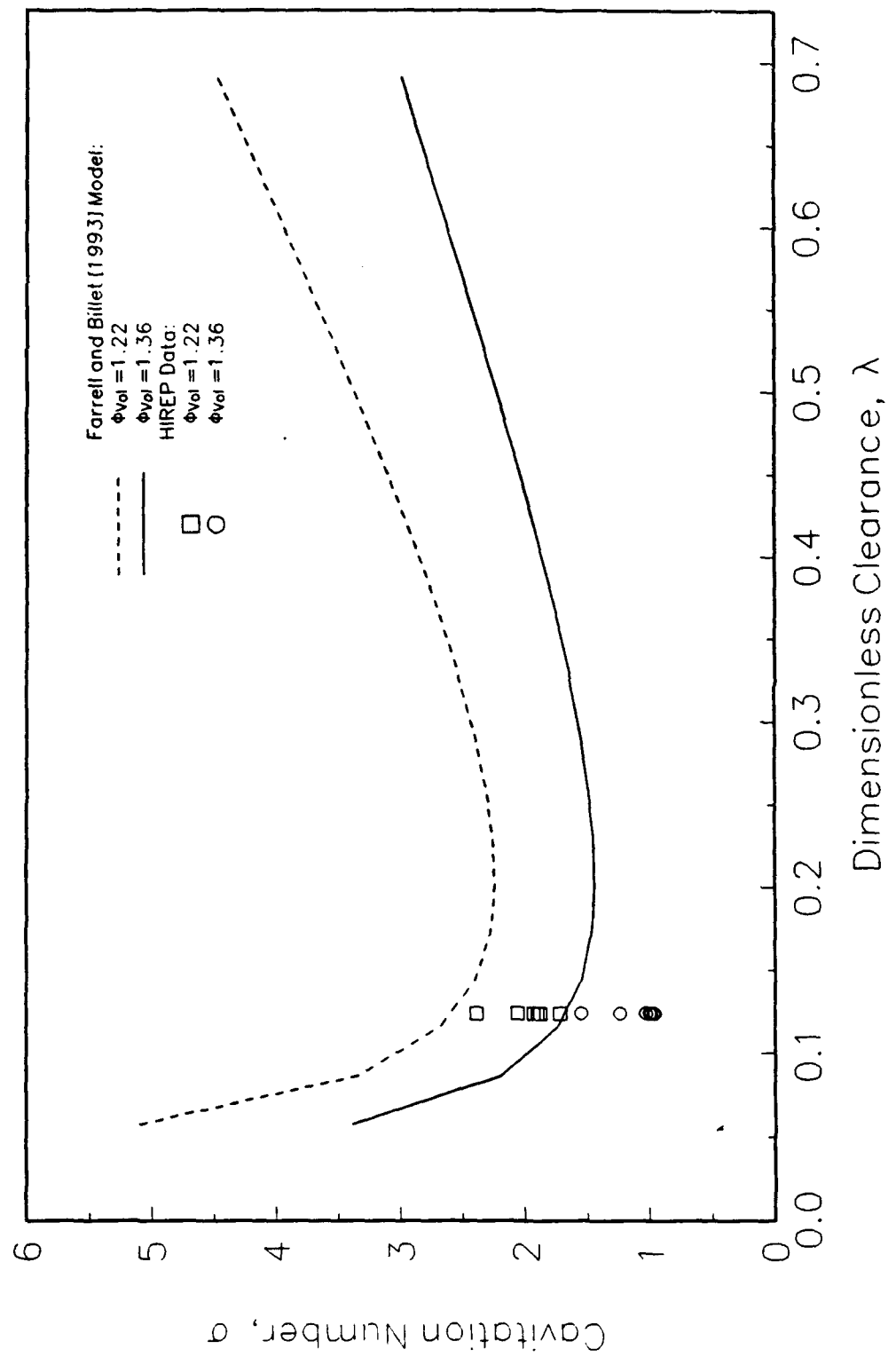


Figure 91. Calculations of Cavitation Inception Using the Model of Farrell [1992]

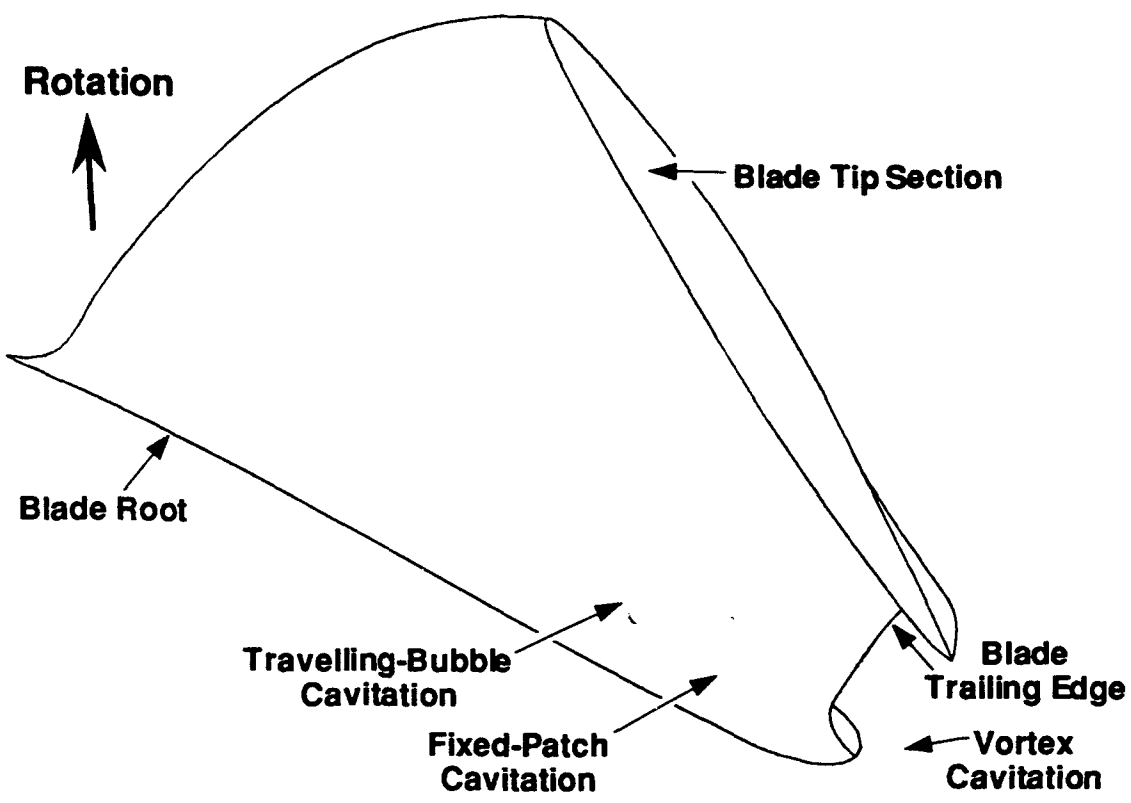


Figure 92. Schematic and Photograph of Cavitation on the Rotor Blade Suction Surface

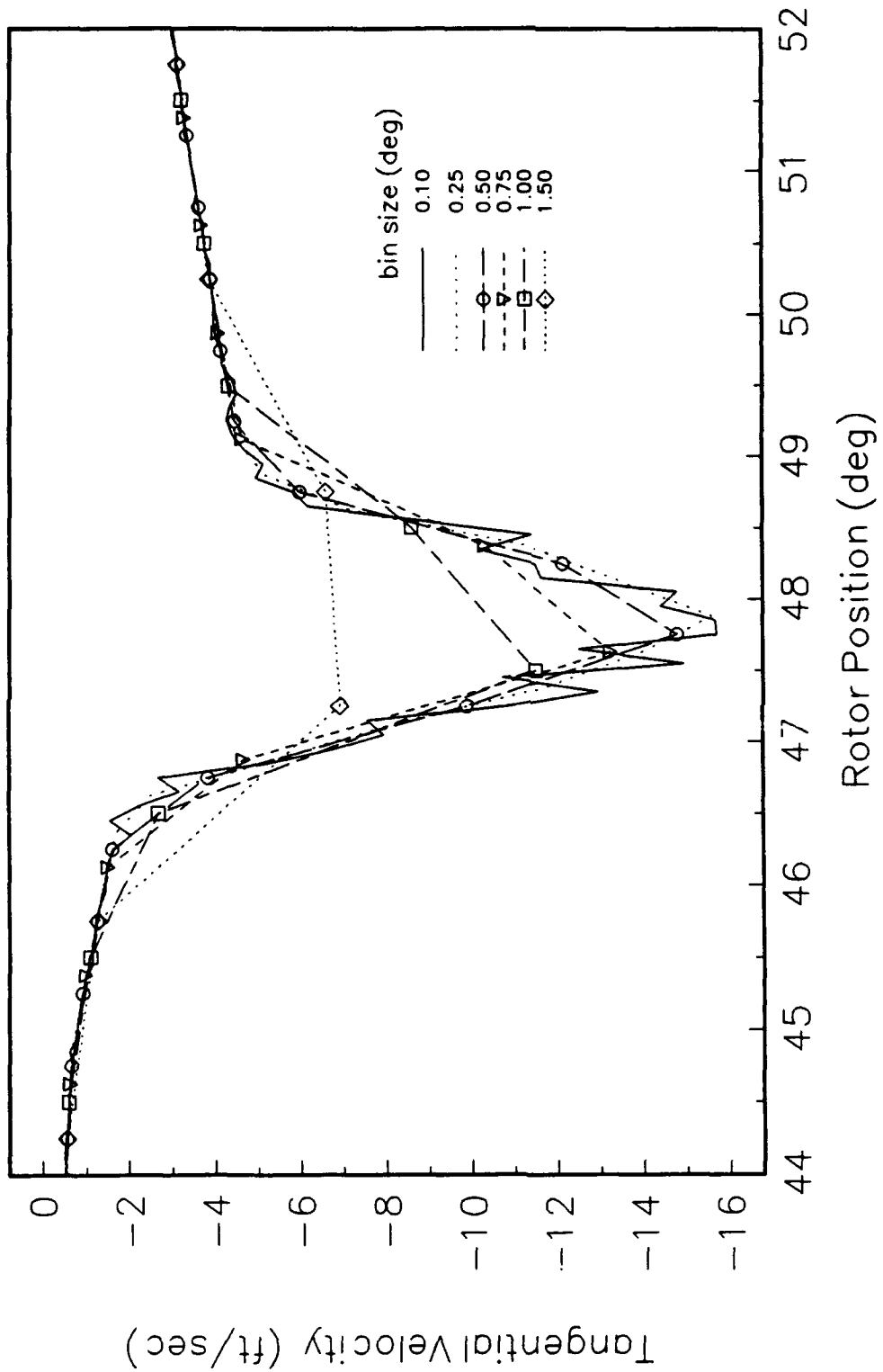


Figure 93. LDV Bin Size Dependence for a Rotor Blade Wake (Tangential Velocity at 76.2% Span and 2.5% Chord Axially Downstream of the Rotor Tip Trailing Edge)